WSRC-MS-93-479

THE EFFECT OF SPACER RIBS ON LEDINEGG TYPE FLOW INSTABILITIES (U)

by

D. A. Coutts

Westinghouse Savannah River Company
Savannah River Site
Aiken, South Carolina 29808

A document prepared for:
dissertation defense
at Columbia, SC
from 10/15/93

DOE Contract No. **DE-AC09-89SR18035**

Preliminary Data -- 9 September 1993

THE EFFECT OF SPACER RIBS ON LEDINEGG TYPE FLOW INSTABILITIES

David Allan Coutts

Bachelor of Science
Western New England College, 1980

Master of Engineering
University of South Carolina, 1985

Submitted in Partial Fulfillment of the Requirements

for the Degree of Doctor of Philosophy in the

College of Engineering

Department of Mechanical Engineering

University of South Carolina

1993

Major Professor

Committee Member

Chairman, Examining Committee

Committee Member

Dean of Graduate School

Available to DOE and DOE contractors from the Office of Scientific and Technical Information, P. O. Box 62, Oak Ridge, TN 37831; prices available from (615) 576-8401.

Available to the public from the National Technical Information Service, U. S. Department of Commerce, 5285 Port Royal Rd., Springfield, VA 22161

ACKNOWLEDGMENTS

I would like to express my thanks to the staff of the Heat Transfer Laboratory at the Department of Energy's Savannah River Site, who supported the test efforts presented in this dissertation. Deserving of special mention are the test engineer, Mark Fowley: the design engineer, George Richardson; the designer, Vince Walker: and the technician, Andy Foreman. Without their help this test program would not have been a success. I am also grateful to Drs. Steimke and Qureshi, and my manager Dave Muhlbaier, for their sound advice and support during the test program.

I would also like to express by sincere appreciation to my advisor, Prof. Larry Hawkins, for his advisement and help in the completing the program requirements and Phyllis Coleman who has supported APOGEE students so enthusiastically and efficiently.

Special thanks go to my grandparents, parents and brother for their nurturing which emphasized a love of learning and discovery.

In addition I would like to thank my wife, Nancy, for her unending patience, support, and understanding throughout the course of this endeavor.

CONTENTS

ILLUSTRATIONS

Figure Page

TABLES

Table | Page

Table Page

Table | Page

Table Page

Table | Page

ABBREVIATIONS

CHF	Critical heat flux
DNB	Departure from nucleate boiling
EHL	End of heated length
FI	Flow instability
HTL	Savannah River Site Heat Transfer Laboratory
HTRF	Heat Transfer Research Facility (Columbia University)
L/D	Length to diameter ratio
M&TE	Measurement and testing equipment
NVG	Net vapor generation
OFI	Onset of flow instability
ONB	Onset of nucleate boiling
OSV	Onset of significant void
SHL	Start of heated length
SI	Le Système International d'Unitès
SRS	Savannah River Site

SYMBOLS

A_f	flow area [m^2]
A_h	heated area [m^2]
a	width of [illegible]dular cross-section [m]
b	depth of rectangular cross-section [m]
c_f	specific heat of inner liquid [J/kg·C]
D	channel diameter for round tubes or hydraulic diameter for non-circular cross-sections [m]
D_e	equivalent diameter defined in equation XX [m]
D_h	heated equivalent diameter [m]
G	mass velocity, [kg/m^2·s]
g	acceleration due to gravity
Δh_i	inlet subcooling in terms of enthalpy [kJ/kg]
h_{fg}	latent heat of vaporization [kJ/kg]
ΔL	differential length [m]
L	length
L_b	distance from incipient boiling to the heated section exit
$L_{b,s}$	distance required to bring the fluid from T_{ib} to T_{sat} where T_{sat} is evaluated at the exit conditions.
L_h	length of heated plate [m]
N	number of samples
$(dp_f/dz)_{LO}$	frictional pressure gradient for flow with total mass flux and liquid-phase properties

Δp	pressure drop [Pa]
Δp_{0-1}	inlet pressure loss from plenum to heated channel caused by contraction
Δp_{1-2}	heated section pressure drop
Δp_{2-3}	exit pressure loss from heated channel caused by expansion
Δp_b	pressure drop over length L_b due to friction and momentum
$\Delta p_{b,s}$	pressure drop for an adiabatic tube with a fluid temperature at T_{ib} and a length $L_{b,s}$
dp_f/dz	frictional pressure gradient
Δp_t	pressure drop [Pa]
p	pressure [Pa]
p_{ehl}	pressure at end of the heated length [Pa]
p_{in}	inlet pressure
p_L	pressure in the liquid feed piping
p_o	time averaged pressure.
Q	volumetric flow rate [m^3/s]
q	rate of heat transfer
S	sample standard deviation, $\sum_{i=1}^{N} \frac{(x_i - \bar{X})^2}{N-1}$
$t_{\alpha/2}$	two-tailed Student-t value at 95% confidence
ΔT_{sat}	wall superheat; difference between the wall temperature and the saturation temperature of the fluid [°C]
ΔT_{sub}	subcooling; difference between saturation temperature and coolant temperature [°C]
T_{ib}	bulk fluid temperature at incipient boiling
T_{sat}	saturation temperature at a specified local pressure

u	coolant velocity [m/s]
x	distance along the lateral axis [m]
x	vapor quality
$\bar{X}$	sample average, $\frac{1}{N}\sum_{i=1}^{N} x_i$
y	distance along the normal axis (i.e., distance from the heated surface) [m]
z	distance along the longitudinal axis (i.e., distance from start of heated length) [m]
z_{ONB}	distance at which nucleate boiling commences
z_{SC}	distance at which $x = 0$
L_b	distance from incipient boiling to the heated section exit
Δp_b	pressure drop over length L_b due to friction and momentum
$\Delta p_{b,s}$	pressure drop for an adiabatic tube with a fluid temperature at T_{ib} and a length $L_{b,s}$
T_{ib}	bulk fluid temperature at incipient boiling
$L_{b,s}$	distance required to bring the fluid from T_{ib} to T_{sat} where T_{sat} is evaluated at the exit conditions.

Greek

α	vapor volume fraction (e.g., void fraction)
ε	surface roughness
ϕ	heat flux
ϕ_{BO}	heat flux at burnout [pcu/hr·ft^2] (Note: A pcu is the energy required to raise 1 pound of water, 1°C. Therefore 1.0 pcu = 1.8 Btu.)
ϕ_c	critical heat flux [W/m^2]
ϕ_{c0}	basic critical heat flux (ϕ_c for $\Delta h_i = 0$) [W/m^2]

η	bubble detachment parameter
μ_b	dynamic viscosity based on bulk fluid conditions
μ_G	gas-phase viscosity
μ_L	liquid-phase viscosity
μ_w	dynamic viscosity based on wall conditions
θ	time [s]
ρ	density [kg/m^3]
ρ_f	liquid density [kg/m^3]
ρ_G	vapor density [kg/m^3]
ρ_v	vapor density [kg/m^3]
ρ_m	mixture density [kg/m^3]
ρ_∞	impulse line density [kg/m^3]
σ	surface tension [N/m^2]
ψ	undefined function

Dimensionless Numbers

f	friction factor
f_{GO}	friction factor for total mass flux with gas properties
f_{iso}	friction factor for isothermal conditions
f_{LO}	friction factor for total mass flux with liquid properties
ϕ_{LO}	pressure drop multiplier defined in equation XX
Γ	error fraction $[(\psi-\psi_f)/(\psi_i-\psi_f)]$
Nu	Nusselt number [hD/k]
Pr	Prandtl number [$c_p\mu/k$]

Q_{ratio}	heat flux ratio, defined in equation XX
R	temperature ratio at OFI, defined in equation XX
Re	Reynolds number $[GD/\mu]$
St	Stanton number $[\phi/Gc_p\Delta T_\lambda]$

Subscripts

0, 1, 2	property or state at location 0, 1,2, refer to Figure 2
1	property or state at location 1, refer to Figure 2
01, 24	property, state or parameter between location 0 and 1, 2 and 4
2	property or state at location 2, refer to Figure 2
3	property or state at location 3, refer to Figure 2
4	property or state at location 4, refer to Figure 2
ehl	end of heated length
exp	experimental
in	channel inlet
l	liquid properties
m	mixture properties
max	maximum
min	minimum
ONB	onset of nucleate boiling
out	channel outlet
v	vapor properties

GLOSSARY

Burnout. An inordinate increase in surface temperature resulting from the change in one of the parameters of the system (e.g., heat flux, mass velocity, fluid temperature) which results in channel failure.

Burnout point. The longitudinal axis position when the liquid film flow on a heated channel wall decreases to zero.

Critical heat flux (CHF). A sudden rise in wall temperature or substantial (>20°F) fluctuations above the nucleate boiling wall temperature.

Demand curve minimum. The minimum pressure drop as specified by the demand curve for flow in a heated channel.

Departure from nucleate boiling (DNB). A shift in the heat transfer mechanism from nucleate boiling where liquid contacts the heated surface to film boiling where liquid contact with the heated surface is prevented and a vapor film forms.

Dryout. A condition where there is no liquid contact with the wall.

Fundamental instability. An instability is fundamental when the mechanism can be identified and studied separately.

Lateral axis. The coordinate axis orthogonal with the longitudinal and normal axes.

Longitudinal axis. The coordinate axis in the direction of flow.

Net vapor generation (NVG). The onset of significant void.

Normal axis. The coordinate axis perpendicular to the heated surface.

Onset of flow instability (OFI). The demand curve minimum in a diabatic channel. This is the threshold for Ledinegg instability.

Onset of nucleate boiling (ONB). The condition where bubbles first start to form on the heated channel surface.

Onset of significant void (OSV). The condition where significant vapor generated starts with the mixing of bubbles in the subcooled liquid core.

Saturated DNB. When the bulk fluid is at saturated conditions at the location where DNB occurs.

Steady flow. The system parameters are functions of space variables, only small fluctuations (due to turbulence, nucleation, or slug flow) exist.

Steady-oscillatory. Flow conditions at a point are ideally repeated at a fixed time interval.

Subcooled DNB. When the bulk fluid is subcooled at the location where DNB occurs.

Transient. System parameters vary as a function of time.

ABSTRACT

An experimental program has been completed which evaluated the effect of a flow obstruction in a heated channel on the onset of flow instability (OFI). The test channel was rectangular (80 x 3 mm), heated on one surface, and equipped with view ports. Tests were conducted in a flow controlled mode at heat fluxes of 370 kW/m^2, and 610 kW/m^2. Direct comparisons were made between the demand curve minimum for the unobstructed channel and a channel equipped with a 2.07 mm wide rib that was parallel to the flow and in contact with the heated surface.

Data at OFI is presented in the nondimensional terms of Q_{ratio} (ratio of heat flux applied to heat flux required to achieve saturated liquid conditions at the exit), and the local Stanton number at the channel exit for each channel arrangement. The Q_{ratio} and Stanton number values for the unobstructed channel and the rib equipped channel are then compared to produce an estimate of the rib effect.

CHAPTER 1

INTRODUCTION

The coolant in production nuclear reactor assemblies such as in the Savannah River Site (SRS) reactors is circulated as a subcooled liquid under normal operating conditions. This coolant is evenly distributed throughout multiple annular flow channels with a uniform pressure profile across each coolant flow channel. Subcooled flow in such a heated channel may exhibit a demand curve with a negative sloped region and a relative maximum and minimum as shown in Figure 1. This type of behavior is common in low pressure water systems (48). The relative minimum is the result of the flow acceleration created by the change in fluid density, and an increase in the frictional pressure loss created by vapor nucleating on the heater surface and effectively increasing the flow channel roughness.

The operating condition for any flow system can be determined by the intersection of the supply and demand curves. For turbulent subcooled isothermal systems only one operating point exists. This is shown as condition a in Figure 1. When a system demand curve has a negatively slope region it is possible that three different operating conditions might exist. Conditions b and d are stable, condition c as shown in Figure 1 is not stable. Attempted operation at condition c will result in an excursion to condition d. Ledinegg (50) identified the threshold limit for subcooled flow in a heated channel to undergo a flow instability as the minimum in the demand curve. When flow is reduced below the demand curve minimum it will undergo a sudden large amplitude excursion

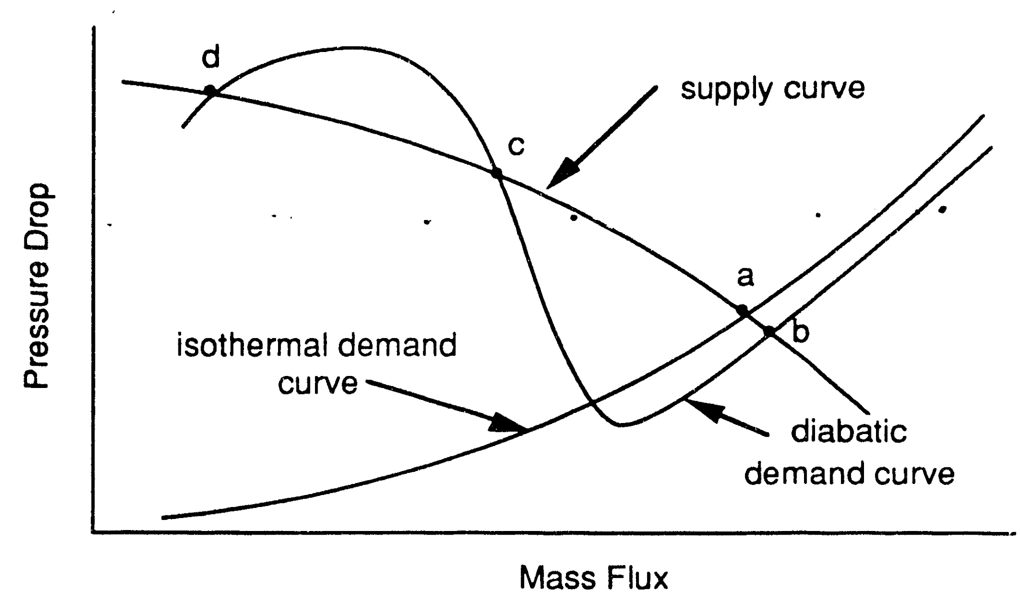

Figure 1. Demand curves for subcooled isothermal and diabatic systems

to a new, stable operating condition. This instability is characterized by a rapid shift in the operating condition from subcooled boiling to high quality steam. Ledinegg analytically demonstrated that the conditions for OFI were a function of channel geometry, friction coefficient, system operating pressure, and inlet subcooling. The OFI threshold was shown to be essentially independent of flow rate, and heat flux.

Operation at condition c in Figure 1 is possible if the supply system is adequate. If the slope of the supply curve is steeper (more negative) than the demand curve (sum of the friction, acceleration, and elevation terms) a Ledinegg type flow instability will not occur (52). The equation for this is:

(1) $$\frac{\partial p_{supply}}{\partial Q} - \frac{\partial p_{demand}}{\partial Q} \leq 0$$

For constant pressure systems ($\partial p_{supply}/\partial Q = 0$) operation at the demand curve minimum is stable for small increases in flow but unstable for small flow decreases. Attempted operation at a flow below the demand curve minimum flow will result in an excursion to the left side of the demand curve. Because of this many researchers have referred to the demand curve minimum condition as the onset of flow instability (OFI) condition. This nomenclature will be used in this report.

In multi-channel parallel flow systems the slope of the supply curve for each individual channel is effectively flat. When flow is reduced to the parallel flow network, the flow through all of the flow channels will decrease. If there are no geometric, heat transfer or power dissimilarities the flow to each channel will be equally reduced. In practice the reactor geometry, heat transfer behavior and power flux are not uniform. Some flow channels may be exposed to higher power levels and greater flow restrictions. Because the pressure drop across each channel is the same (plenum-to-plenum pressure difference), as the pressure drop decreases across the entire network some channels will be more susceptible to unstable flow excursions. If an excursion were to occur in one channel the resulting diversion in flow would be distributed through the other parallel channels and create a negligible increase in network pressure drop.

Flow Excursion Predictions

A Ledinegg flow excursion will result in higher channel operating temperatures which could result in equipment damage. One of the techniques used to assure safe operation during a flow reduction transient such as a defined loss of coolant accident (LOCA) is to operate at a power level below that necessary to initiate a flow excursion. Several correlations have been developed to predict OFI. Whittle and Forgan (67) demonstrated that OFI occurs at:

(2) $$\frac{T_{exit\,@\,OFI} - T_{inlet}}{T_{sat} - T_{inlet}} = R \qquad \text{where: } R = \frac{1}{1 + \frac{\eta}{L_h/D_h}}$$

It is important to note that the value of R is constant for any given geometry and the outlet temperature at the minimum can be predicted based solely on the inlet temperature, saturation temperature, and geometry.

A second correlation to predict OFI and the one used to calculate SRS reactor operating limits is based on a correlation developed by Saha and Zuber (62) to predict the onset of significant void (OSV). Since OSV occurs at a higher flow than OFI, OSV will occur prior to OFI. The equation to predict OSV at high Peclat numbers, based on local conditions is (62):

(3) $$St = \frac{\phi}{Gc_p\left(T_{sat} - T_{bulk}\right)} = 0.0065$$

The SRS design criteria is set at a Stanton number of 0.00455 which is 30% below the best estimate value listed in Equation 3.

Rib Considerations

The assemblies in the SRS reactors consist of concentric aluminum or aluminum clad tubes which form annular flow channels as shown in Figure 2. The annular spacing is maintained by four ribs in each flow channel. The width of these ribs at the tip range from 1.4 mm to 1.7 mm for a Mark 22 assembly. Since the ribs and tube walls are constructed of aluminum (a poor neutron absorber) virtually all of the heat generation occurs in the core of the tubes.

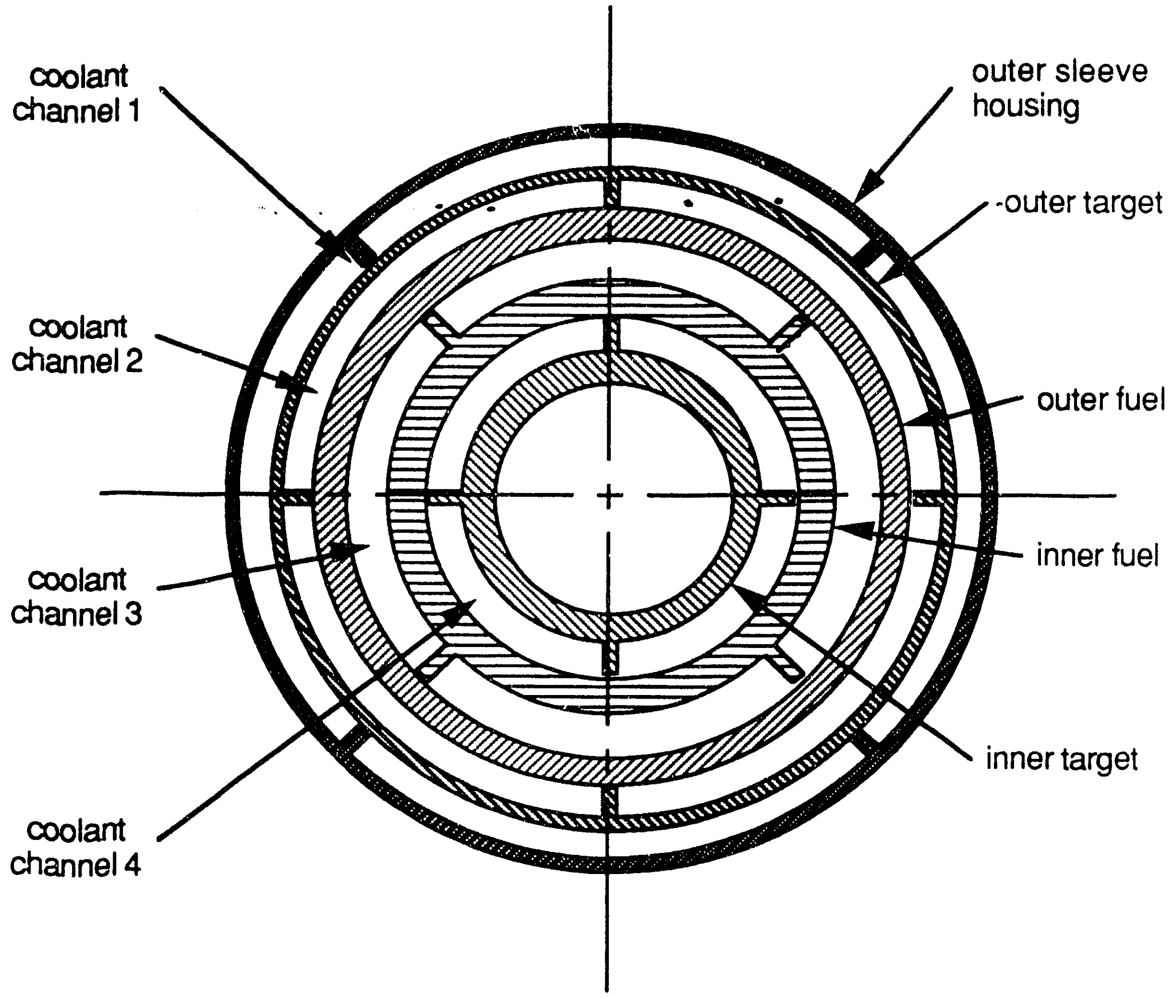

Figure 2. SRS Mark 22 reactor fuel assembly

The ribs will change the local heat transfer in their immediate vicinity. A rib will produce a viscous drag which will reduce the fluid velocity and heat transfer near the rib. The rib in Figure 3a will tend to act as a fin to remove heat from the tube while the rib in Figure 3b where the rib tip approaches the wall may allow the formation of vapor that will tend to insulate a portion of the wall and inhibit heat removal from the wall.

The combined viscous, fin, and insulation effect of the ribs is difficult to predict analytically. The rib presence in the SRS annuli will create an azimuthal

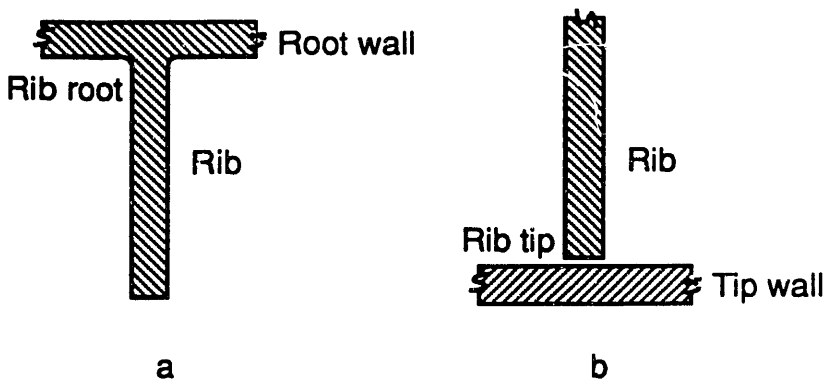

Figure 3. Rib arrangements (a) rib root arrangement (b) rib tip arrangement

heat flux profile and an azimuthal variation in the local Stanton number. To account for this variation the SRS limits methodology (49) reduces the OSV design value of 0.00455 by a rib peaking factor. The rib peaking factor presently in use (49) is 1.209. The resulting equivalent Stanton number OSV limit is therefore 0.00376. While this design value adjusted for rib peaking has been demonstrated as conservative by comparison with benchmarking data produced by Columbia University (20), Creare (49), and Babcock & Wilcox (21), using the SRS FLOWTRAN program; it is desirable to quantify the rib effect experimentally. This will require a separate effects test where a single channel is operated both with a rib and without a rib. This would allow a direct comparison between the two geometries and the calculation of a rib effect.

In the SRS reactors the four centering ribs for any channel are not all in intimate contact with the rib tip wall. Minor amounts of bowing, eccentricity, and kinking in the fuel tubes and targets results in intermittent contact between the rib tip and rib tip wall. This intermittent contact allows flow redistribution between subchannels formed by the spacer ribs. Flow between adjacent subchannels across a rib is referred to as rib flow. In addition to rib flow the intermittent contact will result in areas of stagnate fluid between the rib tip and the rib tip wall. This area of stagnant fluid may allow the development of an insulating layer of vapor.

The coolant channel opposite the rib tip will accept an increase in the heat from the tip wall. This will reduce the peaking factor effect created by the rib. Hodges (34) suggested that the heat split could be estimated based using Equation 3. This rib side heat flux perturbation (RSHFP) factor is the ratio of heat generated under the rib which is transferred to the ribbed channel when compared with the heat which would have be convected to the ribbed channel if the rib were not present.

(4) $$RSHFP = 12.53y^{0.56}, \qquad y \leq 0.0109ft$$

Heat flux peaking factor and similar factors can be generated analytically using a variety of methods. These analytic solutions do not provide information on if the heat flux peaking in the presence of a rib results in premature OSV or Ledinegg instability.

Summary of SRS OFI Program

The SRS conducted a five year research effort to investigate Ledinegg flow instability in reactor assemblies. This effort included contributions from the Savannah River Technology Center (SRTC), Columbia University, Creare Inc., Babcock and Wilcox, Stern Laboratories, Villanova University, and Northwestern University (27). The goal of the SRS OFI program was to develop a database that consisted of steady-state and transient flow instability behavior that could be used to benchmark the SRS OSV design correlation. This effort required the construction of six different test loops, and multiple test channels.

Steady-state demand curves were produced for annular flow channels, annular flow channels with spacer ribs, and six different tube diameters. Transient flow and heat flux data were produced for a single annulus and for a Mark-22 fuel assembly geometry.

The tube tests were conducted at Columbia University (14, 15, 16) to allow separate evaluation of the parameters listed in Table 1. The single annulus and single annulus with spacer ribs also were also separate effects tests which allowed evaluation of the parameters listed in Table 1. They were conducted by both Columbia University (17, 19) and Creare, Inc (9). The Babcock and Wilcox test rig evaluated the behavior of a multi-annular assembly (61). This test produced integrated effects data which allowed benchmarking of the FLOWTRAN computer code (21) for a complicated geometry but provided little parameter effects knowledge.

Table 1.--SRS OFI program test matrix

	Columbia University			Creare Inc.		Babcock & Wilcox
	tube	annulus	ribbed annulus	annulus	ribbed annulus	Multi-annulus
Pressure control vs. flow control	√	√	...	...	...	...
Transient flow	...	√	...	...	...	√
High heat flux	√	√	√	...	...	√
Axial heat flux profile	...	...	...	...	...	√
Azimuthal heat flux profile (power tilt)	...	...	...	√	√	...
Dissolved helium	...	...	...	√	√	...
Aluminum heat transfer surface	...	...	...	√	√	...

The ribbed annulus tests did demonstrate that OFI occurred in ribbed annuli at less severe conditions than for similar non-ribbed annuli. It is not clear however if this is the result of a rib effect or non-symmetry between the subchannels. Since the subchannels were not fully isolated, rib flow between the channels precluded exact determination of the subchannel flow rate. This required the assumption that the flow rate was equally distributed to each flow channel. In addition the local heat flux, saturation temperature, and bulk fluid temperature were not well known. With four subchannels it is also possible for one subchannel to go into instability resulting in flow diverting to the other three.

The test channel designs did not facilitate operation of any annulus both with and without a rib. This introduced an additional unknown: channel-to-channel similarity. Analysis of the Columbia University ribbed and open annular data indicate wetted surface temperatures in excess of that expected for nucleate boiling conditions (27). Since the "open" annulus included spacers to maintain concentricity both types of channels had flow obstructions. This DNB at obstructions has not been previously noted in the literature and warranted further evaluation. Principle unknowns which remain after the completion of the SRS OFI program are:

- What is the effect of spacer ribs on Ledinegg instability?
- Does DNB occur in the presence of flow obstructions?
- What is the effect of flow transients on Ledinegg instability?

The test facility described in Chapter 3 was constructed to investigate these three questions. The study presented in this report is directed at the investigation of the first two open issues.

CHAPTER 2

ANALYSIS

The evaluation of the effect on flow channel obstructions on Ledinegg instability requires consideration of alternate flow instabilities phenomena and heat transfer behavior in addition to hydrodynamic considerations. Each of these subjects is developed separately in the following pages. Their effect on a diabatic flow channel is then presented in the last section of this chapter.

Demand Curves

The pressure gradient in a heated channel may be separated into three individual components: elevation, acceleration, and friction.

(5) $$\left(\frac{\Delta p}{\Delta L}\right)_t = \left(\frac{\Delta p}{\Delta L}\right)_g + \left(\frac{\Delta p}{\Delta L}\right)_a + \left(\frac{\Delta p}{\Delta L}\right)_f$$

For downflow in a vertical channel the gravitational term represents a pressure recovery. Klausner, et al. (46) defined a mixture density term, $\rho_m = \alpha\rho_v + (1-\alpha)\rho_l$. The recovery is:

(6) $$\left(\frac{\Delta p}{\Delta L}\right)_g = +\overline{\rho_m}\, g$$

Acceleration is primarily the result of density changes as the fluid temperature increases as the channel exit is approached. It is not until voiding occurs that the acceleration becomes significant. The frictional pressure gradient term that represents the nonrecoverable pressure losses can be further separated into three terms: inlet (contraction) losses, friction losses, and exit (expansion) losses.

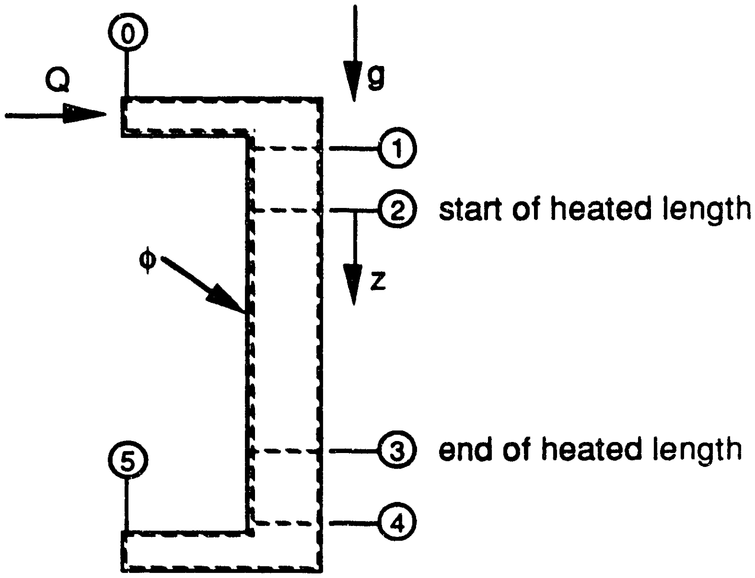

Figure 5, Heated channel nomenclature

Demand curves such as shown in Figure 1 are normally generated by incrementally reducing the flow and measuring the steady state pressure at each flow. This type of test may be conducted for both isothermal and diabatic flows. Demand curves generated for diabatic flows where the heat flux is held constant will normally take the form presented in Figure 6. The pressure gradient relation for this behavior, Equation 5, may be derived from Euler's equation of motion along a streamline (64). The solution is initially developed assuming no frictional losses.

(7) $$\frac{dp}{\rho} + g\,dz + u\,du = 0$$

Multiplying through by the density term, replacing the velocity term, u, with G/ρ and integrating:

(8) $$\int_1^2 dp + \int_1^2 g\,\rho\,dz + \int_1^2 -\left(\frac{G}{\rho}\right)^2 d\rho = 0$$

Completing the integration assuming a constant flow area, and using the definition for the length averaged density.

(9) $$\frac{p_2 - p_1}{\Delta L} - g\,\bar{\rho} + \frac{G^2}{\Delta L}\left(\frac{1}{\rho_2} - \frac{1}{\rho_1}\right) = 0$$

Introducing a loss term and rearranging:

(10) $$\frac{\Delta p}{\Delta L} = g\,\bar{\rho} - \frac{G^2}{\Delta L}\left(\frac{1}{\rho_2} - \frac{1}{\rho_1}\right) - \text{losses}$$

Isothermal Behavior

In isothermal flow the density is constant so the length average density is constant for any geometry and the acceleration term is zero. The demand curve would be as shown in Figure 6. The flow for a closed system can be predicted by the intersection of the demand and supply curves.

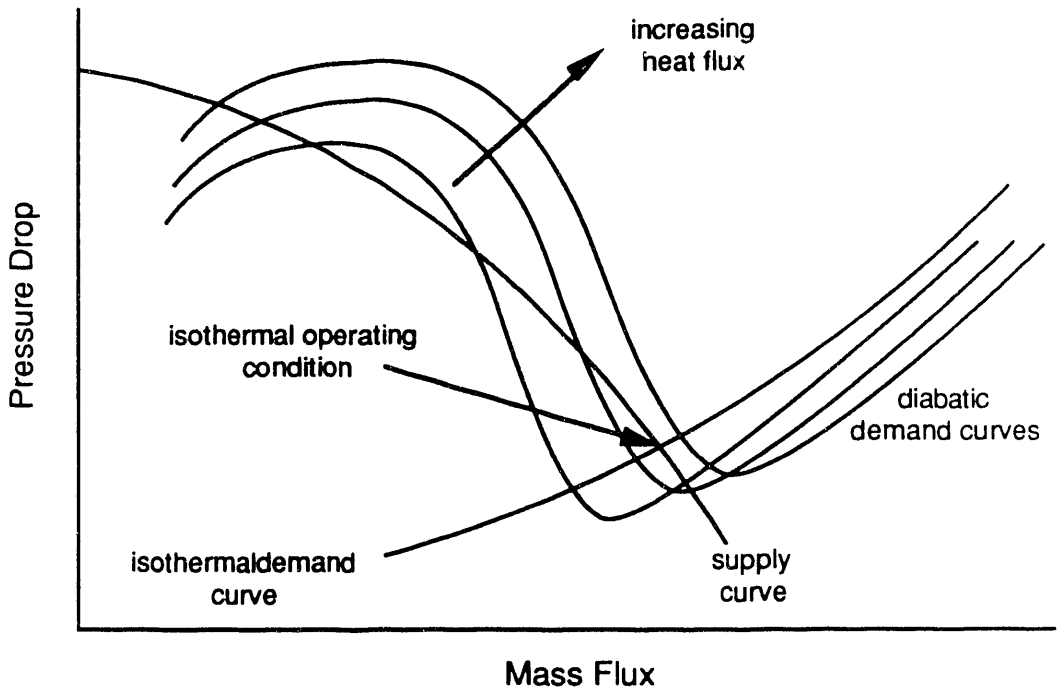

Figure 6, Demand curve prediction of operating conditions

Inlet losses

Maulbetsch and Griffith (52) had good success in predicting the inlet losses using the common expression presented by Rohsenow and Choi (60) where K_C was assumed as 0.5.

(11) $$\Delta p_{0\text{-}1} = \frac{\rho\, u_{in}^2}{2}(1 + K_c)$$

(12) $$\frac{p_0 - p_1}{\rho_{01}} + \frac{u_0^2 - u_1^2}{2} = K_c \frac{u_1^2}{2}$$

where:

(13) $$K_c = \frac{1 - \frac{C_c^2}{\beta_0}\left(\frac{A_1}{A_0}\right)^2 - 2C_c + 2\left(\frac{C_c^2}{\beta_1}\right)^2}{C_c^2} - 1 + \left(\frac{A_1}{A_0}\right)^2$$

(14) $$\frac{1}{\beta} = \frac{1}{A}\int_A \left(\frac{u}{U}\right)^3 dA$$

For highly turbulent flow $\beta = 1$ and for parabolic flow in a circular pipe $\beta = 0.5$.

Exit Losses

For the conditions studied by Maulbetsch and Griffith the pressure recovery was stated to be small (less than 1 psi). The expansion relation presented by Rohsenow and Choi (60) is:

(15) $$\frac{p_2 - p_3}{\rho_{23}} + \frac{u_2^2 - u_3^2}{2} = K_e \frac{u_2^2}{2}$$

where:

(16) $$K_e = 1 - \frac{2}{\alpha_2}\frac{A_2}{A_3} + \left(\frac{A_2}{A_3}\right)^2\left(\frac{2}{\alpha_3} - 1\right)$$

(17) $$\frac{1}{\alpha} = \frac{1}{A}\int_A \left(\frac{u}{U}\right)^2 dA$$

For highly turbulent flow $\alpha = 1$ and for parabolic flow in a circular pipe $\alpha = 0.75$.

Frictional Losses

The frictional pressure losses may be estimated using the friction factor relationship.

(18) $$f \equiv \frac{\Delta p}{(L/D)(\rho V^2/2)}$$

For laminar flow the friction factor is independent of the relative roughness (8):

(19) $$f = 64/Re$$

Zigrang and Sylvester (68) have developed an explicit solution for the friction factor that was found useful for two-phase diabatic modeling by Block, et al. (9):

(20) $$f = \left[-2.0 \log \left\{ \frac{\varepsilon/D_e}{3.7} - \left[\frac{5.02}{Re} \right] \log \left[\frac{\varepsilon/D_e}{3.7} + \frac{13}{Re} \right] \right\} \right]^{-2}$$
± 1.9% (95% coverage)

A more accurate version also suggested by Zigrang and Sylvester (68) is:

(21) $$f = \left[-2.0 \log \left\{ \frac{\varepsilon/D_e}{3.7} - \left[\frac{5.02}{Re} \right] \log \left[\frac{\varepsilon/D_e}{3.7} - \log \left(\frac{\varepsilon/D_e}{3.7} + \frac{13}{Re} \right) \right] \right\} \right]^{-2}$$
± 0.22% (95% coverage)

For smooth pipes in turbulent flow the friction factor can be approximated as (60):

(22) $$f = \frac{0.316}{Re^{0.25}} \qquad 3 \times 10^3 < Re < 2 \times 10^4$$

(23) $$f = \frac{0.184}{Re^{0.20}} \qquad 2 \times 10^4 < Re < 5 \times 10^5$$

The flow relationships discussed above were developed for circular flow channels. When the flow cross section is not circular then an equivalent hydraulic diameter, D, must be estimated. For turbulent flow:

(24) $$D = \frac{4\,A_f}{P} = \frac{4\,(\text{flow area})}{\text{wetted perimeter}}$$

Blevins (8) suggests that errors have been demonstrated using this approach and that more accurate results may be obtained using an equivalent diameter, D_e, defined by:

(25) $$D_e = \frac{64}{k} D$$

where the value k is the friction coefficient for laminar flow (i.e., $k = f\,Re$). For a rectangular cross-section (where $b \le a$) the friction coefficient is (8):

(26) $$k = \frac{64}{\frac{2}{3} + \frac{11}{24}\frac{b}{a}\left(2 - \frac{b}{a}\right)}$$

Combined Flow Losses

The overall channel frictional loss may then be estimated as:

(27) $$\left(\frac{\Delta P}{\Delta L}\right)_f = \left[\frac{\rho_{01}\, u_1^2}{2}(K_c + 1) - \frac{\rho_{01}\, u_0^2}{2}\right] + \left[\frac{2 f G^2}{D_e\, \rho}\right] + \left[\frac{\rho_{23}\, u_2^2}{2}(K_e - 1) + \frac{\rho_{23}\, u_3^2}{2}\right]$$

or

(28) $$\left(\frac{\Delta P}{\Delta L}\right)_f = \frac{K_c\, G^2}{2\,\rho_{01}} + \frac{2 f G^2}{D_e\, \rho} + \frac{K_e\, G^2}{2\,\rho_{23}}$$

Diabatic Behavior

When heat is added to a flowing channel the demand curve may pass through a minimum and maximum as shown in Figure 6. This behavior is common in low pressure water systems; for high system pressures the minimum will not occur (48). The demand curve for any geometry shifts to the right and upward for an increase in heat flux. Increasing the exit pressure has a similar effect.

The flow can be predicted using the intersection of the demand and supply curves as was discussed for the isothermal case. For a flow controlled test the supply curve is vertical as shown in Figure 7, supply curve number 1.

The operating condition is at point a. As the flow is decreased it is possible to follow the entire demand curve. For a pressure controlled test the supply curve is horizontal, supply curve number 2. For parallel channel flow with a large number of flow paths the supply curve will approach that of a pressure controlled system. The initial operating condition is at point b, the right intercept between the supply and demand curve since the flow was established prior to the heat. When the pressure is decreased to point c a small decrease in pressure will no longer be possible with a corresponding small change in flow rate. If a pressure decrease is attempted the system will jump to point d. The design limit of most previous test apparatuses has been such that the operation of the heated channels at this condition has not been possible. If interlocks were not in place rig failure (channel burnout) occurred.

A typical supply curve is presented by supply curve number 3 in Figure 7. The initial operating point will be at location e. When the demand curve slope is steeper than the supply curve slope it is no longer possible to operate on the negative sloped region of the demand curve.

(29) $$\frac{\partial(\Delta p_{suppy})}{\partial Q} - \frac{\partial[\Delta p_{0-1} + \Delta p_{1-2} + \Delta p_{2-3}]}{\partial Q} \geq 0$$

When this criterion is exceeded an excursive flow insatiability will occur.

Maulbetsch and Griffith (52) considered the channel pressure drop to occur over only the heated section; entrance and exit losses were accounted for as part of the external system.

Inlet and Exit Losses

The inlet and exit loss relationships for subcooled flow with no void present will be the same as for isothermal subcooled flow which was discussed earlier. When voids are present at the exit the isothermal relation will no longer hold. Maulbetsch and Griffith (52) estimated the exit loss using a relation by Romie:

$$\Delta p_{2\text{-}3} = \frac{-V_{exit}^2}{2}\left(\frac{A_F}{A_{PL}}\right)^2\left(\frac{2}{1-\alpha}\right) \qquad (30)$$

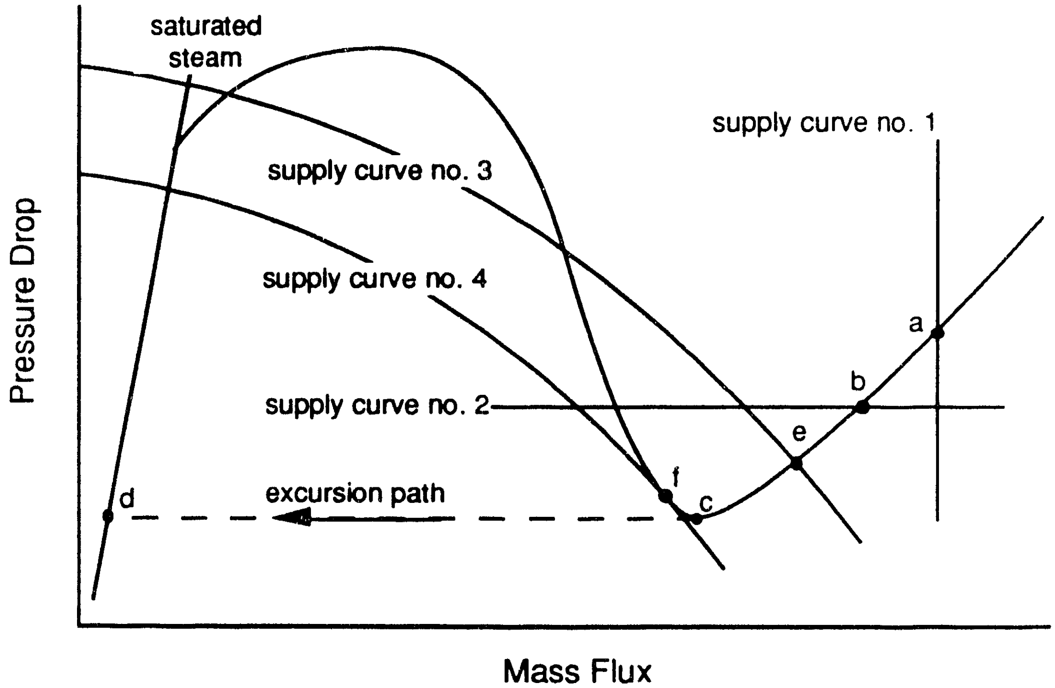

Figure 7, Diabatic demand curve characteristics

Heated Wall Effect

The viscosity of most liquids decreases with increasing temperature. This effect leads to a distortion of the velocity profile (60) for non-isothermal flow. For laminar liquid flow the parabolic profile will flatten as shown in Figure 8. The opposite effect occurs for gases. The result of this profile distortion is that the pressure drop for subcooled diabatic non-boiling flows will be lower than for adiabatic flows at the same inlet conditions. While other factors contribute to this effect the primary variable is viscosity (52).

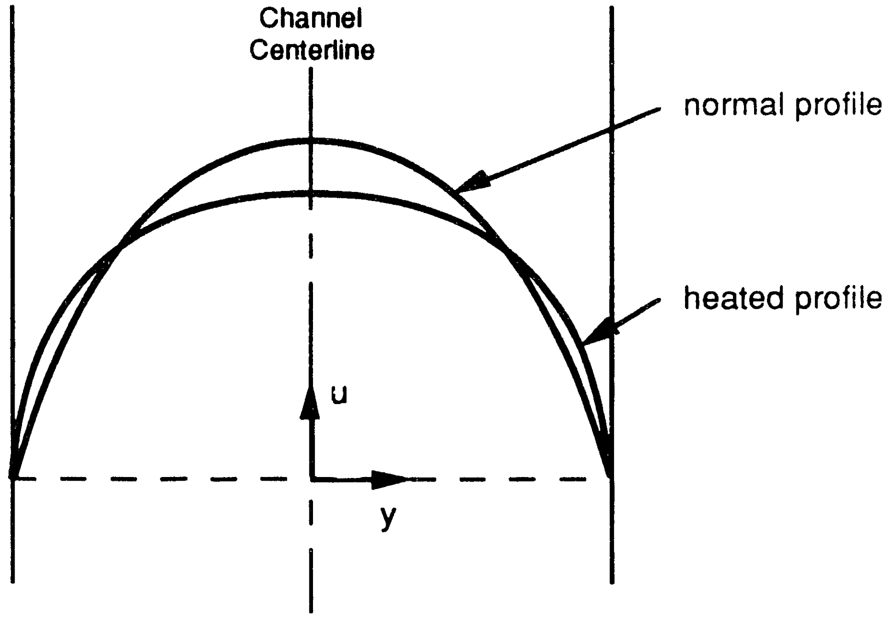

Figure 8, Isothermal and diabatic velocity profiles

Bergles and Dormer (7) present a correlation to predict pressure drop in diabatic non-boiling systems by substituting the adiabatic friction factor with:

$$f = 0.107\,Re^{-0.28}\left(\frac{\mu_w}{\mu}\right)^{0.35} \tag{31}$$

In an earlier report (28) the authors state an alternate of this relation that was successfully used by Maulbetsch and Griffith.

$$\frac{f}{f_{iso}} = \left(\frac{\mu_w}{\mu_b}\right)^{0.35} \tag{32}$$

Friction Multipliers

The friction pressure drop in two-phase flow has commonly been evaluated using a friction multiplier to predict the two-phase frictional pressure gradient using the frictional pressure gradient for flow based on the total mass flux and liquid phase properties (24).

(33)
$$\phi_{LO}^2 = \frac{\left(\frac{dp}{dz}\right)_{2\phi}}{\left(\frac{dp}{dz}\right)_{LO}}$$

Isothermal Friction Multipliers

Collier (24) lists eleven two-phase pressure drop models and correlations. Some are considered acceptable if the standard deviation is in the range of 25 to 50%. Hewitt (32) identifies at least 5 different alternative approaches to estimating pressure drop. Hewitt (32) suggests that most two-phase pressure drop correlations are not very accurate and credits Whalley with the recommended selection process:

> "1. For μ_L/μ_G < 1000, the Friedel (1979) correlation should be used.
> "2. For μ_L/μ_G > 1000, and G > 100 (kg/s·m^2), the Chesholm (1973) correlation should be used.
> "3. For μ_L/μ_G > 1000, and G < 100 (kg/s·m^2), the Martinelli correlation (Lockhart & Martinelli 1949; Martinelli & Nelson 1948) should be used."

Each of the above methods uses a form of Equation 33 in the estimation of two-phase pressure drop.

Heated Frictional Multiplier

For diabatic two-phase flows the vapor void fraction will not be constant. For moderate and high flow rates vapor bubbles will be swept along in the direction of flow so the void fraction will increase along the heated length. For low flow rate in downflow the bubble rise velocity may be greater than the net channel velocity so vapor may collect at the top of the heated section.

Collier (24) states that the frictional pressure gradient will increase over that of an unheated tube for lower quality flow. He attributes to Tarasova a relationship for steam-water systems:

$$(34) \qquad \left[\phi_{fo}\right]^2_{\text{heated tube}} = \left[\phi_{fo}\right]^2_{\text{unheated tube}}\left[1 + 4.4 \times 10^{-3}\left(\frac{\phi}{G}\right)^{0.7}\right]$$

where ϕ is in watts/m^2 and G is in kg/m$^2\cdot$s.

Dormer and Bergles (28) developed a correlation that relates the ratio of the pressure drop in subcooled boiling and the pressure drop in unheated flow ($\Delta p_{SCB}/\Delta p_{ADB}$), with the ratio of the actual heat flux and the heat flux to produce saturated water at the exit (ϕ/ϕ_{sat}). This relationship was later used in the Columbia University OFI test program (14, 15, 16, 17, 18, 19). The relationship is dependent on the channel geometry and is shown in Figure 9. The effect of L/D is most significant with a lesser effect of channel diameter. The effect of L/D decreases as the L/D increases. The range of L/D evaluated was 25 to 200.

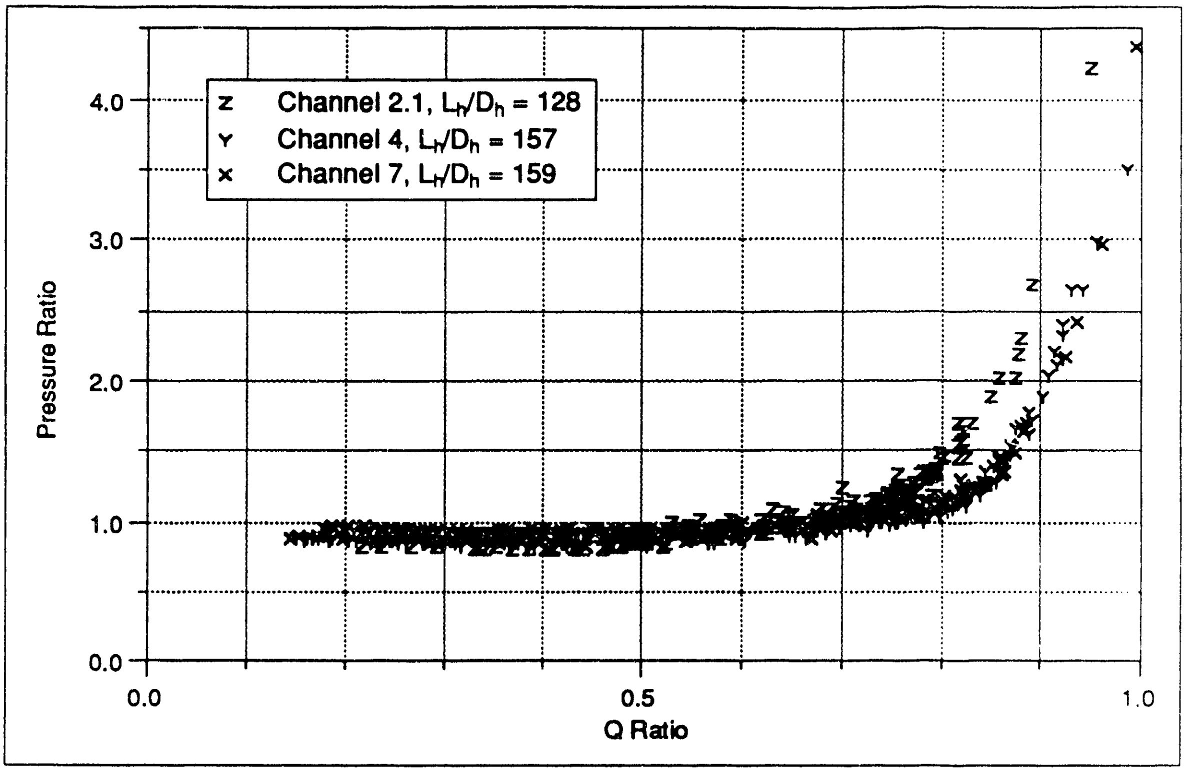

Figure 9, Subcooled boiling curves from Columbia University single tube uniformly heated tests, test sections 2.1, 4 and 7

Bergles and Dormer (7) presented an alternate form of this work which plotted the ratio of the pressure drop over the boiling length, and the pressure drop over the boiling length at saturated conditions ($\Delta p_b/\Delta p_{b,s}$); as a function of the ratio of the boiling length, and the length required to bring the fluid to saturated conditions at the end of the test section ($L_b/L_{b,s}$). For short boiling lengths the pressure ratio approaches zero. The plots presented in this fashion again all tend to vary based on the hydraulic diameter and the L/D ratio where the later is the more significant effect.

The non-boiling length for tubes was estimated using a heat balance and an empirical heat transfer correlation:

(35) $$L_{nb} = \left[T_{w,ib} - T_i - \frac{q''}{h}\right]\left(\frac{w\,c}{q''\,\pi\,D}\right)$$

(36) $$\frac{Nu}{Pr^{0.4}} = 0.0157\ Re^{0.85}$$

Much of the data appears to be for systems where all of the tube length is in boiling. (i.e., The incipient boiling conditions were met at the tube entrance.) There is a slight variation in the pressure drop ratios for tubes which are in partial boiling when compared to a tube with the same $L_b/L_{b,s}$ in total boiling. This variation was attributed to the adiabatic reference; a tube in partial boiling will have a higher bulk fluid temperature.

Researchers at Columbia University (15) defined the ratio of the heat flux to the heat flux required to attain saturated conditions at the channel exit as the Q_{ratio}. The ratio of the heated section pressure drop to the heated section pressure drop at zero heat flux evaluated using inlet condition properties was defined as the pressure ratio.

Demand Curve Milestones

Bankoff, Lee and Knaani (1991) identified four ONB models, and eleven OSV models. Most of this work was published in the 1960's and early 1970's. These works are listed in Table 2. All of the works are based on steady-state forced-convection, subcooled nucleate boiling. The most successful are discussed below.

Table 2.--Subcooled demand curve milestone correlations and models identified by Bankoff, Lee, and Knaani (4)

Researcher(s)	Date	Comment
ONB Models		
Bergles & Rohsenow	1964	Theoretical
Sato & Matsumura	1964	Theoretical
Davis & Anderson	1966	Theoretical
Snoek & Leung	1968	Empirical
OSV Models		
Bowring	1962	Empirical
Thom, et al.	1965	Empirical
Levy	1967	Theoretical
Staub	1968	Theoretical
Ahmad	1970	Empirical
Dix	1971	Empirical
Saha & Zuber	1974	Empirical
Sekoguchi, et. al.	1974	Empirical
Unal	1975	Empirical
Rogers, et al. (59)	1987	Theoretical
HTRF, Columbia University	1990	Empirical

Onset of Nucleate Boiling

The condition when vapor first forms on the heated surface is referred to as the onset of nucleate boiling (4). These bubbles tend to be stable, neither moving or growing in size. Care must be taken in the application of this definition to experimental work since dissolved gases in the subcooled fluid may result in the evolution of bubbles that are not the vapor phase of the working fluid. Many researchers have successfully predicted the wall temperature at incipient boiling using Bergles and Rohsenow ONB correlation (24):

(37) $$q''_{ib} = 15.60\, p^{1.156} (T_w - T_s)^{2.30\, p^{-0.0234}}$$

The units for this equation are: psia, °F, and Btu/hr·ft^2. Collier (24) presents an alternate form in SI units:

(38) $$\left(\Delta T_{SAT}\right)_{ONB} = 0.556\left(\frac{\phi_{ONB}}{1082\left(p/10^5\right)^{1.156}}\right)^{0.0463\left(p/10^5\right)^{0.0234}}$$

Researchers at the Columbia University HTRF observed a depression in the axial surface temperature gradient during tube tests (16); this depression occurred near the conditions predicted for ONB by Equation 37. Equation 37 also compared well with the visually observed ONB in test conducted by Johnston (44).

During the OFI testing in annuli by Creare (1990), it was observed that the pressure gradient in a subcooled heated channel will increase after the wall temperature reaches the fluid saturation temperature. The gradient will be linear prior to and after this change. It was suggested that this change in gradient was an effect of ONB and the resulting effective increase in wall roughness because of the presence of vapor bubbles. These tests were conducted in annuli.

Onset of Significant Voiding

Small amounts of vapor will depart a heated surface prior to the demand curve minimum. This vapor may slide along the surface or enter the liquid core and condense. When a threshold is reached significant vapor generation and mixing of the vapor bubbles in the liquid core will occur (4) defined OSV as "significant vapor generation and mixing of bubbles with the core liquid."

Bowring (11) suggested that the conditions for bubble detachment could be predicted using a bubble detachment parameter, η. The correlation was prepared using test data from rectangular channels with gaps of 2.2, 2.5, 2.6, 6.4, and 12.7 mm. The data covered a wide range of operating pressures, from 1.1 to 13.8 MPa. The operating pressures for the smallest channels (2.2 to 2.6 mm) did not overlap with the operating pressures for the 6.4 and 12.7 mm channels. Data for the smallest channel size only included data above 8.3 MPa while the data for the other two sizes were for operating pressures below 4.3 MPa. The correlation suggested by Bowring to estimate the bubble detachment parameter was:

(39) $$\eta = \frac{u\,\Delta T_{\lambda}}{\phi} = 14 + 0.1\,p$$

where the units are cm/s, C, W/cm^2, and atmospheres.

The uncertainty bands for the low pressure data do not overlap. While Equation 39 does lie within the uncertainty bands for the 12.7 mm channel the calculated bubble detachment parameters for the 6.4 mm channel data is all higher than Equation 39. The calculated bubble detachment parameters for a 6.4 mm channel ranged from 15.52 to 30.55 at a pressure of 1.1 MPa.

Saha and Zuber developed a correlation to predict the average vapor void fraction in subcooled boiling systems. The relation is based on establishing the local equilibrium quality at the point of Net Vapor Generation (NVG). Figure 10 shows how the average vapor void fraction varies with axial position. Region I is characterized by a wall temperature in excess of T_{sat} and a subcooled bulk temperature; bubbles will nucleate along the wall but the bubble layer will remain small.

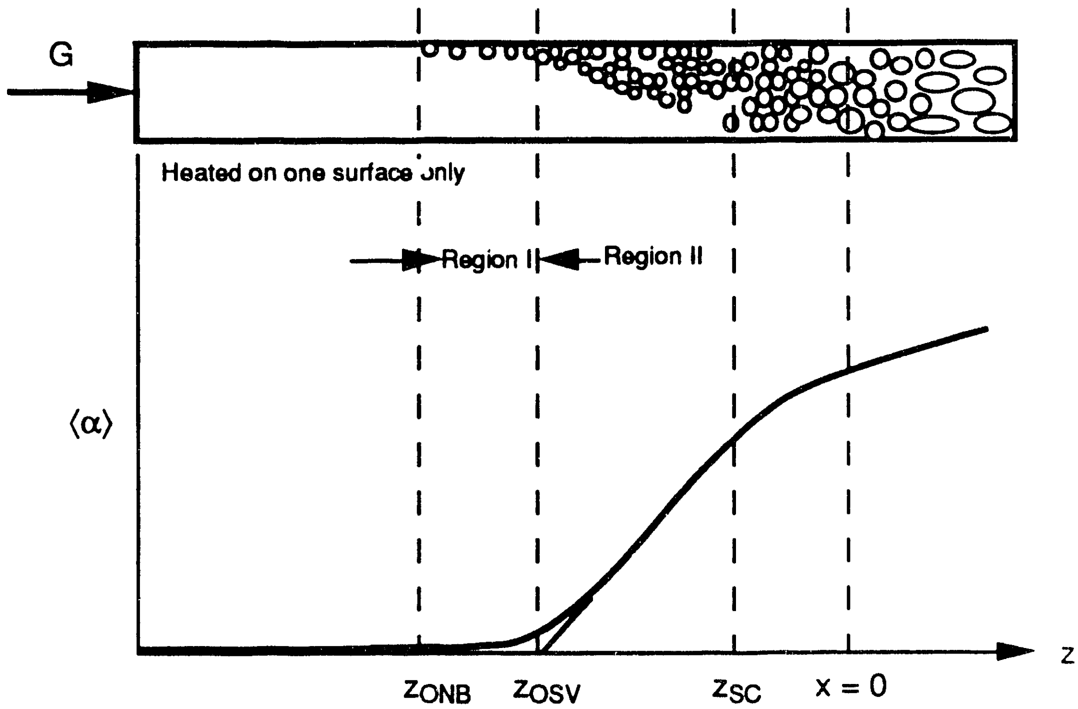

Figure 10, Heated channel bubble formation milestones

It was suggested that the point of NVG does not vary for high and moderate inlet subcoolings. At the point of NVG two criteria must be met: (1) The bubbles must detach from the wall, and (2) The evaporation rate must be greater than the condensation rate as bubbles enter the liquid core. Under different flow conditions one of these two criteria will be controlling. The point of NVG can be predicted using local fluid conditions from:

(40) $$Nu = \frac{\phi D_e}{k_f \Delta T_\lambda} = 455 \text{ if } Pe \leq 70{,}000$$

(41) $$St = \frac{\phi}{G c_{pf} \Delta T_\lambda} = 0.0065 \text{ if } Pe > 70{,}000$$

where:

(42)
$$Pe = \frac{Nu}{St} = \frac{G\, D_e\, c_{pf}}{k_f}$$

The Nusselt number represents the relationship between the evaporation and condensation rates and the Stanton number represents the bubble detachment phenomena criteria. When the mass flow is low (local Peclet number < 70,000) the condensation is governed by a diffusion process and the evaporation and condensation rates will be controlling. This is referred to as the thermally controlled region. The Stanton number criteria will be met before the Nusselt number criteria is met. When the local subcooling is large, vapor bubbles that depart from the wall will condense in the liquid core. Vapor bubbles will only travel in a narrow band close to the heated wall since they condense in the liquid core. The local subcooling will decrease along the flow path. When the local Nusselt number along the flow path reaches 455 the condensation rate of vapor entering the liquid core no longer exceeds the evaporation rate and a significant increase in the void fraction will occur.

When the mass flow is high (local Peclet number > 70,000) the local Nusselt number is already higher than 455 and as soon as the local Stanton number exceeds 0.0065 vapor bubbles will readily enter the liquid core and not condense. This is referred to as the hydrodynamicly controlled region. It was reported that the characteristic value of roughness parameter when bubble detachment occurs is about 0.02. This equates to a Stanton number of 0.0065 for a Prandtl number of 1.

The data used to evaluate the correlation included three fluids (water, Freon 22 and freon 114) and three geometries (tube, channel and annulus). The Stanton number ranged from about 0.0045 to 0.10 and the Peclet number from 5000 to 40,000. Most of the data fell in an error band of 25%.

The point of NVG is synonymous to the Onset of Significant Void (OSV). Since OSV has been found to precede flow excursion the NVG correlation may be used to predict the local conditions which precede flow instability. The point of NVG critical may be restated in terms of OSV: For OSV to occur the Nusselt number must be greater than 455 and the Stanton number must be greater than 0.0065.

Demand Curve Minimum

When demand curves in diabatic systems are generated under controlled flow conditions it is possible to operate at flows which are less than the flows at the minimum pressure drop. The pressure drop minimum will occur sometime between the ONB and saturated bulk conditions (quality equal to zero) at the exit. Maulbetsch and Griffith (52) reported that the minimum pressure drop occurred at well subcooled conditions (-28°C) with little nonequilibrium void fraction (i.e., vapor) present. They attributed the increased pressure to the left of the demand curve minimum to "increased wall friction caused by agitation at the wall when bubbles are growing and collapsing very rapidly" rather than Bernoulli-type acceleration.

Whittle and Forgan (67) noted that the demand curve slope changes were abrupt for all of the controlled flow tests. A description from a visual test states "as the flow rate was reduced though the value corresponding to the S-curve [demand curve] minimum, the steam void fraction near the channel exit increased very rapidly." (67) They suggested that this minimum might coincide with the detachment of water vapor from the channel walls.

Dorra, Lee, and Bankoff (69) reviewed eight sets of OFI and OSV data and present the data in terms of hydraulic diameter, local pressure, heat flux, mass flux, subcooling at minimum, and saturation temperature. Using this data it is possible to calculate both the Stanton number and Peclet number. Table 3 presents this calculated information for selected data sets. Table 4 presents the OFI data presented by Whittle and Forgan. The OFI and OSV data have been plotted separately in Figures 12 and 13. Using portions of this data Gehrke and Bankoff (77) prepared an altenate OFI correlation.

(42) $$St = 0.076\ Pe^{-1/5}$$

Table 3.--Mean Stanton numbers at OSV derived from data presented by Dorra, Lee, and Bankoff for Peclet numbers greater than 70,000

Data set	Geometry	Number of data sets where Pe>70,000	Mean Stanton number	Sample standard deviation
Edelman & Elias*	tube	0	0.1049	0.0617
Evangelisti & Lupoli†	annulus	2	0.0064	0.0008
Ferrell†	tube	1	0.0102	...
Rogers, et al.	annulus	0	0.0601	0.0372
Sekoguchi, et al.	tube	3	0.0032	0.0009
Staub, et al.	rectangle	8	0.0214	0.0023

*The Peclet numbers for all of this data set were below 70,000.

†Peclet numbers were both above and below 70,000, only data for Peclet numbers above 70,000 were used in the calculations.

Table 4.--Mean Stanton numbers at OFI for open flow areas

Data set	Geometry	N	Mean Stanton number	Sample standard deviation
Columbia (20)*	tube	48	0.0063	0.0008
Whittle & Forgan (67)†	rectangle	57	0.0101	0.0012
Whittle & Forgan (67)	tube	9	0.0076	0.0008

*Stanton numbers below 0.003 as listed in Table XX, Appendix 5 were not used in the calculation of the sample number, sample mean, or sample standard deviation.

†Data where the Peclet number was below 70,000 as listed in Table XX, Appendix 5 were not used in the calculation of the sample number, sample mean, or sample standard deviation.

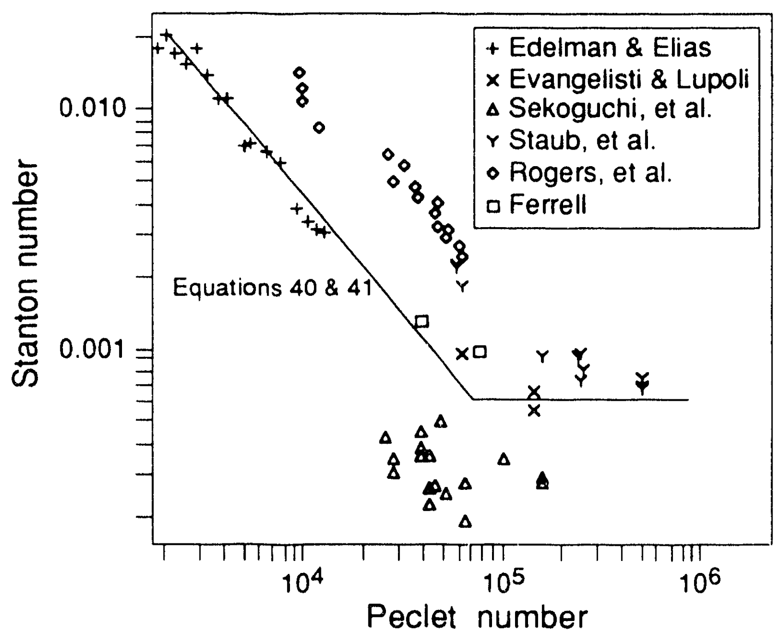

Figure 12, Experimental OSV test data summarized by Dorra, Lee, and Bankoff (69) See Table 5-1.

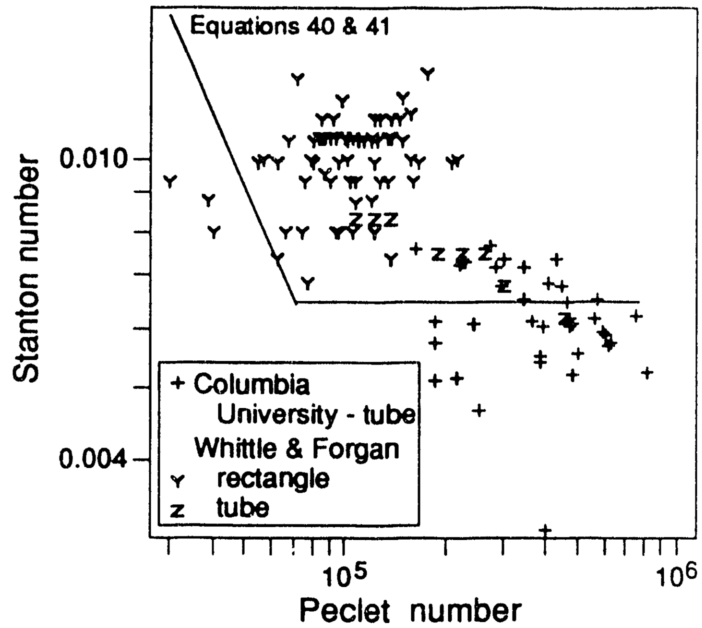

Figure 13, Experimental OFI test data

Heater Channel Construction

Whittle and Forgan (67), Maulbetsch and Griffth (52), and researchers at Columbia University (16) used direct heating of the flow channel by applying a DC voltage between both ends of the heated length. The construction materials used by these researchers are listed in Table 5. No significant thermo-hydraulic differences are apparent when comparing the various construction materials used. Columbia University HTRF completed a separate effects test (tube program) to compare the OFI for 304 stainless steel tubes and 600 series Inconnel. Little variation was observed. (16)

Table 5.--Channel construction materials used in previous demand curve testing

	Channel material	Channel geometry
Whittle and Forgan (67)	phosphor bronze	rectangular
Maulbetsch and Griffith (52)	304 stainless steel or nickel*	tube
Cheh, et al. (17)	304 stainless steel and Inconnel	tube

*The test section construction material was not explicitly stated, however reference is made to the description by Dormer and Bergles (1964) where both 304 stainless steal and nickel were used in the construction of the test section.

Researchers at Creare (9) conducted a series of steady state tests in indirectly heated aluminum channels. Resistance element heaters were installed in the inner and outer annular wall. These heaters were electrically isolated from the wetted aluminum. No change in demand curve behavior was observed when compared to directly heated test sections.

Heater Channel Geometry

Whittle and Forgan (67) generated demand curves for four different rectangular geometries and one round tube. The rectangular sections were heated on two surfaces with less than 1 percent of the heat transmitted to the fluid from the gap walls. Based on these tests a correlation to predict the onset of flow instability (minimum demand curve pressure drop) was developed.

(43)
$$R = \frac{1}{1+\dfrac{\eta}{L_h/D_h}} = \frac{T_{OFI}-T_{inlet}}{T_{sat}-T_{inlet}}$$

The bubble detachment parameter, η, corresponds with that suggested by Bowring (11) which is defined in Equation 39. For the two operating pressures evaluated by Whittle and Forgan the bubble detachment parameter is either 14.1 or 14.2. With such a small variation it is doubtful that a pressure effect would be observed. A better fit of the test data (29) was obtained using a value of 25.

The form of Equation 43 is the same form as the Q_{ratio} which was defined earlier in Equation 33. If the OFI temperature occurs at the exit then the Q_{ratio} is equal to the temperature ratio, R.

(44)
$$\begin{aligned} Q_{ratio} &= \frac{\phi}{\dot{m}c_p(T_{sat}-T_{in})} \\ &= \frac{\dot{m}c_p(T_{out}-T_{in})}{\dot{m}c_p(T_{sat}-T_{in})} \\ &= \frac{T_{out}-T_{in}}{T_{sat}-T_{in}} \end{aligned}$$

Researchers at Columbia University (29) produced 116 downflow deionized water demand curves during 1988 and 1990 as part of the SS OFI program. The diameters of these tubes range from 9.1 to 28.4 mm. The bubble detachment parameter, η, estimated using a least square fit for this data 41.93. The operating pressures for these tests were 240 kPa and 450 kPa abs. The bubble detachment parameter predicted by Equation 39 would be 14.2 and 14.4. While the bubble detachment criterion for the Whittle and Forgan data does fall within the band of the data used by Bowring (11) to develop Equation 39, the parameter predicted for the Columbia University tube data does not.

For channel with a uniform heat flux the Stanton number as defined by Saha and Zuber (62) can be compared with Equation 39. To demonstrate how the concept of a constant Stanton number local phenomena agrees with the constant R value that is a global phenomena.

(45) $$St = \frac{\phi}{u\rho c_p \Delta T_\lambda} = \frac{1}{\rho c_p \eta}$$

Since the product of the density and specific heat varies only slightly with temperature a Stanton number at OFI can be predicted using the bubble departure parameter, η. At one atmosphere over at temperature range of 20 to 150°C the Stanton number estimate will range from 0.0170 to 0.0178. This is much higher than suggested by Saha and Zuber (62). For the bubble detachment parameter of 41.93 the Stanton number ranges from 0.0057 to 0.0060. Bowring's (11) low value bubble detachment parameter might be explained best by a review of the Peclet numbers for some of the data used in his analysis. One set of tests for a hydraulic diameter of 20.3 mm operated at 1.1 MPa abs, the operating velocity ranged from 0.40 to 0.85 m/s. Since the subcoolings only varied from 2 to 19°C the value of $\rho \cdot c_p/k$ may be considered as 5,800,000 s/m^2. This translates into a range of Peclet numbers between 47,000 to 100,000. For a small channel (hydraulic diameter of 11.3 mm) the Peclet numbers range from 36,000 to 82,000.

A modified form of Equation 44 for the Q_{ratio} at the demand curve minimum was suggested by Dougherty, et al. (29) using the previously mentioned Columbia tube data.

(46) $$Q_{ratio} = \frac{1}{1 + \frac{0.25}{St\,(L/D)}}$$

For a majority of the data (L/D = 86, 96, 129, 156, and 160) the predicted heat flux at the demand curve minimum is shown to be well predicted the Equation

43 with η = 41.93 and Equation 46, and was over predicted by Equation 43 with η = 25. The heat flux for higher L/D (154 and 267) is better predicted by Equation 43 with η = 25 and under predicted by the other two equations (Equation 43 with η = 41.93 and Equation 46).

Equation 46 is specific to tube geometries. Appendix XX presents the development of a more general form.

(47)
$$Q_{ratio} = \frac{1}{1 + \frac{A_f}{A_h St}}$$

Researchers at Columbia University (17, 19) conducted downflow OFI tests as part of the SRS OFI program in a uniformly heated annulus channel (59.61 mm x 73.63 mm x 3.66 m long) constructed of two Inconel 625 tubes which were electrically isolated. The outer tube was also thermally insulated. The demand curve minimum for a round tube with the same L/D (260) under the same boundary conditions will occur at a slightly lower flow rate than the annular section.

The demand curve minimum occurring at the same Q_{ratio} for any given heat flux and heater geometry has been demonstrated to hold for the variations listed in Table 6.

Table 6.--Boundary condition separate effects evaluations on OFI

	Range of condition evaluated	
Dissolved gas effect (saturation pressure, kPa)		
Creare	108	204
Exit Pressure, kPa		
Columbia annular tests	239	446
Columbia tube tests (29)	239	446
Whittle & Forgan (67)	120	170
Flow direction		
Whittle & Forgan (67)	up	down
Heat flux, kW/m^2		
Creare (9)	315	1,180
Columbia annular tests (17)	631	2,520
Columbia tube tests (29)	1,262	3,155
Maulbetsch and Griffith (52)	1580	15,800
Inlet pressure (kPa)		
Creare (9)	377	520
Inlet temperature (°C)		
Columbia tube tests (29)	25	50
Whittle & Forgan (67)	35	75
Columbia annular tests (17)	25	80
L/D		
Maulbetsch and Griffith (52)	25	250
Whittle and Forgan (67)	83	191
Columbia University tube tests (29)	86	267

Behavior Comparison of Flow and Pressure Controlled Systems

The behavior of dabatic channel is very dependent on the control scheme used in the operation the test loop. For pressure controlled systems where the demand curve is traced by incrementally decreasing the supply pressure (normally by increasing the flow through a bypass line in parallel with the heated test channel) when the pressure decreases below the demand curve minimum a flow excursion will occur. For flow controlled systems flow is incrementally decreased to generate the demand curve. If the supply system is adequate, operation at flows below the OFI flow is possible and an excursion will not occur.

Maulbetsch and Griffith (52), and Whittle and Forgan (67) demonstrated no variation between the flow at excursive instability for pressure controlled test and the demand curve minimum for flow controlled tests. During the Columbia University HTRF tube tests (29) no flow instabilities (excursions) were observed during controlled flow tests, however FI did occur during each controlled pressure test.

Heater Channel Flux Profile

Whittle and Forgan (67) tested one rectangular channel with a nonuniform heat flux. The axial heat flux variation had no significant effect on the Q_{ratio} at the demand curve minimum. Researchers at the Columbia University HTRF (29) completed a series of downflow tests (14) with deionized water as the working fluid, a heated length of 2.44 m and an L/D of 154 with directed heated Inconnel 625 tubes. Four different profiles were evaluated. These profiles are listed in Table 7. The tests were conducted for a heat flux range of 0 to 3155 kW/m^2, 240 and 450 kPa at the channel exit, and 19 and 103°C inlet temperature. The Peclet numbers for these tests were in excess of 100,000. The observed effect of heat flux profiles was considered minimal. For the same average heat flux the OFI flow was within 10% of the uniformly heated demand curve flow.

Table 7.--Axial heat flux profiles evaluated by the Columbia University HTRF (29)

	Profile description	Observed effect on OFI		
		N	$\bar{X}$	S
Uniform	Heat flux was uniform over heated length	11	0.816	0.037
Cosine	A chopped cosine wave with a maximum flux equal to 1.26 times the average heat flux.	10	0.878	0.038
Double Peak	A flux peak occurs at z/L equal to 0.2 and 0.8 with a maximum flux that is 1.2 times the average heat flux.	4	0.836	0.043
Exit Peak	The flux peak occurs at z/L equal to 0.6 with a maximum flux that is 1.5 times the average heat flux.	4	0.836	0.037

In the Columbia University Annular tests (17) both uniform and asymmetric heating were evaluated. Asymmetric heating consisted of providing heat to only one annulus wall or providing an unequal heat to each wall. It was observed that the flow rate at OFI will be higher for a non-symmetric heated annulus. Part of the Creare program was to investigate the effect of azimuthal variations in the heat flux profile of an annular channel; little effect on the demand curve minimum was observed.

Operation on the Negative Portion of the Demand Curve

All of the experimental test data for flow controlled OF tests include subcooled flows below the OFI flow. Mirshak (53, 54) presents demand curves in heated tubes where test data has been obtained both at the demand curve minimum and the local maximum. Mirshak (54) attributes to Toyoda the criteria for stable operation on the negative portion of the demand curve. For stable operation Equation 48 must be true.

$$\frac{\partial p_{supply}}{\partial Q} \leq \frac{\partial p_{demand}}{\partial Q} \quad (48)$$

Maulbetsch and Griffith (52) presented an analytical development of this criterion for stability. When restated the criterion is: If the slope of the demand curve is steeper than the supply curve, an excursive flow instability could occur.

Flow Instabilities

The Ledinegg instability is not the only flow instability that can occur in a diabatic system. Bouré, Bergles and Tong (10) separated two-phase flow instabilities into two types: static and dynamic. A static instability can lead to either an alternate steady state condition or an oscillatory condition. A Ledinegg instability is a fundamental static flow instability where a small Fluctuation in flow conditions results in a new steady state conditions substantially different from the initial condition. There are several other static flow instabilities. These are listed in Table 8.

Instabilities are considered fundamental when the instability mechanism can be identified and evaluated without interaction with other thermal-hydraulic instability behaviors. A Ledinegg instability also fits into this classification.

Table 8.--Static flow instability classifications suggested by Bouré, Bergles and Tong (10)

	Description
	Fundamental
Ledinegg instability	The fluid supply system cannot provide an adequate pressure and flow to meet demand curve of the heated section.
Boiling crisis	The heat removal mechanism is not able to remove the amount of energy being transmitted to the heated surface.
	Fundamental relation instability
Flow pattern transition instability	The flow oscillates from one regime to a second created by variations in the heat transfer efficiency and pressure gradient between the two regimes
	Compound relaxation instability
Bumping	The heat transfer mechanism transitions between natural convection and boiling.
Geysering	Liquid and vapor are cyclically expelled from a closed end tube.
Chugging	Flow is cyclically expelled from the ends of a heated flow channel.

Boiling Crisis

Bouré, Bergles and Tong (10) characterize boiling crisis as the ineffective removal of heat from the heated surface and suggest that this crisis is characterized by excursions of the wall temperatures and flow oscillations. Leung's (51) statement on CHF illustrates how the definition of CHF has varied in the literature:

> Critical heat flux (CHF) condition in a forced convection boiling system is characterized by a sudden reduction in the heat transfer

coefficient as indicated by a temperature oscillation or excursion of the heated surface. Other names such as burnout, boiling crisis, dryout and boiling transition have been used. The maximum heat flux just before this crisis occurs is termed the critical heat flux."

Collier (24) suggests that dryout is when "complete evaporation of the liquid film occurs" during annular flow. It is thus limited to events where the heat transfer mechanism is principally evaporation of the liquid. Leung (51) suggests that dryout occurs when the film thickness becomes very thin and breaks down allowing dry patches to form. The wall temperature during dryout will only experience a moderate temperature excursion.

DNB occurs in flows where convection is the primary heat transfer mechanism between the wall surface and the liquid. It is characterized by extreme wall temperature excursions and flow oscillations. Collier (24) describes three types of CHF: Dryout, subcooled DNB, and saturated DNB. Subcooled DNB occurs "when the bulk fluid is subcooled at the location where the critical heat flux is exceeded." Saturated DNB occurs when the bulk fluid is at saturated conditions at the location where critical heat flux is exceeded.

Leung's (51) description of DNB is limited to bubbly flow when the bubbly boundary layer prevents liquid from contacting the hot surface. This creates a vapor film. The wall temperature will increase as a result of the increased heat transfer resistance. The wall temperature will often increase in an excursive manner.

Bergles, Lopina, and Fiori (6) evaluated the flow regime in small diameter (<6.15 mm) diabatic tubes. The test section was equipped with an electric void probe and a sight glass section at the test section exit. For low pressure systems (<240,000 Pa, 35 psia) the flow regime will transition from bubbly to slug flow. The exit quality at this transition varied from approximately -2 to -1 percent exit quality for L/D's greater than 60. This relationship was evaluated over a mass flux range from 270 to 3400 kg/m^2·s (0.2 to 2.5 M#$_m$/hr·ft^2). The heat flux was approximately 3 kW/m^2. A transition from slug to annular flow did not occur until the exit quality was greater than zero. For subcooled exit conditions the critical heat flux decreased with tube diameter and the quality at the exit. The critical heat flux verses exit quality was observed to pass though a minimum near an exit quality of zero. This minimum disappeared at the exit pressure increase above 280,000 Pa (40 psia). The slug flow in this region was composed of irregular vapor bubbles that were several tube diameters long and separated by liquid containing small bubbles. The flow and pressure both experience pressure pulsations at the end of the test section.

Kawamura, Tachibana, and Akiyama (45) provide a good description of a DNB event: "After a void setback, many small bubbles grow and collapse repeatedly on a heating surface. Test piece surface temperature rises very slowly in this nucleate boiling region. After a certain time interval, some of the small bubbles coalesce to form a vapor film on the surface. The rising rate of the surface temperature increases again at that time. This the critical point or the DNB point in the transient boiling. After the DNB point, the vapor film once spreads to cover the surface."

Hodges (34, 35) evaluated the effect of ribs on burnout in rectangular channels that were equipped with flat aluminum strips mounted on one wall serving as the heaters. The rib was a rectangular nonconducting fiberglass that was in contact with the heated surface. The parameters for this testing are listed in Table 9. Two different modes of heater failure were identified during the testing: (1) near the rib tip at the liquid surface, and (2) local melting under the rib. The transition between these two failure modes was predictable using a finning parameter, $x_o/\sqrt{ky}$, and the heat flux parallel to the surface at the edge of the rib, $\phi x_o/y$. For aluminum the finning parameter is

(49) $$P = \frac{x_o}{\sqrt{ky}}$$

The region of operation that resulted in true burnout (failure mode 1) was for finning parameters that were less than 0.003 to 0.004 m·(°C/W)$^{1/2}$ (0.007 to 0.009 ft·(hr·°C/pcu)$^{1/2}$).

Table 9.--Expermental conditions investigated by Hodges (35)

Heat flux	2.499 pcu/ft^2·hr
Flow velocity	5.5 to 42.5 fps
Subcooling	20 to 107·C
Pressure	40 to 80 psig
Hydraulic diameter, D	0.44 to 0.5"
Channel width, a	1 to 2.05"
Rib width, x_o	0 to 0.25"

Fundamental Relation Instability

Flow instabilities can be created in systems where two or more flow regimes can exist. The flow pattern may oscillate between annular, and bubbly or slug flow. The pressure drop in bubbly-slug flow is greater than in annular flow. The higher pressure drop in bubbly flow will result in flow decrease, an increase in the void fraction, and a transition to annular flow. If the vapor generation rate in not adequate to maintain annular flow then bubbly flow will reoccur. The flow pattern will then oscillate between these two flow regimes (10).

During slug flow as the vapor portion passes over a section of wall, the wall temperature will rise because of the low heat transfer coefficient. The wall will then be quenched by the following liquid slug. If the heater wall temperature is not sufficiently lowered by the liquid slug burnout can occur. For low pressure systems "this flow pattern is encountered only at very low qualities of the order of 0 to 7%" (52).

Compound Relaxation Instability

Repetitive expulsion of coolant from the heated channel can be caused by the sudden vaporization of the liquid phase and the corresponding rapid increase in the specific volume of the mixture. Alternate names for this instability are: Bumping, geysering, and chugging (10). This behavior while repetitive is not necessary periodic. These instabilities are created by restrictions to efficient heat transfer that are metastable.

Maulbetsch and Griffith (52) identity two different mechanisms for nucleation instabilities or "flashing" instabilities. Both mechanisms produce a sudden and rapid vaporization of the liquid phase which a corresponding rapid increase in the specific volume of the mixture. When there is a deficit of nucleation sites (e.g., a smooth, clean surface) a large wall superheat can be expected. "Under these conditions, when a bubble does start to grow, it will grow violently and eject liquid from the heated channel. This process will cool the remaining liquid and the heater surface with the result that further nucleation will be snuffed out, until the required degree of superheat is reestablished. Such behavior can be sustained at a frequency associated with the time required for bubble growth, ejection and runback of the liquid, and re-establishment of the superheat" (52). Bouré, Bergles and Tong (10) referred to this mechanism as a vapor burst.

The second "flashing" mechanism occurs when a large reservoir is above a vertical heated channel. A description of this situation is: "When a bubble does start to grow it would be displaced into the reservoir. This caused the pressure at the bubble, which was just comprised of the hydrostatic head of the liquid above it, to drop. The reservoir was large enough so that the pressure there remained constant. Hence, near the bubble, the local saturation temperature would decrease, raising the superheat and causing the bubble to grow faster. The end result would be the violent ejection of the liquid from the tube followed by runback of cold water and reinitiation of nucleation. This behavior would continue indefinitely at a fairly regular frequency." (52)

Bouré, Bergles and Tong (10) suggest that the term chugging be reserved for flow channels where fluid can be expelled from one or both ends, while the term geysering is more appropriate for closed end tubes. Bumping refers to an irregular cyclic transition between natural convection and boiling most commonly observed in liquid metals.

Dynamic Instabilities

Dynamic instabilities occur in flows where the inertia and other feedback effects are part of the instability process. In such cases the application of steady-state solutions is not sufficient to predict system behavior, or event the event for threshold prediction (10). The instability is considered compound since several elementary mechanisms interact and cannot be evaluated separately. Several types of compound instabilities are listed in Table 10.

Table 10.--Dynamic flow instability classifications as proposed by Bouré, Bergles and Tong (10)

	Description
	Fundamental dynamic instabilities
Acoustic oscillations	Resonance of pressure waves induces oscillations.
Density wave oscillations	Interactions between flow rate, density, and pressure drop create oscillating behavior.
	Compound dynamic instabilities
Thermal oscillations	Variable heat transfer caused by shifting of flow transition locations creates thermal oscillations.
BWR instability	Interaction of void reactivity coupling with flow dynamic and heat transfer to create flow and power oscillations.
Parallel channel instability	Interaction between parallel channels where the flow regimes vary in each channel with time.
	Compound dynamic instability as a secondary phenomena
Pressure drop oscillations	A flow excursion is initiates because of a dynamic interaction between the heated channel and compressible volume.

Fundamental Dynamic Instabilities

High frequencies are the characteristic of acoustic or pressure wave oscillations. The oscillation period is normally of the same magnitude as the pressure wave system residence time. (Time for pressure wave to travel through system.) The reported frequency range for this instability is 10 to 10,000 Hz (10).

There are several alternative names for density wave oscillations. These include: flow-void feedback instabilities; time-delay oscillations; density wave oscillations, and density effect mechanism. The behavior is described by Bouré, Bergles and Tong (10):

> A temporary reduction of inlet flow in a heated channel increases the rate of enthalpy rise, thereby reducing the average density. This

disturbance affects the pressure drop as well as the heat transfer behavior... For boiling systems, the oscillations are dues to multiple regenerative feedbacks between the flow rate, vapor generation rate, and pressure drop... These low frequency oscillations in which the period is approximately one to two times the time required for a fluid particle to travel though the channel.

Compound Dynamic Instabilities

For constant heat flux systems that are operating with film boiling present, large amplitude thermal oscillations have been observed. These oscillations are attributed to dryout point shifting location and local conditions alternating between film boiling and transition boiling. Bouré, Bergles and Tong (10) suggest that a primary phenomenon such as density wave oscillations must be required to destabilize the film boiling is caused by an interaction between hydraulic and power generation. If the time constant for the hydraulic oscillation is similar to the time constant of the nuclear fuel element nuclear-coupled flow instability can occur.

Oscillatory behavior has been observed for two-phase flow conditions in parallel channel systems. Ozawa, Akagawa, and Sakaguchi (56) identified two types of pressure drop oscillations for an adiabatic gas-liquid flow system (air and water) with compressibilities in both the gas and liquid systems: Relaxation oscillation and quasi-state oscillation. During relaxation oscillation the volumetric liquid flux is constant or nearly constant and the gas flow and pressure drop will oscillate. During quasi-state oscillation the liquid flow rate, gas flow rate and pressure drop will oscillate. This second type of instability occurs in the presence of relatively high compressibility in the liquid feed pipe.

Compound Dynamic Instability as a Secondary Phenomena

Maulbetsch and Griffith (52) suggest that pressure drop oscillatory instability is a result of an energy storage mechanism such as superheated liquid, heat capacity of the heated surface or a compressible volume located just upstream, or in the diabatic channel. These oscillations occur during operation on the negative sloped portion of the demand curve (10). This phenomenon is characterized by very low frequencies (0.1 Hz). Maulbetsch and Griffith (52) demonstrated that a pressure drop instability will not occur unless the Ledinegg instability limit is also exceeded. The failure mechanisms for Ledinegg and compressible volume oscillatory burnout tests were run to destruction of the test section. Maulbetsch and Griffith (52) describe the failure mechanisms as quite different:

> In the excursion case [pressure controlled OFI], the tubes, after burnout, were quite ragged and showed evidence of overheating along most of their length. This is typical of burnout caused by sudden flow starvation. The tubes which failed due to the presence of a compressible volume, on the other hand, exhibited a very clean break, with no evidence of overheating outside of a very narrow region on either side of the burnout location. In this respect they were similar to the ordinary stable burnout tests."

Boiling Curves

Boiling cures are classified into two categories based on the fluid boundary conditions. Pool boiling curves represent the behavior of a heated surface which is immersed in a standing fluid. In this situation fluid density is a significant factor, and natural convection is the mode of heat transfer prior to vapor forming. The second category of boiling curve is for a subcooled liquid flowing over a heated surface. The surface may be a heated channel or an obstruction inserted into the flow stream. The effect of density is normally negligible and the turbulence of the subcooled liquid tends to increase the heat transfer effectiveness.

Pool Boiling

Pool boiling curves such as shown in Figure 14 are generated in several different ways. The most common is to incrementally increase the heat flux for a uniformly heated surface starting with natural convection heat transfer (A to B), transitioning to nucleate boiling until point C is reached. At this point any additional increase in heat flux will result in an excursion to point E. During this transition the heater normally melts hence point C is commonly referred to as the burnout point. It has been possible to operate in the transition region (C to D) using a condensing-vapor for heat generation rather than electrical heating (Rohsenow & Choi) such that the system is wall temperature controlled.

Collier (24) suggests that the peak pool boiling heat flux can be estimated from:

(50)
$$\phi_{peak} = K h_{fg} \rho_v \left[\frac{\sigma g (\rho_l - \rho_v)}{\rho_v^2} \right]^{1/4}$$

where the value of K ranges from $\pi/24$ to 0.149.

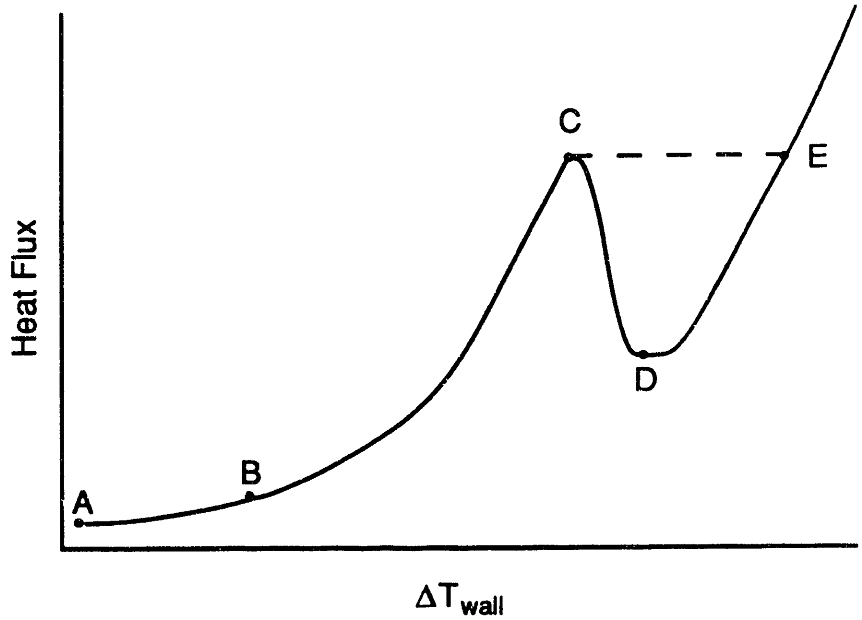

Figure 14. Typical pool boiling curve

Forced Convection Boiling

The flow of a subcooled liquid across a heated surface will increase the heat transfer effectiveness as compared with natural convection and pool boiling. A typical forced convection boiling curve is shown in Figure 15. This curve is for a single flow velocity. The region from A to B is non-boiling forced convection. The wall temperature may be predicted using the Dittus-Boelter equation (Thom, et al.):

(51) $$Nu = \left[\frac{\phi D_e}{k_f (T_w - T_{sat})} \right] = 0.023 Re^{0.8} Pr_f^{0.4}$$

Fully developed nucleate boiling is present in the region between C and D in Figure 15. Thom et al. (72) present a correlation for water to predict the wall superheat (T_w-T_{sat}) in this region

(52) $$\Delta T_{sat} = \frac{0.072\,\phi^{0.5}}{e^{p/1260}}$$

where temperature, T, is in °F, heat flux, ϕ, is in Btu/hr·ft^2 and pressure, p, is in psia. An alternate form of Equation 52 in SI units presented by Collier (24) is:

(53) $$\left(T_w - T_{sat}\right) = 22.65\left(\frac{\phi}{10^6}\right)^{0.5} e^{-p/8,700,000}$$

The region between B and C is a transition region; the wall heat transfer in this region was successfully predicted by Block et al. (9) based on a relation by Bowring (11).

(54) $$\phi = \phi_{sb} + \phi_{fc}$$

Hino and Ueda (33) investigated alternative relations to Equation 54 comparing them with experimental data produced with Refrigerant 113. The alternative, more complex, correlations provided only slightly improved accuracy. Hino and Ueda (33) noted on their boiling curves the point of OSV and CHF. OSV occurred at the transition between partial nucleate boiling and fully developed nucleate boiling. CHF occurred at a point high on the nucleate boiling curve.

The region D to E in Figure 15 is a transition region from nucleate boiling to film boiling while the region beyond point E is in film boiling. Several researchers have developed boiling curves by using a transient technique (22). A large metal block is heated to a predetermined temperature. The test is initiated by diverting flow into the hot block. This flow cools the block; temperature data is recorded as a function of time. The heat flux is then calculated based on the thermal mass of the block and the measured temperatures. For distilled water at a mass flux of 136 $kg/m^2 \cdot s$, and subcoolings which range from 0 to 27.8°C, Cheg, Ng, and Heng (23) measured a film heat flux ranging from 300 to 800 kW/m^2. The film heat flux increased with increased subcooling. The peak heat flux (point D in Figure 15) was relatively insensitive to subcooling and was approximately 2,000 kW/m^2. The wall temperature at the peak heat flux was approximately 150°C. The peak heat flux was found to increase with mass flux although at 203 $kg/m^2 \cdot s$ and 0°C subcooling the value was still about 2,000 kW/m^2.

Feng, and Johannsen (30) evaluated the maximum transition boiling temperature (MTBT) between transition boiling and film boiling. The point of MTBT occurred at the wall heat flux minima. The axial location of this minima varied with the inlet conditions and heat flux. While the majority of the data presented was for positive local equilibrium quality some data was for subcooled local conditions. For large subcoolings (30°C) at 700 kPa the MTBT did not vary with local equilibrium quality. The MTBT did increase with increasing heat flux. For a subcooling of 15°C the MTBT increased as the local equilibrium increased (became less negative). For a mass flux of 300 $kg/s \cdot m^2$ the MTBT was approximately 380°C.

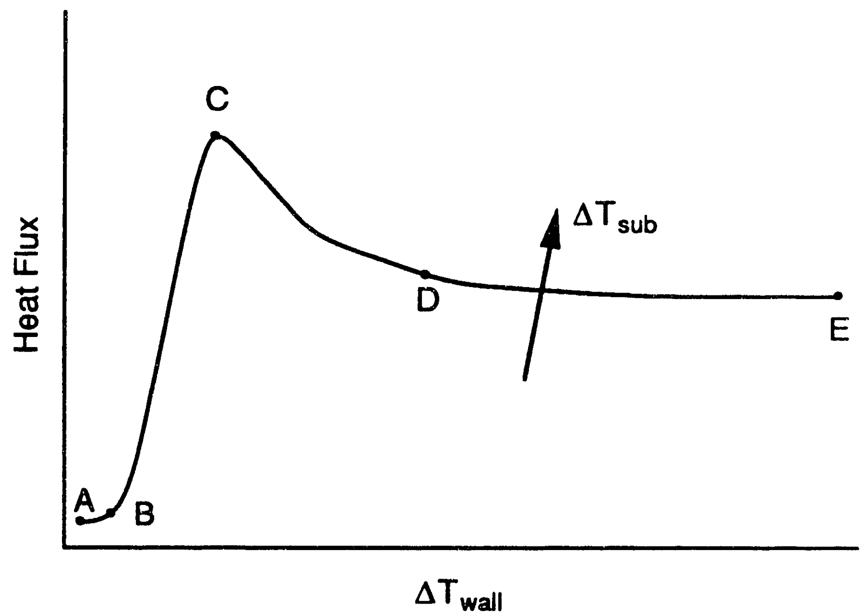

Figure 15. Typical forced convection boiling curves for subcooled liquid

Boiling Curve Hysterises

The boiling curve shown in Figure 15 does not indicate an important behavior which occurs during the transition between forced non-boiling convection and fully developed nucleate boiling. For a channel where the heat flux is increasing nucleate boiling may not readily occur until an adequate number of cavities activated. Activation of these sites requires more energy than would be required to maintain the sites as active. Figure 16 presents the variation between increasing and decreasing heat flux behavior. Hino and Ueda demonstrated that the region of increasing heat flux the boiling curve trajectory follows the path A-F-G. The path by Equation 55.

$$\frac{\phi D_e}{k_l\,(T_w - T_l)} = 0.023\ Re^{0.8}\ Pr^{1/3} \qquad (55)$$

When the necessary number of activation sites is available the wall superheat will decrease to that of location H, where the boiling curve trajectory will then follow the path described earlier. For decreasing heat flux the boiling curve trajectory will be B-H-F-A. The cession of vapor formation coincides approximately with the point of ONB.

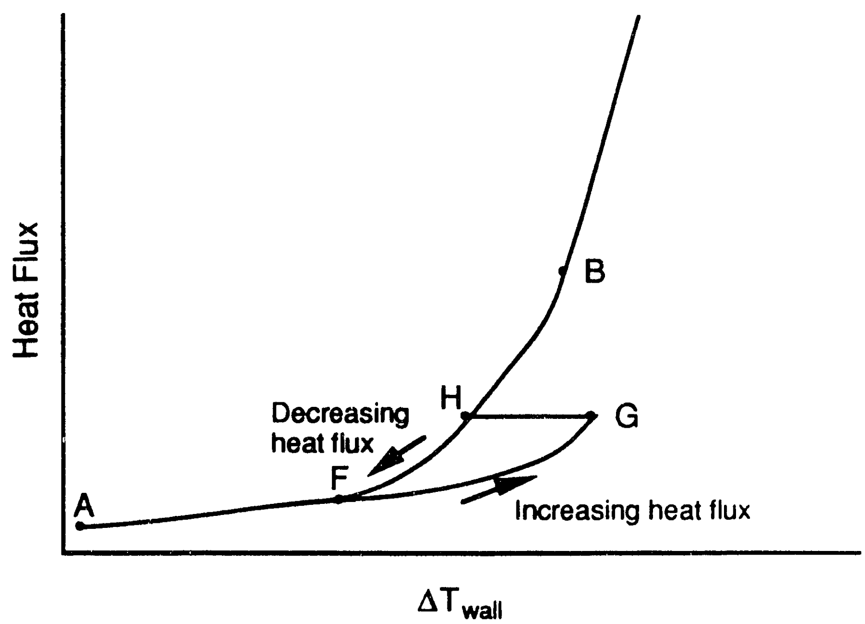

Figure 16. Forced convection boiling curve hysteresis, AFGHB for increasing heat flux, BHFA for decreasing heat flux

Alternate Transition Boiling Curve

Witte and Lienhard, 1982, based on studies with n-pentane suggested that there were possibly two transition boiling curves. The first curve is approached from the left as shown in Figure 17. The second curve lies below the first and is approached from the right. The investigation of alternate transition curves was expanded by Ramilison, 1985. Ramilison and Lienhard (1987) suggested that when the effect of the condensation process is included the form of the alternate transition curve would be as shown in Figure 17. The effect was found to be more pronounced for rough surfaces and the minimum heat flux (point J in Figure 17) was lower than the maximum heat flux (point C in Figure 17) The lowest measured wall superheat on the film boiling curve was approximately twice the wall superheat at the peak heat flux (point C, Figure 17).

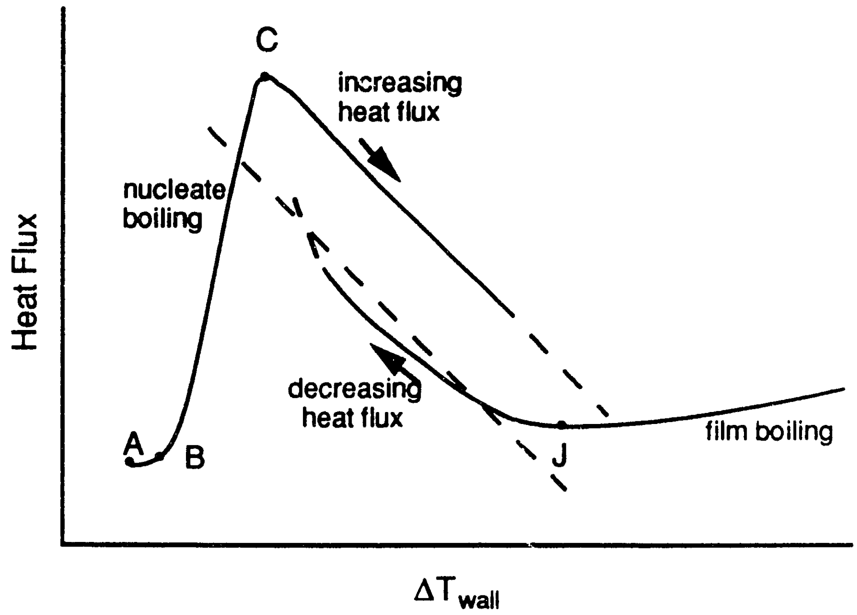

Figure 17. Alternate transition boiling curves as suggested by Ramilison and Lienhard (1987)

Obstruction Effects on Boiling

Ishibashi, and Nishikawa (37) evaluated the effect of a surface placed near a heated surface during pool boiling. It was demonstrated that below a gap of 3 mm the boiling behavior was significantly different from larger gaps. In narrow gaps vapor coalesced to blanket the heated surface, for larger gaps only isolated bubbles formed. It was shown in this work by using both water and water solutions that the bubble behavior for narrow gaps was independent of surface tension.

Preliminary Data -- 9 September 1993

Sharon, Chen, and Bankoff (63) observed that the wall superheat at ONB on the outside of a heated tube at a tubesheet occurs at very low wall superheats. The lower values occurred for the gap of 0.191 mm (typically 0.2°C), while the higher value occurs for a gap of 0.317 mm (typically 3°C). The tube diameter was 19.05 mm and the plate thickness was 19.05 mm. For the conditions (heat flux and local pressure) where ONB was observed the expected range of superheat based on the Bergles and Rosenhow ONB correlation is 2 or 3°C.

Flow Obstruction Effects on OFI

Ribbed flow channel behavior prior to burnout has been described and filmed by Hodges (35). He describes three regions of boiling behavior in a rectangular heated channel with an insulating rib. A small region near the rib is in stable film boiling. This was attributed to the reduced fluid velocity near the rib. Adjacent to this is a region of intermittent film boiling which was 6 mm (1/4") wide while the remainder of the channel remains in nucleate boiling. At 20 fps and 55 psia the intermittent vapor films were 6 to 13 mm (1/4" to 1/2") long, and appeared to move upward while the bulk flow direction was downward. Hodges (DPST-73-206) presents a hydrodynamic explanation for this behavior.

> This apparent upward film motion is explained as follows: the film forms and tries to spread in all directions. A boundary layer develops on the film surface. This boundary layer is laminar along the forward (upstream) part of the film but becomes turbulent after a short distance and transition to turbulent flow occurs at approximately the same Reynolds' number as for a flat plate (3×10^5), the stable film length is calculated to be approximately 0.4 inch, which agrees well with the observed length. The film spreads upward (and appears to move upwards) because it is growing upwards and is being destroyed downstream.

Johnston and Neff observed that in a downward flow uniformly heated ribbed annuli the variation between subchannels of the wall superheats at the test section exit were negligible except at the demand curve minimum. At the minimum the unheated wall temperature for the subchannel with the highest wall temperature was the same at the top and bottom. They suggested that a flow redistribution had occurred and that the flow in the hot channel was stalled. This redistribution was the result of vapor forming at the rib tip with the accompanying density change creating increased resistance to flow in the affected subchannel thus creating a Ledinegg instability within the test channel.

The presence of fins can enhance the removal of heat during nucleate boiling. Kowalski, Mills, and Shim (47) evaluated the effect of a conducting rib on ONB, OSV, and heat transfer. The test apparatus consisted of an outer glass tube surrounding the inner ribbed heated tube. Eight ribs were equally spaced around the heater. These ribs were 1.027 mm high, 0.822 mm wide. The annular gap appears to have been 4.111 mm. Both ONB and OSV occurred first in the space between the ribs on the primary surface. For high mass flux (>1500 kg/m^2·s) the bubble detachment occurred after the bubbles first slid along the inner wall. The Peclet number at this transition is 66,000. For this testing the range of operation included: mass fluxes of 1000 to 5900 kg/m^2·s, pressures of 110 to 350 kPa, and inlet subcoolings of 30 to 80°C. The Peclet number for these conditions is approximately 44,000 to 261,000. Kowalski, Mills, and Shim (47) suggested Equation 56 as a best fit of the data from their work.

$$St = 0.0446\ Pe^{-0.18} \tag{56}$$

Conducting Spacer Ribs

Block, et al. as part of the SRS OFI program, constructed and operated test channels with aluminum heat transfer surfaces. Two different annular geometries were evaluated: Ribbed and ribless, and two test sections of each type were tested. The ribless channel was a "pure" annulus with the exception of centering pins (0.094" diameter for first construction and 0.109" x 0.75" long for second construction) which were used to hold the inner annulus pipe in position. The flow area was held constant for these tests. Four ribs were an integral part of the inner annular wall for the ribbed tests. The average clearance between the ribs and the outer wall ranged from 0.020 to 0.045 inches. The geometries for the test sections are provided in Table 11.

Table 11.--Annular geometries used in OFI testing

	Non-ribbed geometry	Ribbed geometry
Creare		
Inner diameter, mm	60.15	59.79
Outer diameter, mm	73.46	73.55
Heated length, m	3.96	3.96
Hydraulic diameter, mm	13.35	11.89
Spacer rib material	...	aluminum
Flow area, mm^2	1403	1394
Columbia University		
Inner diameter, mm	59.61	59.61
Outer diameter, mm	73.63	73.46
Heated length, m	3.66	3.66
Hydraulic diameter, mm	14.02	14.00
Spacer rib material	...	phenolic asbestos
Rib width, mm	...	1.59
Flow area, mm^2	1465	1400
Johnston & Neff		
Inner diameter, mm	80.09	80.09
Outer diameter, mm	83.24	83.24
Heated length, m	0.59	0.59
Hydraulic diameter, mm	3.15	...
Spacer rib material	...	fiberglass
Flow area, mm^2	404	...

Table 12.--Summary of demand curve minimum data for open and ribbed channels

	Number of samples	Q_{ratio} at minimum $\pm t_{\alpha/2} \cdot S_m$	Stanton number $\pm t_{\alpha/2} \cdot S_m$
open annulus			
Creare	5	0.889 ± 0.067	0.0080 ± 0.0044
Columbia			
Heated both sides	14	0.937 ± 0.020	0.0063 ± 0.0023
Heated on inside	2	0.839 ± 0.305	0.0084 ± 0.0022
Heated on outside	2	0.891 ± 0.314	0.0082 ± 0.0040
Johnston & Neff	22	...	0.0075 ± 0.0005
ribbed annulus			
Creare	14	0.826 ± 0.015	0.0042 ± 0.0004
Columbia	9	0.879 ± 0.017	0.0052 ± 0.0009
Johnston & Neff	18	...	0.0055 ± 0.0005

Table 13.--Expermental rib-effect-ratios for annuli equipped with spacer ribs

	$\frac{(Q_{ratio})_{ribbed}}{(Q_{ratio})_{open}}$	$\frac{St_{ribbed}}{St_{open}}$
Creare	0.929	0.525
Columbia	0.938	0.667
Johnston & Neff	...	0.733

The hydraulic perimeters of the non-ribbed and conducting rib geometry have been calculated from given flow area and hydraulic diameter. The hydraulic perimeter for the insulating rib is estimated based on a rib height of:

$$\frac{2.896" - 2.353"}{2} = 0.272" \qquad \text{(4 ribs = 0.181 ft.)} \tag{57}$$

The hydraulic diameter for the insulating rib is based on this perimeter. All of the L/D values were calculated. The predicted heat flux ratio at the demand curve minimum is almost the same for all three geometries in Table 14. The data as presented in Table 12 shows that a significant rib effect exists which is not predicted by the present theory.

The exit fluid temperature in each flow subchannel was monitored during the ribbed tests. One channel consistently was hotter than the average fluid temperature. The variation between an individual subchannel temperature and the average for the four appears very consistent with the magnitude of the difference increasing as the minimum is approached. Near the minimum the subchannel temperature differences tended to decrease and then return to their previous relationship with decreasing flow. This was very apparent for a test at a heat flux of 375 kBtu/hr-ft2 when the fluid temperature difference decreased by 50 percent as the minimum was approached. This might be the result of flow redistribution as the vapor generation reached significant levels.

Table 14.--OFI predictions for Creare channel based on Equation 2

	Non-ribbed, build 2	Ribbed, build 4	
		Conducting rib	Insulating rib
Hydraulic diameter, mm	13.4	11.9	11.9
Heated diameter, D_h, mm	13.4	11.9	13.5
L_h/D_h	292	328	289
R (η = 25)	0.921	0.929	0.920

Non-Conducting Spacer Ribs

Columbia University built and operated two annular channels as part of the SRS OFI program. The first rig was constructed to represent and "open" annulus. Both surfaces of the annulus were constructed on Inconnel tubes and directed heated. The inner heater was centered and supported in the outer heater using 5.46 mm diameter insulating pins (36). The dimensions of the channel are listed in Table 11. The simulated spacer ribs were 1/16" thick phenolic asbestos and held in place with small clips.

The mean of the Q_{ratio} at the demand curve minimum for the Columbia University ribbed annulus data is 0.879 ± 0.017 (95% coverage). For an L_h/D_h of 270 the critical temperature ratio predicted by Equation 2 would be 0.915. This is outside the range of the mean predicted by the test data. The mean of the Stanton number calculated at the demand curve minimum conditions was 0.0052 ± 0.0009 (95% coverage). This range is below the 0.0065 suggested by Saha and Zuber. If the non-uniform heat flux curve is neglected (the curve that was produced at rig burnout) the mean Stanton number at OFI is 0.00496 ± 0.0006 (95% coverage).

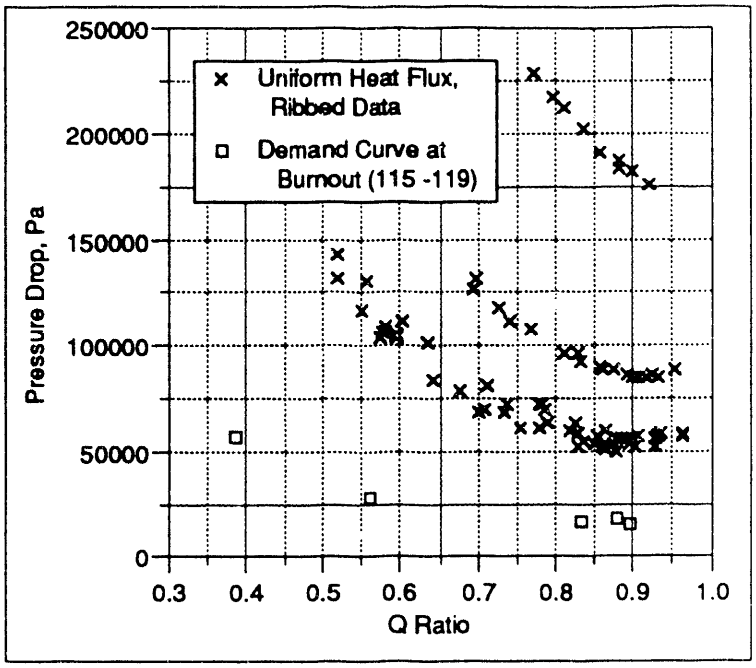

Figure 18, Columbia University ribbed annulus demand curves

To allow a more detailed comparison between the Columbia University OFI test program ribbed and open annuli, tests at the conditions described in Table 15 have been compared. For these conditions there is one documented demand curve for the open annulus (Reference 1) and five (one is not complete because of premature thermal trips, Reference 2) demand curves in the ribbed annulus. These are listed in Table 16.

Table 15.--Nominal conditions used in analysis of Columbia University wall temperature effects

Inner heat flux	400,000 Btu/hr·ft2	127 kW/m^2
Outer heat flux	400,000 Btu/hr·ft2	127 kW/m^2
Inlet temperature	25°C	25°C
Outlet pressure	20 psig	240,000 N/m^2 abs

Table 16.--Demand curve descriptions

Curve number	Date	Test section	Description (reference)
0	5/18/90	1.0	ribless annulus (17)
1	2/1/92	3.0	ribbed annulus (19)
2	3/6/92	3.1	ribbed annulus (19)
3	3/7/92	3.1	ribbed annulus with bypass (19)
4	3/7/92	3.1	ribbed annulus with bypass (19)
5	6/13/92	3.2	ribbed annulus (19)

The mass flux-pressure loss demand curves are plotted in Figure 19. Figure 20 provides a detail of the minima region. The curves are consistent and display no unanticipated behavior. Figure 21 presents the pressure loss as a function of the Q_{ratio}. This figure clearly demonstrates that the Q_{ratio} at the demand curve minimum is not the same for the ribbed and ribless annuli. The estimated value of the Q_{ratio} for the ribbed and ribless annuli based on Equation 2 is 0.913 and 0.915 (L/D = 261 and 270). The observed variation in Figure 21 is not expected from basic theory and no explanation for this discrepancy other than the existance of a rib effect is readily apparent.

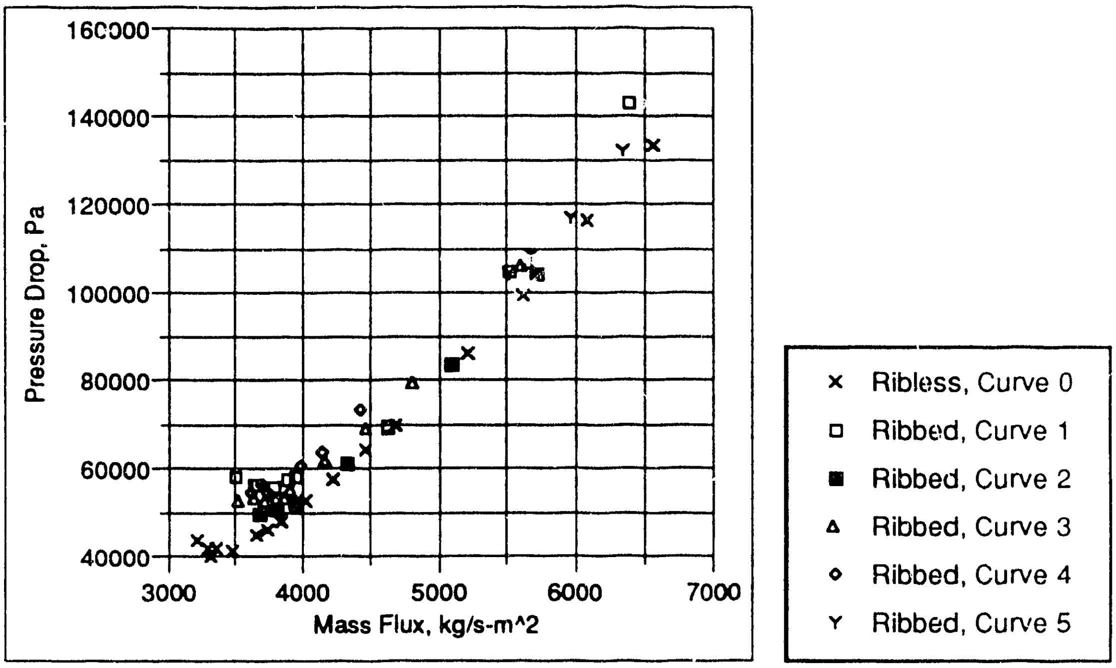

Figure 19, Demand curves

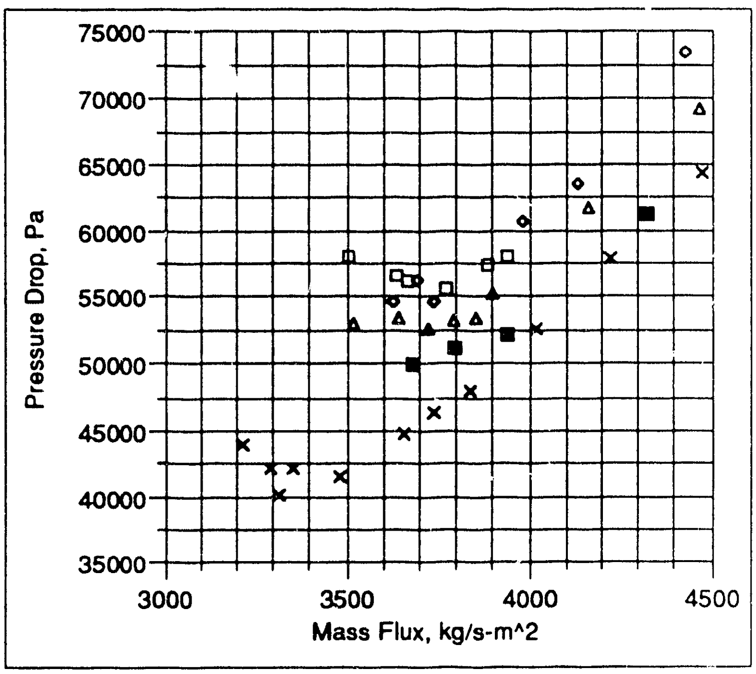

Figure 20, Demand curve details

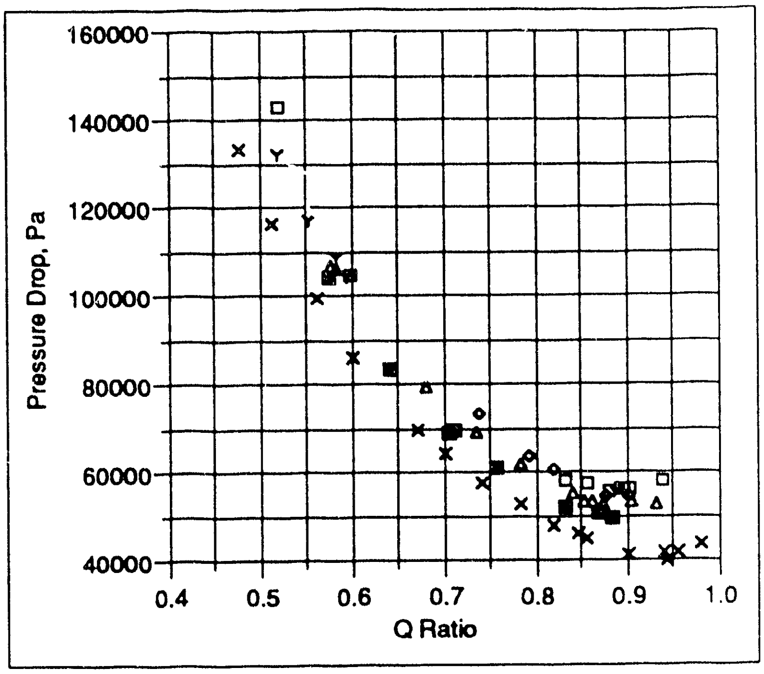

Figure 21, Q_{ratio} demand curves

Wall Temperature Evaluation

The wall temperatures measured during the Columbia University OFI program were measured with both brazed and cemented thermocouples. The cemented thermocouples were considered the most accurate (XX). Figures 22 and 23 present the averaged and maximum indicated temperatures for the cemented thermocouples described in Table 17. These thermocouples were located just above the start of the heated length. These figures show that the indicated wall temperatures are not consistent; for curves 1 and 4; there appears to be a rapid increase in wall temperature as the demand curve minimum is approached.

Table 17.--Cemented thermocouple locations for Columbia University annular OFI tests

	Ribless		Ribbed	
	Channel	Location	Channel	Location
Inner heater	...	...	77	132w
	...	...	78	132nw
	...	...	79	132e
	...	...	80	132se
Outer heater	94	143n	101	143sw
	95	143se	102	143se
	96	142n	103	143ne
	97	142se	104	143nw

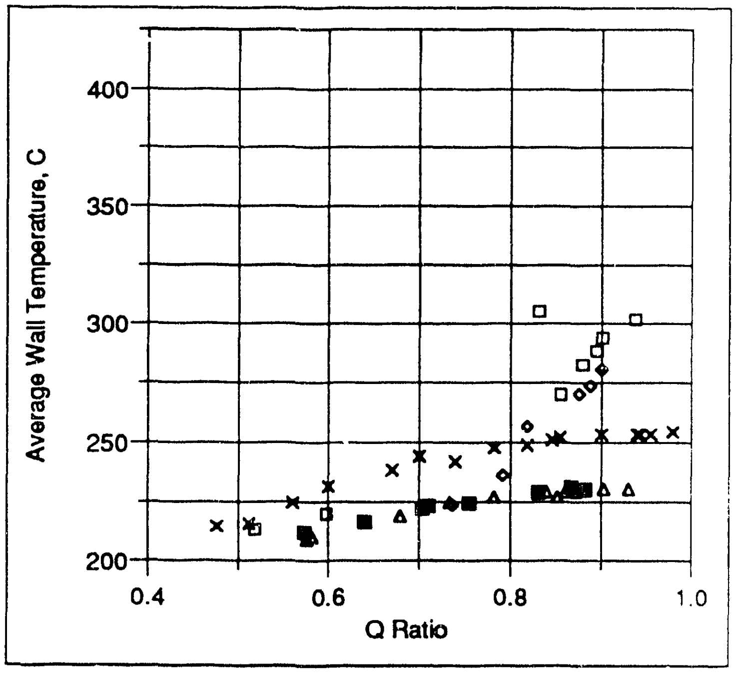

Figure 22, Average indicated temperatures for cemented TCs near the test section exit

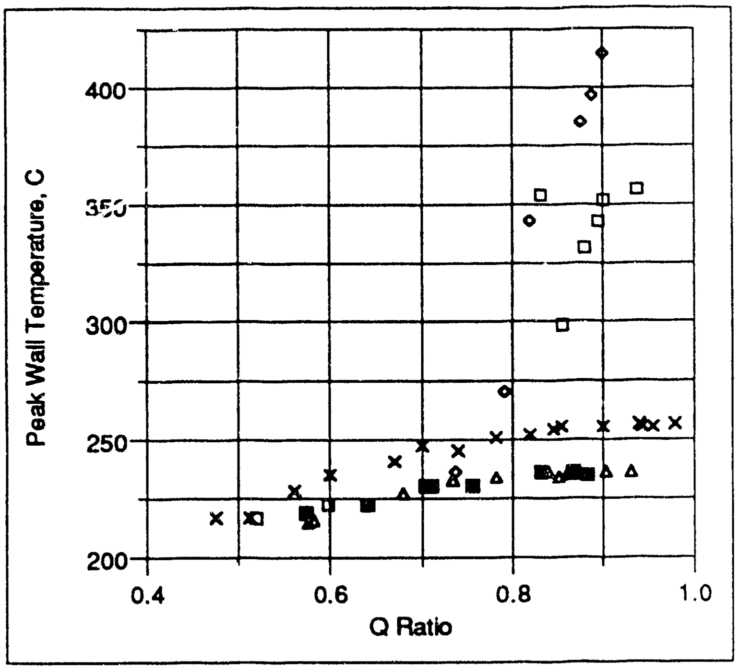

Figure 23, Maximum indicated temperatures for cemented TCs near the test section exit

Table 18.--Columbia ribbed heater wall temperature gradient

Heat flux kW/m2	T_{dry}, °C	T_{ave}, °C	k (74) KW/m2	Temperature gradient, °C
127	255	213	12.5	-83
127	364	327	14.2	-73
190	335	276	13.2	-118
190	410	375	14.7	-106

Wall Superheat Predictions

The wetted wall temperature may be estimated using a one-dimensional heat conduction analysis based on Fourier's law of heat conduction. Since the geometry is fixed, the temperature correction can be estimated for any combination of outer wall temperature (which dictates the thermal conductivity) and heat flux. If the behavior is assumed linear, a temperature correction term can be calculated by fitting the data in Table 18:

$$\Delta T = 106.4 - 0.0917\, T_{dry} \quad (127\ kW/m^2) \tag{58}$$

$$\Delta T = 171.6 - 0.160\, T_{dry} \quad (190\ kW/m^2) \tag{59}$$

The wall superheat can then be estimated based on the local saturation temperature and measured wall temperature. Figure 24 shows how a boiling curve can be produced by combining Equations 51, 53, and 54. Figures 25, 26, 27, and 28 illustrate how the experimental wetted wall temperatures vary from nucleate boiling theory at the test section exits. All ribbed annulus data for 127 and 190 kW/m^2 (0.4 and 0.6 MBtu/hr·ft^2) tests is presented in the respective plots. No pattern is readily apparent. Figure 29 presents a boiling curve on alternate coordinates for four different dates of operation. For lower velocities the predicted temperatures follow the boiling curve theory as observed for the same data in Figure 29. The two curves where deviation was observed in Figure 22 also deviate from theory in Figure 29. The poor behavior in the transition from forced convection to nucleate boiling is probably due to boiling curve hysteresis as discussed by Hino and Ueda (33).

A thin nonuniform layer of deposits formed on the heater surface during the ribbed testing. Holman suggests a design value fouling factor for distilled water of 0.00088 °C·m^2/W. For a heat flux of 127 kW/m^2 (0.4 MBtu/hr·ft^2) the expected temperature gradient due to this level of fouling would be 111°C. The gradient would be expected to remain relatively constant, independent of the wall temperature or to gradually increase with time. Figure 29 indicates this is not the case.

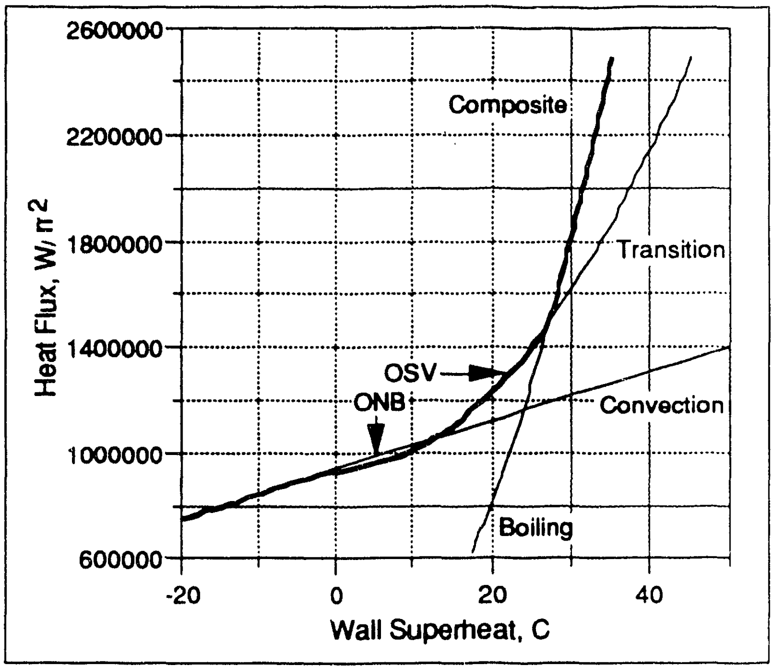

Figure 24, Boiling curve at end of test section for Columbia University ribbed annulus at a velocity of 4m/s and an exit pressure of 20 psig

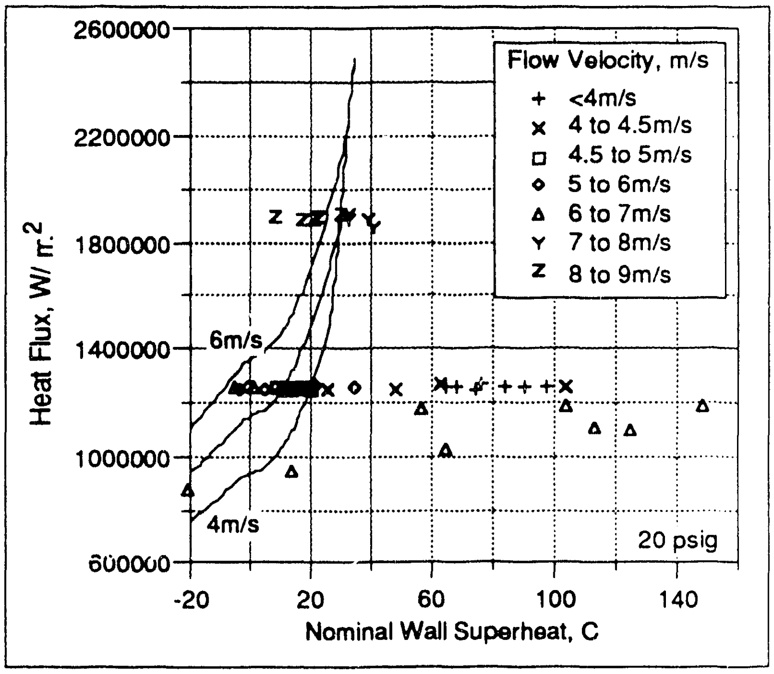

Figure 25, Nominal experimental wall superheat (20 psig)

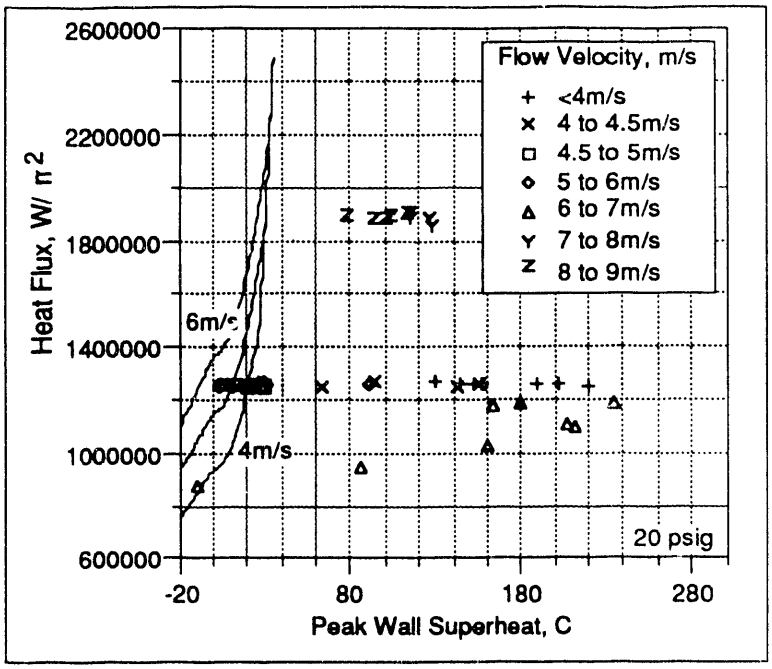

Figure 26, Peak experimental wall superheat (20 psig)

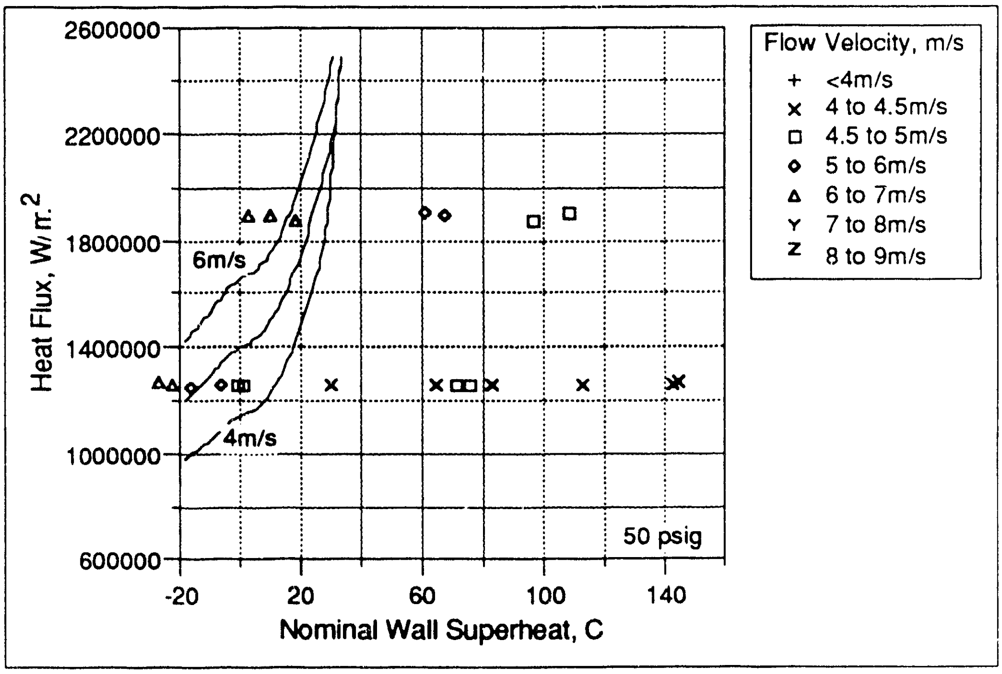

Figure 27, Nominal experimental wall superheat (50 psig)

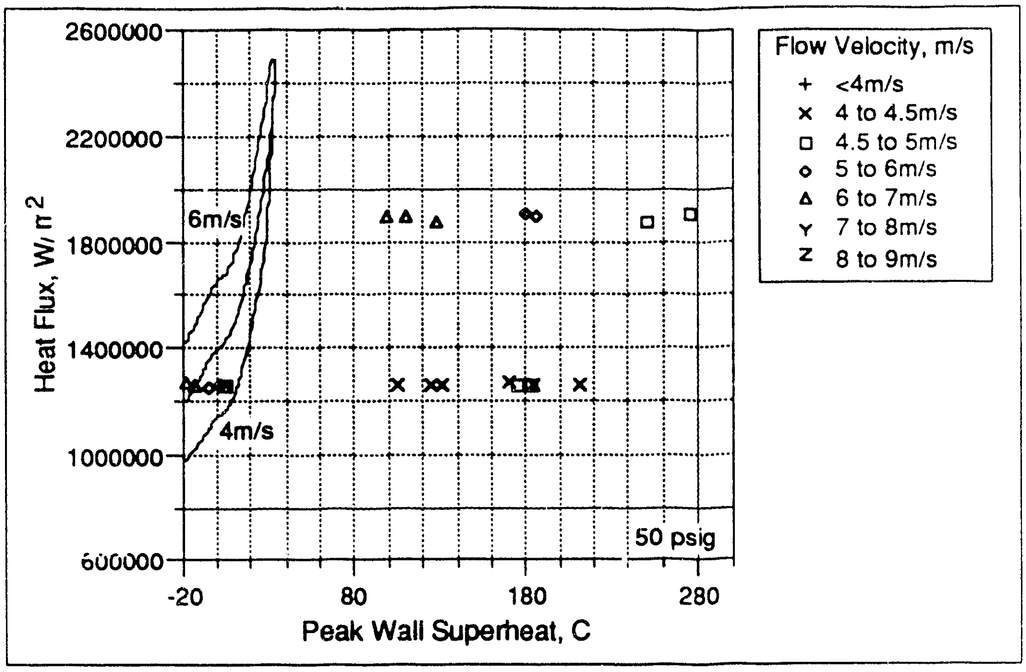

Figure 28, Peak experimental wall superheat (50 psig)

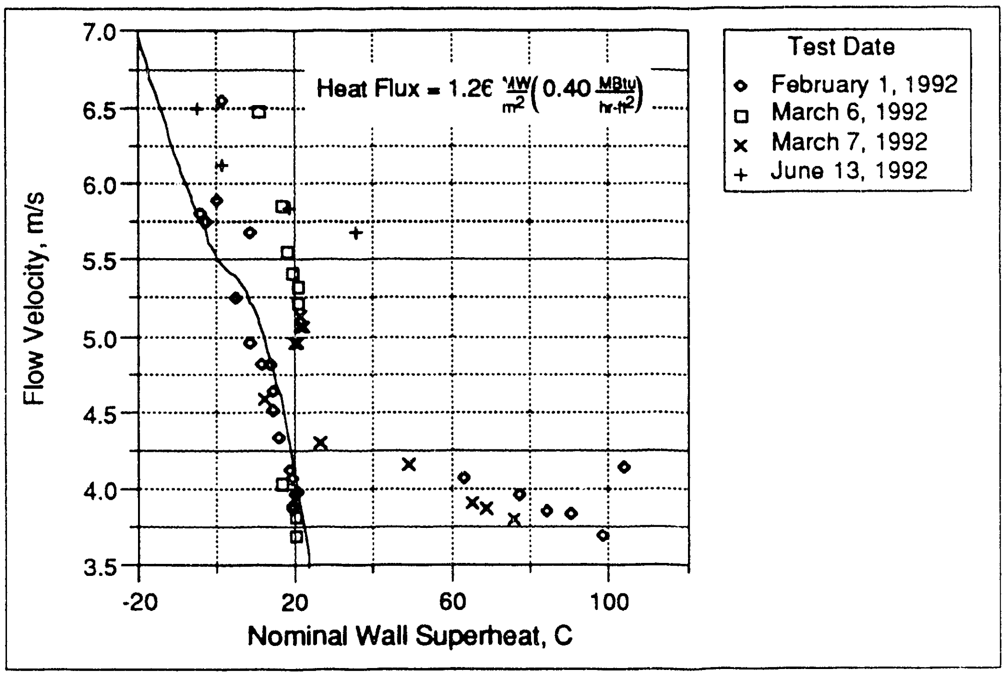

Figure 29, Superheat variation by date of test for a heat flux of 1.26 MW/m2 (0.4 MBtu/hr-ft2) and 20 psig at the exit.

Wall Temperature Hysterisis

Figure 30 provides the Q_{ratio} Demand Curve for Curve 1 in Table 16. The numbers in this figure refer to the consecutive Run Numbers that are assigned to each steady-state data set. The demand curve minimum occurred at Run Number 554. The flow was decreased beyond this minimum to the operating point at Run Number 555. The flow was then increased to operating condition 556 and the demand curve was traced a second time. Run Number 558 occurs at the same boundary conditions as Run Number 554. Figure 31 presents the axial temperature profile for Run Numbers 546, 549, 554 and 556. The highest wall temperatures shown in this figure do not occur at the demand curve minimum but occur for Run Number 556; the operating condition that was approached by increasing the flow after the demand curve minimum was reached. Figures 32, 33, 34, and 35 present the indicated wall temperatures at the demand curve minimum (Run Number 554), beyond the demand curve minimum (Run Number 555), the recovered flow conditions (Run Number 556) and the second demand curve minimum operation point (Run Number 558). The indicated wall temperature profiles for the two demand curve minimum conditions are different. The recovered flow condition while displaying no hysteresis in the measured pressure drop (Figure 30) has a few wall temperatures (both at rib locations and flow channel centerlines) that are higher than at the demand curve minimum. It is possible that a condition occurred at a flow in the region of the demand curve minimum flow that changed the heat transfer conditions near the ribs and that recovery from this condition did not occur after increasing the flow.

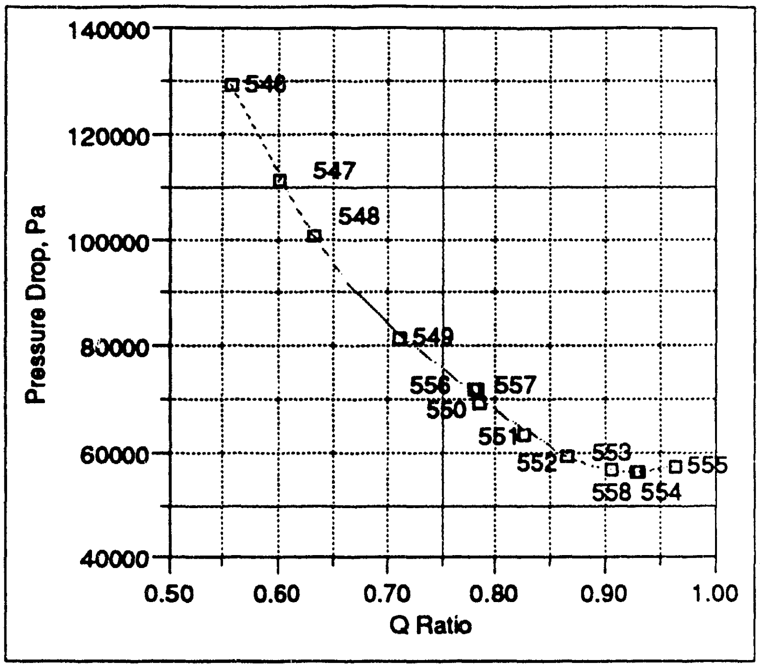

Figure 30, Q_{ratio} Demand curve for curve number 1 (run numbers 546 to 558)

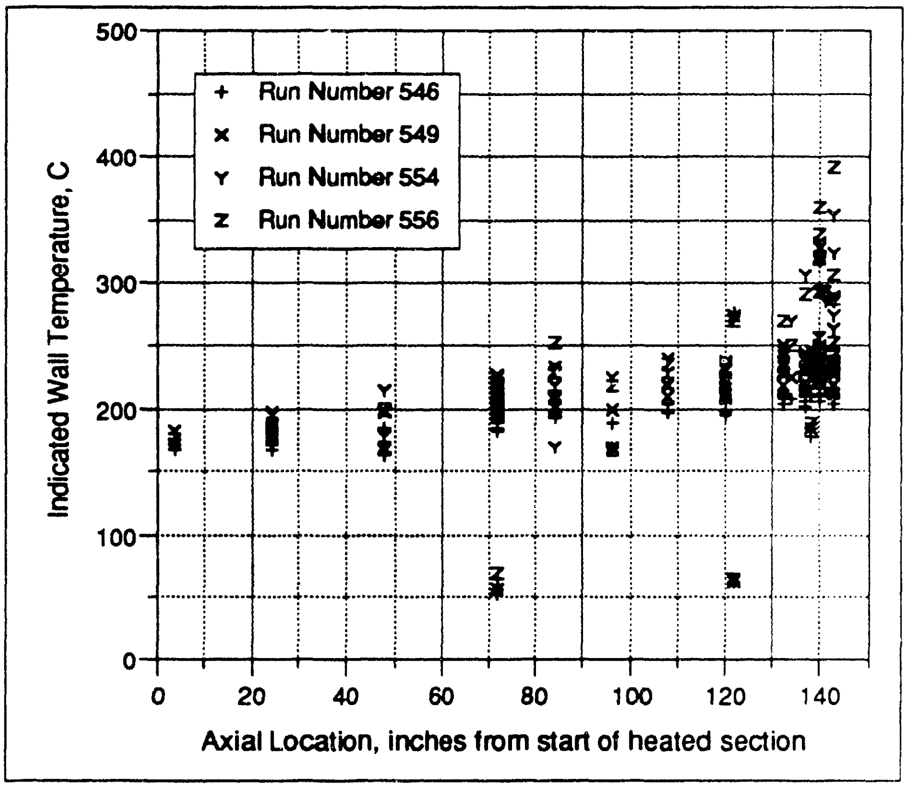

Figure 31, Axial temperature profile for selected run numbers from curve number 1

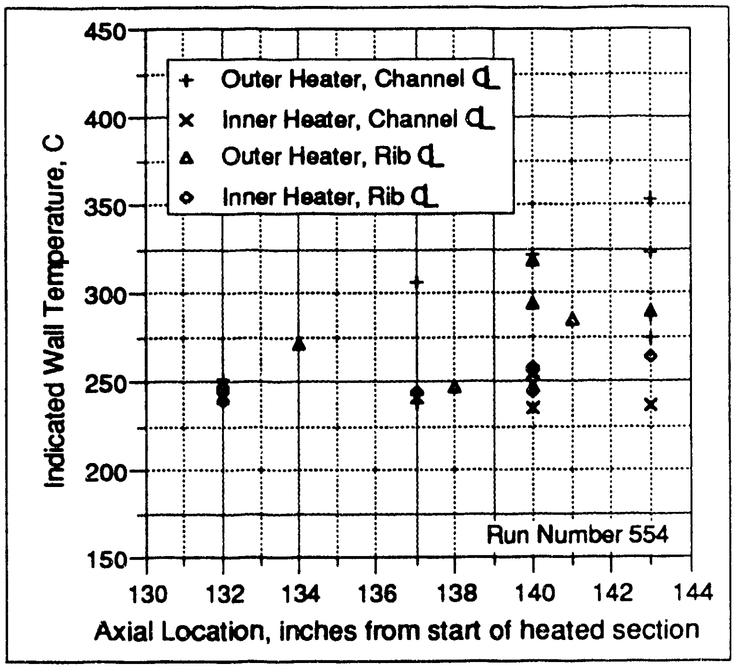

Figure 32, Axial temperature profile details for run number 554

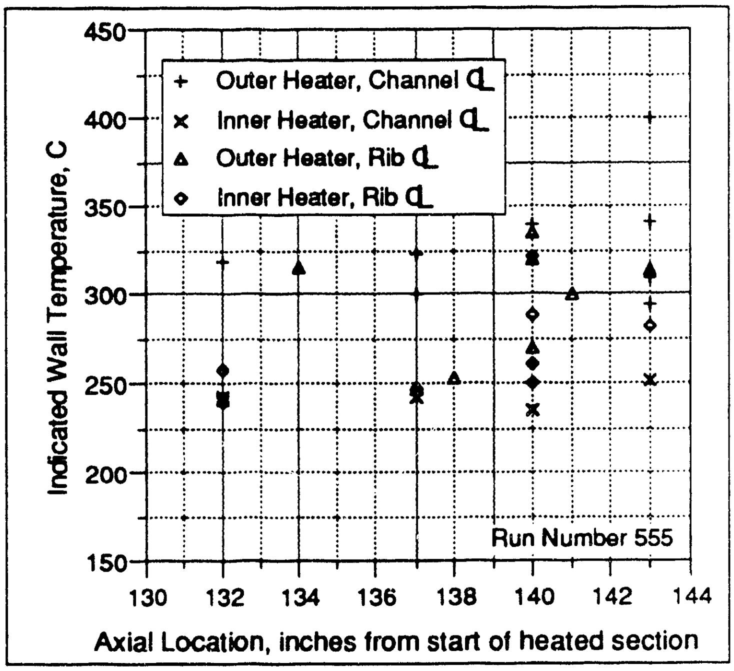

Figure 33, Axial temperature profile details for run number 555

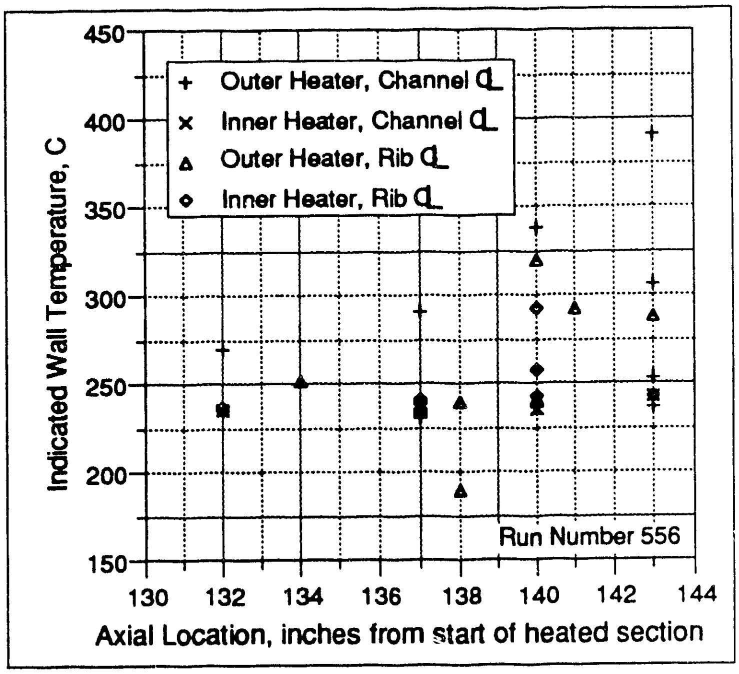

Figure 34, Axial temperature profile details for run number 556

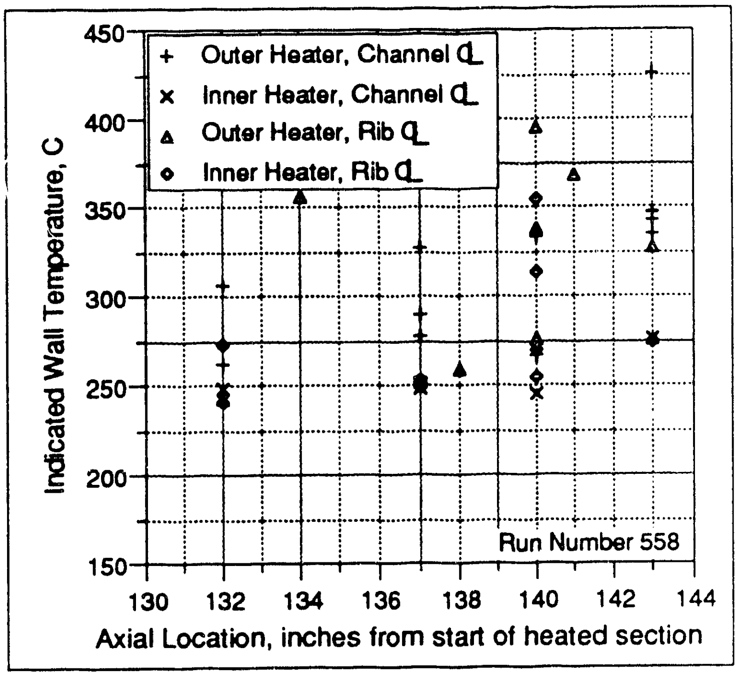

Figure 35, Axial temperature profile details for run number 558

Constant Flow with Increasing Heat Flux

Several test runs were made where the flow was held constant at 140 gpm and the heat flux was slowly increased. These test runs are presented in Table 19. Figures 36 and 37 plot the actual measured wall temperature (dry side) as a variable of the axial position. A deviation from nucleate boiling occurs between run numbers 1 and 2 (Figure 36). This is at a heat flux between 0.88 and 0.94 MW/m^2 (0.278 and 0.299 MBtu/hr·ft^2). The exit subcooling (T_{sat} - T_{bulk}) for these runs varied from 52 to 65°C. The mass flux was 6400 kg/s·m^2.

The heat balance of run number 6 is lower than run number 7. This is because at run number 6 the test channel was still coming to steady state equilibrium after a power increase. This condition seems to have created hot spots (Figure 37) during the transient between two steady state conditions. These hot spots might precipitate the development of a localized stable vapor film where steady state theory would only indicate nucleate boiling.

The unpredicted wall temperature behavior has not been limited to the Columbia University ribbed annulus (27). Deviations from nucleate boiling theory were also observed in the non-ribbed annulus. In some cases these deviations occur in the heat fluxes of 1.3 MW/m^2. Variations were also observed in Creare tests (9).

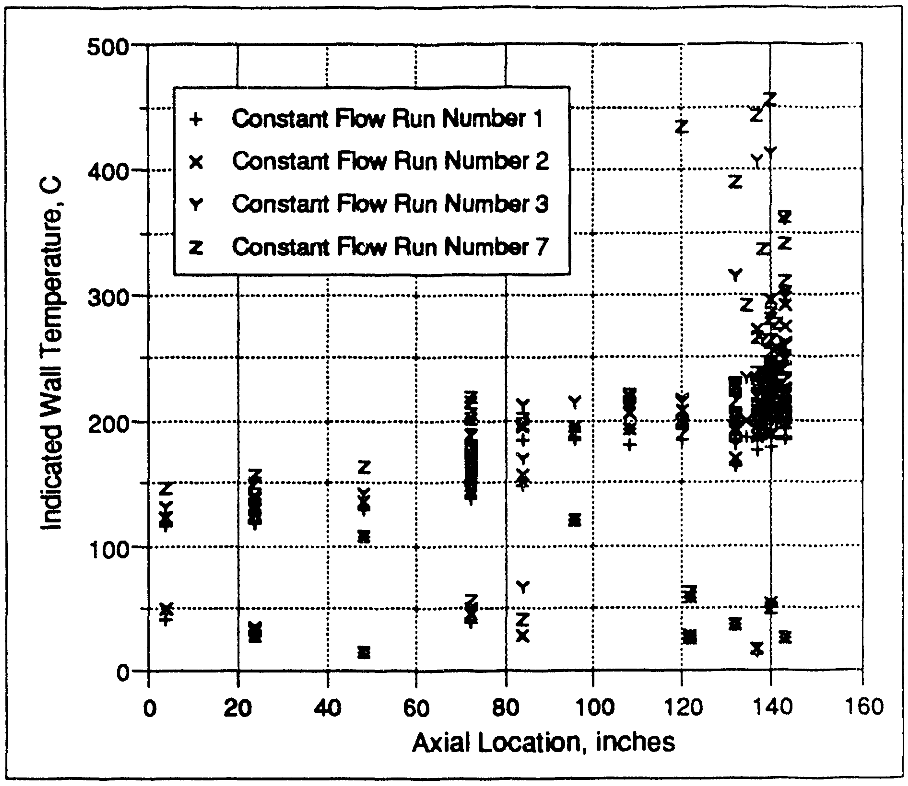

Figure 36, Axial temperature profiles for selected constant flow tests

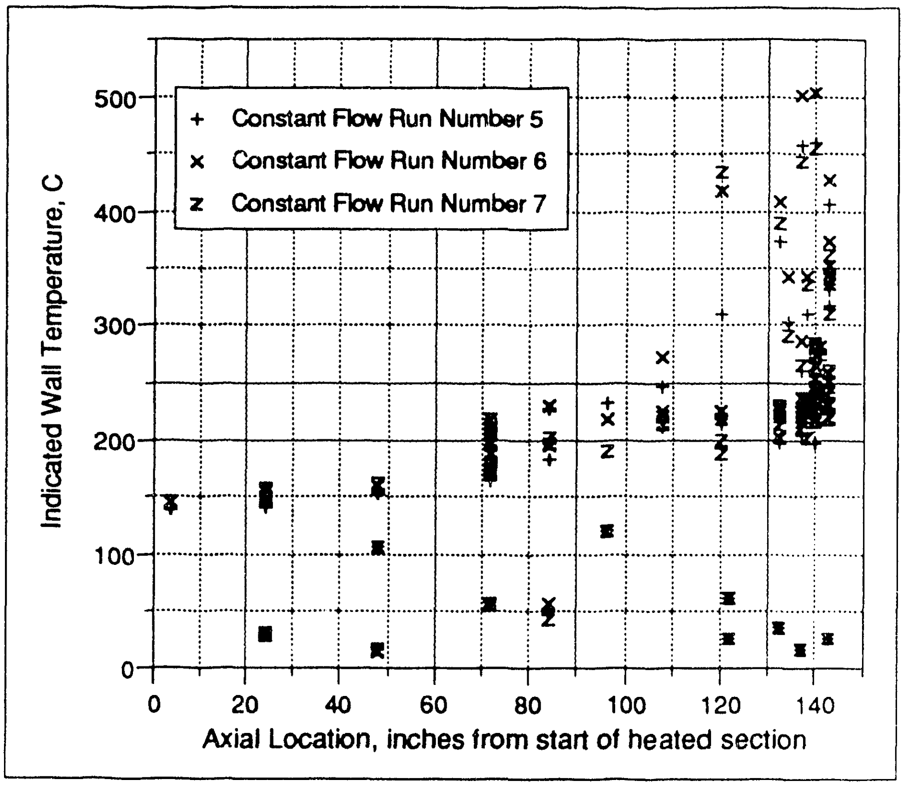

Figure 37, Axial temperature profiles for selected constant flow tests

Table 19. Operating conditions for constant flow tests (Columbia University ribbed annulus)

Run Number	Inner Heat Flux Btu/hr-ft^2	Outer Heat Flux Btu/hr-ft^2	Pressure Ratio	Q_{ratio}	Heat Balance
1	0.276	0.278	0.8970	0.3581	0.9816
2	0.303	0.299	0.8966	0.3858	0.9762
3	0.328	0.326	0.8985	0.4197	0.9627
4	0.347	0.352	0.9167	0.4508	0.9647
5	0.353	0.349	0.9201	0.4531	0.9737
6	0.374	0.378	0.9372	0.4881	0.9640
7	0.372	0.374	0.9597	0.4845	0.9924
8	0.399	0.376	0.9466	0.5035	0.9630

Three run numbers (546, 570, and 629) satisfy the conditions listed in Table 15 and are at a flow rate of 140 gpm. The Run Number 7 from the constant flow rate test has the same flow rate and a heat flux approaching the heat flux in Table 15 (375,000 vs. 400,000 Btu/hr-ft^2). The temperature profiles for each of these four runs is presented in Figure 17. The temperature profile for Run Number 7 is similar to the non-nucleate boiling temperature profiles in Figure 4 although the temperatures near the end of the heated section are much higher.

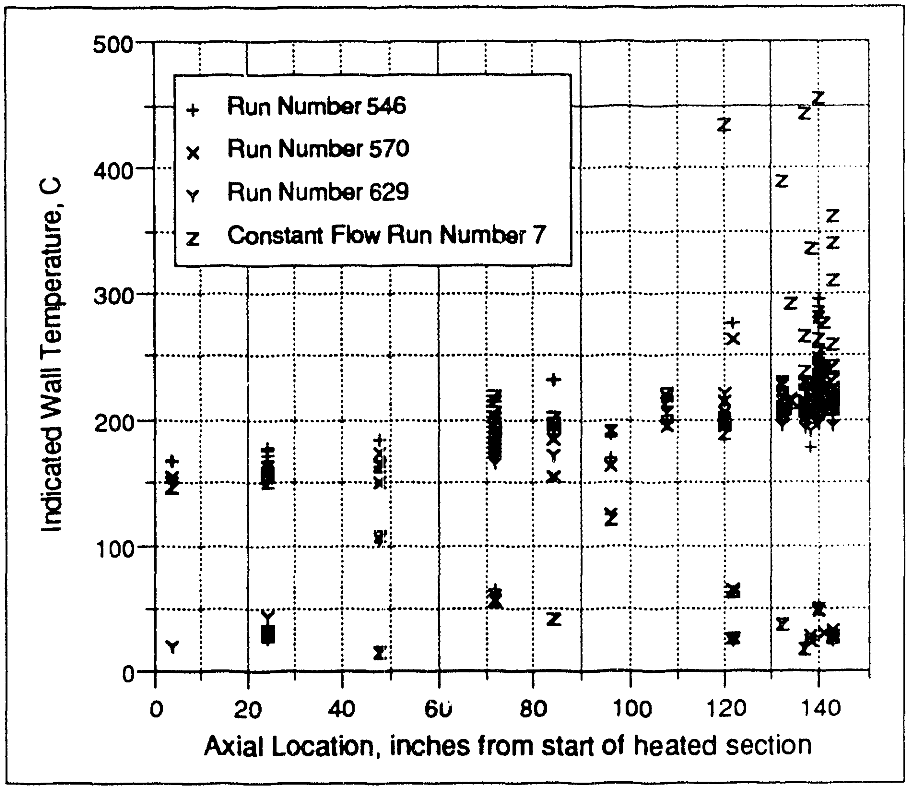

Figure 38, Axial temperature profile for a flow rate of 140 gpm

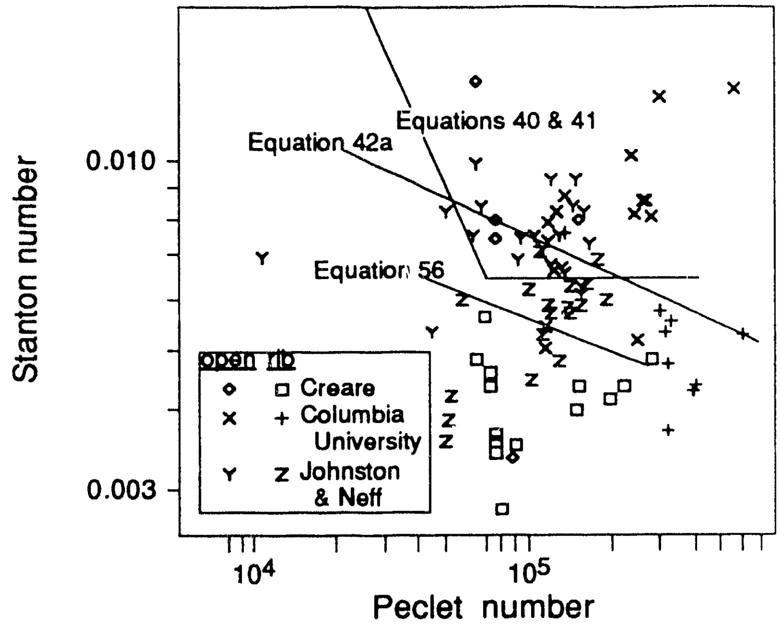

Figure 39. OFI data for geometries with spacer ribs

This behavior although describing conditions near burnout can be used to explain the behavior observed during rib testing at Columbia University. Because of the reduced velocity near the rib normal nucleate boiling correlations probably do not hold. In the limit, the region near the rib tip will approach pool boiling conditions.

While the ribbed channels in OFI testing are heat flux controlled the local phenomena in the vicinity of the rib will behave in a temperature controlled mode. The local heat transfer at the rib will transition between convection, nucleate and film boiling regimes depending on the local conditions. Once film boiling is established near the rib it will probably be stable and will remain in place until the heat flux is reduced below the limit shown in Figure 17. As discussed earlier in the section on transition boiling this threshold could be as low as 300 kW/m^2.

Ribbed Annular Excursions at Columbia University

During the ribbed annular tests conducted at the HTRF at Columbia University several DNB events occurred (19). These events were not anticipated by pretest analysis, however in retrospect it is apparent that the OFI operating limit was close to the CHF limit when a peaking factor is considered. Yang (75) suggested that the first excursion took place between 180 and 205 gpm and an inlet condition between 27 and 38°C. The analysis will be completed for the conditions listed in Table 20.

The exit temperature is first computed using an energy balance:

(60)
$$\begin{aligned} T_{out} &= \frac{\phi A_h}{Q\rho c_p} + T_{in} \\ &= \frac{\left(2.52\frac{MW}{m^2}\right)\left(1.529m^2\right)}{\left(0.0121\frac{m^3}{s}\right)\left(997\frac{kg}{m^3}\right)\left(4191\frac{J}{kg\cdot K}\right)} + 32.2°C \\ &= 108°C \end{aligned}$$

The bulk fluid temperature would then be:

(61)
$$T_{bulk} = \frac{148°C - 32.2°C}{2} \approx 72°C$$

The heat flux necessary to bring the system to saturation may be computed using an energy balance.

(62)
$$\begin{aligned} \phi_{sat} &= \frac{Q\rho c_p}{A_h}\left(T_{sat} - T_{in}\right) \\ &= \frac{\left(0.0121\frac{m^3}{s}\right)\left(997\frac{kg}{m^3}\right)\left(4191\frac{J}{kg\cdot K}\right)}{\left(1.529m^2\right)}\left(148°C - 32.2°C\right) \\ &= 3.83\frac{MW}{m^2} \\ &= 1.21\frac{MBtu}{hr\cdot ft^2} \end{aligned}$$

Using the most recent CHF correlation developed by Columbia University for Inconnel is (18):

$$\phi_{CHF} = 0.591\left(1.21\tfrac{MBtu}{hr \cdot ft^2}\right) + 0.628$$
(63)
$$= 1.34\tfrac{MBtu}{hr \cdot ft^2}$$
$$= 4.24\tfrac{MW}{m^2}$$

The rib effect as propsed by Yang (75) would then be:

(64)
$$K_{rib} = \frac{2.52\frac{MW}{m^2}}{4.24\frac{MW}{m^2}} = 0.594$$

Table 20.--DNB and burnout conditions in the Columbia University ribbed annulus test

	First DNB event	Second DNB event	Burnout
Heat flux, MW/m^2	2.52	1.91	1.40
Flow, m^3/s	0.0121	0.00630	0.00221
Inlet temperature, °C	32.2	27.3	25.1
Exit pressure, Pa abs	446,000	442,000	447,000
Temperature for fluid properties, °C	72	78	75
Saturation temperature, °C	148	147	148
Velocity, m/s	8.6	4.88	1.71
Heat flux at CHF, MW/m^2	4.24	3.22	2.97
Rib effect	0.594	0.594	0.471

A second temperature excursion occurred during the third demand curve test (runs 614 to 620) near the OFI flow rate (99 gpm).[47] The conditions near excursion are listed in Table 20.

The last demand curve attempted using the ribbed annular rib resulted in a burnout. Figure 1 presents a schematic of the heater damage. The horizontal crack was 11-1/2" from the end of the heater. An 18" long black burn mark started 23-3/8" from the end of the heater. Near the horizontal crack the burn was 1-1/2" wide. It is not clear if this failure was the result of CHF or pressure drop oscillations. The heater damage is similar to that observed by Maulbetch and Griffith (52) in their investigation of the pressure drop oscillation FI. The heated diameter increased for this test to 1.18" with an L_h/D_h of 122, since only the inner wall is heated. The revised heated area would be 0.685 m^2. The Q_{ratio} would then be 0.83. At the excursion the Q_{ratio} was 0.84. Figure 20 does not indicate a minimum had been reached, however, the curve is so flat it is possible that operation was at a flow below the minimum. The conditions just prior to the burnout are listed in Table 20.

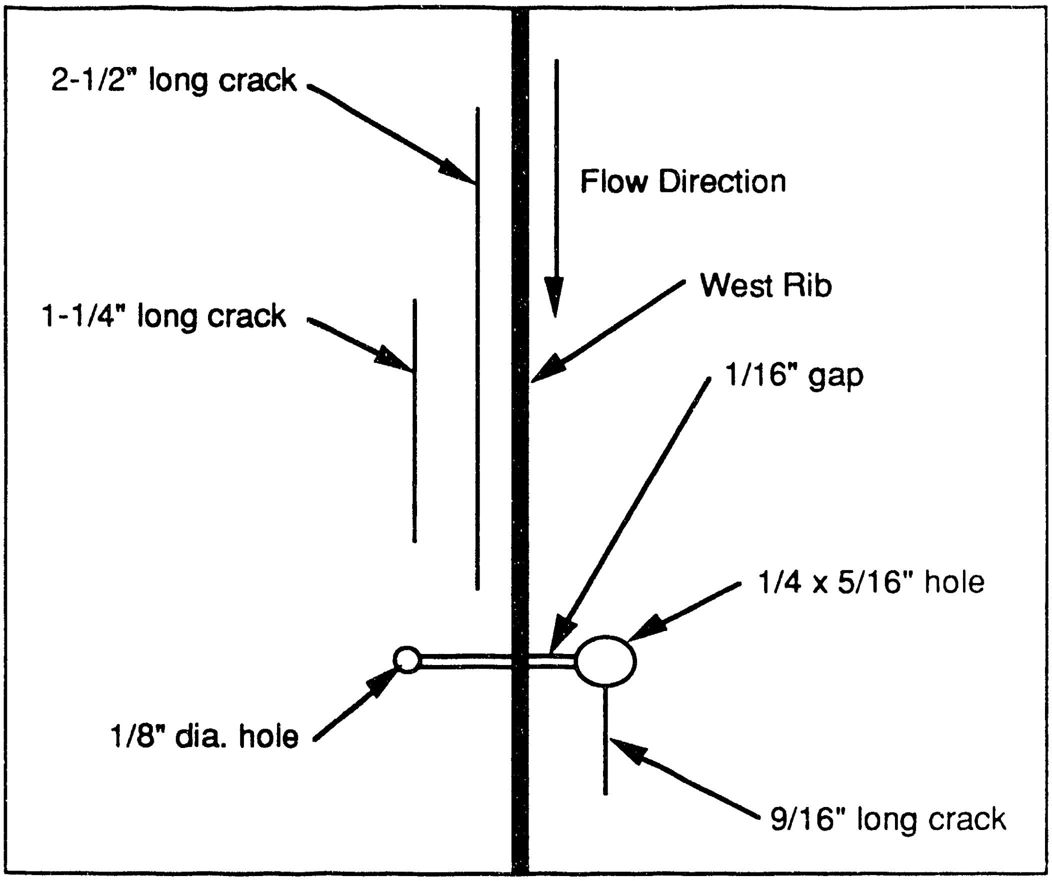

Figure 40, Schematic of Columbia University ribbed annuls burnout

Jones, McAssey, and Yang (38) developed an analytical solution for the peaking factor in the presence of a non-conducting rib. Their basic assumption is that the heat transfer at the rib tip must be zero and the solution is of the form:

$$\frac{Bi(x)}{Bi_o} = \left(1 + 0.001\ \eta_v^{-P}\right)^{-1} \quad (65)$$

where the Biot number is defined as $Bi(x) = h(\eta_v)y_{plate}/k_{plate}$, and η_v is the non-dimensionalized distance (x/H_v) from the rib as shown in Figure 41. The solution was for uniform internal heat generation it is interesting that the peaking factor estimate did not vary appreciably for a wide range of values of both p and η_v. The calculated rib effect was __________, this is consistant with the three DNB events during the Columbia University ribbed annulus testing. While

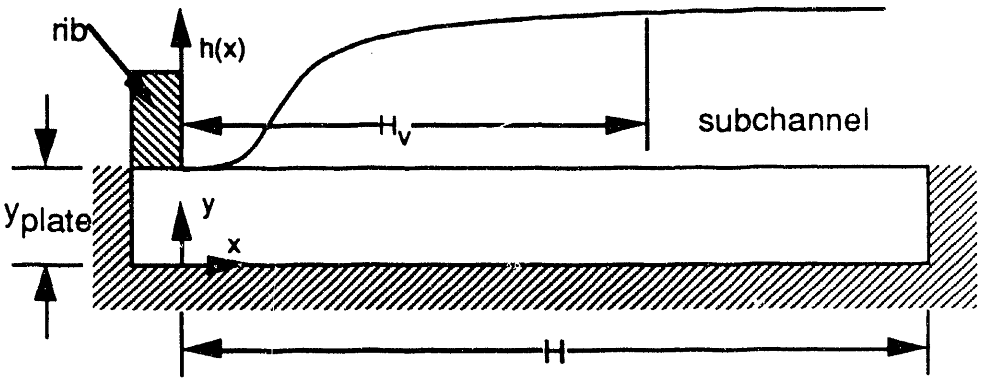

Figure 41. Nomenclature as used for analysis by Jones, McAssey, and Yang.

Rib Effects on Channel Hydraulics

The effect of placing an obstruction such as a rib in a channel to create two subchannels will be an increase in the frictional pressure drop. This can be demonstrated using the following example. The frictional pressure loss in a channel is proportional to the mass flux squared and the inverse of the hydraulic diameter.

(66) $$\Delta p \propto \frac{G^2}{D_e}$$

For a rectangular channel (a by b) at a given mass flux:

(67) $$\Delta p \propto \frac{a+b}{2a \bullet b}$$

A thin rib inserted in the flow channel will increase the hydraulic diameter such that:

(68)
$$\Delta p \propto \frac{a+2b}{2a \bullet b}$$

A rib effect based on the hydraulic diameter effects would than be:

(69)
$$K_{rib} = \frac{\Delta p_{rib}}{\Delta p_{open}} = \frac{a+2b}{a+b}$$

When the rib thickness, x_o, is included:

(70)
$$K_{rib} = \frac{a(a+2b-2x_o)}{(a+b)(a-x_o)}$$

For the test section used in this program the hydraulic diameter rib effect would be 1.016 or a 1.6 percent increase in pressure drop for a give set of mass flux conditions.

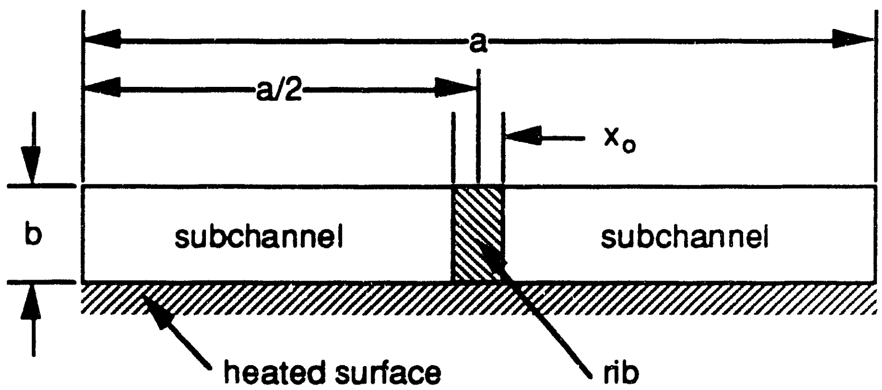

Figure 42. Schematic of subdivided flow channel

Using Equation 2, OFI Q_{ratio} for a rectangular flow channel with and without a rib can be predicted. The heated diameters of the open and ribbed channel shown in Figure 42 are equal.

(71)
$$D_h|_{open} = \frac{4ab}{a} = 4b$$

(72)
$$D_h|_{ribbed} = \frac{4(ab - bx_o)}{a - x_o} = 4b$$

(73)
$$D_h|_{subchannel} = \frac{4\frac{(ab - bx_o)}{2}}{\frac{a}{2} - \frac{x_o}{2}} = 4b$$

Using the relation by Whittle and Forgan no rib effect would be predicted however because of non-similarities (hot spots, mechanical imperfections, etc.) between the subchannels a flow excursion would be expected to first occur in one subchannel.

CHAPTER 3

TEST FACILITY

The test facility used for all of the diabatic tests was a closed loop system which could be operated in both a steady state and transient mode. The system was designed to allow independent control of flow rate, exit pressure, inlet temperature and heat flux. Typical measurements made during testing included: volumetric flow rate, channel exit pressure, channel pressure drop, fluid inlet temperature, channel fluid exit temperature, heater surface temperature, heater electrical current, and heater voltage. These measurements were made using a Macintosh II, computer. The flow loop was installed at in the Heat Transfer Laboratory, Building 786-A at the Savannah River Site in Aiken, South Carolina. The test loop is pictured in Figure 43.

Instrumentation Nomenclature

The nomenclature used in assigning the instrument numbers is presented in Table 21. This nomenclature was maintained in all of the DAS data collection worksheets, data reduction programs, and data analysis work.

Flow Loop

Figure 44 provides the flow loop schematic. Table 22 lists the principle loop components. The three supply pumps provided an almost constant supply pressure at the pump discharge header. The flow controller valve was designed to maintain a set flow regardless of downstream pressure variations. The nominal flow dimensions for the heated channel were 3.2 mm by 76 mm

Figure 43, Test loop assembly -- Insulation is removed from the pump discharge header and the 2" vertical supply (Photograph 93-1414-19)

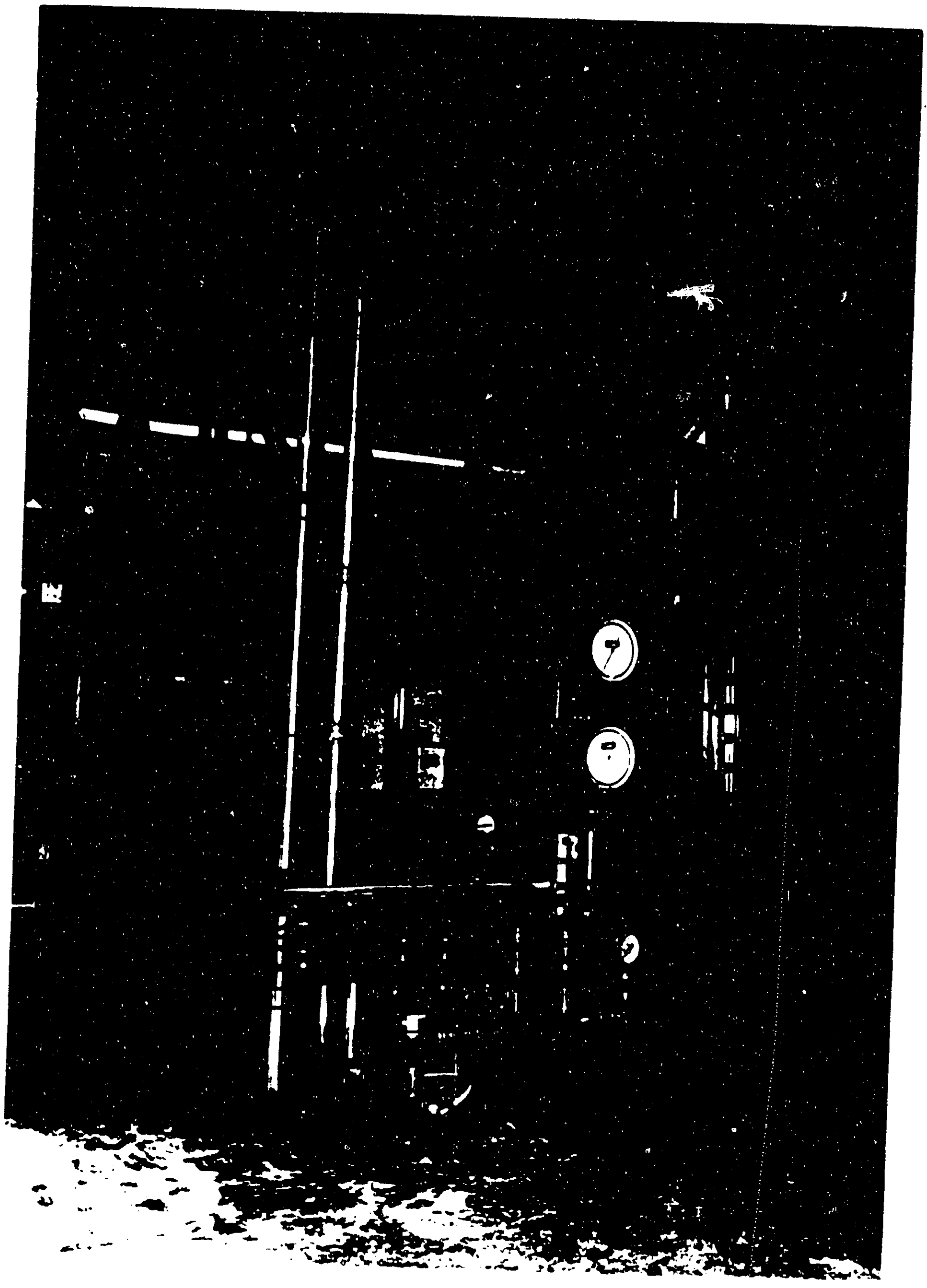

93-1414-19

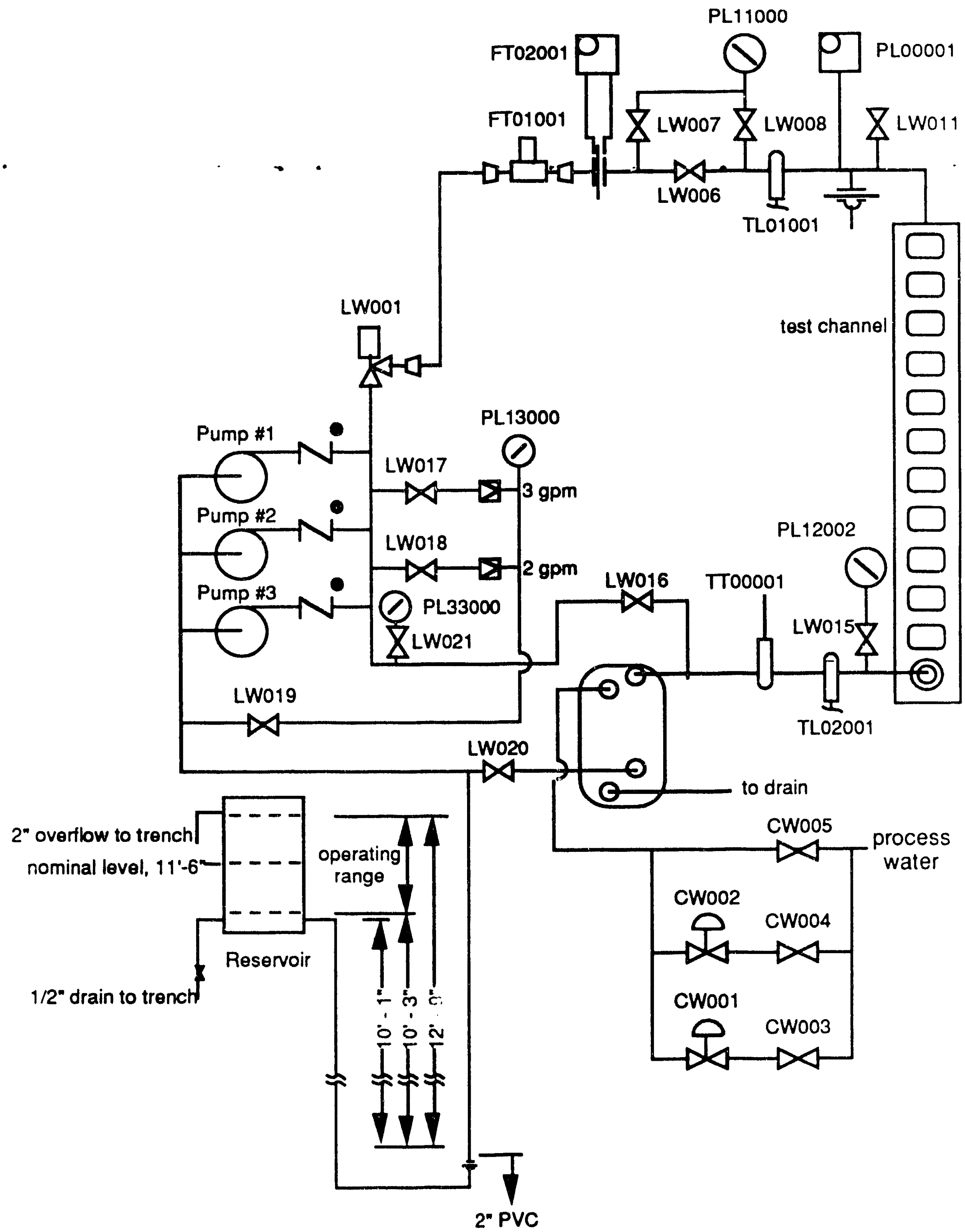

Figure 44, Test loop schematic

Table 21.--Instrument loop number first two letter nomenclature

	Measurement type	Measurement location
FT	Fluid flow	Flow loop
PB	Barometric pressure	Building
PD	Differential pressure	Heated channel
PG	Local channel pressure	Heated channel
PL	Local pressure	Flow loop
TC	Temperature	Channel structure
TF	Fluid temperature	Heated channel
TL	Fluid temperature	Flow loop
TP	Temperature	Heater plate
TT	Thermometer temperature	Flow loop
WC	Heater current	Rectifier controller
WV	Heater voltage	Heater buss connections

Table 22.--Flow loop instrumentation

Instrument loop number	Channel number	Instrument description
PL11000	...	Pressure gauge, channel inlet pressure
PL12002	...	Pressure gauge, channel exit pressure
PL13000	...	Pressure gauge, pump suction pressure
PL33000	...	Pressure gauge, pump discharge pressure
TT00001	...	Thermometer, channel exit temperature
TC00003	39	Thermocouple, Impulse line temperature
TL01001	52	Thermocouple, channel inlet temperature
TL02001	53	Thermocouple, channel exit temperature
TL03001	54	Thermocouple, pump discharge temperature
TL03002	55	Thermocouple, head tank temperature
FT01002	63	Orifice flow meter, loop flow
FT01001	73	Turbine flow meter, loop floe
CW001	...	Secondary coolant regulator, 40.6 to 62.8°C
CW002	...	Secondary coolant regulator, 65.6 to 87.8°C

(0.125" x 3"). Flow exiting the heated channel was directed into a flat plate heat exchanger for cooling. The pressure at the discharge of the heat exchanger was regulated using a standpipe. The height of the standpipe was adjusted to achieve the desired test section exit pressure.

Supply System

The booster pumps used in the flow loop were model 2PC45 manufactured by Dayton Electrical Manufacturing Company. The nominal rating of these pumps is 560 gph at 140 psig (65). The system supply curve is provided in Figure 45. The flow controller valve was a Kates , model GB11T-A valve with a range of 1.5 to 20 gpm. This valve was designed to maintain a set flow regardless of downstream pressure variations. Flow was regulated by manually positioning this flow controller.

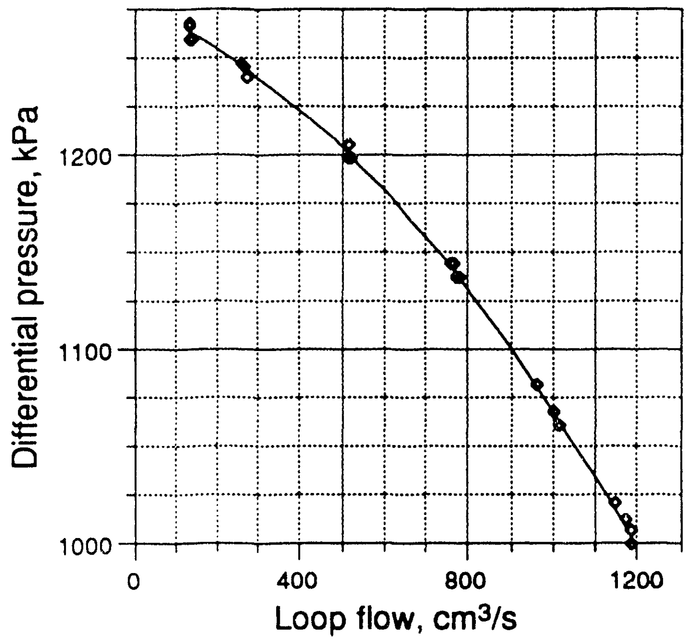

Figure 45. Test loop supply curve (pressure differential between pump suction and pump header) on 27 July 1993.

Loop Instrumentation

The flow supplied to the heated channel was measured using two devices, a turbine flow meter, instrument number FT01001, and an orifice meter, FT01002. The turbine meter was a 3/4" model FT-12NEXW-LAD-1, manufactured by Flow Technology Inc. The rated capacity of this meter was 1600 cm^3/s (25 gpm). The orifice meter consisted of a standard 1-1/2" 300# flange tap assembly with a 0.435" orifice diameter. The pressure transducer was a model 1151DP manufactured by Rosemount. The calibration curves used for data reduction are presented in Appendix 7, Table 7-2. The calibration calculations are presented in Appendix 2.

Heat Rejection

Heat was removed from the flow loop using a Alfa-Laval type M10-BFG flat plate heat exchanger. The secondary coolant fluid was building process water. The temperature of this water is nominally 22 ± 4°C. The secondary coolant flow rate was designed to be controlled using one of two reverse acting (temperature rise opens valve) temperature control valves that were equipped with capillary tubes. The capillary tubes were inserted into the piping at the heat exchanger exit. The ranges of these control valves are listed in Table 22.

While these control valves could maintain temperatures during steady state operation, their response was too sluggish to be of use during diabatic demand curve testing. Secondary cooling during diabatic demand curve testing was accomplished manually using valve CW006. The need for this valve was identified during the debugging stage of the experiment. Except for operations below 25°C the secondary valves CW003, CW004, and CW005 remained closed.

Exit Pressure Control

The pressure at the exit of the heat exchanger was regulated by use of the standpipe shown in Figure 44. The nominal water level was 3.5 m (138") above the pump suction, 1.78 m (70") above the nominal SHL, 3.00 m (118") above the nominal EHL, and 3.30 m (130") above the centerline of the test section exit. Since the reservoir level was set to achieve a specified heated channel exit pressure, density variations in the water column have been accounted for.

Process Fluid Chemistry

Deionized water was used in the flow loop to limit contamination of the heated surface. Virtually all of the wetted components were aluminum or stainless steel. These two dissimilar metals were kept electrically isolated. Other materials in the flow loop included plastic pump parts, neoprene seals, and RTV seals. Water was sampled and analyzed for conductivity during the test program. The conductivity did not exceed 3 μS/cm.

Heated Channel

The heated rectangular channel was nominally 79.38 (3.125") wide, and 3.18 mm (0.125") deep. The flow channel cross section is presented in Figure 46. The nominal heated length was 1.219 m (48"). The best estimate channel dimensions are presented in Table 23.

The heater formed one side of the flow channel. The opposite side was an aluminum plate fitted with eleven 3/8" thick glass view ports. (See Figure 47.) These view ports were each 79.5 mm (3.13") wide and 101.6 mm (4.00") long. The side with the view ports was considered the "front" of the channel. The two remaining sides were formed with Lexan. The thickness of the Lexan was too great to allow viewing.

Table 23.--Channel dimensions

	open channels			rib channel
Construction:	1	3	4	2
Channel width, a, mm	79.7	79.6	79.8	79.6
Channel depth, b, mm	2.90	2.45	3.16	3.09
Rib width, x_o, mm	...	...	...	2.07
Length, hydraulic, L, m	1.3970	1.3970	1.3970	1.3970
Length, heated, L_h, m	1.156	...	1.156	1.156
Heated width, a_h, mm	76.2	...	76.2	74.1
Hydraulic diameter, D, mm	5.60	4.75	6.08	5.72
Equivalent diameter, D_e, mm	3.91	3.30	4.27	4.22
Heated diameter, D_h, m	12.1	...	13.2	12.9
$k = f\,Re$, Equation 26	91.5	92.2	91.1	86.9
Flow area, A_f, mm^2	231.1	195.0	252.2	239.6
Heated area, A_h, m^2	0.0881	...	0.0881	0.0857
Hydraulic L/D	250	294	230	244
Heated L/D	95.3	...	87.3	89.4

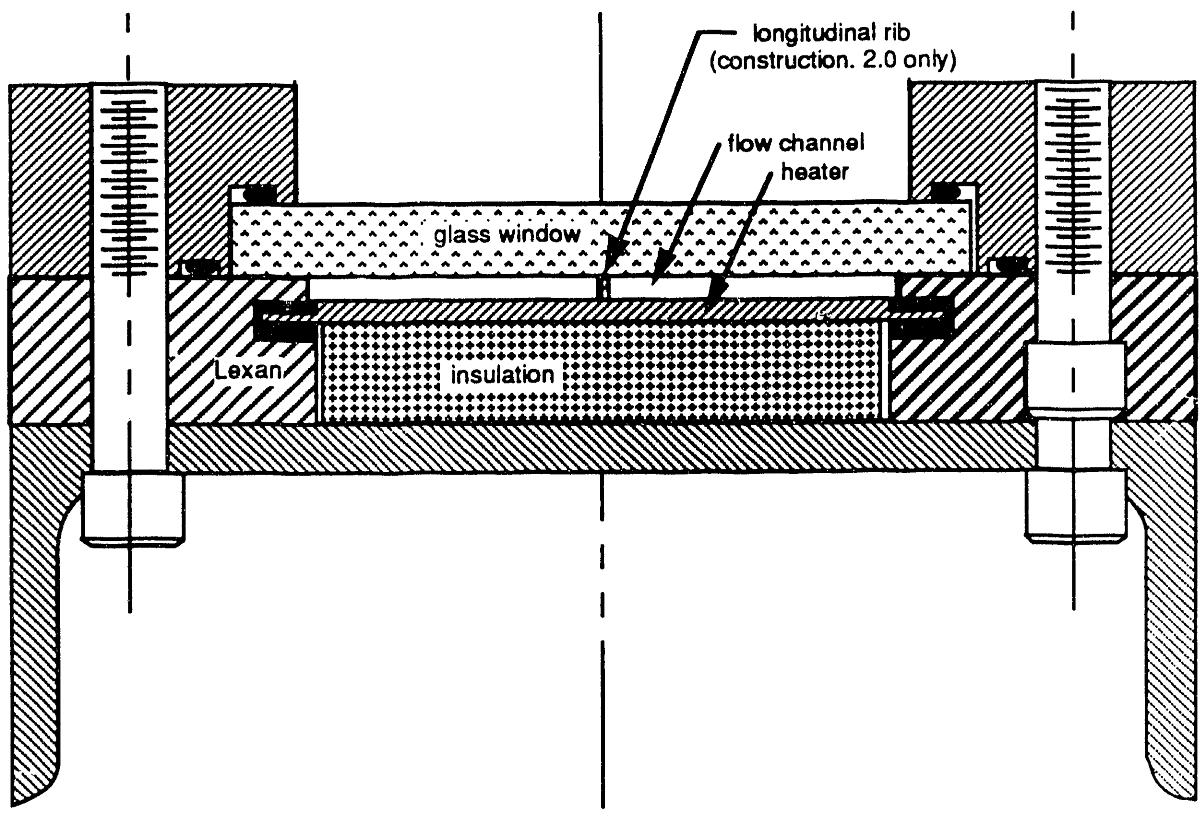

Figure 46 Test channel cross section

Figure 47, Channel view port details -- Construction 2.0 at the end of the heated length (Photograph 93-1566-12)

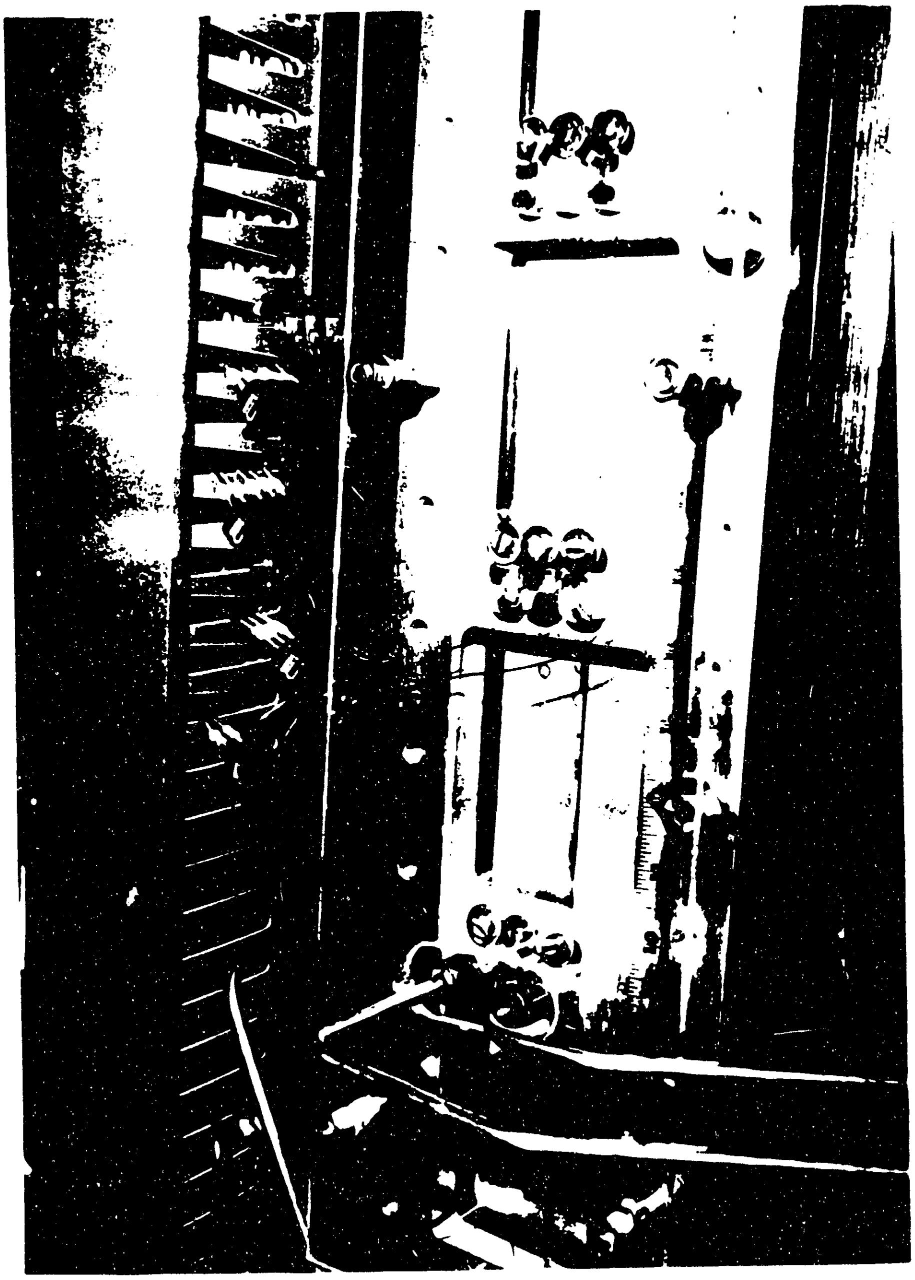

93-1566-12

Channel Heater

The channel heater utilized a plasma sprayed design which allowed indirect heating of the wetted surface. The heater consisted of 3 layers. These layers are presented schematically in Figure 48. Heat is generated in the conductive layer by electric resistance heating. The core layer was 3.20 ± 0.04 mm (0.125 ± 0.002") thick with a total electrical resistance of 37.0 mΩ. This resistance measurement was completed at ambient conditions. The resistance under powered operation varied from this measurement. Power to generate this heat was provided by DC rectifiers which were capable of generating 120 volts and 5000 amps. The heater core was electrically isolated from the wetted surface by an electrically resistive aluminum oxide and titanium oxide layer. This layer was approximately 0.27 ± 0.04 mm thick. The bond coat was 0.07 mm thick while the conductive layer of nickel aluminum was 0.21 mm thick.

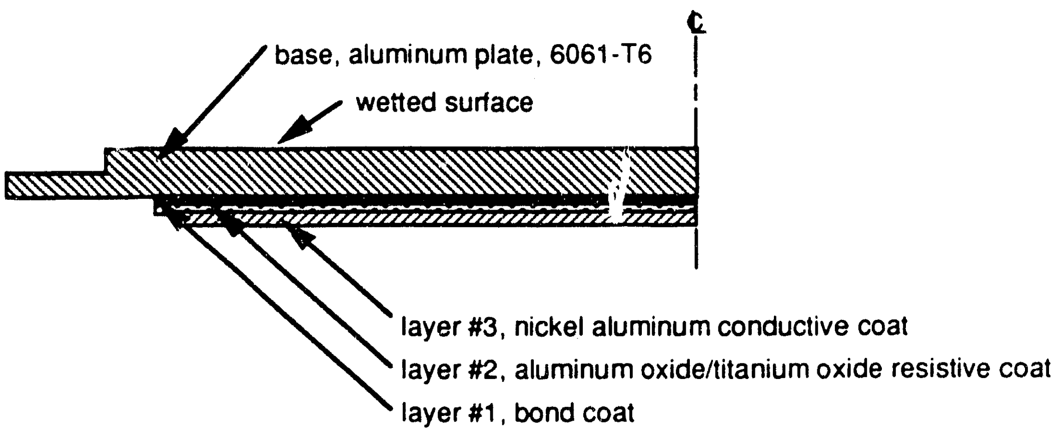

Figure 48. Heater cross-section schematic

Instrumentation

The fluid channel and heater wall temperatures were measured using type E thermocouples. The locations where these measurements were made are listed in Table 24. Table 25 summarized the other types of channel instrumentation. Channel pressure measurements included differential, absolute, and gauge pressures. The differential measurements were used to produce both isothermal and diabatic demand curves. The absolute transducers were used to estimate the local saturation temperature, and the gauge transducers were used for operation diagnostics. Instrumentation ports were installed between each of the glass viewports as shown in Figure 49. Different instrument inserts were used to support temperature and pressure measurements. These inserts are shown in Figure 50. Blank inserts were installed in all unused ports.

In addition to temperature and pressure measurements, channel instrumentation included both heater voltage and heater current measurements. These measurements were used to compute heater power and heat flux.

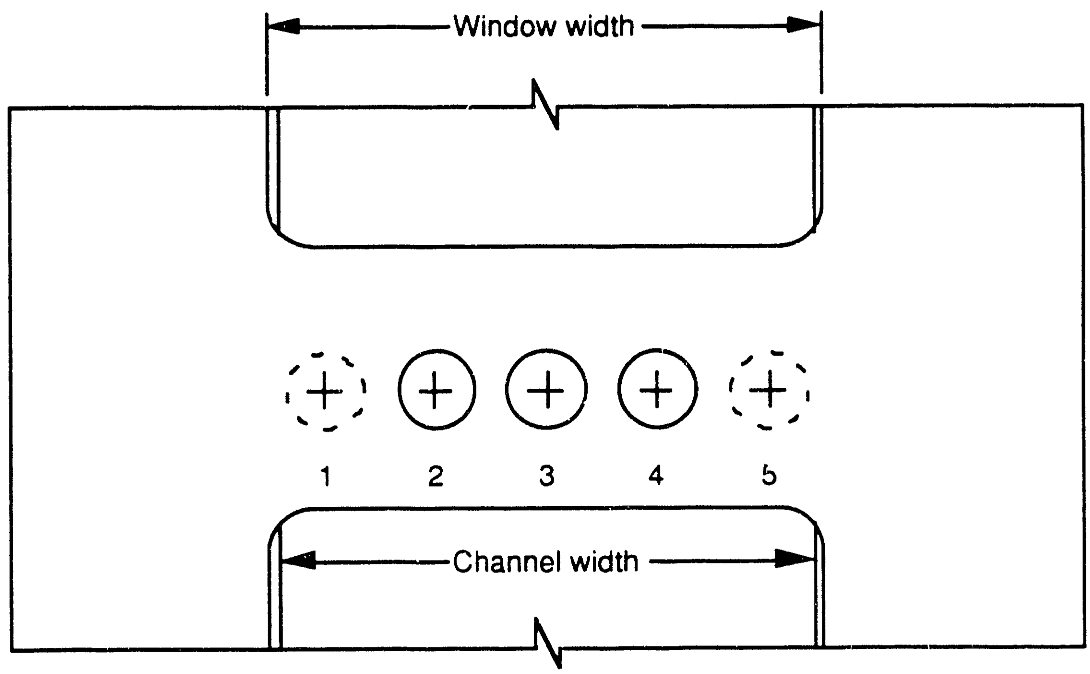

Figure 49. Test channel instrument port identification, positions 1 and 5 were not installed, position 3 was used to hold the rib in position

Table 24.--Channel temperature instrumentation

Instrument number	Channel number	z meters	y mm	x mm	comment
TP01317	1	0.032	-2.92	42.60	Heater, dry side
TP01308	2	0.034	-0.41	53.72	Heater, wet side
TP01413	3	0.036	-2.92	26.72	Heater, dry side
TP01702	4	0.042	-0.42	21.97	Heater, wet side
TP01505	5	0.038	-0.43	37.85	Heater, wet side
TP11917	6	0.302	-2.92	42.60	Heater, dry side
TP12008	7	0.304	-0.43	53.72	Heater, wet side
TP12113	8	0.306	-2.92	26.72	Heater, dry side
TP12105	9	0.308	-0.43	37.85	Heater, wet side
TP12302	10	0.312	-0.41	21.97	Heater, wet side
TP22917	11	0.582	-2.92	42.60	Heater, dry side
TP23008	12	0.583	-0.47	53.72	Heater, wet side
TP23013	13	0.585	-2.92	26.72	Heater, dry side
TP23105	14	0.587	-0.46	37.85	Heater, wet side
TP23302	15	0.592	-0.47	21.97	Heater, wet side
TP33917	16	0.862	-2.92	42.60	Heater, dry side
TP34013	17	0.864	-2.92	26.72	Heater, dry side
TP33908	18	0.862	-0.52	53.72	Heater, wet side
TP34105	19	0.867	-0.50	37.85	Heater, wet side
TP34302	20	0.871	-0.47	21.97	Heater, wet side
TP45008	21	1.142	-0.18	53.72	Heater, wet side
TP45105	22	1.146	-0.18	37.85	Heater, wet side
TP45302	23	1.150	-0.18	21.97	Heater, wet side
TP45613	24	1.159	-2.92	26.72	Heater, dry side
TP45717	25	1.160	-2.92	42.60	Heater, dry side
TP45808	26	1.162	-0.18	53.72	Heater, wet side
TP45905	27	1.166	-0.20	37.85	Heater, wet side
TP46102	28	1.171	-0.20	21.97	Heater, wet side
TP46308	29	1.176	-0.30	53.72	Heater, wet side
TP46217	30	1.175	-2.92	42.60	Heater, dry side
TP46413	31	1.179	-2.92	26.72	Heater, dry side
TP46505	32	1.181	-0.16	37.85	Heater, wet side
TP46602	33	1.185	-0.18	21.97	Heater, wet side
TP46808	34	1.189	-0.16	53.72	Heater, wet side
TP47005	35	1.193	-0.19	37.85	Heater, wet side
TP47202	36	1.198	-0.20	21.97	Heater, wet side
TC00001	37	1.270	-5.60	76.20	Channel seal
TC00002	38	1.270	-5.60	76.20	Channel seal
TF01202	40	-0.305	1.59	22.23	Channel fluid
TF01204	41	-0.305	1.59	53.98	Channel fluid
TF02522	42	0.032	1.59	22.23	Channel fluid
TF02524	43	0.032	1.59	53.98	Channel fluid
TF04172	44	0.451	1.59	22.23	Channel fluid

Table 24.--Continued

Instrument number	Channel number	z meters	y mm	x mm	comment
TF04174	45	0.451	1.59	53.98	Channel fluid
TF05822	46	0.870	1.59	22.23	Channel fluid
TF05824	47	0.870	1.59	53.98	Channel fluid
TF06922	48	1.149	1.59	22.23	Channel fluid
TF06924	49	1.149	1.59	53.98	Channel fluid
TF08022	50	1.429	1.59	22.23	Channel fluid
TF08024	51	1.429	1.59	53.98	Channel fluid

Table 25.--Flow loop instrumentation

Instrument loop number	Channel number	Instrument description
PA20072	61	Absolute pressure, left side of channel, 1.29 m from the start of the heated length (SHL)
PD22472	62	Differential pressure, left side of channel, between -0.11 and 1.29 m from the SHL
PG00024	64	Local gauge pressure, right side of channel, -0.11 from the SHL
PD00024	66	Differential pressure, right side of channel, between -0.55 and -0.11 m from the SHL
PA00072	67	Absolute pressure, right side of channel, 1.29 m from the SHL
PD02472	68	Differential pressure, right side of channel between -0.11 and 1.29 m from the SHL
PD00072	69	Differential pressure, right side of channel, between -0.55 and 1.29 m from the SHL
PL00002	70	Local gauge pressure at test channel exit 1.52 m from the SHL (after expansion)
PD07284	71	Differential pressure, right side of channel, between 1.29 and 1.52 m from the SHL
PD00084	72	Differential pressure, right side of channel, between -0.55 and 1.52 m from the SHL
WV00001	74	Heater voltage (buss block to buss block)
WC00001	75	Heater current

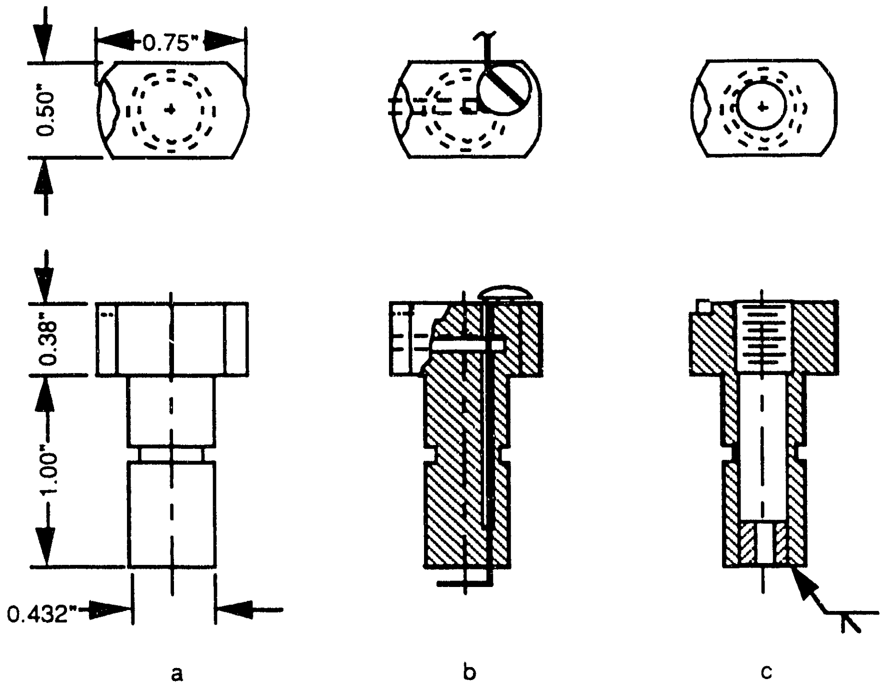

Figure 50. Fluid channel instrument port connections: (a) Blank, (b) Thermocouple using a 0.020" stainless steel sheathed type E thermocouple, (c) Tube connection, 1/16" NPT with a 1.59 mm through hole.

Fluid Instrumentation

Fluid temperature measurements were made using 0.020" type E thermocouples. Three different styles were used. These are listed in Appendix 2, Table 2-1. The preferred type was a grounded tip, the other types were used because of availability. These thermocouples were installed through the instrument ports on the front of the test channel. The thermocouples were held in place using the instrument inserts shown in Figure 49b.

The local absolute pressure at the end of the heated length was measured using Rosemount 1151AP pressure transducers. The instrument port was equipped with the instrument insert shown in Figure 50c. This port was located 2.75 mm (0.1 inches) from the end of the nominal heated length. The local gauge pressures were measured using a Rosemount 1144 pressure transducer using a Figure 50c instrument insert near the start of the heated length. A second gauge pressure measurement was made in the 2" pipe which served as the channel exit.

Six differential pressures were measured in the heated channel using Rosemount 1151DP pressure transducers. Figure 50c inserts were used for these pressure measurements. The locations of the ports used for these measurements is shown in Figure 52. The arrangement of the transducer rack is presented in Figure 51.

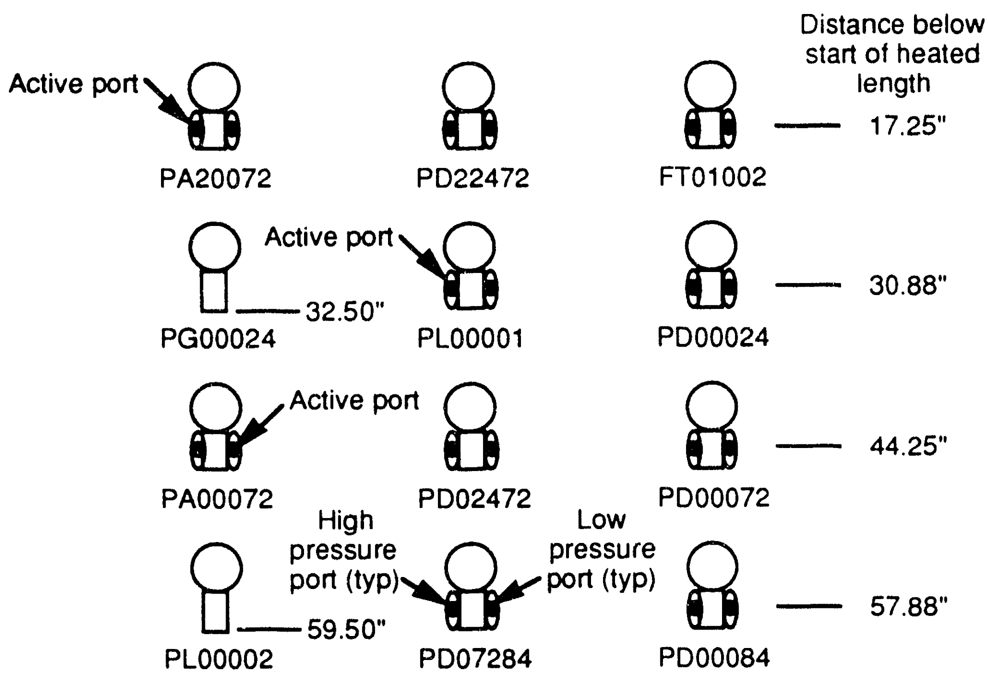

Figure 51. Pressure transducer elevations

Heater Instrumentation

The internal temperature of the heater plate was measured using 0.020" sheathed, grounded type E thermocouples. These were mounted as shown in Figure 53. The wetted wall thermocouples were inserted into the

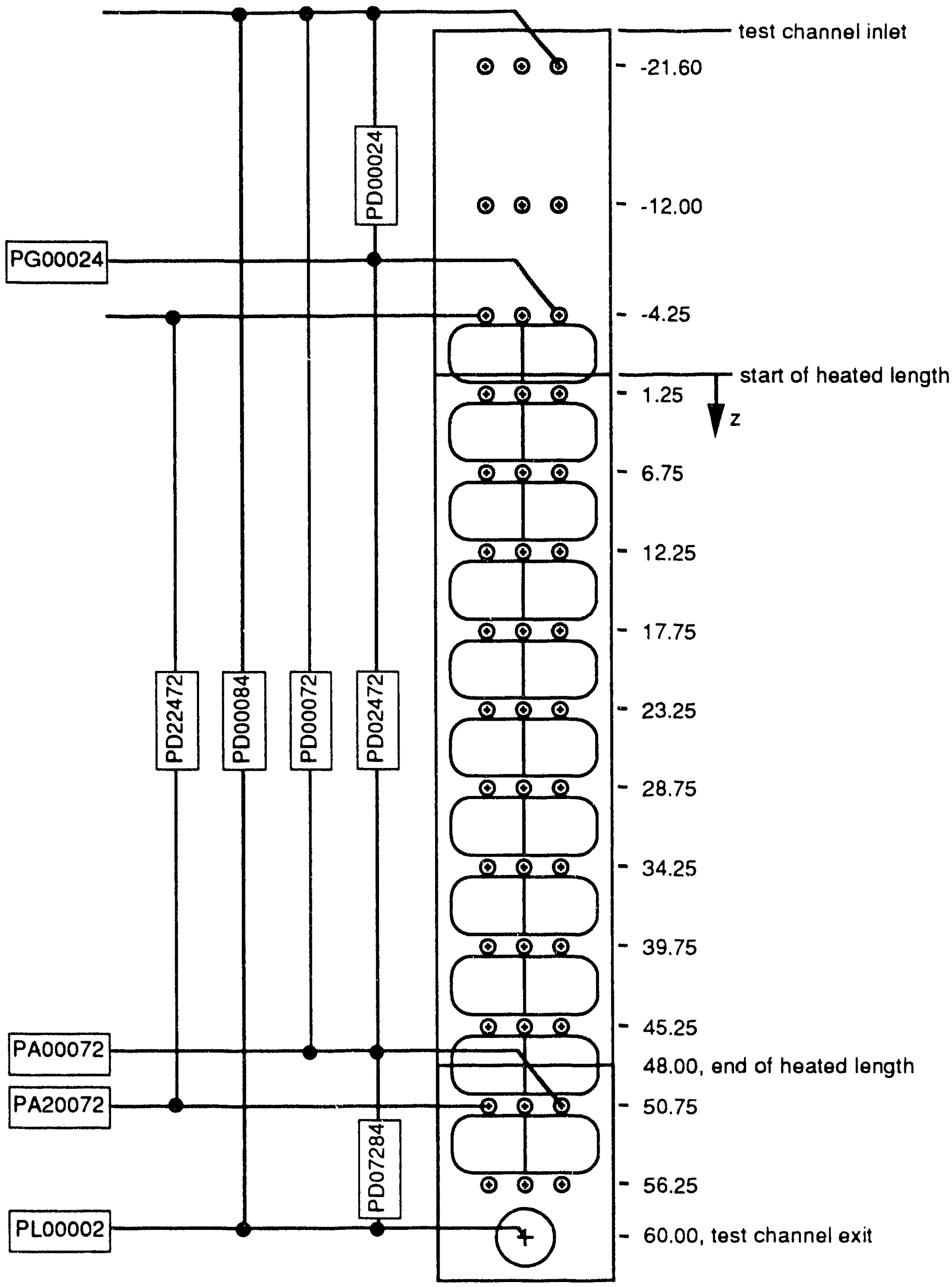

Figure 52, Test channel pressure instrumentation schematic

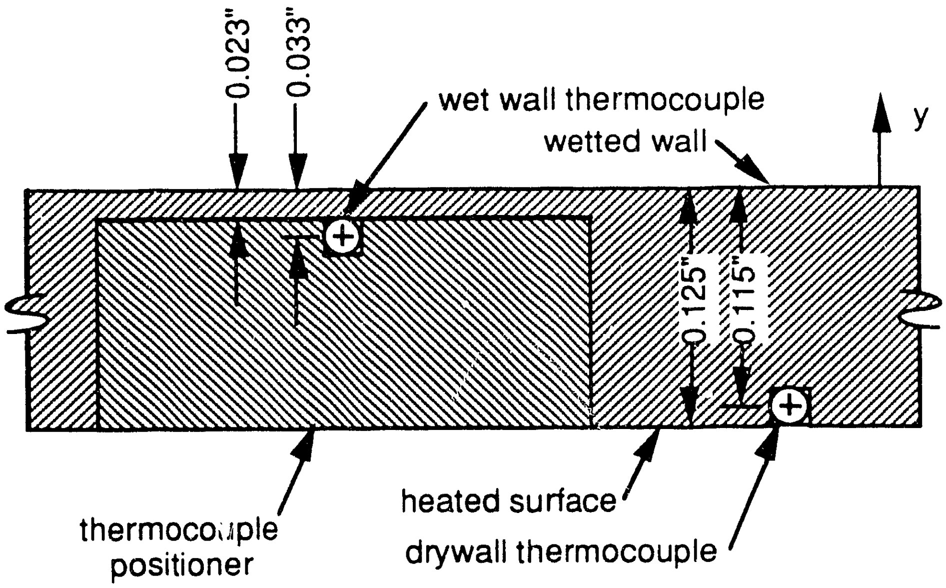

Figure 53. Thermocouple installation details (dimensions shown are nominal)

holes shown in Figure 54 and held in positions using aluminum buttons. Dry wall thermocouples and the leads from the wetted wall thermocouples were pressed into the slots and held in position by rolling the slot edges over the thermocouple sheaths.. After installation of these thermocouples the plasma spayed layers were installed.

Power Instrumentation

The electrical power measurement instrumentation schematic is shown in Figure 55. Both the applied voltage and the resulting current were measured. The power was calculated using the equation. The voltage was measured across the buss connections using a voltage transducer. Two different transducers were used. On 2 June 1993 the original transducer with a range of 0 to 50 volts was replace with a unit with a range of 0 to 150 V. All data collected on 3 June 1993 and thereafter was collected using the second

Figure 54, Heater base plate ready for installation of thermocouples
(Photograph 92-1769-4)

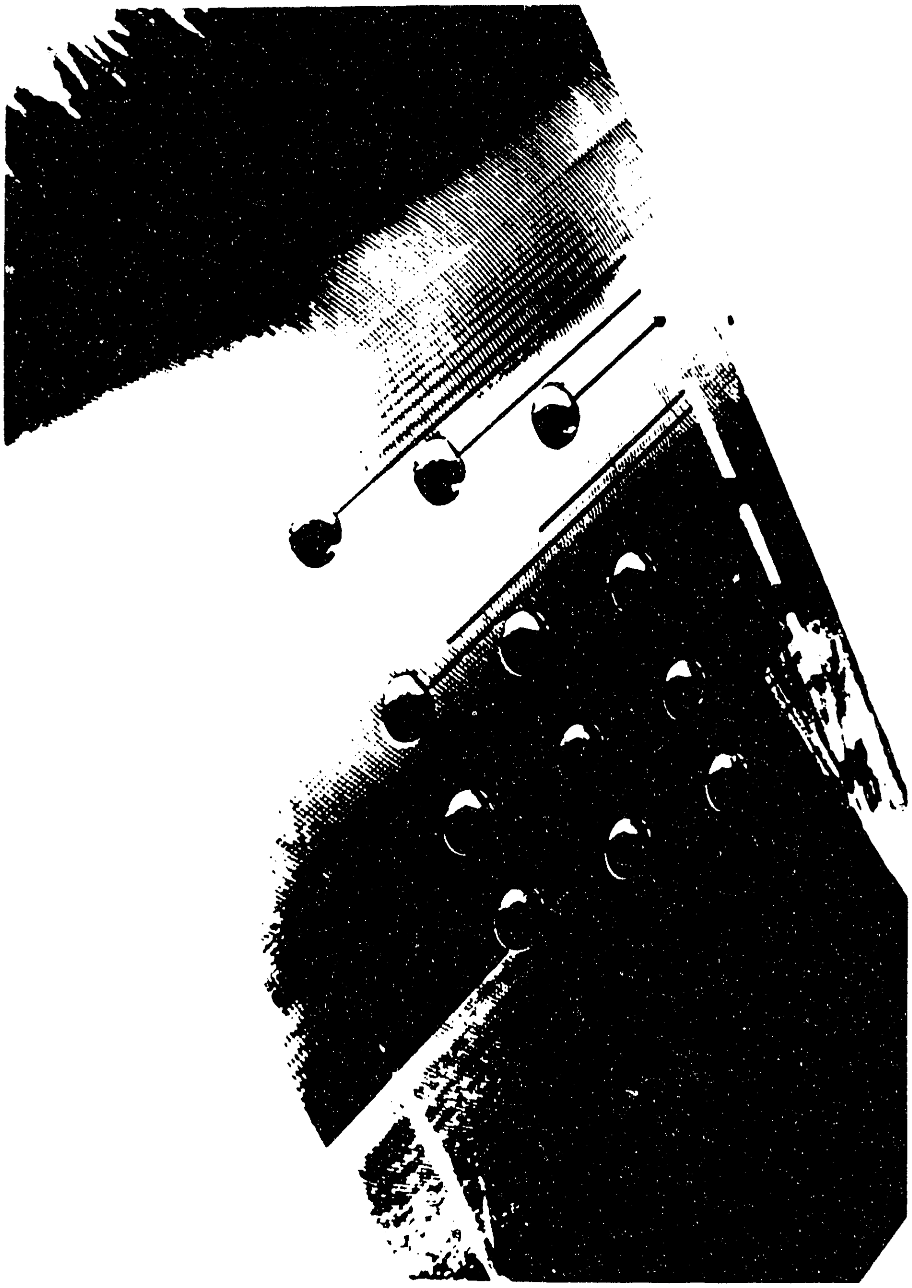

92-1769-4

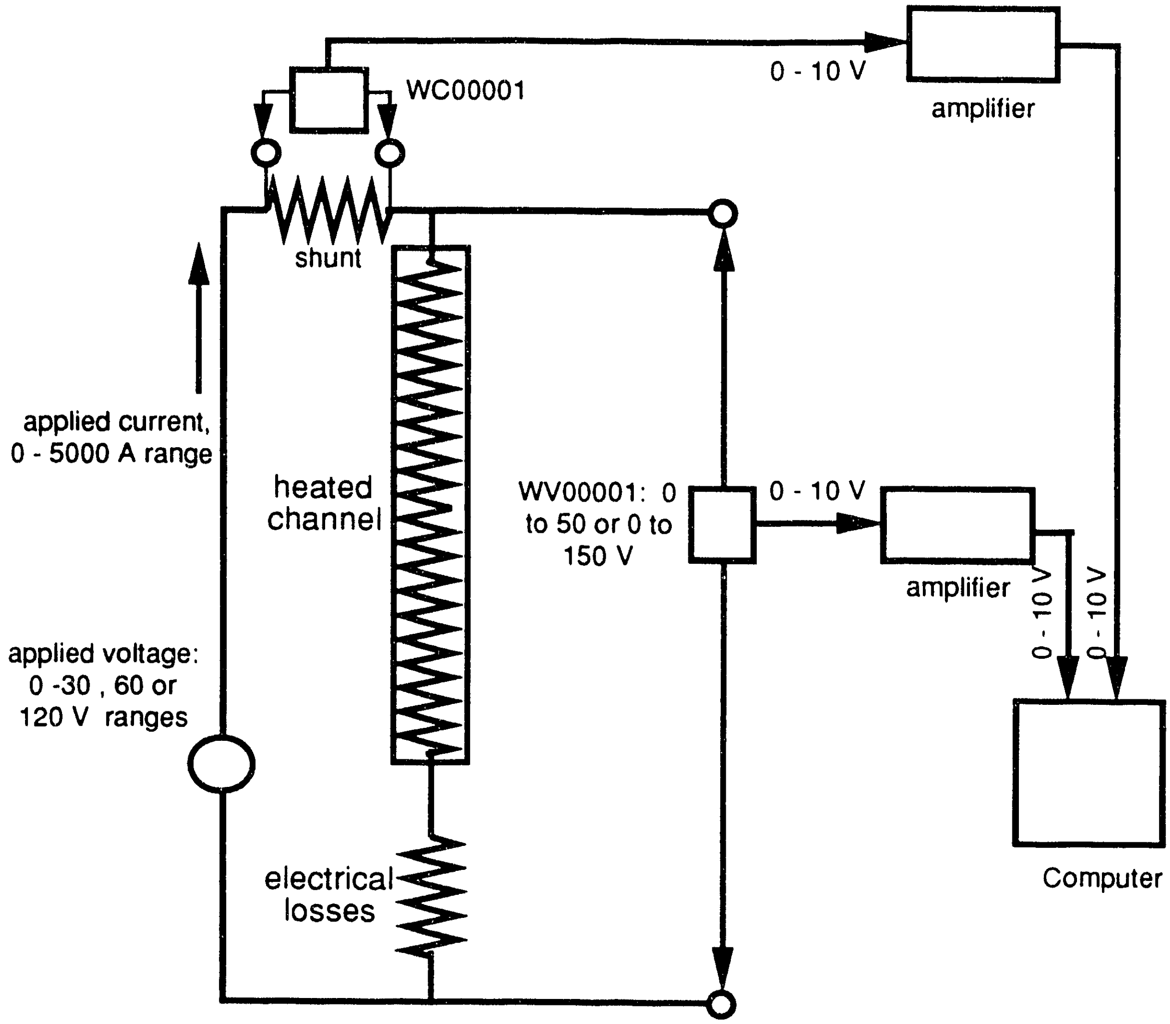

Figure 55, Applied Power Instrument Schematic

transducer. The calibration curves for both transducers are provided in Appendix 2.

Structural Instrumentation

Temperature measurements were made at two additional locations in the heated channel structure. The primary purpose of these thermocouples was to verify the operating temperatures and to ensure that seals were not operated outside of their design limits. TC00001 was place against the heater 114 mm above the end of the heated length near the right RTV seal. TC00002 was also placed in a similar manner 30 mm below the end of the heated length at the buss connection.

Rib Details

A rib was installed in Construction 2.0 as shown in Figure 47. The rib details are provided in Figure 56 with the nominal rib dimensions. The rib was held in position using modified instrument port plugs. (See Figure 57.) The rib holder inserts were inserted into the slots shown in Figure 56. The slots permitted longitudinal rib expansion. Longitudinal movement of the rib was restrained at the lowest slot which was only slightly larger than the rib holder insert.

Data Acquisition

The test loop was operated to obtain both isothermal and diabatic demand curves. The types of curves were generated by incrementally varying the flow over a specified range and recording the conditions at each operating set-point. The conditions at each set-point were held steady for a minimum of tow minutes prior to recording data. When this condition was meet a one minute long data set was recorded and assigned a filename as described in Table 26. Each file contains approximately 120 samples per instrument. Appendix 6 presents a detailed description of the test operation procedures.

The data acquisition system consisted of a Macintosh II computer equipped with WorkBench™ software (73). Field instrumentation signals were conditioned using amplifiers as shown in Figure 58. The amplifiers were equipped with 300 Hz filters designed to minimize the effect of electrical noise produced by the heater power circuits. Instrument measurements were collected and recorded in voltage units. The DAS produced raw data files that

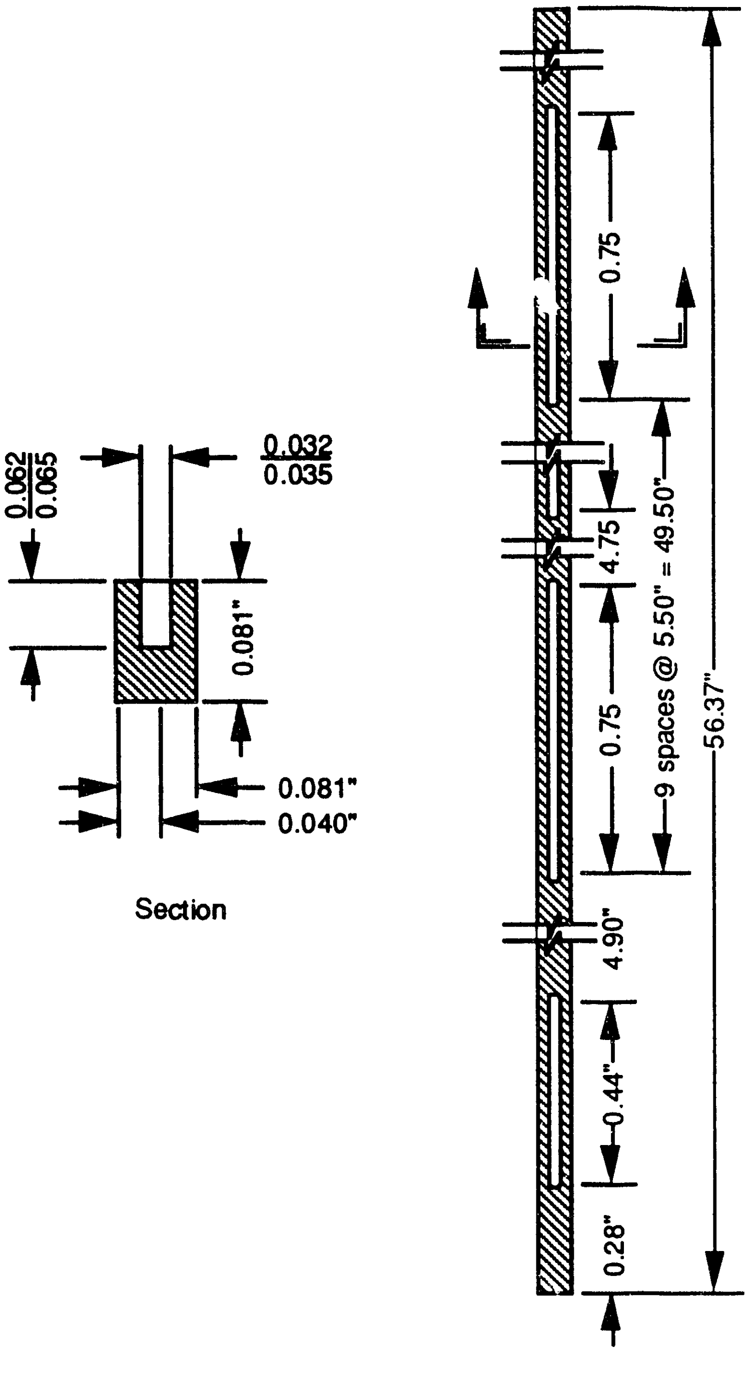

Figure 56, Rib details

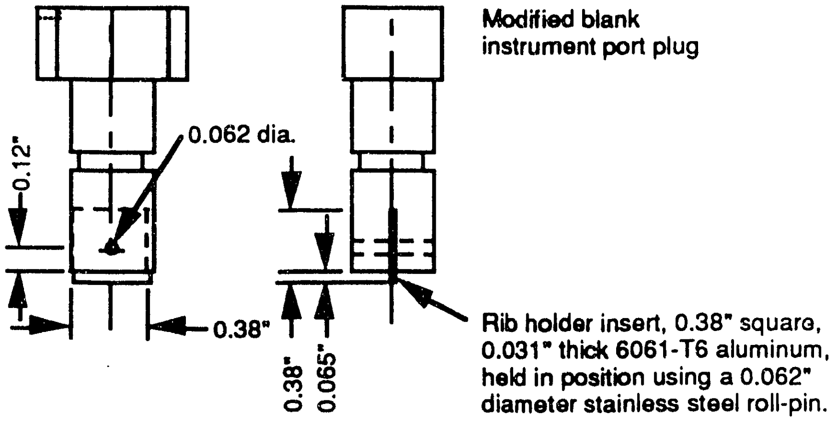

Figure 57, Rib support plugs

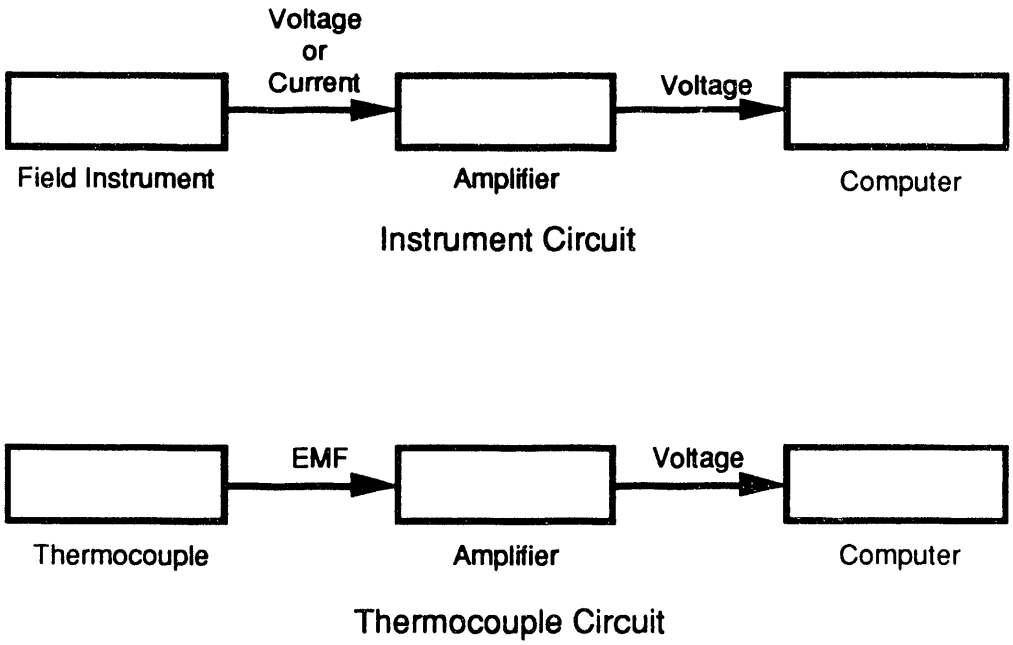

Figure 58, Basic instrument schematic

Table 26.--File nomenclature

		Description
WW_YYMMDD_HHHH		
WW	file prefix	
	LP	loop calibration file
	SN	daily span calibration check file
	ZO	daily zero calibration check file
	FW	daily flow calibration check file
	FS	steady state flow data file
	FT	transient flow data file
	SF	special file
YYMMDD	date created	year, month and day
HHHH	time created	military time

were tab delimited with the headers listed in Appendix 7, Table 7-1. These files were considered the raw data files.

Data Management, and Reduction

The raw data files were imported into the statistical software program, JMP (39). A column was added to each raw data file which consisted of the file name. The raw data file was then stored as a JMP data file. The column means and sample standard deviations listed in Appendix 7, Table 7-1 were then calculated for each JMP data file. The column means and sample standard deviations were then appended into a reduced raw data file consisting of the columns listed in Appendix 7, Table 7-1. This file was considered the reduced raw data file and was still in voltage units.

Data was converted from voltage units to engineering units using the formulas listed in Appendix 7, Table 7-2. The development of these formulas is presented in Appendix 2. Selected engineering units were then placed in the JMP data tables listed in Appendix 7 (Tables 7-3, 7-4, 7-5, and 7-6). Each of these JMP data tables was used to evaluate specific aspects of the channel behavior. The data reduction equations used in these data tables are presented in Appendix 7.

Primary Measurements

Flow data reported in this report, except where specifically noted, is based on the turbine flowmeter, FT01001. This simplification was made to reduce the data reduction effort and because the turbine meter had a lower systematic uncertainty then the orifice meter, FT02001. Voltage measurements were made with two separate instruments. All data collected prior to 3 June 1993 should be converted to engineering units using the first equation listed in Appendix 7, Table 7-2, data taken on or after that date should be converted using the second equation.

Pressure measurements reported in this report include a correction to account for the static head of the impulse lines. This correction is based on Equation 5. The fluid density was calculated using the temperature indicated by the thermocouple TC00003. The elevation corrections were computed based on the data in Figures 51 and 52.

Fluid Properties

Density

Equation 74 presents a correlation to predict the density of water at saturated conditions based on temperature (76). The coefficients for this equation are defined in Table 27. This equation has been used in the data reduction to estimate the fluid density. An implied assumption in its use is that the density of subcooled water is the same as water at saturated conditions.

(74) $$\rho = \sum_{i=1}^{4} c_i T^{(i-1)} \left[\frac{kg}{m^3}\right] \quad 10 \le T \le 300^\circ C$$

Table 27--Water property equation coefficients for density, specific heat and thermal conductivity

i	Density	Specific heat	Thermal conductivity
1	1004.8897	5615.8	570.32432
2	-0.26847207	-9.02077	1.7996615
3	-0.18136391e-2	0.014177	-0.72881959e-2
4	-0.17041217e-5	...	0.32412245e-5

Specific Heat

Equation 75 presents a correlation to predict the specific heat of water at saturated conditions based on temperature (31). The coefficients for this equation are defined in Table 27. This equation has been used in the data reduction to estimate the fluid specific heat. An implied assumption in its use is that the specific heat of subcooled water is the same as water at saturated conditions.

$$c_p = \sum_{i=1}^{3} c_i T^{(i-1)} \left[\frac{J}{kg\text{-}K}\right] \quad 273.15 \leq T \leq 373.15 \text{ K} \tag{75}$$

Thermal Conductivity

Equation 76 presents a correlation to predict the thermal conductivity of water at saturated conditions based on temperature (76). The coefficients for this equation are defined in Table 27. This equation has been used in the data reduction to estimate the fluid thermal conductivity. An implied assumption in its use is that the thermal conductivity of subcooled water is the same as water at saturated conditions.

(76) $$k=\sum_{i=1}^{4} c_i T^{(i-1)} \left[\frac{W}{m\text{-}K}\right] \quad 10 \leq T \leq 300°C$$

Dynamic Viscosity

Equation 77 presents a correlation to predict the dynamic viscosity of water at saturated conditions based on temperature (76). The coefficients for this equation are defined in Table 28. This equation has been used in the data reduction to estimate the fluid viscosity. An implied assumption in its use is that the viscosity of subcooled water is the same as water at saturated conditions.

(77) $$\mu = \exp \sum_{i=1}^{6} c_i \left(\frac{1}{T_r} - 1\right)^{(i-1)} \left[\frac{\mu N\text{-}s}{m^2}\right] \quad 283.15 \leq T \leq 573.15 \text{ K}$$

where:

$$T_r = \frac{T}{647.14 \text{ K}}$$

Table 28--Water property equation coefficients for viscosity and saturation temperature

i	Viscosity	Saturation temperature
1	4.2529199	375.46530
2	2.3790677	89.679811
3	-3.8810805	11.149468
4	8.0014055	0.99075812
5	-6.2882872	0.052882025
6	1.8383557	0.0012471856

Saturation Temperature

Equation 78 presents a correlation to predict the saturation temperature of water based on the local pressure (76). The coefficients for this equation are defined in Table 28. This equation has been used in the data reduction to estimate the saturation temperature at the end of the heated length based on the pressure transducers PA00024, and PA20024.

(78) $$T_{sat} = \sum_{i=1}^{6} c_i Y^{i-1} \ [°C] \qquad 1.2277 \text{ kPa} \le P \le 8.592 \text{ MPa}$$

where:

$$Y = \ln\left(\frac{P}{22.064 \text{ MPa}}\right)$$

Bulk Fluid Temperature

The bulk fluid temperature was estimated as the mean of the inlet temperature as measured by TL00001, and the exit temperature as measured by TL00002.

Demand Curve Analyses

Demand curves were plotted in four different formats: (1) measured pressure drop versus measured flow, (2) friction factor versus Reynolds number, (3) measured pressure drop versus Q_{ratio}, and (4) pressure ratio versus Q_{ratio}. The pressure drop plotted in these figures is the measured pressure difference between the ports, Δp_{23}, shown in Figure 52 for the instruments PD02472, and PD22472. The stated pressure would include elevation recovery, acceleration effects, and frictional pressure losses. The measured frictional pressure loss, Δp_f, was calculated using Equation 79 where the acceleration term has been neglected.

(79) $$\Delta p_f = \Delta p_{23} + g\,\overline{\rho_m}\,|L_{23}|$$

The friction factor has been calculated using Equation 18 and the frictional pressure loss from Equation 79. The fluid properties for the friction factor and Reynolds number calculations were estimated using the bulk temperature. Table 23 presents the flow geometry dimensions which were used for the calculations. The diameter has been calculated using Equation 24; the hydraulic diameter, except where specifically noted.

The Q_{ratio} was calculated using the same relation as the temperature ratio, R (Equation 2). The pressure ratio is based on Equation 33. It is a ratio of the isothermal frictional pressure loss (where fluid properties are calculated at the inlet conditions) and the measured frictional pressure loss. An elevation recovery term is included in estimating the frictional pressure loss. The isothermal friction factor was estimated using Equation 22.

System Continuity Checks

Several continuity checks were possible for this test program. Comparison of independent measurements was done to quantify the uncertainties of the experiment and verify system operation. Two independent power calculations were possible: (1) electrical power applied to heater, and (2) heat transferred by the fluid. Three heat flux calculations were possible. Two were from the electrical and fluid power calculation, the third from the temperature gradient in the heater plate. The control boundary diagrams for each of these calculations is presented in Figure 59. In addition to these checks, the isothermal data was compared with accepted theories, and daily instrument checks were made to demonstrate consistency.

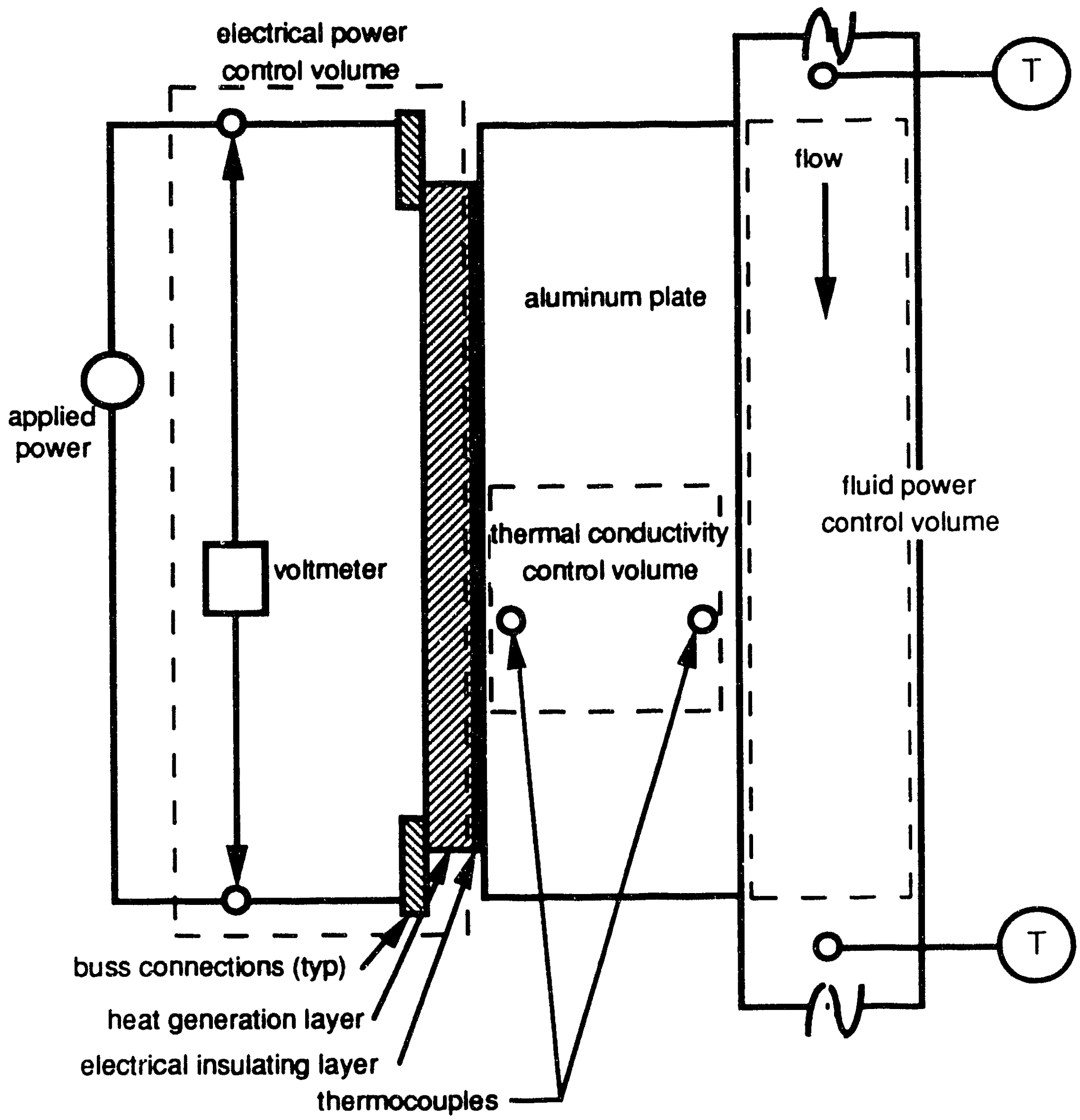

Figure 59. Power calculation control volumes

Temperature and Pressure Profiles

Temperature profile plots were prepared from raw engineering units data. No adjustments for installation effects (e.g., stem conduction) have been made. Pressure profile plots present the measured pressure indication with a correction for the static head in the impulse lines. The absolute pressures were adjusted to gauge by deducting the barometric pressure. The barometric pressure was taken at the measured value if available, or at the mean of the daily checks for that day.

The theoretical pressure profiles were assumed linear through the rectangular flow channel; only frictional losses and elevation recovery were considered. The profile was forced though the mean of PA00072 and PA20072. Acceleration effects where considered negligible. The entrance and exit losses were assumed negligible. Equations 8, 17, and 22 were used in calculating the profile.

Uncertainty Analysis

Appendix 3 contains a detailed analysis of the systematic measurement uncertainties for this test program. The random measurement uncertainties have been considered negligible. Since the final analysis includes a term for the variability of the resultants random measurement uncertainty has be folded into the final analysis. Geometric uncertainty estimates are presented in Appendix 1. Instrument measurement uncertainties have been estimated from the daily checks and the calibration information. This information is presented in Appendix 2.

The systematic uncertainties presented in Appendices 1, 2, and 3 have been propagated to resultants (25) using Equation 80.

(80)
$$B_r^2 = \sum_{i=1}^{J} \left[\theta_i^2 B_i^2 + \sum_{k=1}^{J} \theta_i \theta_k \rho_{ik} B_i B_k (1-\delta_{ik}) \right]$$

where:
$$\delta_{ik} = \begin{cases} 1 & i = k \\ 0 & i \neq k \end{cases}$$

The term ρ_{ik} is the coefficient of correlation between the terms x_i and x_k. If the errors are completely correlated ρ_{ik} is equal to 1. If the terms are not correlated (i.e., not independent) the value of ρ_{ik} is equal to 0. For most of the uncertainty estimates the elemental parameters, i, have been assumed independent. Correlated uncertainties have been discussed where they are known to exist. It should be noted that $\rho_{ik} = \rho_{ki}$.

Absolute Uncertainties

The absolute uncertainty in the context of this report is the uncertainty which exists in a stated measurement as compared with a defined true value (e.g., a known condition or correlation). Table 32 summarizes the systematic elemental measurement uncertainties for this test program. The random uncertainties for individual measurements have been assumed negligible. The random components for resultants have been estimated based on the variability of the resultant using the Equation 81.

$$P_r = \frac{t_v S_r}{\sqrt{N}} \tag{81}$$

where: t is the Student-t value at 95% confidence and the degrees of freedom, ν, is taken as N-1. The total measurement uncertainty, U, is then estimated using Equation 82.

$$U_r = \sqrt{B_r^2 + P_r^2} \tag{82}$$

Table 33 summarizes the combined resultant measurement uncertainties for the data presented in this report.

Table 32--Nominal elemental measurement uncertainties

	units	instrument loop number	x	B
Flow	cm^3/s	FT01001	200	1.4
			400	1.2
Pressure, absolute	kPa	PA00072	...	0.46
		PA20072	...	0.46
Pressure, differential	kPa	PA00072	...	0.4
		PA20072	...	0.4
Temperature	°C	...	...	0.53
Voltage	V	WV00001	...	0.001
Current	A	WC00001	...	0.1

Table 33--Nominal elemental measurement uncertainties

	Const.	R	B_r	P_r	U_r
Isothermal resultants					
Friction factor	4	0.0316	0.0083		
		0.0266	0.0046		
	2	0.0316	0.0077		
		0.0266	0.0052		
Reynolds number	4	10,000	113		
		20,000	176		
	2	10,000	120		
		20,000	206		
Diabatic resultants					
Energy balance ratio					
Q = 495 cm^3/s		0.97	0.042		
Q = 1260 cm^3/s		0.97	0.10		
Heat flux, kW	4	330	7		
	2	339	15.6		
Resultants at OFI					
Q_{ratio}	4	0.7616	0.011		
	2	0.6195	0.011		
Stanton number	4	0.00844	0.00079		
	2	0.00414	0.00037		

Comparative Uncertainties

Correlation of terms is an important consideration in comparison testing (13) where two different operating conditions or constructions are being compared by use of a ratio.

(83) $$\eta = \frac{\psi_{alt}}{\psi_{control}}$$

The uncertainty of the comparison ratio, η, when all of the systematic uncertainty terms are correlated and the corresponding sensitivity coefficients are equal (i.e. $q_{i,\,alt} = q_{i,\,control}$) is zero. It is this reason that back-to-back comparison testing can be such a powerful method to identify slight variations between two different configurations. For Equation 83 the uncertainty term summation based on Equation 80 is:

(84) $$B_\eta^{\ 2} = \left(\frac{\partial\eta}{\partial\psi_a}\right)^2 B_{\psi_a}^{\ 2} + \left(\frac{\partial\eta}{\partial\psi_c}\right)^2 B_{\psi_c}^{\ 2} + 2\left(\frac{\partial\eta}{\partial\psi_a}\right)\left(\frac{\partial\eta}{\partial\psi_c}\right) B_{\psi_a} B_{\psi_c}^{\ 2}$$

$$= \left(\frac{\eta}{\psi_a}\right)^2 B_{\psi_a}^{\ 2} + \left(\frac{-\eta}{\psi_c}\right)^2 B_{\psi_c}^{\ 2} + 2\left(\frac{\eta}{\psi_a}\right)\left(\frac{-\eta}{\psi_c}\right) B_{\psi_a} B_{\psi_c}^{\ 2}$$

If there is no variation between the two configurations $\Psi_a = \Psi_c$ and if the systematic uncertainties are also equal (i.e., $B_{\Psi_a} = B_{\Psi_c}$) then the combined systematic uncertainty would be zero. In practice there will always be some variation between the alternate and the control so some systematic uncertainty will always exist.

CHAPTER 4

RESULTS

The results presented in this section have been separated into five different categories: (1) isothermal test results, (2) diabatic demand curve results, (3) diabatic pressure profiles, (4) visual observations at OFI, and (5) temperature profiles. Ledinegg flow instabilities when operating a flow below the OFI flow were avoided since the channel was operated in a flow controlled mode. Some dryout patches were observed during demand curve 3.003 for Construction 2. No significant difference in the operating conditions has been identified which would have resulted in dryout for this curve and not for curves at equivalent operating conditions.

Isothermal Test Results

Figures 59 and 60 present the isothermal demand curve for the four different constructions evaluated during this study. The pressure drop for Construction 1 (open channel) was higher than for Constriction 2 (ribbed channel). This decrease in pressure drop after adding the rib was considered the result of an increase in flow area when the rib was added. Figure 61 provides a detail of the heater seal. During the operation of Construction 1 the rig began to leak. The eight bolts which hold the channel to the strong back were tightened the leak was substantially reduced, however, the pressure drop increased significantly. It appears that tightening the strongback bolts provided a preload on the heater seal. This could only occur if the heater insulation pressed on the back of the heater.

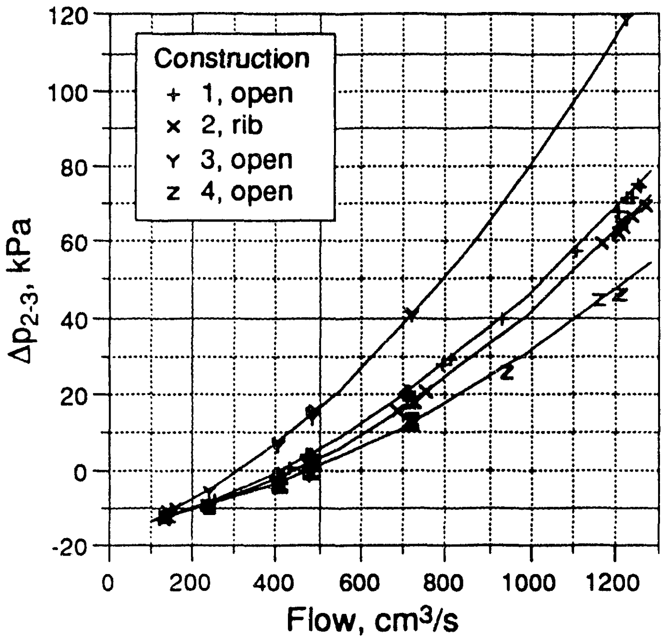

Figure 59, Isothermal demand curves for an inlet temperature range of 20 to 25°C

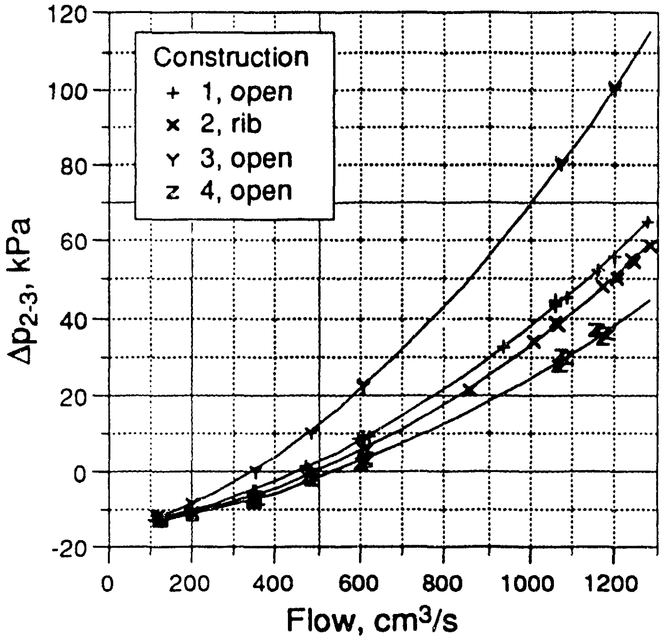

Figure 60, Isothermal demand curves for an inlet temperature range of 57.5 to 62.5°C

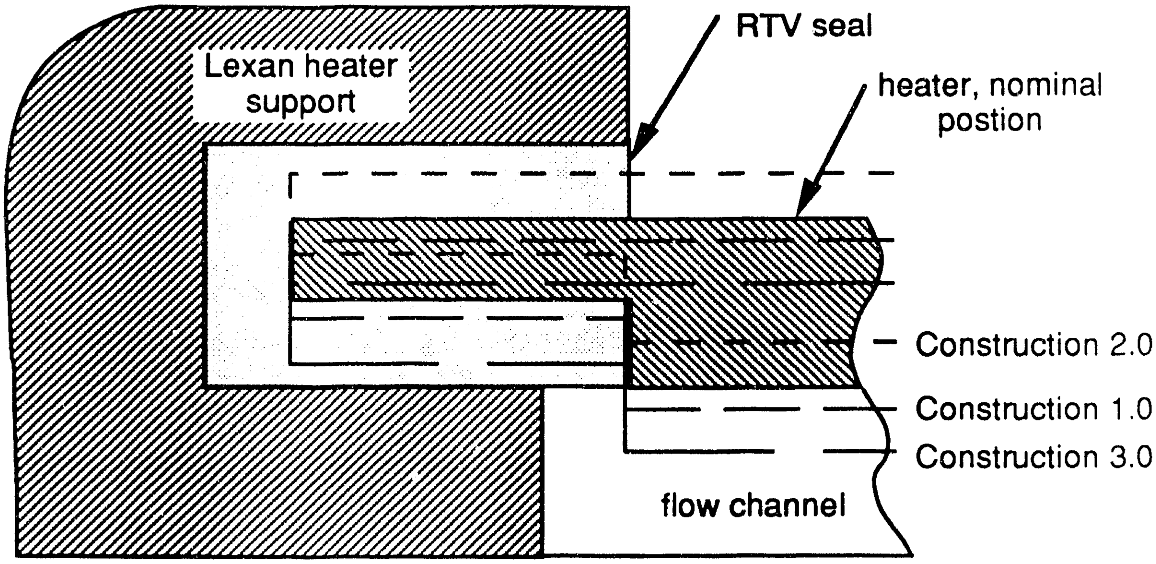

Figure 61, Heater seal detail

When the rib was installed the original heater gasket was reused. This was done to minimize any variation between the channel geometries. The rib required a fixed minimum distance between the faceplate and the heater. Since the rib height was 3.20 mm (0.126") the channel depth was increased above the nominal 3.18 mm (0.125"). This shift in the heater position shifted the strongback loading. The strongback now pressed on the insulation rather than the Lexan heater supports. The heater was therefore sandwiched between the rib and the ceramic insulation blocks. As a result the heater seal did not have any preload beyond the designed interference fit. This agrees with the observed leak rate during channel operation. When operating at ambient temperature the rig leaked approximately 1 cm^3/hr at a flow of 1260 cm^3/s. When the operating temperature was increased to 60°C thermal expansion sealed virtually all of the leakage.

The increase in channel depth when the rib was added was not readily apparent until Figures 59 and 60 were available. To diagnose the problem the rib was removed from the channel. To accomplish this the strongback was removed; the ceramic insulation was higher than the Lexan side supports. This verified that the strongback was indirectly pressing on the heater and compressing the heater against the rib rather than the Lexan heater supports. The rib support plugs were removed, and the bolts which held Lexan heater supports to the face plate (which holds the view ports) loosened one-half turn. This allowed the rib to be slipped out through the bottom of the channel. The channel was then reassembled as Construction 3.0. The channel depth measurements were measured using a depth micrometer. The distance from the front of the face plate to the wetted surface of the heater at multiple instrument ports. The channel depth was then calculated by deducting the thickness of the faceplate. The depth measurements are presented in Appendix 1.

The channel depth for Construction 1 was estimated to provide a friction factor demand curve which coincided with the friction factor demand curves for Constructions 3.0 and 4.0. Justification for the remainder of the channel dimensions is presented in Appendix 1.

Pressure Profiles

Figure 62 presents a typical pressure profile for the isothermal tests. Note the lack of variation between the duplicate pressure instruments (i.e., PD02472, and PD22472; and PA00072, and PA20072). For low flows such as shown in Figure 62 the elevation recovery exceed the frictional pressure loss and the pressure increased in the longitudinal direction. Figure 63 provides a profile for a high flow where the pressure gradient is negative since the frictional pressure drop exceeds the elevation recovery.

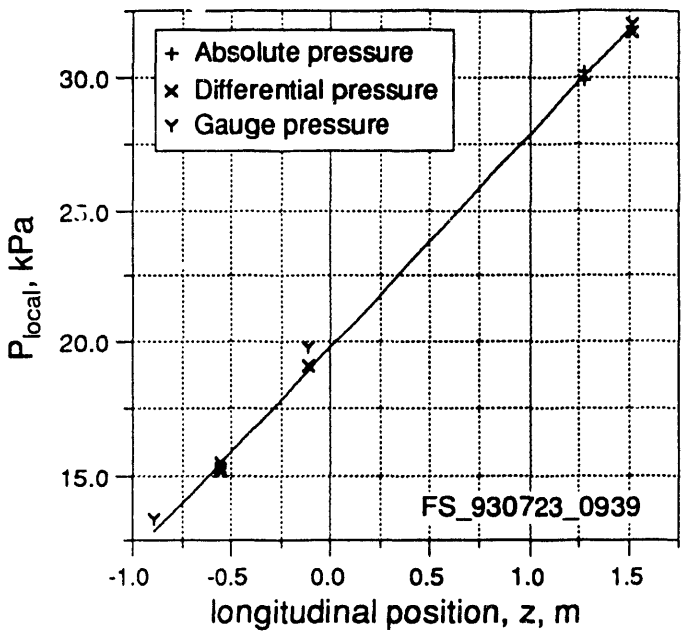

Figure 62, Isothermal longitudinal pressure gradient for open channel from File FS_930723_0939 (Construction 4.0, T_{in} = °C, ϕ = 0.0 kW/m^2, Q = low flow cm^3/s, p_{ehl} = kPa)

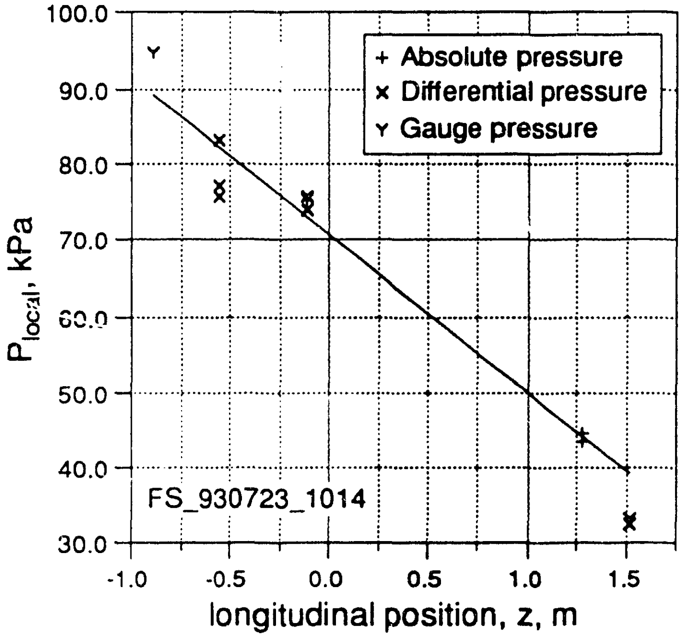

Figure 63, Isothermal longitudinal pressure gradient for open channel from File FS_930723_1014 (Construction 4.0, T_{in} = °C, ϕ = 0.0 kW/m^2, Q = 1077.6 cm^3/s, p_{ehl} = kPa)

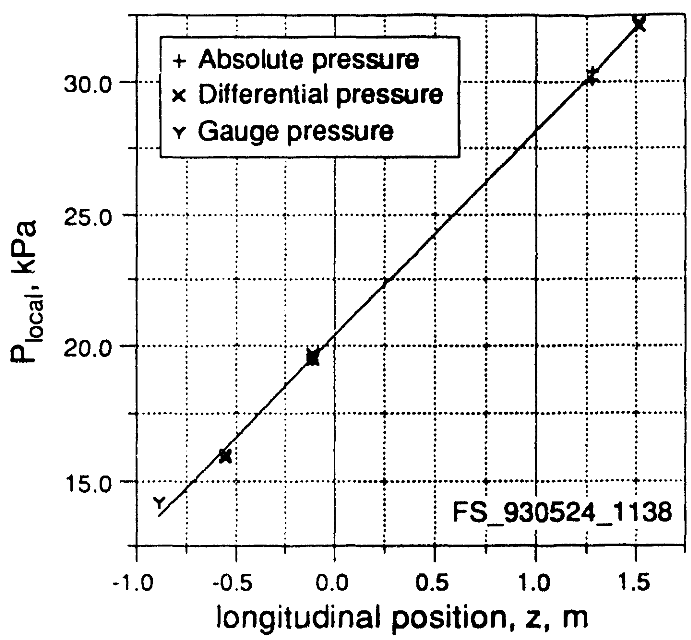

Figure 64, Isothermal longitudinal pressure gradient for open channel from File FS_930524_1138 (Construction 2.0, T_{in} = °C, ϕ = 0.0 kW/m^2, Q = low flow cm^3/s, p_{ehl} = kPa)

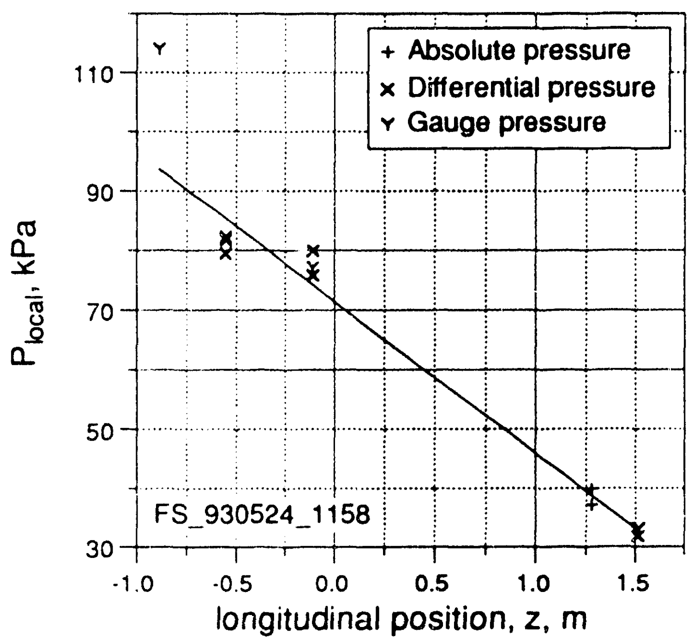

Figure 65, Isothermal longitudinal pressure gradient for open channel from File FS_930524_1158 (Construction 2.0, T_{in} = °C, ϕ = 0.0 kW/m^2, Q = high flow cm^3/s, p_{ehl} = kPa)

Figures 64 and 65 provide pressure profiles for similar conditions to those in Figures 62 and 63 and allow a comparison of the channel behavior with and without a rib. There is little variation between the pressures measured by PD02472 and PD22472 at the lower flows. At higher flows some variation does occur but the effect is not significant enough to allow a conclusion.

Effective Channel Diameter

Two different methods were used to estimate the hydraulic diameter. Figure 66 presents the friction factor demand curve where the effective channel diameter has been estimated using the effective diameter defined by Equation 25. The results do not approach that expected for a smooth channel. The hydraulic diameter calculated using Equation 24 was used to produce Figure 67. The results for Constructions 3.0 and 4.0 compare favorably with smooth channel behavior. Since the channel geometry of Construction 1 was selected to match the friction factor demand curves of the other open channel data sets their results are expected.

The friction factor for the ribbed channel was higher than the open channel for any given flow conditions. This would be expected since flow between the subchannels was observed. This flow between subchannels would probably increase the turbulence near the rib and result in an increase in non-recoverable losses. A linear fit of the data in Figure 67 was made for each construction. Equation 85 provides the final form for this fit. The results are presented in Table 33. The results agree very well with Equation 22.

(85) $$f = C_1 \, Re^{C_2}$$

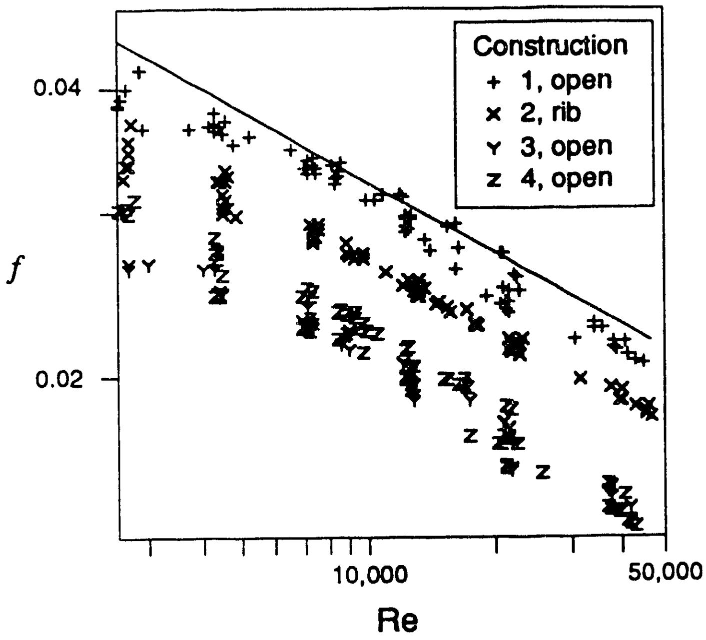

Figure 66, Isothermal friction factor demand curves based on equivalent diameter calculated using Equation 25.

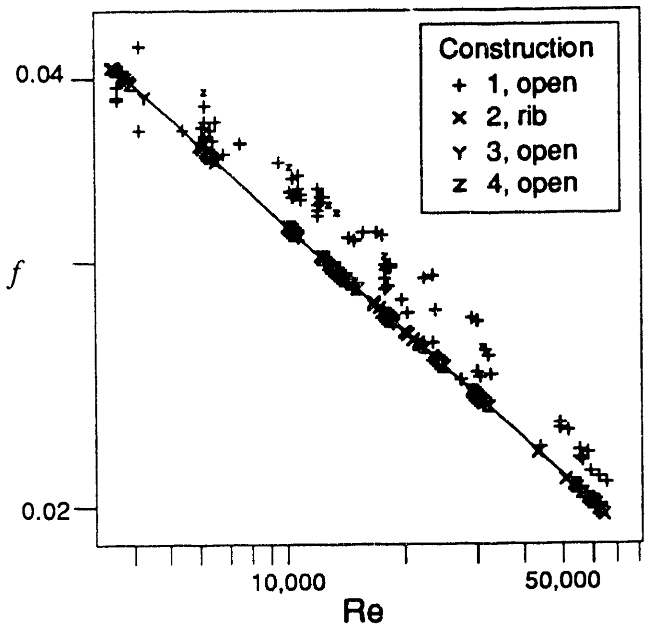

Figure 67, Isothermal friction factor demand curves based on hydraulic diameter calculated using Equation 24.

Table 33.--Isothermal demand curve fits

Construction	Geometry	C1	C2
1	open	0.28905	-0.23520
2	rib	0.25625	-0.22542
3	open	0.26566	-0.22996
4	open	0.38427	-0.26657
Equation 22	...	0.316	-0.25

Heater Inspection

After disassembly of Construction 3 the heater was visually inspected. The heater portion had turned a dull golden color. With just two exceptions the discoloration increased uniformly along the longitudinal axis. Highlights of the inspection are presented in Figure 68. The discoloration at the end of the heated length did not stop abruptly. Discoloration occurred downstream of the end of the heated length. This is probably the result of axial conduction in the heater and the high water temperature in this region. A detailed discussion of the heated area dimensions is included in Appendix 1.

Diabatic Test Results

Nine diabatic demand curves were generated in open channels and four diabatic demand curves in a channel with a longitudinal rib. Two different constructions were tested in the open configuration. The channel depth of these two open channels bracketed the channel depth with a rib present. The rib had a significant effect on the heated channel behavior. The presence of a longitudinal rib increased the flow at the demand curve minimum when compared with an open channel of similar construction. This is shown in Figures 69 and 70. Figure 69 shows a typical overall demand curve for

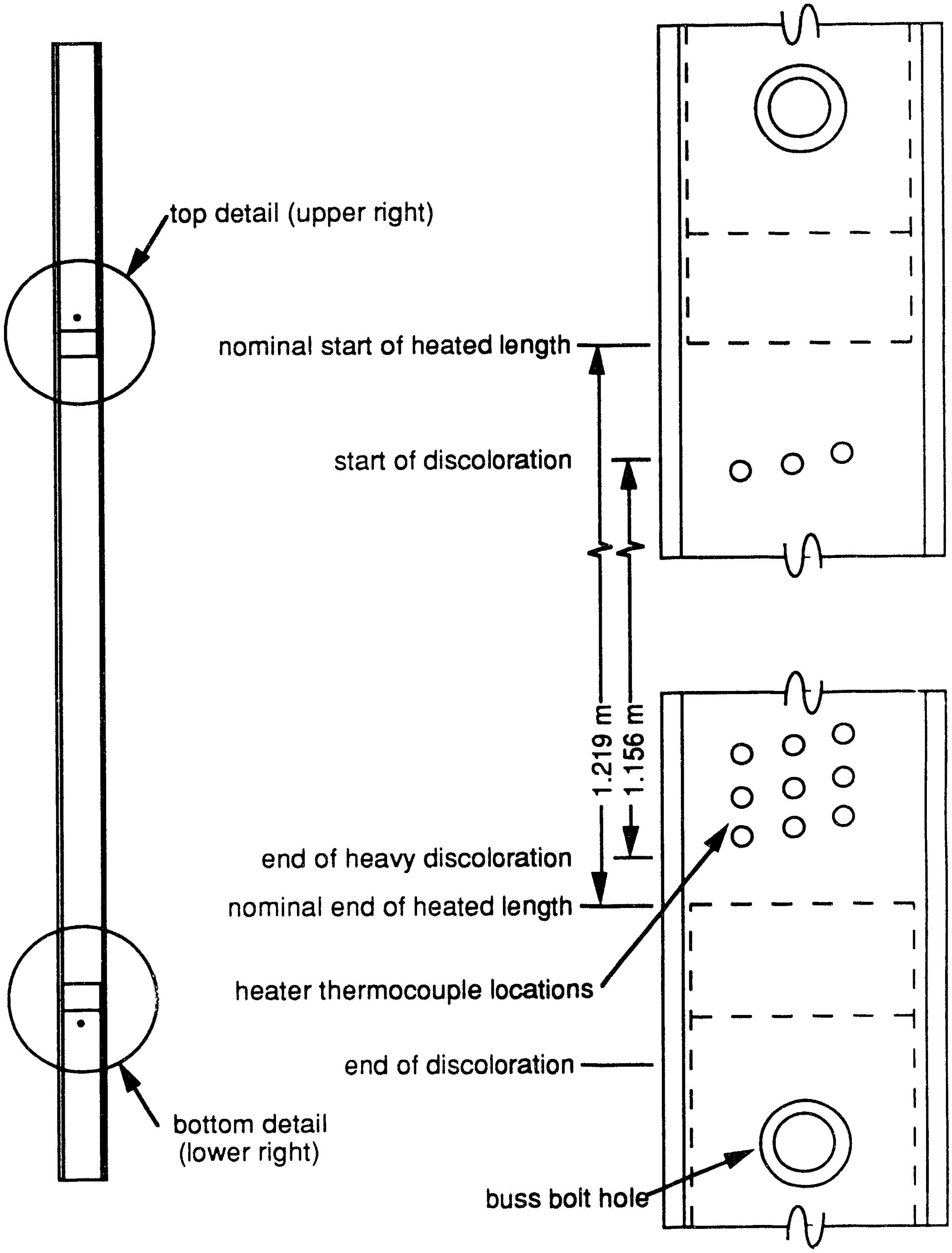

Figure 68. Heater inspection results

Constructions 2.0 and 4.0. The demand curve minimum for the ribbed channel occurs at a higher flow rate in the ribbed channel than for the open channel.

Demand Curve Comparisons

The Q_{ratio} demand curve is presented in Figure 71 for the three constructions. As has been seen in other work the demand curve shifts up for higher power levels (compare demand curves 3.003 and 4.001). The minima region for Figure 71 is presented in Figure 72. The Q_{ratio} at the demand curve minimum for Construction 2.0 (demand curve 2.004) and Construction 4.0 (demand curve 2.009) do not vary significantly. This follows the theory that the Q_{ratio} is dependent on the heat L/D rather than the hydraulic L/D.

A comparison of the diabatic demand curves for Construction 2.0 with the isothermal demand curve indicates little difference in the test section pressure drop for a given flow rate. (See Figure 73.) At flows slightly higher than at OFI the test section pressure drop was slightly lower for diabatic demand curves. This is expected as discussed in Chapter 2. The Q_{ratio} at the demand curve minimum did not vary with a change of heat flux with the longitudinal rib present. (See Figure 75.) The pressure drop multiplier as a function of the Q_{ratio} is presented in Figure 76. There is a general trend that suggests that the multiplier is constant for a given geometry.

Table 34 presents a summary of the OFI data for the thirteen demand curves which were generated. Replication of the demand curves for the three different constructions was very successful. Table 35 presents a summary of the most significant OFI parameters with the applicable uncertainty terms. The presence of the rib tends to decrease the exit temperature, Q_{ratio}, and Stanton number at OFI when compared to the open channels. The Q_{ratio} at OFI for the

Table 34.--Diabatic demand curve OFI conditions

Const.	Curve number	Date	T_{inlet} °C	p_{EHL} kPa abs	Heat flux kW/m²	OFI Conditions				
						T_{exit} °C	Flow cm³/s	Q_{ratio}	St #	Pe #
1	2.001	5/10/93	57.86	129.62	325.67	93.38	215.4	0.772	0.006171	31,877
	2.002	5/11/93	59.91	129.62	328.70	96.60	213.4	0.778	0.008223	31,499
	2.003	5/11/93	59.38	129.42	328.88	95.73	216.7	0.763	0.007514	32,005
	2.004	5/12/93	59.81	129.08	330.05	95.32	221.2	0.754	0.007164	32,720
	Mean	N=4	59.24	129.47	328.3	95.26	216.7	0.767	0.007268	32,025
	S		0.95	0.25	1.9	1.36	3.3	0.011	0.000854	511
2	3.001	5/26/93	59.20	129.9	337.1	88.79	261.5	0.618	0.004080	38,242
	3.002	6/1/93	59.25	129.0	339.0	88.80	259.5	0.620	0.004182	37,944
	3.003	6/1/93	59.32	128.9	338.7	88.89	262.1	0.622	0.004162	38,327
	Mean	N = 3	59.26	129.3	338.3	88.83	261.0	0.620	0.004141	38,171
	S		0.06	0.5	1.0	0.06	1.4	0.002	0.000054	201
	4.001	6/3/93	59.66	129.7	577.3	88.93	439.2	0.617	0.004203	64,210
4	5.001	7/7/93	60.42	126.3	328.7	94.23	254.3	0.737	0.006527	37,403
	2.006	7/12/93	59.60	126.1	328.1	95.31	211.3	0.765	0.008641	31,079
	2.007	7/15/93	59.40	129.4	326.4	95.09	211.6	0.750	0.007891	31,120
	2.008	7/16/93	59.32	129.3	329.1	95.34	209.7	0.756	0.008210	30,845
	2.009	7/20/93	59.75	129.3	327.6	96.37	208.4	0.775	0.009034	30,635
	Mean	N=4	59.52	128.5	327.8	95.53	210.2	0.761	0.008444	30,920
	S		0.19	1.5	1.2	0.57	1.5	0.011	0.000054	225

Table 35.--Demand curve minimum results (nominal conditions: T_{in} = 60°C, P_{ehl} = 130 kPa, P = , ϕ_{open} = 330 kW/m^2, ϕ_{rib} = 340 kW/m^2)

	Const.	Mean	P	B	U
T_{exit}, °C	1	95.26	2.16376	0.50	2.22
	2	88.83	0.149060 29	0.50	0.52
	4	95.53	0.90687	0.50	1.04
Flow, cm^3/s	1	216.7	5.3	1.4	5.4
	2	261	3.5	1.4	3.7
	4	210.2	2.4	1.4	2.8
Q_{ratio}	1	0.767	0.018	0.011	0.021
	2	0.620	0.005	0.014	0.015
	4	0.761	0.018	0.011	0.021
Stanton number	1	0.00727	0.00136	0.00079	0.00157
	2	0.00414	0.00013	0.00037	0.00039
	4	0.00844	0.00009	0.00079	0.00079

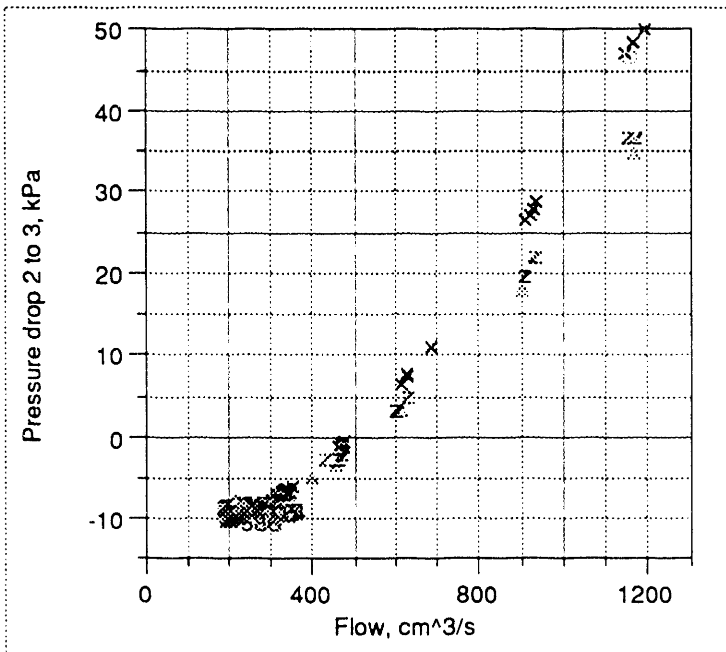

Figure 69, Diabatic demand curve data for Constructions 2.0 and 4.0, T_{in} = 60°C, ϕ_{open} = 330 kW/m^2, ϕ_{rib} = 340 kW/m^2, P = 29 kW, p_{ehl} = 130 kPa

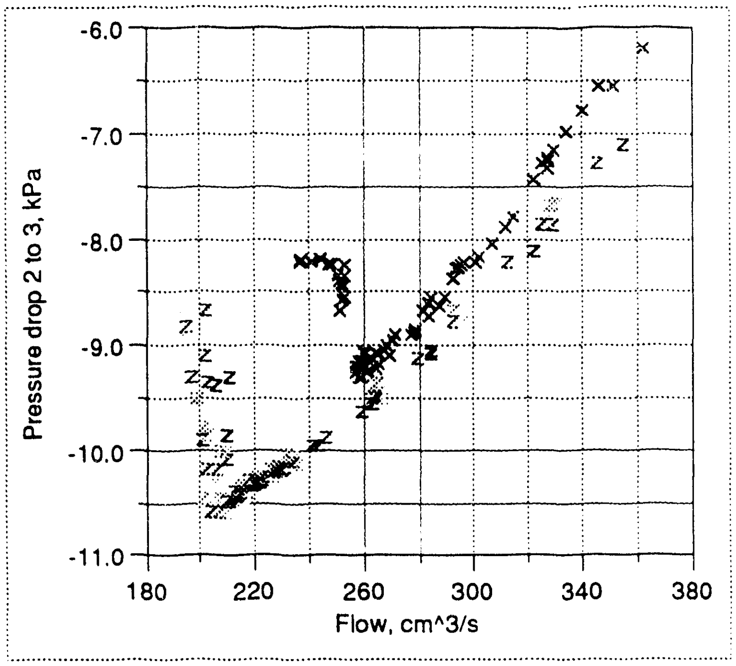

Figure 70, Minima region of the diabatic demand curve data for Constructions 2.0 and 4.0, T_{in} = 60°C, q = 30.5 kW/m^2, p_{ehl} = 130 kPa

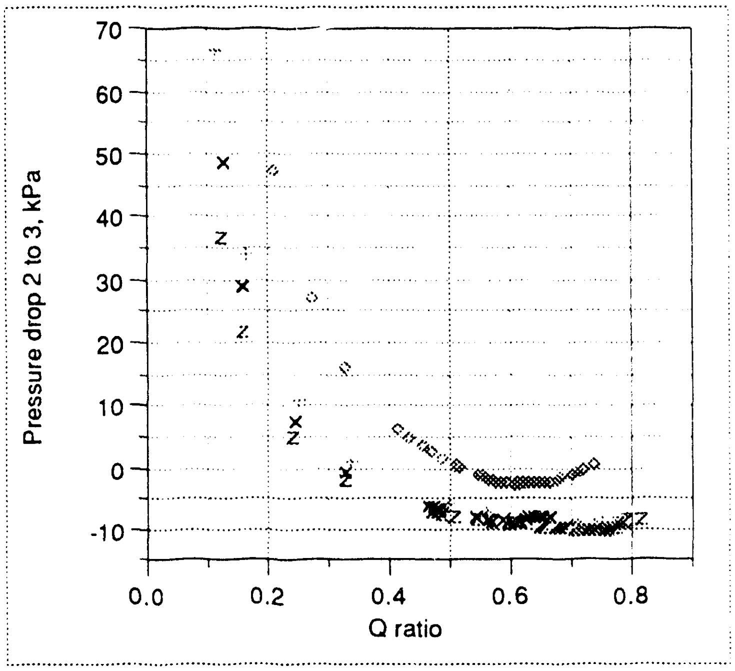

Figure 71, Diabatic demand curve comparisons for Constructions 1.0, 2.0 and 4.0. (Curves 2.004, 2.009, 3.003, and 4.001 are shown)

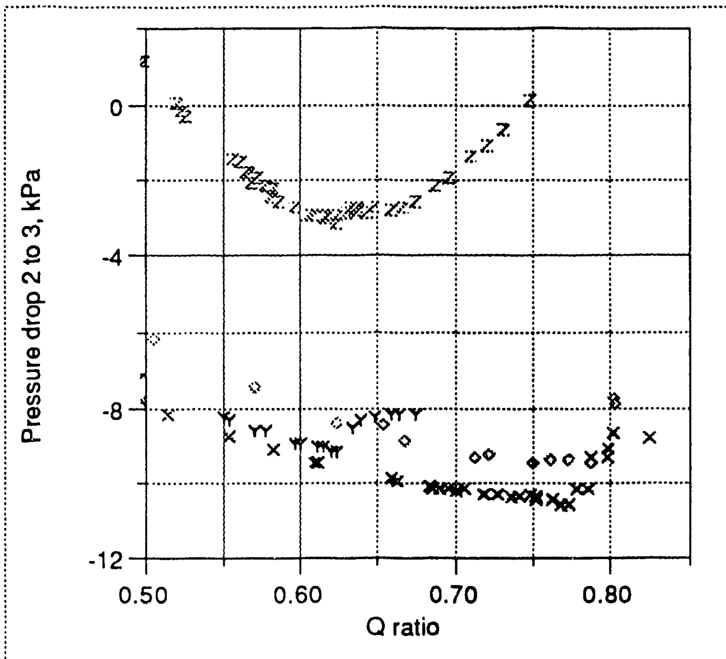

Figure 72, Minima region of the diabatic demand curve comparisons for Constructions 1.0, 2.0 and 4.0. (Curves 2.004, 2.009, 3.003, and 4.001 are shown)

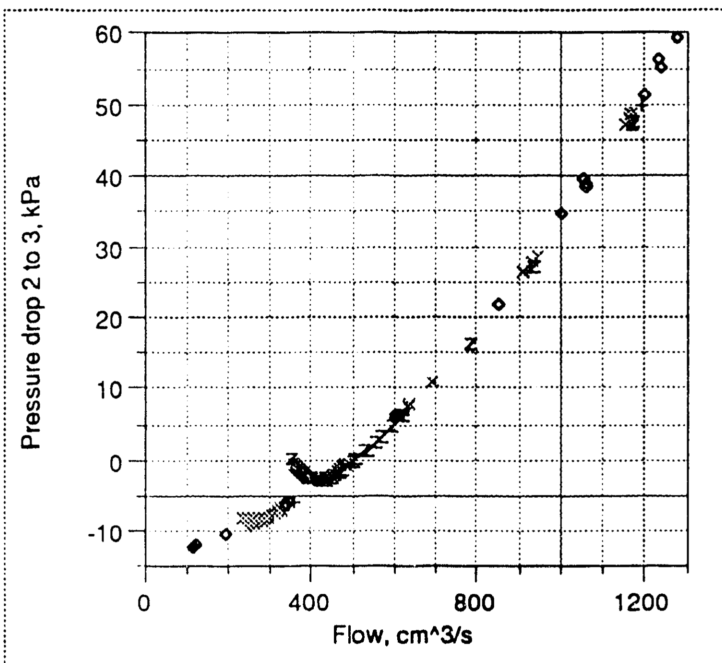

Figure 73, Minima region of the diabatic demand curve comparisons for Constructions 2.0 (Curves 1.000, diamond, 3.001 +, 3.002 X, 3.003 Y, 4.001 Z)

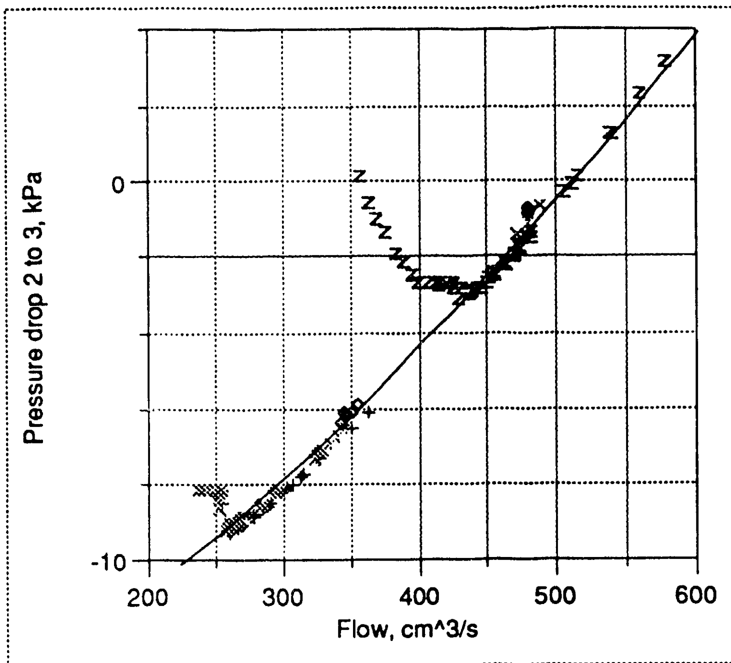

Figure 74, Minima region of the diabatic demand curve comparisons for Constructions 2.0 (Curves 1.000, diamond, 3.001 +, 3.002 X, 3.003 Y, 4.001 Z)

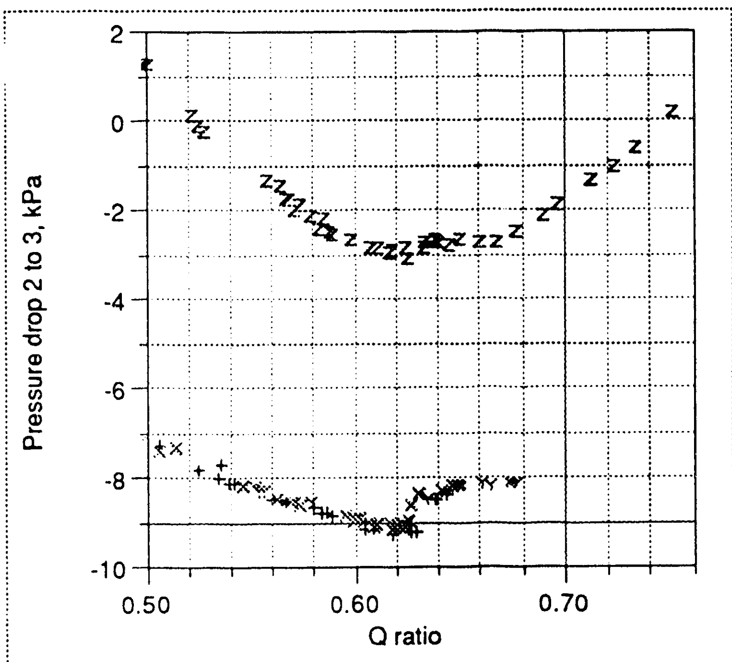

Figure 75, Minima region of the diabatic demand curve comparisons for Constructions 2.0 (Curves 1.000, diamond, 3.001 +, 3.002 X, 3.003 Y, 4.001 Z)

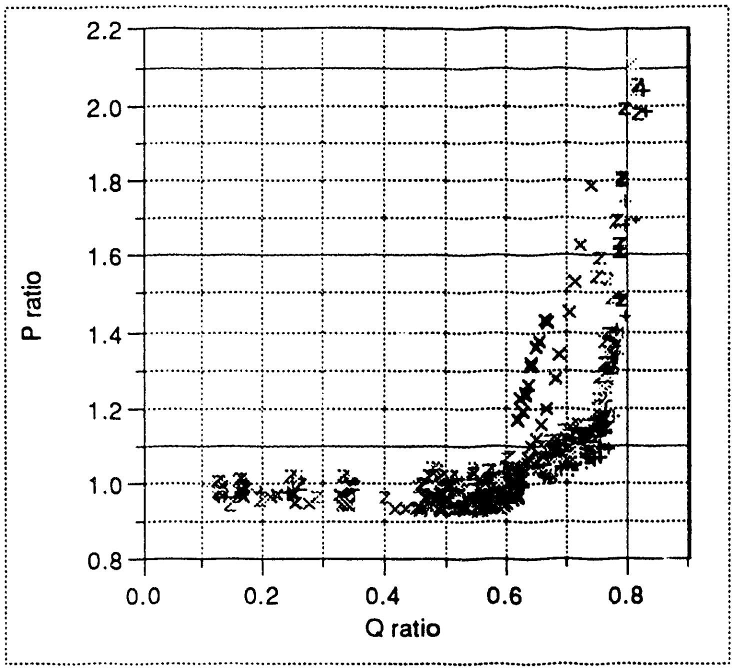

Figure 76, Pressure drop correlation for subcooled boiling

two open constructions was almost identical. For the open channels the Stanton number at OFI was lower for the rib with the smaller depth (Construction 1).

Q_{ratio} rib-effect-ratio

The Q_{ratio} rib-effect-ratio for channel with the longitudinal rib (Construction 2) when compared with the open channel (Construction 2) is 0.817. Equation 86 presents the random uncertainty estimate for this rib-effect-ratio.

$$(86) \qquad P_{\eta} = \left\{ \left[\frac{\partial \eta}{\partial Q_{ratio,\ rib}} P_{ratio,\ rib} \right]^2 + \left[\frac{\partial \eta}{\partial Q_{ratio,\ open}} P_{ratio,\ open} \right]^2 \right\}^{1/2}$$
$$= \left\{ [(1.318)(0.005)]^2 + [(-1.076)(0.018)]^2 \right\}^{1/2}$$
$$= 0.020$$

The partial differential solutions presented in Equation 86 are estimated in Appendix 3. The total uncertainty of the Q_{ratio} rib-effect-ratio would then be:

$$U_\eta = \{[0.020]^2 + [0.019]^2\}^{1/2} = 0.028 \tag{87}$$

If no rib effect existed the Q_{ratio} rib-effect-ratio would be 1. Since the rib-effect-ratio is less than unity by more than the uncertainty calculated in Equation 87 a longitudinal rib effect is considered to exist.

Stanton number rib-effect-ratio

The Stanton number rib-effect-ratio for channel with the longitudinal rib (Construction 2) when compared with the open channel (Constriction 2) is 0.490. The random uncertainty estimate for this rib-effect-ratio is calculated as was done for the Q_{ratio} rib-effect-ratio.

$$\begin{aligned} P_\eta &= \left\{\left[\frac{\partial\eta}{\partial St_{rib}} P_{ratio,\,rib}\right]^2 + \left[\frac{\partial\eta}{\partial St_{open}} P_{ratio,\,open}\right]^2\right\}^{1/2} \\ &= \{[(118.4)(0.00039)]^2 + [(-58.08)(0.00079)]^2\}^{1/2} \\ &= 0.065 \end{aligned} \tag{88}$$

$$U_\eta = \{[0.065]^2 + [0.026]^2\}^{1/2} = 0.070 \tag{89}$$

If no rib effect existed the Stanton number rib-effect-ratio would be 1. Since the rib effect ratio is less than unity by more than the uncertainty calculated in Equation 89 a longitudinal rib effect is considered to exist.

Pressure Profiles

Pressure profiles for Construction 2 and 4 are presented in Figures 77, 78, 79, and 80. There is no noticeable variation between the duplicate pressure instruments (i.e., PD02472, and PD22472; and PA00072, and PA20072). This indicates that a significant pressure gradient did not exist across the rib. The large difference between the predicted local pressure and the gauge pressure readings shown in Figure 79 may partially be due to an error in the barometric pressure. The gradient parallels the gauge readings near the start of the heated length and at the channel exit. Since the gradient is forced through the mean of the absolute gauges (corrected for barometric pressure) a variation in the barometric pressure could have created the shift.

It does not appear that the installation of a longitudinal rib in a rectangular channel has an unanticipated impact on the pressure gradient during subcooled diabatic flow.

Visual Observations

Open Channel

Bubble nucleation behavior in the open channel was similar to that discussed in the literature. Small vapor bubbles (~ 1 mm in diameter) formed at specific sites along the heated surface. As the flow through the test channel was reduced bubble nucleation would first occur near the end of the heated section. The first nucleation sites would move up (opposite flow) the channel as the flow was further reduced. The vapor nucleation sites were distinct. Vapor bubbles would grow and collapse at specific locations on the heater. These sites seemed to remain consistent for the test program.

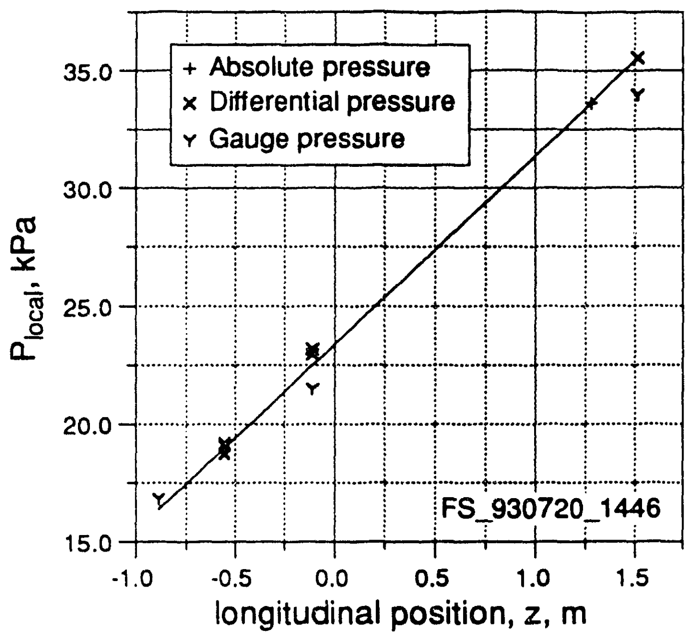

Figure 77, Longitudinal pressure gradient for diabatic open channel (File FS_930720_1446, Construction 4.0, T_{in} = 59.29°C, ϕ = 327.6 kW/m^2, Q = 205.9 cm^3/s, p_{ehl} = 129.2 kPa)

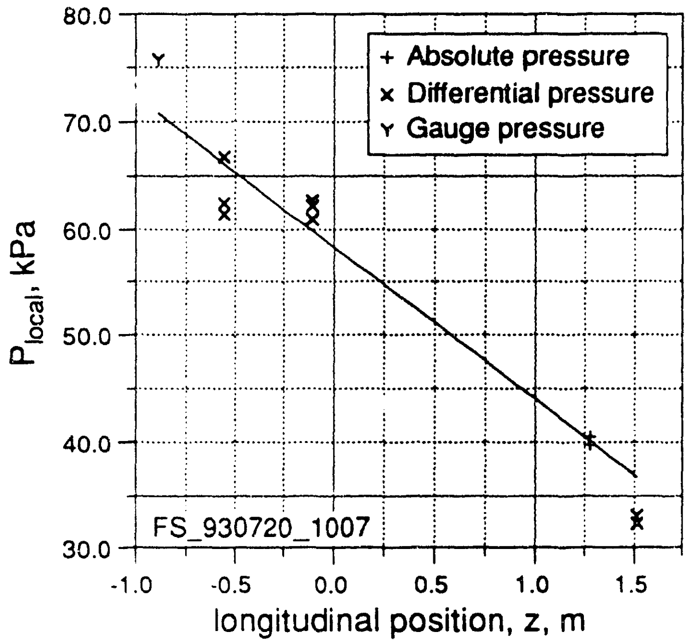

Figure 78, Longitudinal pressure gradient for diabatic open channel (File FS_930720_1007, Construction 4.0, T_{in} = °C, ϕ = kW/m^2, Q = high cm^3/s, p_{ehl} = kPa)

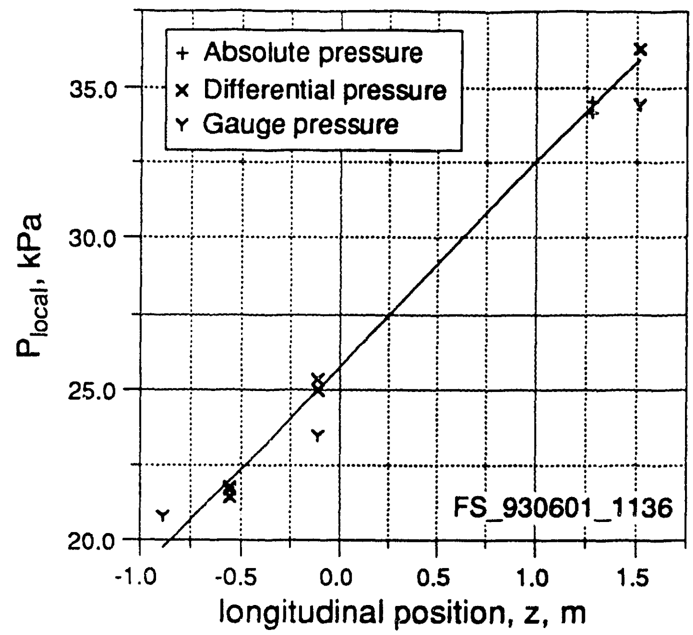

Figure 79, Longitudina' pressure gradient for diabatic open channel with a longitudinal rib (File FS_}300601_1136, Construction 2.0, T_{in} = 59.19°C, ϕ = 330.0 kW/m², Q = 259.5 cm³/s, p_{ehl} = 129.0 kPa)

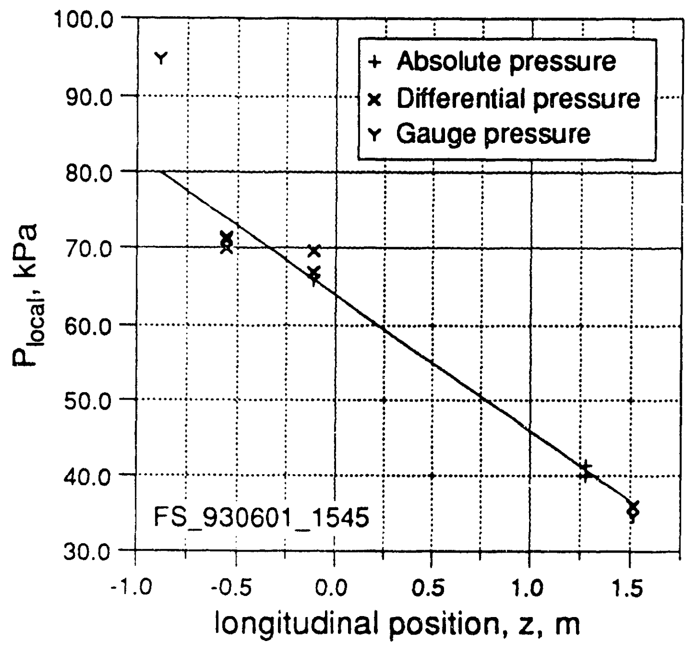

Figure 80, Longitudinal pressure gradient for diabatic channel with a longitudinal rib (File FS_930601_1545, Construction 2.0, T_{in} = °C, ϕ = 0.0 kW/m², Q = high flow cm³/s, p_{ehl} = kPa)

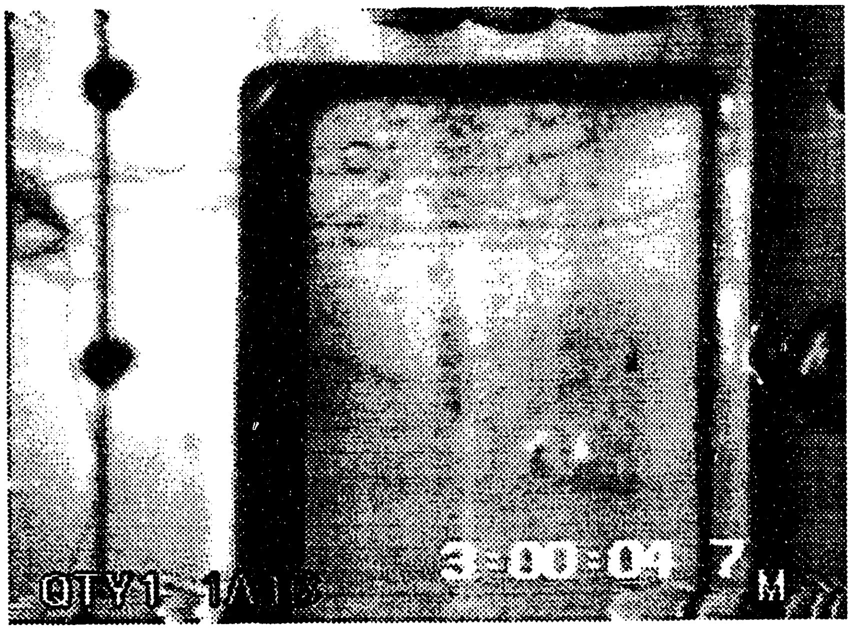

a

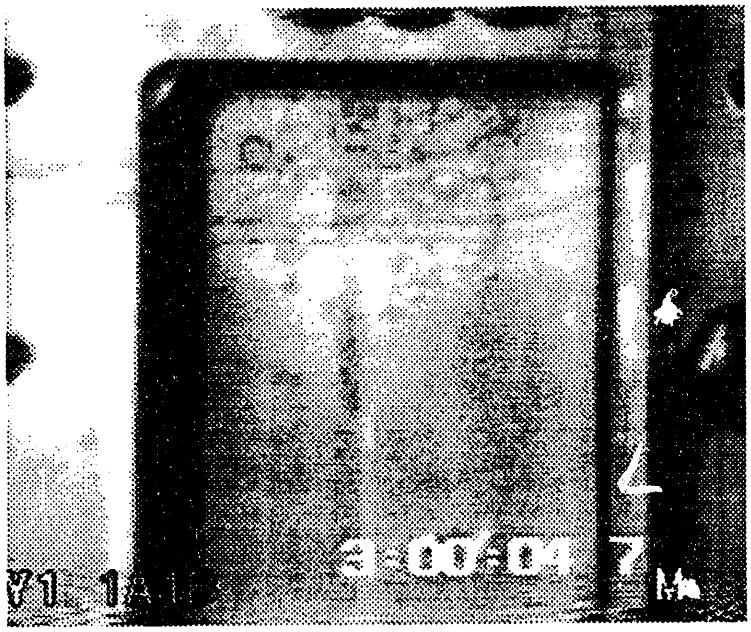

b

Figure 81, Vapor behavior at OFI, Construction 4.0, videotape LFIE-93-11-M, film time 3:00:04.7; a) frame 4, b) frame 5 (File FS_930720_1446, T_{in} = 59.29°C, ϕ = 327.6 kW/m^2, Q = 205.9 cm^3/s, p_{ehl} = 129.2 kPa)

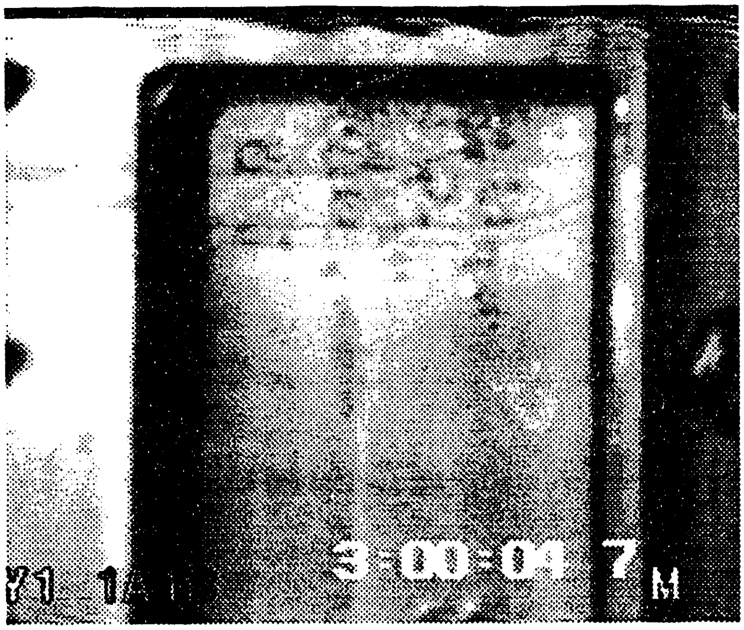

a

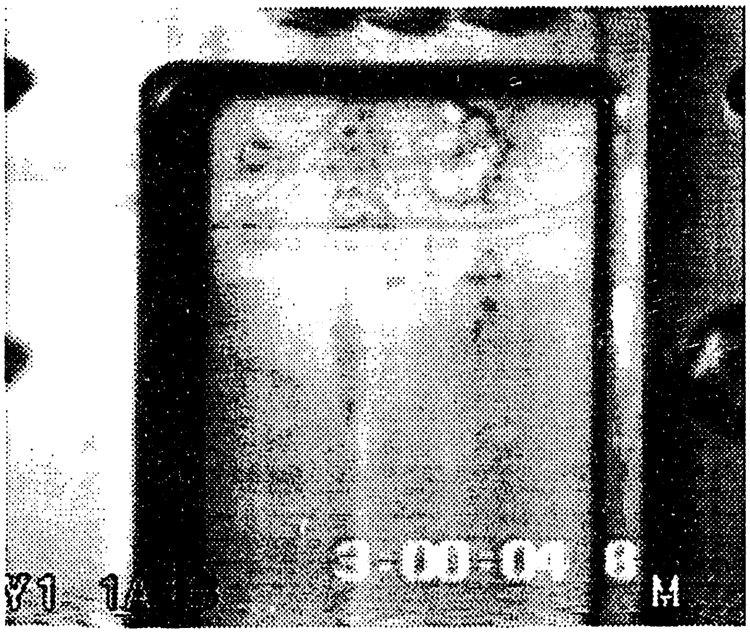

b

Figure 82, Vapor behavior at OFI, Construction 4.0, videotape LFIE-93-11-M: a) film time 3:00:04.7, frame 6, b) film time 3:00:04.8, frame 1 (File FS_930720_1446, T_{in} = 59.29°C, ϕ = 327.6 kW/m^2, Q = 205.9 cm^3/s, p_{ehl} = 129.2 kPa)

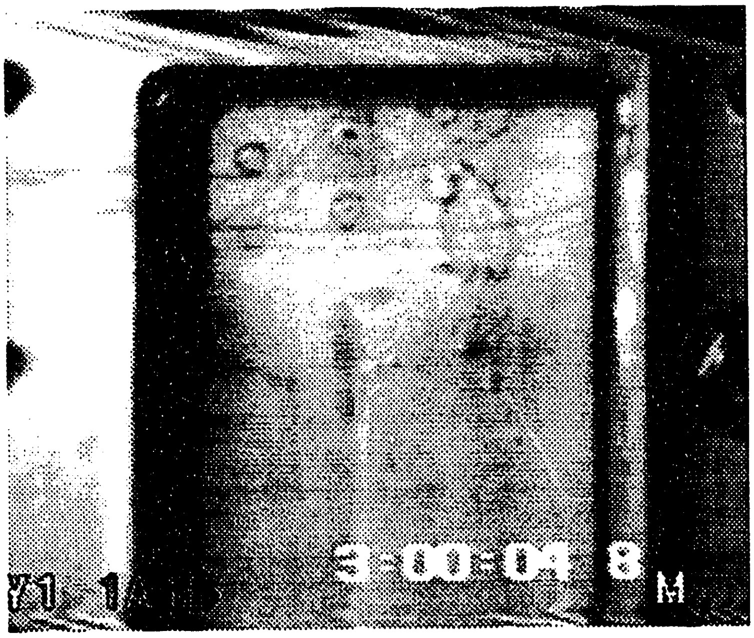

a

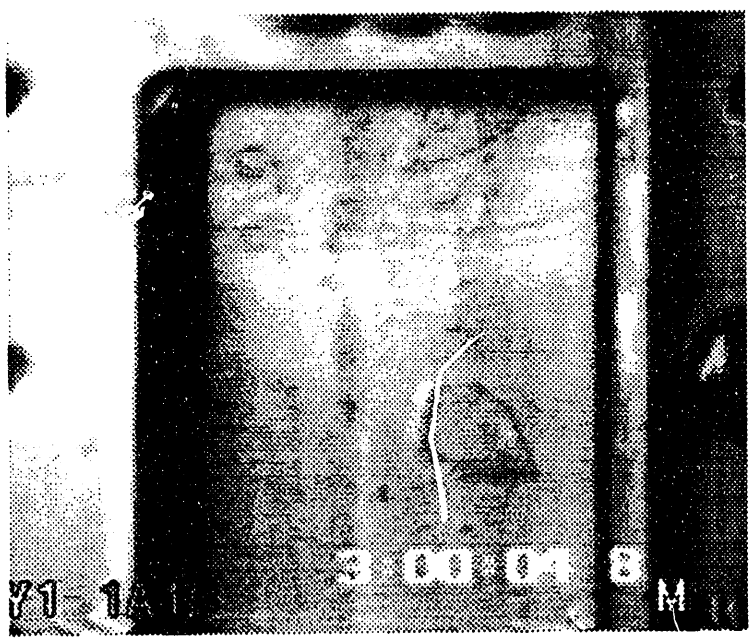

b

Figure 83, Vapor behavior at OFI, Construction 4.0, videotape LFIE-93-11-M, film time 3:00:04.8: a) frame 2, b) frame 3 (File FS_930720_1446, T_{in} = 59.29°C, ϕ = 327.6 kW/m^2, Q = 205.9 cm^3/s, p_{ehl} = 129.2 kPa)

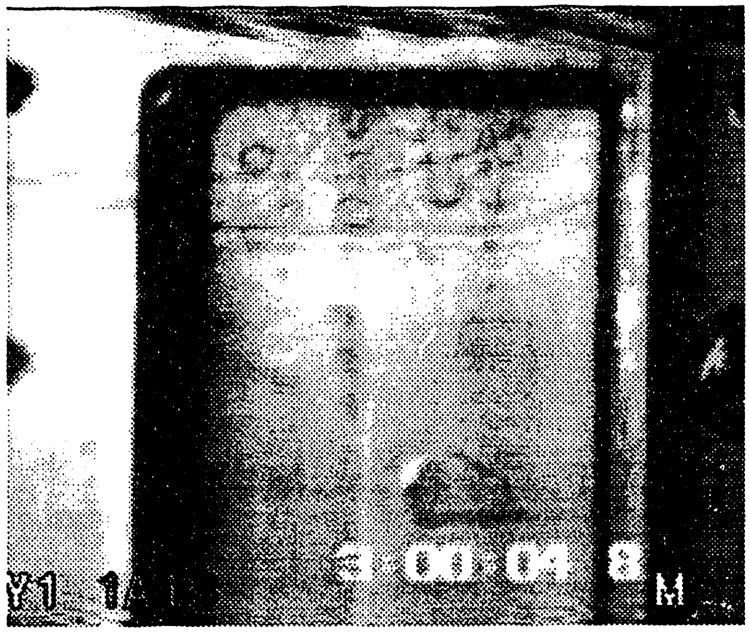

a

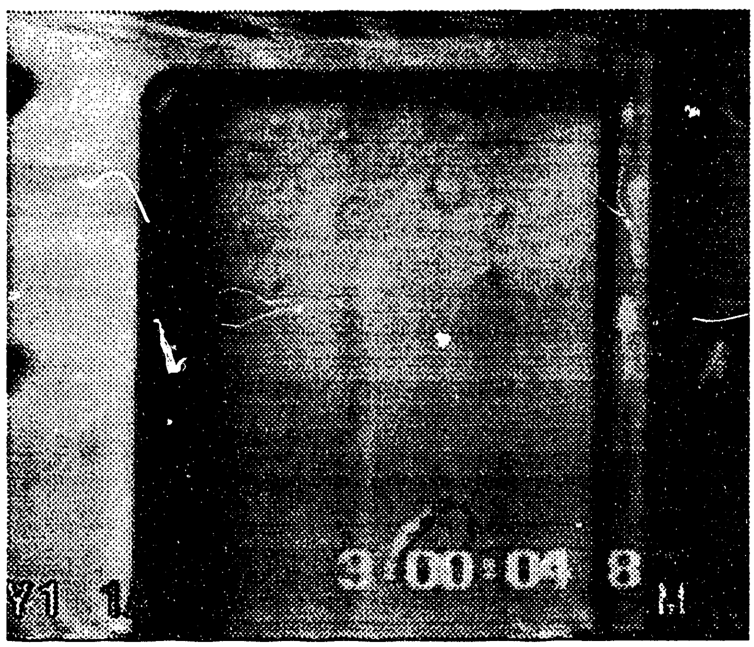

b

Figure 84, Vapor behavior at OFI, Construction 4.0, videotape LFIE-93-11-M, film time 3:00:04.8: a) frame 4, b) frame 5 (File FS_930720_1446, T_{in} = 59.29°C, ϕ = 327.6 kW/m^2, Q = 205.9 cm^3/s, p_{ehl} = 129.2 kPa)

Preliminary Data -- 9 September 1993

Occasionally bubbles formed at the corners of the heated channel where the RTV seal and the hear plate abut. These nucleation sites exhibited a different behavior than the nucleation sites in the free-stream area of the plate. The bubble width was about 1 mm. These bubbles varied in length sometimes exceeding 10 mm. They also appeared to slide along the surface in the direction of flow.

The first signs of vapor departure from the heated surface also occur near the end of the heated section. The bubbles at departure were approximately 1 mm diameter. Departure occurred in two modes. (1) Bubbles would depart the heated surface into the flow at the bubble nucleation site. (2) Bubbles would slide along the heater surface (5 to 20 mm) prior to departing the heated surface.

The boiling behavior at OFI changed appreciably. Near the bottom of the heated section the bubbles departing the heated surface would coalesce, forming distinct large vapor bubbles. These bubbles were approximately 200 mm in diameter with a depth which approached the flow channel depth. These vapor bubbles would then be swept out of the heated region of the test channel where they would collapse. Figures 81, 82, and 83 present as series of photographs which were transcribed from videotape which demonstrate this cyclic nature of this bubble formation. Table 35 presents a description of each frame. Since the film speed is 60 frames per second each frame represents a change of 0.01667 seconds. The bubble in Figure 81a is well formed and moving downward. This bubble is just leaving the field of view in Figure 82a. In Figure 82a vapor departing the heated surface (over the last 100 mm) displays a disorganized pattern different from the discrete nucleation sites described earlier. Emerging from this chaotic pattern discrete bubbles start to form.

Table 35.--Bubble formation sequence for the open channel, Construction 4.0 (File FS_930720_1446, T_{in} = 59.29°C, ϕ = 327.6 kW/m^2, Q = 205.9 cm^3/s, p_{ehl} = 129.2 kPa, videotape LFIE-93-11-M)

Film time	Frame	Figure	Description
3:00:04.7	4	81a	Well-formed bubble on right side of channel approximately 40 mm below the end of the heated length.
	5	81b	Chaotic vapor at end of heated section, original bubble in Figure 81a is moving downward.
	6	82a	Vapor starts to coalesce, original bubble is exiting the field of view.
3:00:04.8	1	82b	Single large bubble starting to form.
	2	83a	All small bubbles are gone, one large bubble is visible at the end of the heated section.
	3	83b	New bubble moves down through channel
	4	84a	Chaotic vapor starts to form at end of heated section. The new bubble is near the position of the original bubble in Figure 81a.
	5	84b	The new bubble continues to travel in the direction of flow.

These discrete bubbles coalesce to form a single bubble in Figure 83a. At this point the heater section over the last 100 mm is relatively free of nucleating bubbles. The vapor formation pattern was cyclic with a frequency of approximately 10 Hz.

Channel with Longitudinal Rib

The installation of a longitudinal rib changed the vapor generation pattern significantly. ONB was first initiated at the corner formed by the heater and rib. Vapor nucleating along this surface would form intermittent bubbles that extended to the end of the heated section. These bubbles were normally less than 15 mm in length. Figure 85 presents two consecutive videotape frames of nucleate boiling behavior. A description of these frames is presented in Table 36. Bubbles traveled in the direction of flow along the rib. As they

Table 36.--ONB along rib, Construction 2.0 (File FS_930601_1130, T_{in} = 59.21°C, ϕ = 356.8 kW/m², Q = 265.6 cm³/s, p_{ehl} = 129.1 kPa, videotape LFIE-93-05-M)

Film time	Frame	Figure	Description
38:25:3	4	85a	Vapor bubbles cover most of the region near the end of the heated length (top third of picture).
	5	85b	A gap appears in the bubble flow on the right side of the rib, near the heated length. Note the bubble that is in the process of collapsing near the end of the bottom of the picture.

exited the heated section they would collapse. During this bubble movement the rib remained wetted. While the bubble movement was intermittent, it did not appear to be cyclic.

As flow was decreased bubble nucleation sites on the free-stream portions of the heated plate would be activated. These nucleation sites exhibited the same boiling behavior as the nucleation sites in the open channel.

The bubble movement at OFI was distinctly different from that observed for the open channel. Figures 86 through 89 provide as series of videotape stills for the flow channel with the longitudinal rib. Long bubbles would slide along the rib in the direction of flow. These bubbles would separate from the rib and start to form fronts which as shown in Figure 86b. The cross section of the bubble at the end of the heated length would vary from about 1 mm to the 15 mm shown in Figure 89a. During this variable bubble formation the rib remained wetted. In some cases the flow was reduced below the OFI flow such that more than half the flow channel was filled with vapor. The vapor tended to travel along the rib while the liquid moved on the outer edges of the channel. Even under this demanding condition the rib visually appeared to remain wetted.

Table 37.--Bubble formation sequence along a rib, Construction 2.0 (File FS_930601_1136, T_{in} = 59.19°C, ϕ = 330.0 kW/m^2, Q = 259.5 cm^3/s, p_{ehl} = 129.0 kPa, Video tape LFIE-93-05-M)

Film time	Frame	Figure	Description
46:36:3	2	86a	Left side of rib at end of heated section has minimal amount of vapor, right side has large vapor bubble moving down the channel
	3	86b	Vapor staring to coalesce in left channel, vapor bubble exiting heated section right channel
	4	87a	Vapor is still coalescing on the left side of the rib while there is little vapor on the right side
	5	87b	Both sides of the rib are covered by a bubble.
	6	88a	The bubbles are starting to move past the end of the heated length.
46:36:4	1	88b	The large bubbles are exiting the field of view and new bubbles are expanding at the end of the heated length.
	2	89a	The bubbles at the end of the heated length continue to expand.
	3	89b	The expanded bubbles start to exit the heated section.

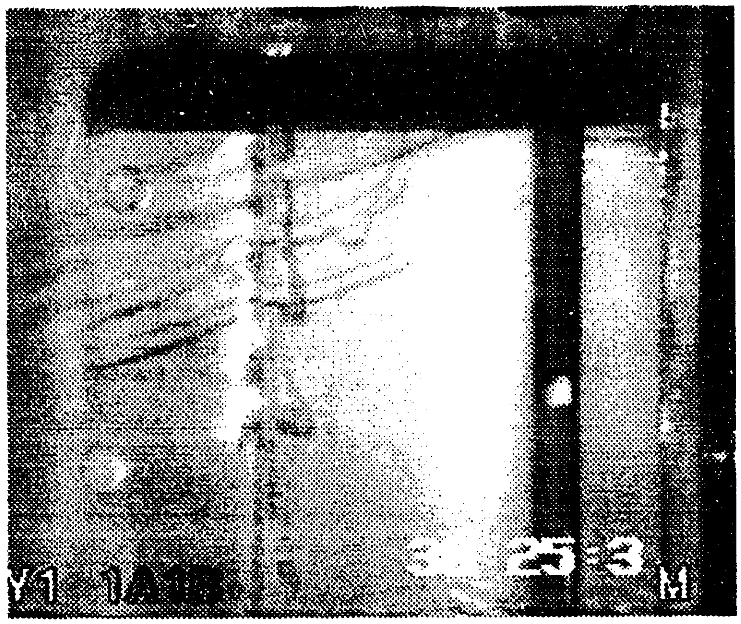

a

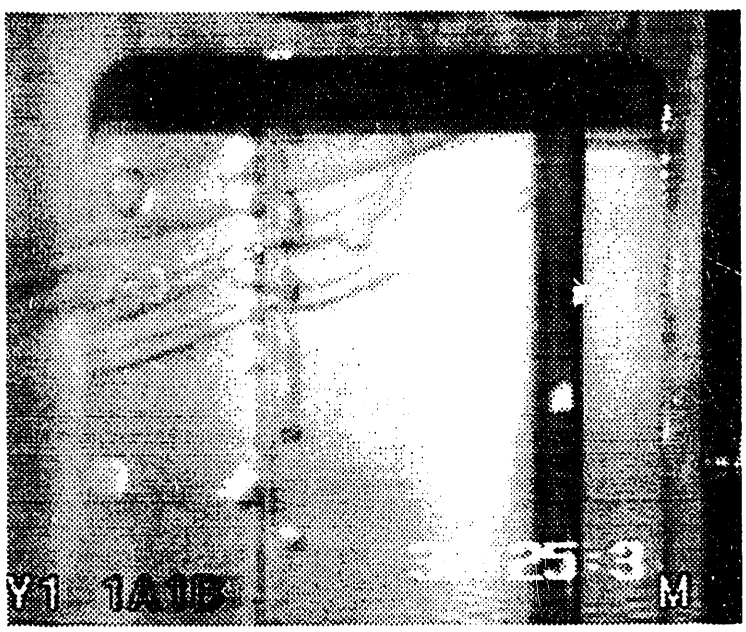

b

Figure 85, ONB along rib, Construction 2.0, videotape LFIE-93-05-M, film time 38:25:3; a) frame 4, b) frame 5 (File FS_930601_1130, T_{in} = 59.21°C, ϕ = 356.8 kW/m^2, Q = 265.6 cm^3/s, p_{ehl} = 129.1 kPa)

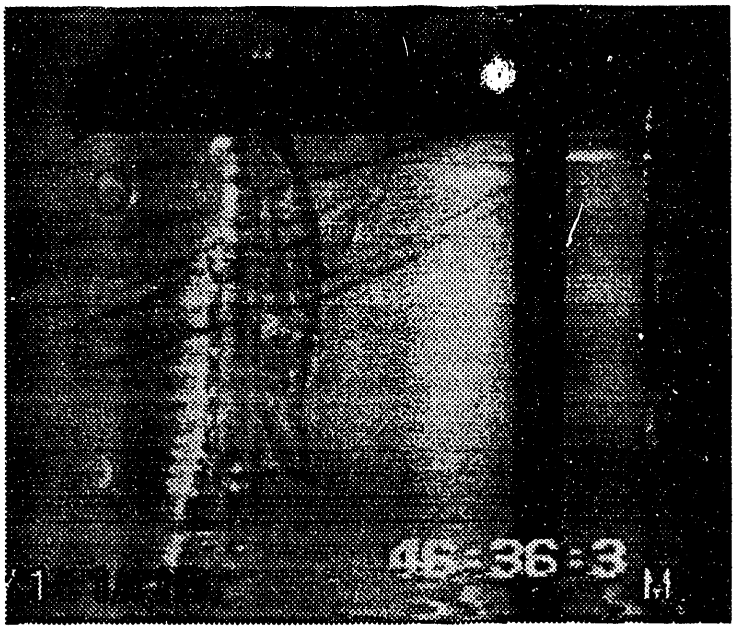

a

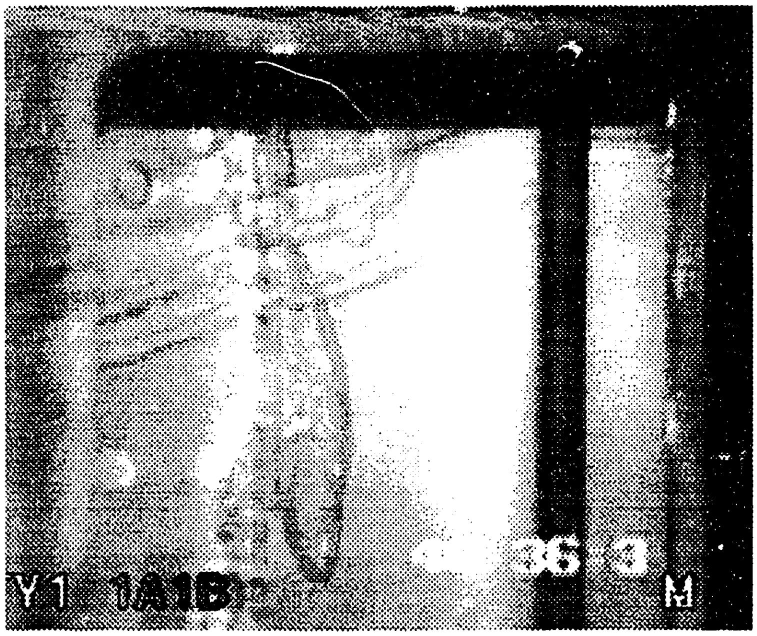

b

Figure 86, Vapor behavior at OFI, Construction 2.0, videotape LFIE-93-05-M, film time 46:36:3; a) frame 2, b) frame 3 (File FS_930601_1136, T_{in} = 59.19°C, ϕ = 330.0 kW/m^2, Q = 259.5 cm^3/s, p_{ehl} = 129.5 kPa)

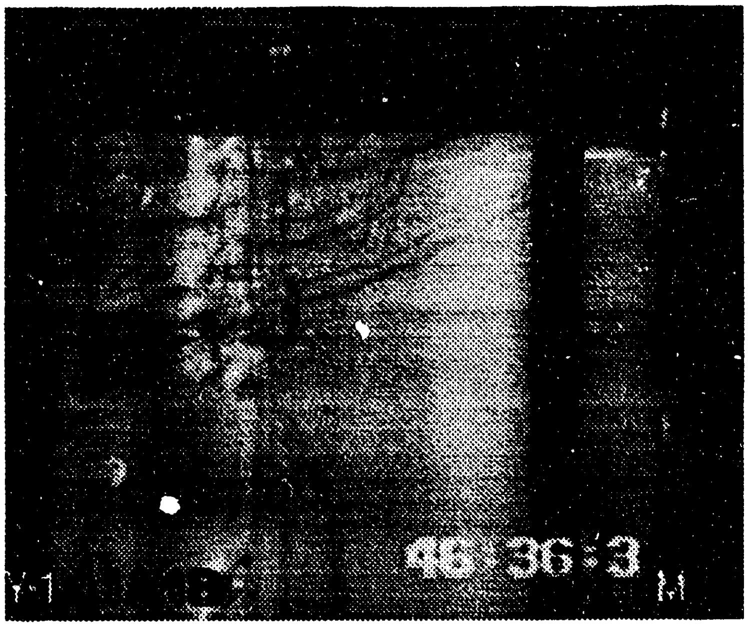

a

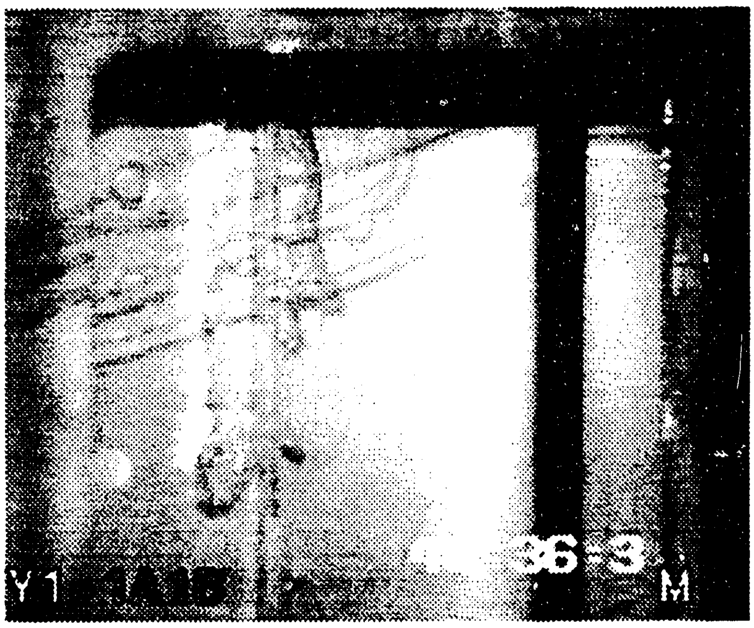

b

Figure 87, Vapor behavior at OFI, Construction 2.0, videotape LFIE-93-05-M, film time 46:36:3; a) frame 4, b) frame 5 (File FS_930601_1136, T_{in} = 59.19°C, ϕ = 330.0 kW/m^2, Q = 259.5 cm^3/s, p_{ehl} = 129.5 kPa)

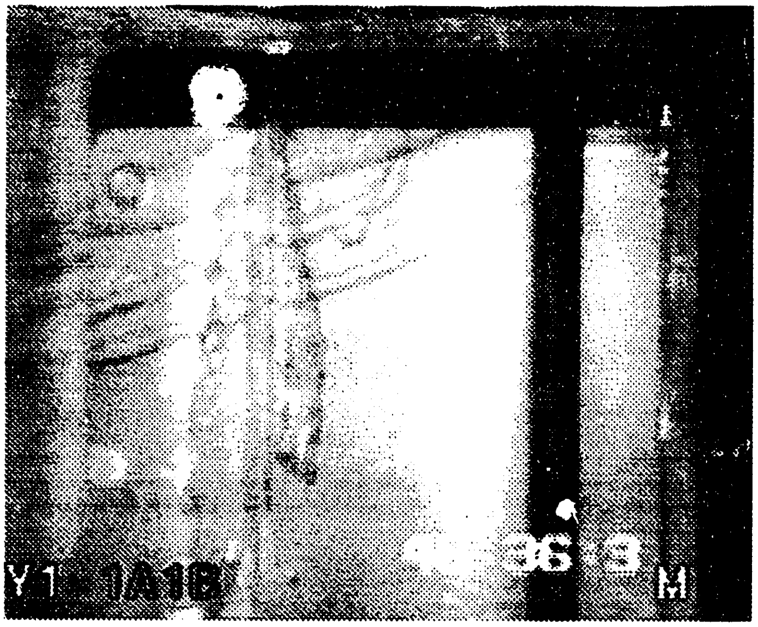

a

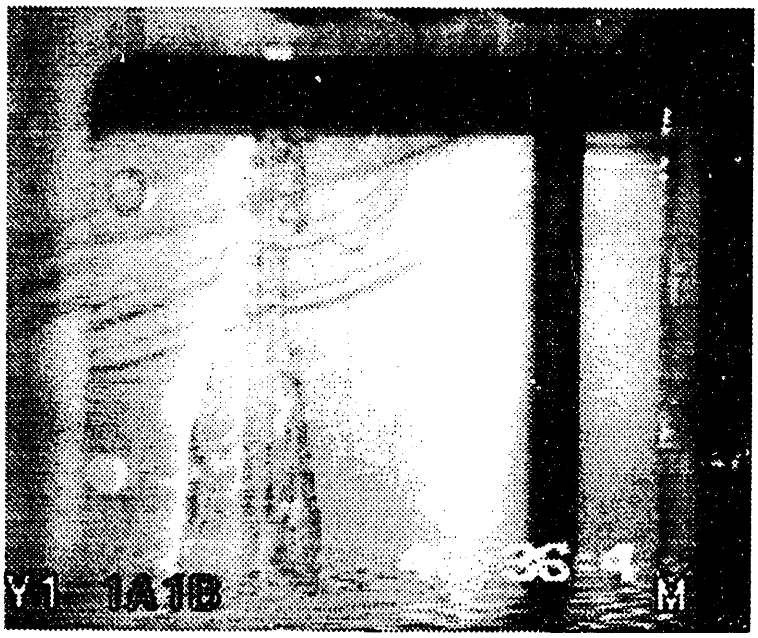

b

Figure 88, Vapor behavior at OFI, Construction 2.0, videotape LFIE-93-05-M, a) film time 46:36:3, frame 6, b) film time 46:36:4, frame 1 (File FS_930601_1136, T_{in} = 59.19°C, ϕ = 330.0 kW/m^2, Q = 259.5 cm^3/s, p_{ehl} = 129.5 kPa)

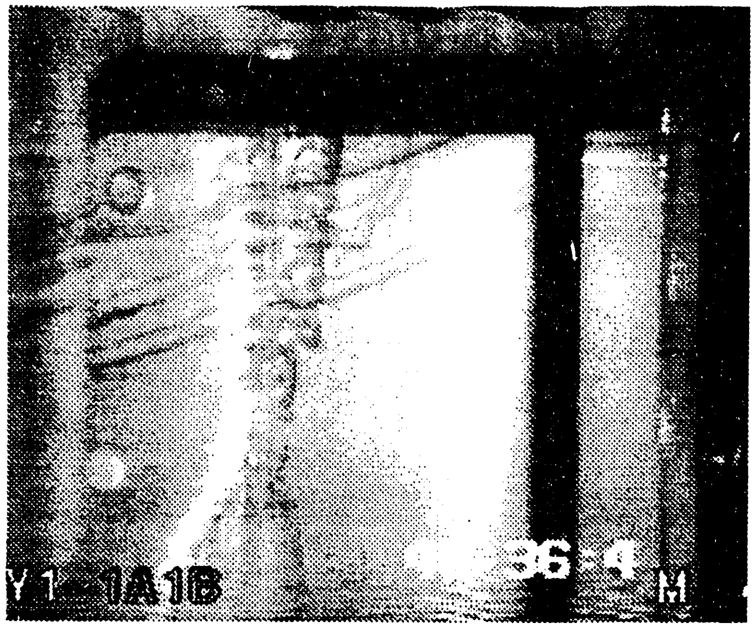

a

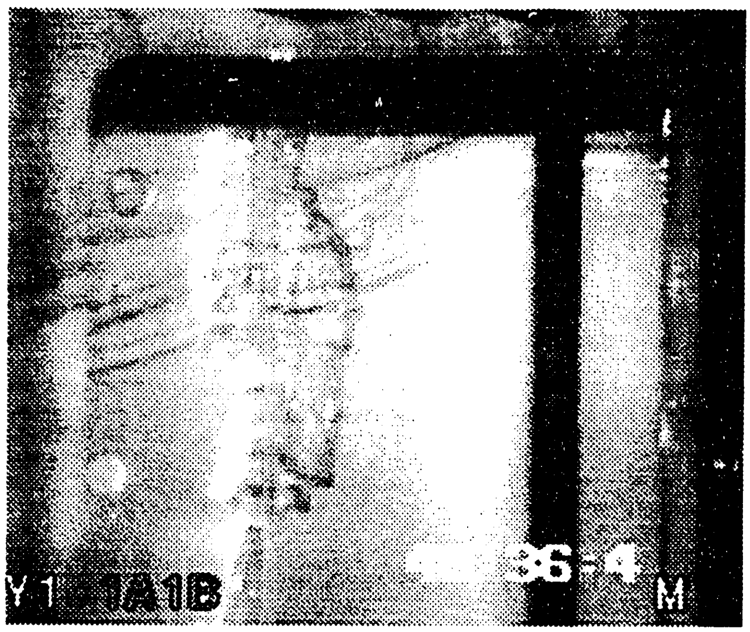

b

Figure 89, Vapor behavior at OFI, Construction 2.0, videotape LFIE-93-05-M, film time 46:36:3; a) frame 2, b) frame 3 (File FS_930601_1136, T_{in} = 59.19°C, ϕ = 330.0 kW/m^2, Q = 259.5 cm^3/s, p_{ehl} = 129.5 kPa)

Temperature Profiles

The heated wall and fluid temperatures were measured in multiple locations during the testing. In general both the fluid, and wall temperatures increased in the longitudinal direction during diabatic flow. As expected the dry side wall temperatures were higher than the wet side wall temperatures when the heater was operating. In addition the wet wall temperatures were higher than the fluid temperatures during diabatic flow. The temperature profiles were basically symmetric in the lateral direction for all of the tests that were reviewed.

Open Channel Temperature Profiles

Figures 90, 91, and 92 present the temperature profile information at the OFI for Curve 2.009. This test was conducted using Construction 4.0, which did not contain any obstructions. The fluid temperature increased along the longitudinal direction. This increase was very close to linear with axial position. This is expected since the fluid density and specific heat vary little with temperature. The wall temperature did not increase consistently in the longitudinal direction. There is a noticeable temperature decrease for the thermocouples between 0.582 and 0.592 m from the SHL. This depression in the longitudinal temperature profile is probably the result of the ONB effect.

Figures 93, 94, and 95 present the temperatures over the last 80 mm of the heated length. The wall temperatures are relatively uniform in both the longitudinal and lateral directions.

Tables 38 and 39 summarize the temperature data from File FS_930720_1446. Differences in the dry wall temperatures were negligible. The wet wall temperature on the left side of the cannel was slightly cooler (~2°C) than the center and right locations. Since the heater spray was applied

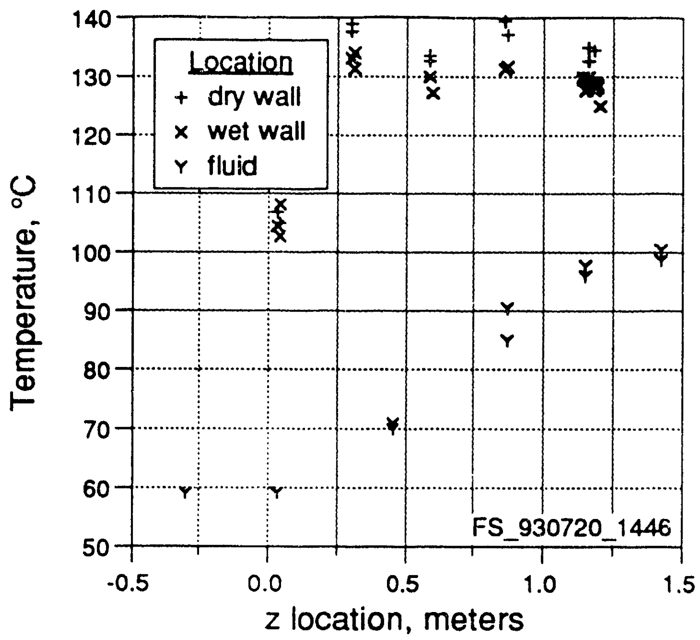

Figure 90, Longitudinal temperature profile from File FS_930720_1446 (Construction 4.0, T_{in} = 59.29°C, ϕ = 327.6 kW/m^2, Q = 205.9 cm^3/s, p_{ehl} = 129.2 kPa)

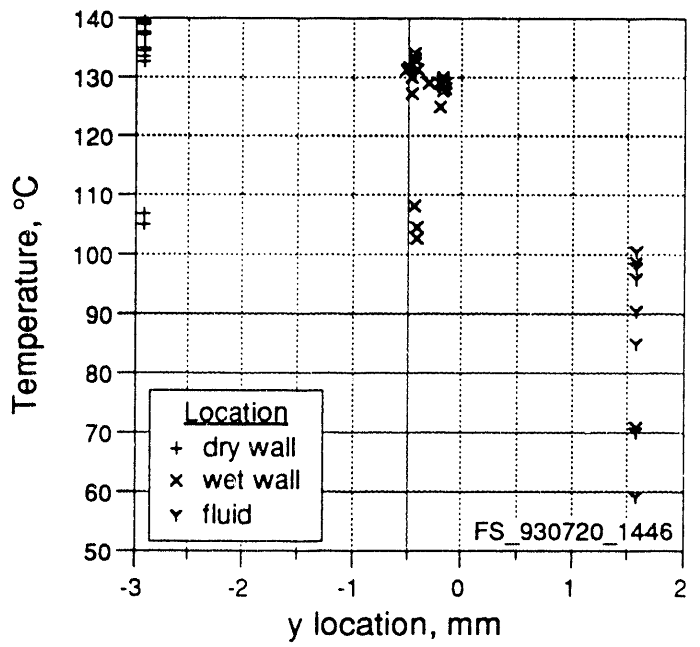

Figure 91, Normal temperature profile from File FS_930720_1446 (Construction 4.0, T_{in} = 59.29°C, ϕ = 327.6 kW/m^2, Q = 205.9 cm^3/s, p_{ehl} = 129.2 kPa)

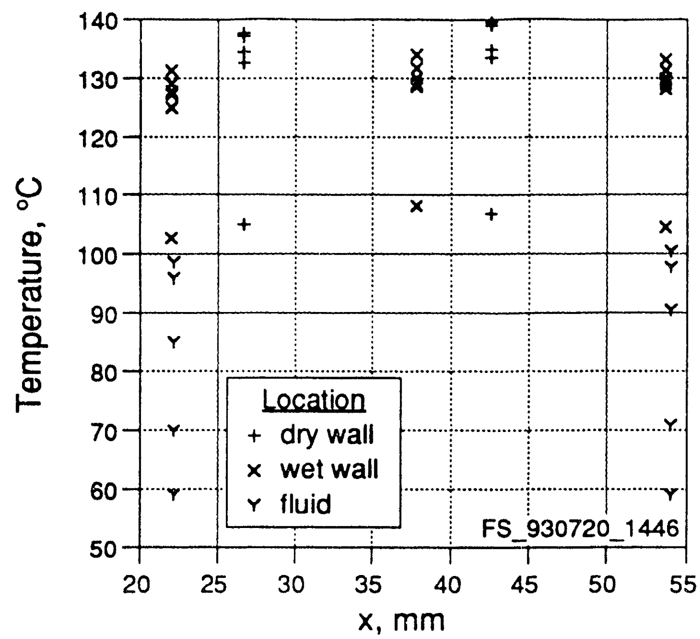

Figure 92, Lateral temperature profile from File FS_930720_1446 (Construction 4.0, T_{in} = 59.29°C, ϕ = 327.6 kW/m^2, Q = 205.9 cm^3/s, p_{ehl} = 129.2 kPa)

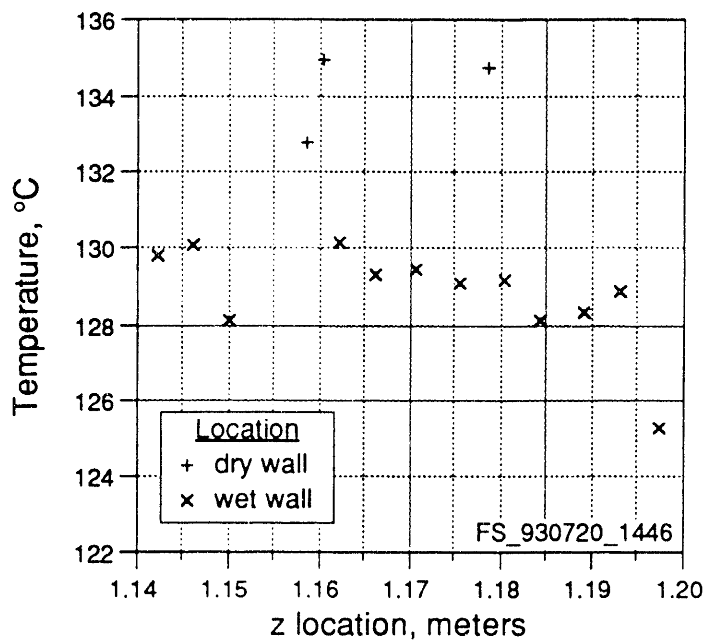

Figure 93, Longitudinal temperature profile at EHL from File FS_930720_1446 (Construction 4.0, T_{in} = 59.29°C, ϕ = 327.6 kW/m^2, Q = 205.9 cm^3/s, p_{ehl} = 129.2 kPa)

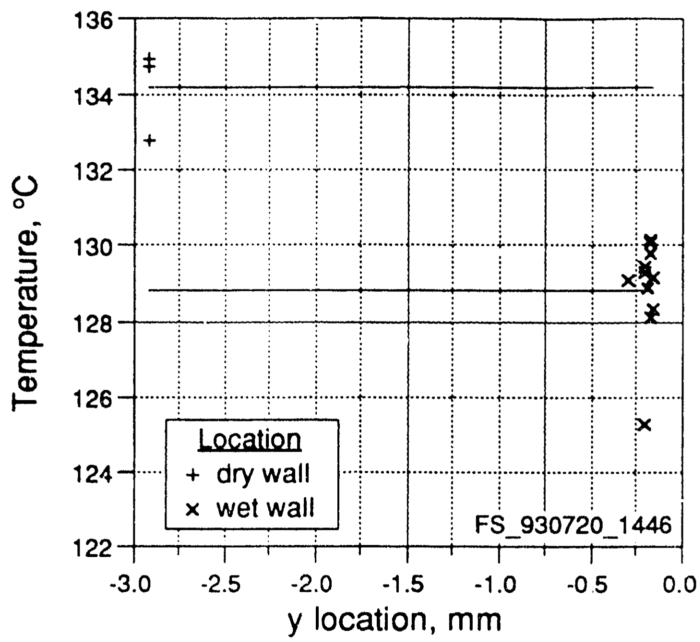

Figure 94, Normal temperature profile at EHL from File FS_930720_1446 (Construction 4.0, T_{in} = 59.29°C, ϕ = 327.6 kW/m^2, Q = 205.9 cm^3/s, p_{ehl} = 129.2 kPa)

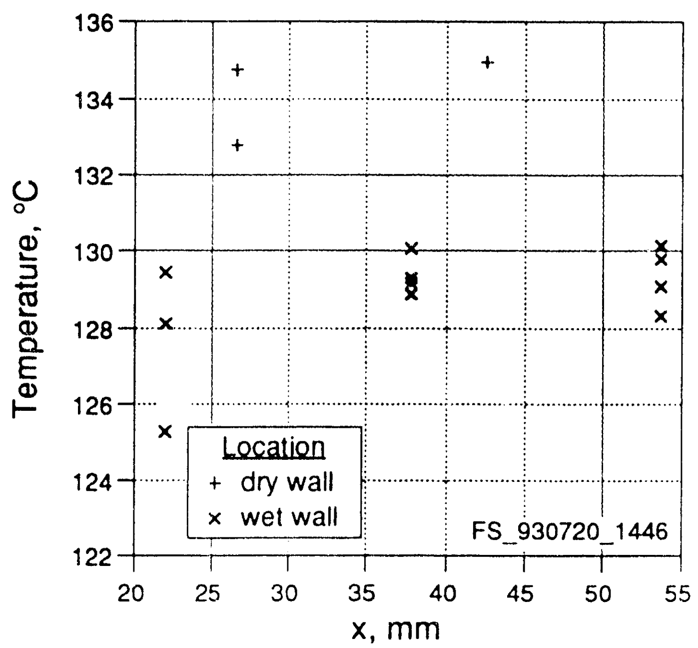

Figure 95, Lateral temperature profile at EHL from File FS_930720_1446 (Construction 4.0, T_{in} = 59.29°C, ϕ = 327.6 kW/m^2, Q = 205.9 cm^3/s, p_{ehl} = 129.2 kPa)

Table 38.--Mean heater temperature based on lateral position from File FS_930720_1446 (Construction 4.0, T_{in} = 59.29°C, ϕ = 327.6 kW/m^2, Q = 205.9 cm^3/s, p_{ehl} = 129.2 kPa)

	N	x mm	$\overline{T}$ °C	S °C	S_m °C
dry	5	26.72	135.25	2.58	1.15
dry	4	42.60	136.91	2.93	1.47
wet	6	21.97	128.37	2.08	0.85
wet	7	37.85	130.61	1.96	0.74
wet	6	53.72	130.50	1.89	0.77
mean, dry	9	...	135.99	2.70	0.90
mean, wet	19	...	129.87	2.14	0.49

Table 39.--Mean heater temperatures based on lateral position over the last 80 mm of the heated length; from File FS_930720_1446 (Construction 4.0, T_{in} = 59.29°C, ϕ = 327.6 kW/m^2, Q = 205.9 cm^3/s, p_{ehl} = 129.2 kPa)

	N	x mm	$\overline{T}$ °C	S °C	S_m °C
dry	2	26.72	133.82	1.42	1.01
dry	1	42.60	135.06	...	...
wet	4	21.97	127.81	1.77	0.88
wet	4	37.85	129.42	0.52	0.26
wet	4	53.72	129.41	0.80	0.40
mean, dry	3	...	134.23	1.24	0.71
mean, wet	12	...	128.88	1.31	0.38

by moving laterally, heater fabrication techniques should not have produced this variation. Further work with plasma spray heater technology is necessary to evaluate if this is the reason for the variation. As expected the dry wall temperature was higher than the wet wall temperature.

Rib Channel Temperature Profiles

Figures 96, 97, and 98 present the temperature profile information at the OFI for Curve 3.002. This test was conducted using Construction 2.0, which included the longitudinal rib. The fluid temperature increased along the longitudinal direction. This increase was very close to linear with axial position. This is expected since the fluid density and specific heat vary little with temperature. The wall temperature did not increase consistently in the longitudinal direction. There is a noticeable temperature decrease for the thermocouples between 0.582 and 0.592 m from the SHL. This depression in the longitudinal temperature profile is probably the result of the ONB effect.

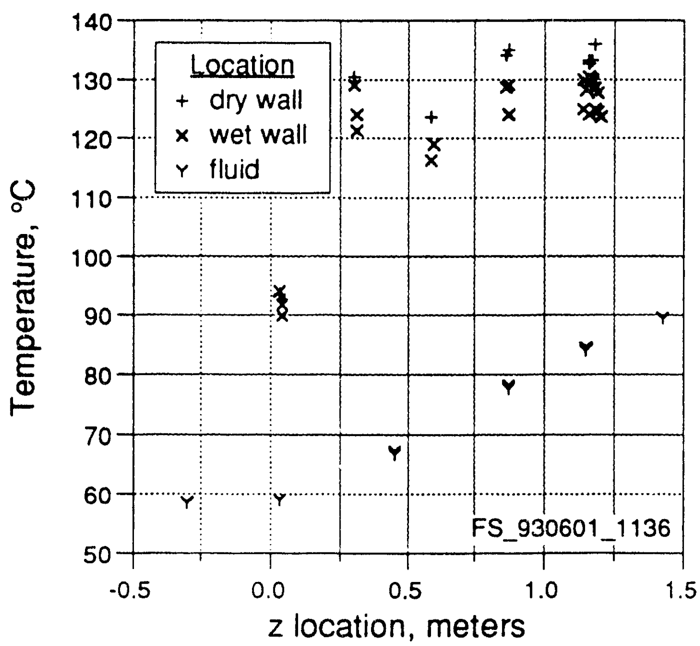

Figure 96, Longitudinal temperature profile from File FS_930601_1136 (Construction 2.0, T_{in} = 59.19°C, ϕ = 330.0 kW/m^2, Q = 259.5 cm^3/s, p_{ehl} = 129.0 kPa)

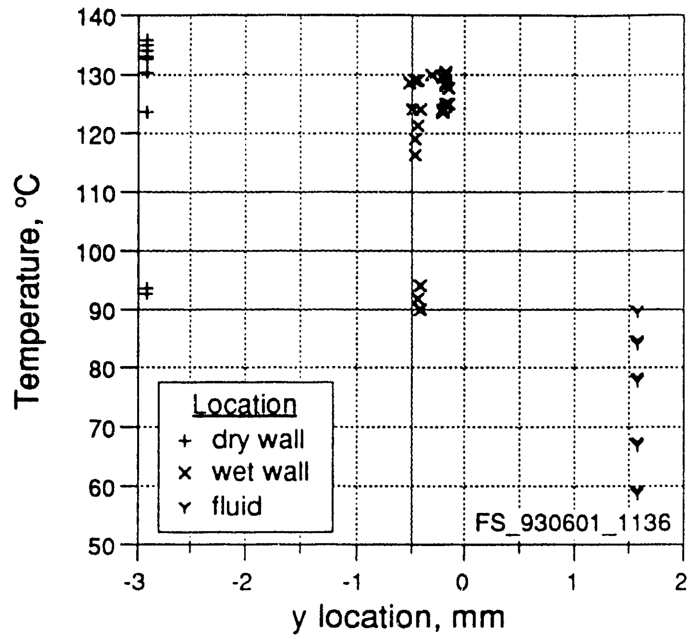

Figure 97, Normal temperature profile from File FS_930601_1136 (Construction 2.0, T_{in} = 59.19°C, ϕ = 330.0 kW/m^2, Q = 259.5 cm^3/s, p_{ehl} = 129.0 kPa)

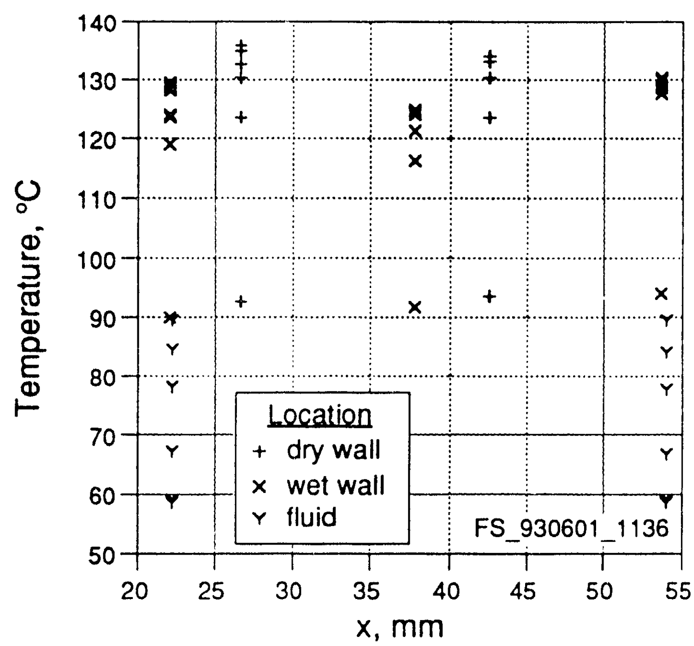

Figure 98, Lateral temperature profile from File FS_930601_1136 (Construction 2.0, T_{in} = 59.19°C, ϕ = 330.0 kW/m^2, Q = 259.5 cm^3/s, p_{ehl} = 129.0 kPa)

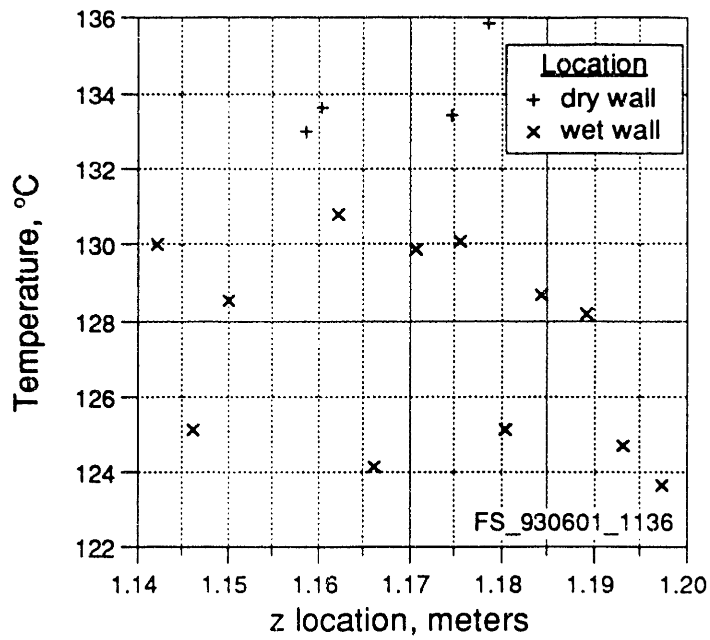

Figure 99, Longitudinal temperature profile at EHL from File FS_930601_1136 (Construction 2.0, T_{in} = 59.19°C, ϕ = 330.0 kW/m^2, Q = 259.5 cm^3/s, p_{ehl} = 129.0 kPa)

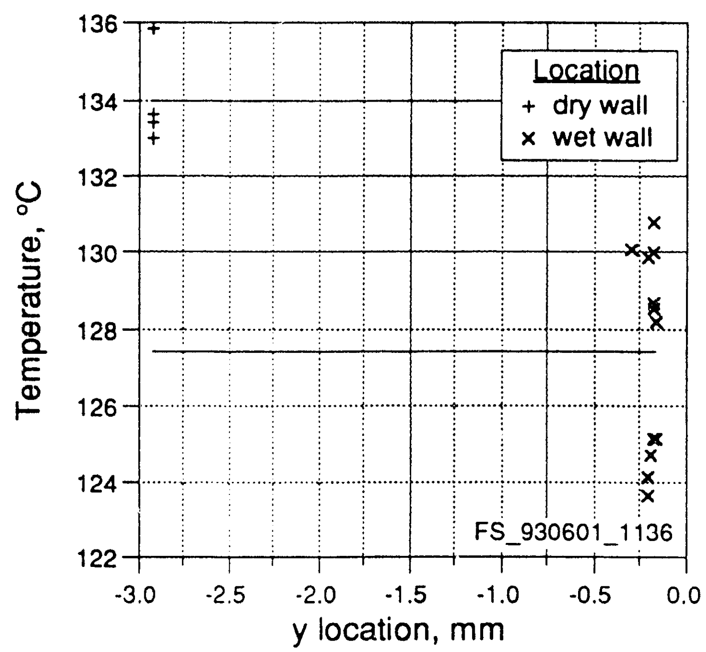

Figure 100, Normal temperature profile at EHL from File FS_930601_1136 (Construction 2.0, T_{in} = 59.19°C, ϕ = 330.0 kW/m^2, Q = 259.5 cm^3/s, p_{ehl} = 129.0 kPa)

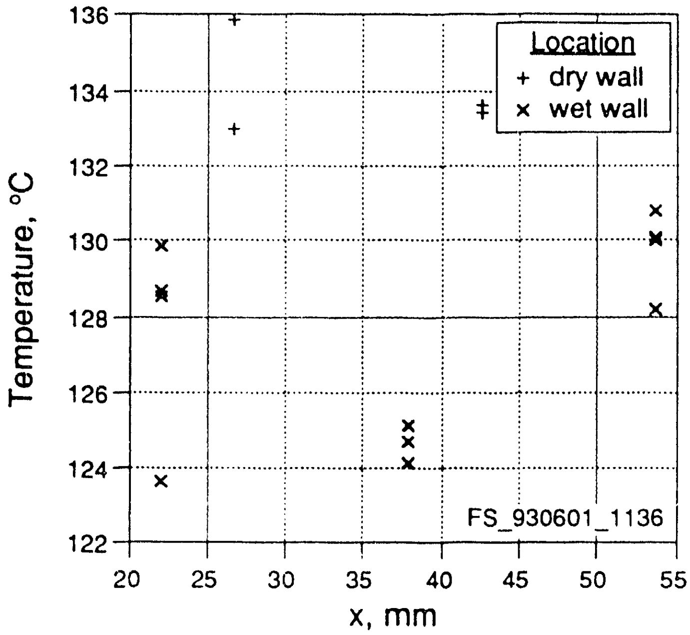

Figure 101, Lateral temperature profile at EHL from File FS_930601_1136 (Construction 2.0, T_{in} = 59.19°C, ϕ = 330.0 kW/m^2, Q = 259.5 cm^3/s, p_{ehl} = 129.0 kPa)

Figures 99, 100, and 101 present the temperatures over the last 80 mm of the heated length. The wall temperature near the rib is lower than that of the lateral positions that are away from the rib. This difference is 3.9°C over the 80 mm of heated length and 4.7°C over most of the heated section. Tables 40 and 41 summarize this information.

Isothermal Temperature Profiles

Figures 102, 103, and 104 present the temperature profile information for an isothermal condition where the fluid temperature was held at 60°C. This test was conducted using Construction 4.0, which did not contain any obstructions. Tables 42 and 43 present a summary of the temperature data in

Table 40.--Mean heater temperature based on lateral position from File FS_930601_1136 (Construction 2.0, T_{in} = 59.19°C, ϕ = 330.0 kW/m², Q = 259.5 cm³/s, p_{ehl} = 129.0 kPa)

	N	x mm	$\bar{T}$ °C	S °C	S_m °C
dry	5	26.72	131.77	4.80	2.15
dry	5	42.60	131.17	4.39	1.96
wet	7	21.97	126.22	3.98	1.50
wet at rib	7	37.85	123.13	3.11	1.18
wet	6	53.72	129.53	0.95	0.39
mean, dry	10	...	131.47	4.35	1.38
mean, wet	20	...	126.13	3.91	0.87

Table 41.--Mean heater temperatures based on lateral position over the last 80 mm of the heated length; from File FS_930601_1136 (Construction 2.0, T_{in} = 59.19°C, ϕ = 330.0 kW/m², Q = 259.5 cm³/s, p_{ehl} = 129.0 kPa)

	N	x mm	$\bar{T}$ °C	S °C	S_m °C
dry	2	26.72	134.44	2.09	1.48
dry	2	42.60	133.52	0.18	0.13
wet	4	21.97	127.68	2.74	1.37
wet at rib	4	37.85	124.82	0.47	0.23
wet	4	53.72	129.77	1.13	0.56
mean, dry	4	...	133.98	1.32	0.66
mean, wet	12	...	127.42	2.63	0.76

the same format as the earlier temperature profile information was presented. These tables and the three figures indicate that the temperature behaviors discussed earlier in this section are not the result of thermocouple variations.

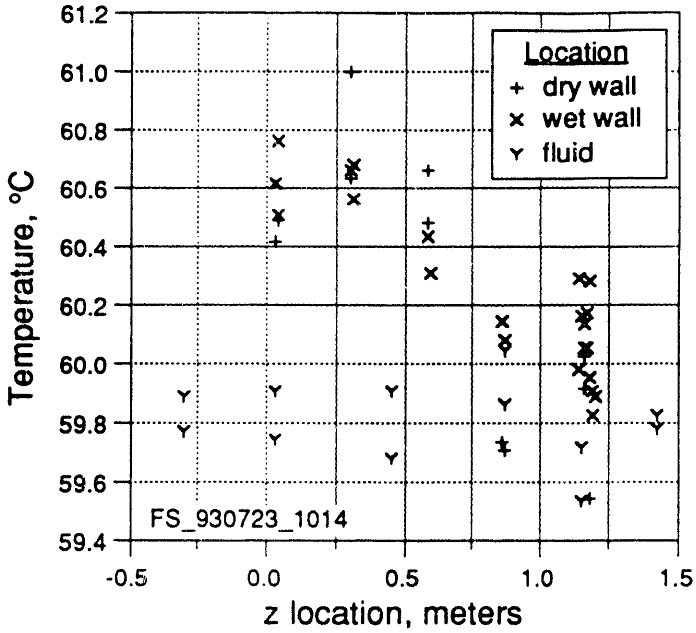

Figure 102, Longitudinal temperature profile from File FS_930723_1014 (Construction 4.0, T_{in} = °C, ϕ = 0.00 kW/m^2, Q = cm^3/s, p_{ehl} = kPa)

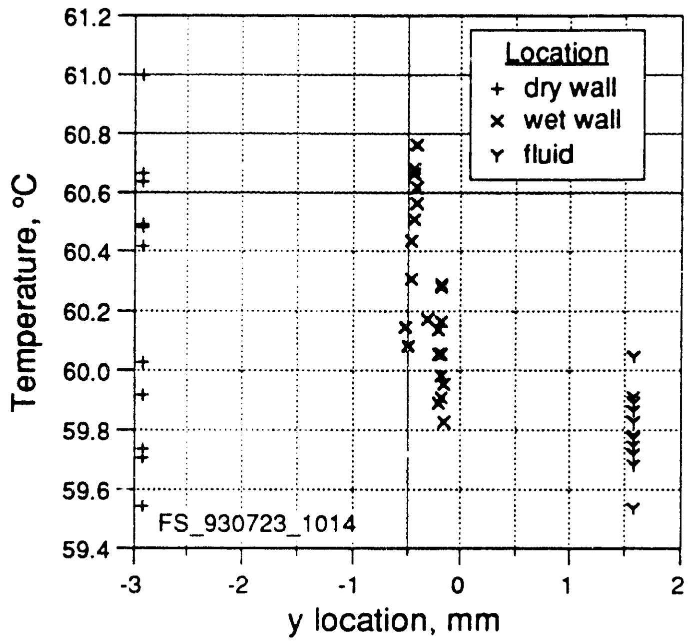

Figure 103, Normal temperature profile from File FS_930723_1014 (Construction 4.0, T_{in} = °C, ϕ = 0.0 kW/m^2, Q = cm^3/s, p_{ehl} = kPa)

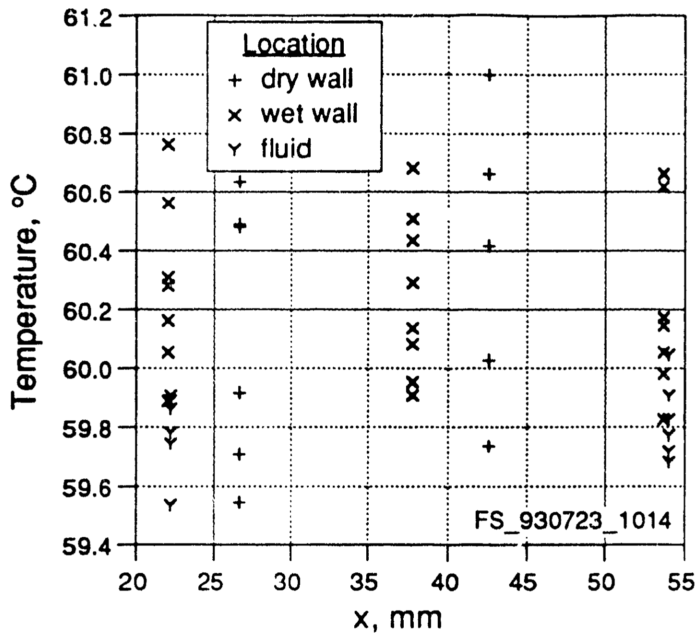

Figure 104, Lateral temperature profile from File FS_930723_1014 (Construction 4.0, T_{in} = 60°C, ϕ = 0.0 kW/m^2, Q = cm^3/s, p_{ehl} = kPa)

Table 42.--Mean heater temperature based on lateral position from File FS_930723_1014 (Construction 4.0, T_{in} = 60°C, TT00001 = 60°C, ϕ = 0.0 kW/m^2, Q = cm^3/s, p_{ehl} = kPa)

	N	x mm	$\overline{T}$ °C	S °C	S_m °C
dry	5	26.72	60.06	0.48	0.22
dry	4	42.60	60.36	0.58	0.29
wet	6	21.97	60.22	0.23	0.09
wet	7	37.85	60.22	0.28	0.10
wet	6	53.72	60.15	0.28	0.12
mean, dry	9	...	60.20	0.52	0.17
mean, wet	19	...	60.20	0.25	0.06
mean, fluid	12	...	59.81	0.13	0.04

Table 43.--Mean heater temperatures based on lateral position over the last 80 mm of the heated length; from File FS_930723_1014 (Construction 4.0, T_{in} = 60°C, TT00001 = 60°C, ϕ = 0.0 kW/m², Q = cm³/s, p_{ehl} = kPa)

	N	x mm	$\overline{T}$ °C	S °C	S_m °C
dry	2	26.72	59.73	0.26	0.19
dry	1	42.60	60.03	...	...
wet	4	21.97	60.10	0.17	0.08
wet	4	37.85	60.08	0.17	0.09
wet	4	53.72	60.02	0.14	0.07
mean, dry	3	...	59.83	0.25	0.15
mean, wet	12	...	60.07	0.15	0.15
mean, fluid	2	...	59.63	0.12	0.09

CHAPTER 5

DISCUSSION

Demand Curve Minimum Conditions

The Q_{ratio} was demonstrated to be independent of the heat flux for the channel with the longitudinal rib. This is further confirmation of the work presented by the researchers at Columbia University. The bubble detachment parameter, η, defined by Equation 2 has been estimated for the three constructions using the data presented in Table 35. This information is presented in Table 44. The values calculated for the open channels compare favorably with the value of 25 suggested by Whittle and Forgan. The value for the ribbed channel was much higher than can be explained by present theory.

The Stanton numbers at OFI are higher than expected for the open channels. For the channel with the logitudianl rib hey are lower than the nominal 0.0065 value suggested by Saha and Zuber. The Nusselt numbers evaluated during this test program range from 156 to 277. These are well below the 455 criteria (Equation 40) necessary to allow vapor to enter the liquid core. The narrow depth of the test channel might create a situation where the core survival mechanism inherent in Equation 40 does not hold.

Table 44.--Bubble detachment parameters

Geometry	Construction	L_h/D_h	N	η	S_η
Open	1	95.3	4	29.0	1.7
	4	89.4	5	28.8	2.3
Rib	2	87.3	4	53.7	0.5

The introduction of a longitudinal spacer rib in a rectangular heated channel will change the behavior of the test channel at OFI. For the comparison of Construction 2 with Construction 4 the Q_{ratio} rib-effect-ratio is 0.817 ± 0.028. The Stanton number rib-effect-ratio is 0.49 ± 0.07. Both of these values are more severe than has been observed in annuli equipped with spacer ribs. (See Table 13.) This variation may not be the result of the rectangular channel test but the presence of centering pins in the "open" annuli which may depress the Q_{ratio} and Stanton number values at OFI.

Boiling Behavior

The boiling behavior observed prior to OFI in the open channel conformed with expectations for nucleate boiling behavior. The cyclic formation of vapor bubbles at OFI conditions can probably be attributed to a form of flow pattern transition instability. It appears that avoidance of OFI conditions will also prevent this form of flow instability.

The boiling behavior for the channel equipped with the longitudinal rib conformed with the mechanisms which Hodges (35) used to explain his observations in a similar te geometry. The behavior did differ in that bubbles could be observed breakir free from the corner surfaces and traveling down the heated channel. For the bubbles presented in Figure 85 the flat plate turbulent length would be:

(90) $$z = \frac{\mathrm{Re}\,\mu}{u\,\rho} = \frac{(3.2e5)\,(386.3\ \mu\mathrm{Pa\cdot s})}{\left(1.1086\ \frac{m}{s}\right)\left(974.5\ \frac{kg}{m^3}\right)} = 114\ \mathrm{mm}$$

The observed bubble lengths are much shorter than the value in Equation 90 so some other characteristic length, as used to define the critical Reynolds number, is probably more appropriate.

Wall Temperatures

The wall temperature at the water to liquid interface will be slightly lower than the measured temperature since the thermocouple is set back into the heated surface. A correction can be estimated using a conduction analysis. Equation 91 provides a corrected temperature at the wall-to-liquid interface.

(91) $$T_{wall} = T_{dry} - y_{dry}\,\frac{T_{dry} - T_{wet}}{y_{dry} - y_{wet}}$$

The corrected wall temperatures and the wall temperatures calculated using the Thom, et al. correlation (Equation 53) for the previously discussed files are presented in Table 45. The wall temperature estimated using equation 91 is higher then that estimated using Equation 53. While temperature measurement uncertainty may create some of this discrepancy it is more likely that the difference exists for other reasons. The evaluation of these reasons would require further testing that is beyond the scope of this program.

Table 45.--Wall temperature evaluation

File name:	FS_930601_1136	FS_930720_1446
Dry wall temperature (y = -2.92 mm)	131.47	135.99
Wet wall temperature (y = -0.322 mm)	126.13	129.87
Temperature at wall-to-liquid interface (Equation 91)	125.47	129.11
Nucleate boiling temperature (Thom, et al. correlation, Equation 53)	120.13	120.12
ONB temperature (Equation 38)	113.98	113.89

CHAPTER 6

CONCLUSIONS

The existence of a rib effect on Ledinegg instability has been demonstrated. For the configuration tested the effect in terms of Q_{ratio} is 0.82 ± 0.03. In terms of Stanton number the effect is 0.49 ± 0.07. These values are applicable only to the configuration tested. It appears that the vapor generation and movement near the vicinity of the rib lowers both the Q_{ratio} and Stanton number at OFI.

The data generated during this program can be used to benchmark the rib effect calculations necessary to evaluate fuel assemblies with spacer ribs. The rib effect in previous data sets has been confounded with other parameters such as centering pins, annulus concentricity, and rig-to-rig geometry variations. These effects were eliminated by the use of a rectangular geometry that eliminated the need for centering pins. The test channel was fabricated to allow installation and removal of the rib thus significantly reducing the previous rig-to-rig geometry effects.

APPENDIX 1

TEST CHANNEL GEOMETRY MEASUREMENTS

Direct measurement of the channel dimensions was found to be a considerable challenge during the first two constructions. This measurement problem is more fully described in Chapter 4. Because the test results are sensitive to the correctness of the channel geometry a detailed description of the channel configuration estimates is warranted. This appendix presents a detailed description of the measurement techniques used to evaluate the channel geometry. With the exception of the rib width, rib height, and hydraulic length all channel dimensions have been calculated from multiple measurements or derived from operating post-test inspections. Table 23 summarizes the channel geometry measurements. Table 1-2 presents details of the non-calculated channel dimensions.

Table 1-2.--Directly measured channel dimensions

	N	$\bar{X}$	S	B
Rib width, x_o, mm	6	2.07	0.01	0.04
Rib height, b_o, mm	6	3.25	0.00	0.03
Length, hydraulic, L, m	1	1.3970	...	0.0008
Length, heated, L_h, m	1	1.156	...	0.001
Heated width, open channel, a_h, mm	1	76.2	...	1.6

Channel Width, a

The open channel width was estimated by measuring the overall width of the channel as shown in Figure 1-1. The width of the heater supports was then deducted to determine the overall channel width, a. Table 1-3 presents the results of the overall channel measurements. During the disassembly of Construction 3 roll pins were added as shown in Figure 1-1. These pins were installed -0.110 (-4.31), 0.635 (25.00), and 1.289 m (50.75 inches) from the start

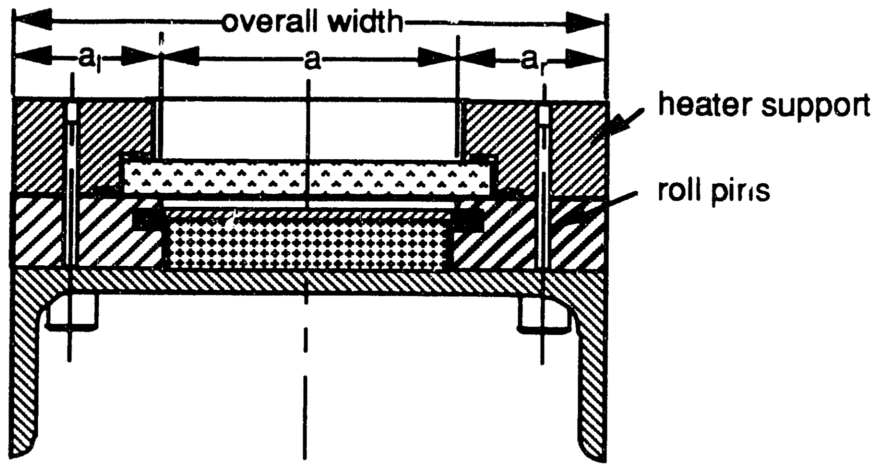

Figure 1-1, Channel width measurement technique

of the heated length. The first and third locations coincide with the location of the pressure ports for the heated section pressure drop measurements. Dimensions measured after the pins were installed are presented in Table 1-4. These dimensions were used to estimate the heater support widths. For construction 1 and 2 the means of the heater support widths were used rather than the widths for the specific location since the overall channel widths were made at different longitudinal positions.

Channel Depth, b

Direct measurement of the channel depth has been difficult. The original estimate was made by measuring the gap at the top to verify the manufacturing tolerances. The appropriateness of this method was demonstrated as inadequate when an attempt was made to slide the rib into place from the end of the channel without disassembly. The rib struck the bottom piece of glass firmly. After reassembly of the channel with the rib in place, it was apparent that the rib height was actually greater than the original channel depth as measured from the heater to the glass.

Table 1-3.--Channel width measurements

Distance from start of heated length, m	Date	Overall channel width, mm	Total heater support width, mm	a, mm
Construction 1, open				
-0.53	14 May '93	152.88	73.069	79.814
-0.23	14 May '93	152.55	73.069	79.484
0.08	14 May '93	152.76	73.069	79.687
0.38	14 May '93	152.86	73.069	79.789
0.69	14 May '93	152.96	73.069	79.890
0.99	14 May '93	152.86	73.069	79.789
1.30	14 May '93	152.91	73.069	79.839
1.53	14 May '93	152.65	73.069	79.585
Mean				79.735
Sample standard deviation, S				0.139
Construction 2, rib				
-0.53	14 May '93	152.58	73.069	79.509
-0.23	14 May '93	152.58	73.069	79.509
0.08	14 May '93	152.53	73.069	79.458
0.38	14 May '93	152.71	73.069	79.636
0.69	14 May '93	152.76	73.069	79.687
0.99	14 May '93	152.73	73.069	79.662
1.30	14 May '93	152.55	73.069	79.484
1.53	14 May '93	152.48	73.069	79.408
-0.53	15 June '93	152.78	73.069	79.713
-0.23	15 June '93	152.60	73.069	79.535
0.08	15 June '93	152.58	73.069	79.509
0.38	15 June '93	152.88	73.069	79.814
0.69	15 June '93	152.76	73.069	79.687
0.99	15 June '93	152.76	73.069	79.687
1.30	15 June '93	152.58	73.069	79.509
1.53	15 June '93	152.68	73.069	79.611
Mean				79.589
Sample standard deviation, S				0.113

Table 1-3.--Continued

Distance from start of heated length, m	Date	Overall channel width, mm	Heater support width, mm	a, mm
Construction 3, open				
-0.30	22 June '93	152.55	73.051	79.502
-0.10	22 June '93	152.55	72.974	79.578
0.18	22 June '93	152.78	73.051	79.731
0.58	22 June '93	152.91	73.101	79.807
1.02	22 June '93	152.76	73.000	79.756
1.30	22 June '93	152.45	73.203	79.248
1.42	22 June '93	152.53	73.101	79.426
Mean				79.578
Sample standard deviation, S				0.202
Construction 4, open				
-0.30	29 June '93	152.91	73.051	79.858
-0.10	29 June '93	152.71	72.974	79.731
0.18	29 June '93	152.83	73.051	79.782
0.58	29 June '93	152.98	73.101	79.883
1.02	29 June '93	153.01	73.000	80.010
1.30	29 June '93	152.55	73.203	79.350
1.42	29 June '93	152.88	73.101	79.782
Mean				79.771
Sample standard deviation, S				0.207

The thickness of the faceplate was measured using a depth micrometer from the front of the faceplate. The bottom positions were established by placing a flat bar across the opening. The results from this measurement are presented in Table 1-5. Table 1-6 presents the raw as-measured data. Table 1-7 presents the channel depth estimates based on the data in Tables 1-5 and 1-6.

Table 1-4.--Channel width dimensions after installation of roll pins, 24 June 1993, prior to final assembly of construction 4.0

Nominal longitudinal position m	Overall assembly width mm	Heater support width, mm		a, mm		
		left	right	measured	calculated	delta
-0.30	152.27	36.551	36.500	79.324	79.223	0.102
-0.11	152.40	36.474	36.500	79.578	79.426	0.152
0.17	152.83	36.525	36.525	79.807	79.782	0.025
0.59	152.91	36.576	36.525	79.807	79.807	0.000
1.01	153.11	36.449	36.551	80.010	80.112	-0.102
1.29	152.71	36.601	36.601	79.502	79.502	0.000
1.43	152.40	36.551	36.551	79.451	79.299	0.152
Mean		36.533	36.536	79.640	79.593	0.047
S		0.054	0.035	0.242	0.319	0.093

Table 1-5.--Face plate dimensions used for channel depth calculation, measured on 23 June 1993

Longitudinal position m	Lateral position mm	Face plate thickness	
		inch	mm
-0.30	53.98	1.003	10.742
-0.30	22.23	1.002	10.731
-0.11	53.98	1.006	10.774
-0.11	22.23	1.005	10.764
0.17	53.98	1.006	10.774
0.17	22.23	1.004	10.753
0.59	53.98	1.005	10.764
0.59	22.23	1.005	10.764
1.01	53.98	1.007	10.785
1.01	22.23	1.007	10.785
1.29	53.98	1.012	10.839
1.29	22.23	1.009	10.806
1.43	53.98	1.012	10.839
1.43	22.23	1.011	10.828

Table 1-6.--Channel depth measurements, distance from front of face plate to front of heater

Longitudinal position z m	Lateral position x mm	Distance from face plate to heater, inch			
		Pretest		Post-test	
		horizontal	vertical	horizontal	vertical
Construction 2.0, ribbed					
		...	...	14 June '93	14 June '93
-0.11	53.98	...	...	1.132	1.134
-0.11	22.23	...	...	1.127	1.129
0.17	53.98	...	...	1.130	1.129
0.17	22.23	...	...	1.121	1.122
0.59	53.98	...	...	1.129	1.129
0.59	22.23	...	...	1.120	1.121
1.01	53.98	...	...	1.129	1.128
1.01	22.23	...	...	1.123	1.122
1.29	53.98	...	...	1.135	1.135
1.29	22.23	...	...	1.131	1.132
Construction 3.0, open					
		16 June '93	17 June '93	22 June '93	...
-0.30	53.98	...	1.127	1.129	...
-0.30	22.23	...	1.123	1.123	...
-0.11	53.98	1.125	1.126	1.125	...
-0.11	22.23	...	1.122	1.119	...
0.17	53.98	1.100	1.100	1.100	...
0.17	22.23	1.095	1.097	1.094	...
0.59	53.98	1.101	1.100	1.099	...
0.59	22.23	1.097	1.096	1.096	...
1.01	53.98	1.102	1.101	1.102	...
1.01	22.23	1.099	1.098	1.098	...
1.29	53.98	1.130	1.118	1.114	...
1.29	22.23	1.129	1.117	1.113	...
1.43	53.98	...	1.130	1.131	...
1.43	22.23	...	1.128	1.131	...

Table 1-6.--Continued

Longitudinal position z m	Lateral position x mm	Distance from face plate to heater, inch			
		Pretest		Post-test	
		horizontal	vertical	horizontal	vertical
Construction 4.0, open					
		29 June '93	1 July '93	...	23 July '93
-0.30	53.98	1.130	1.130	...	1.139
-0.30	22.23	1.132	1.132	...	1.138
-0.11	53.98	1.132	1.132	...	1.138
-0.11	22.23	1.133	1.133	...	1.139
0.17	53.98	1.131	1.132	...	1.136
0.17	22.23	1.132	1.132	...	1.134
0.59	53.98	1.128	1.129	...	1.127
0.59	22.23	1.128	1.128	...	1.125
1.01	53.98	1.130	1.130	...	1.129
1.01	22.23	1.132	1.132	...	1.130
1.29	53.98	1.134	1.132	...	1.129
1.29	22.23	1.135	1.133	...	1.127
1.43	53.98	1.134	1.130	...	1.119
1.43	22.23	1.134	1.129	...	1.117

The height of the rib was measured as 3.25 mm (0.128 inches) using a micrometer. No variation was observed along the rib's length. Since the channel depth measurement estimate presented in Table 1-7 suggest that the depth of construction 2.0 was 3.08 mm (0.122 inches) it is possible that a bias exists in the depth measurement. While it is possible that a bias exists in the channel depth measurement it is more likely that the two subchannels were not the same depth except at the rib.

Figure 1-2 presents the variation in channel depth in the longitudinal direction. For construction 3.0 the mean of the channel depth a presented in Table 1-7 is much larger than the channel depth over the heated portion of the channel. Table 1-8 presents the channel depth mean for the longitudinal measurements between -0.11 and 1.29 m.

Table 1-7.--Channel depth measurements

Longitudinal position z m	Lateral position x mm	Channel depth, mm (Arithmetic difference of tabulated data in Table 1-6 and face plate thickness as presented in Table 1-5.)			
		Pretest		Post-test	
		horizontal	vertical	horizontal	vertical
Construction 2.0, ribbed					
		···	···	14 June '93	14 June '93
-0.11	53.98	···	···	3.200	3.251
-0.11	22.23	···	···	3.099	3.150
0.17	53.98	···	···	3.150	3.124
0.17	22.23	···	···	2.972	2.997
0.59	53.98	···	···	3.150	3.150
0.59	22.23	···	···	2.921	2.946
1.01	53.98	···	···	3.099	3.073
1.01	22.23	···	···	2.946	2.921
1.29	53.98	···	···	3.124	3.124
1.29	22.23	···	···	3.099	3.124
Mean		···	···	3.076	3.086
Standard deviation, σ		···	···	0.095	0.102
Construction 3.0, open					
		16 June '93	17 June '93	22 June '93	···
-0.30	53.98	···	3.150	3.200	···
-0.30	22.23	···	3.073	3.073	···
-0.11	53.98	3.023	3.048	3.023	···
-0.11	22.23	···	2.972	2.896	···
0.17	53.98	2.388	2.388	2.388	···
0.17	22.23	2.311	2.362	2.286	···
0.59	53.98	2.438	2.413	2.388	···
0.59	22.23	2.337	2.311	2.311	···
1.01	53.98	2.413	2.388	2.413	···
1.01	22.23	2.337	2.311	2.311	···
1.29	53.98	2.997	2.692	2.591	···
1.29	22.23	3.048	2.743	2.642	···
1.43	53.98	···	2.997	3.023	···
1.43	22.23	···	2.972	3.048	···
Mean		2.588	2.701	2.685	···
Standard deviation, σ		0.329	0.328	0.342	···

Table 1-7.--Continued

Longitudinal position z m	Lateral position x mm	Channel depth, mm (Arithmetic difference of tabulated data in Table 1-6 and face plate thickness as presented in Table 1-5.) Pretest horizontal	Pretest vertical	Post-test horizontal	Post-test vertical
Construction 4.0, open					
		29 June '93	1 July '93	...	23 July '93
-0.30	53.98	3.226	3.226	...	3.457
-0.30	22.23	3.302	3.302	...	3.454
-0.11	53.98	3.200	3.200	...	3.353
-0.11	22.23	3.251	3.251	...	3.404
0.17	53.98	3.175	3.200	...	3.302
0.17	22.23	3.251	3.251	...	3.302
0.59	53.98	3.124	3.150	...	3.099
0.59	22.23	3.124	3.124	...	3.048
1.01	53.98	3.124	3.124	...	3.099
1.01	22.23	3.175	3.175	...	3.124
1.29	53.98	3.099	3.048	...	2.972
1.29	22.23	3.200	3.150	...	2.997
1.43	53.98	3.099	2.997	...	2.718
1.43	22.23	3.124	2.997	...	2.692
Mean		3.177	3.157	...	3.144
Standard deviation, σ		0.064	0.093	...	0.249

Table 1-8.--Channel depth measurements based on data presented in Figure 1-2

Construction	N*	Mean mm	Sample standard deviation, mm
2	10	3.09	0.10
3†	10	2.45	0.16
4	10	3.16	0.09

*Only longitudinal measurements between -0.11 and 1.29 m were used in the calculation of the mean.

†The values at -0.11 and 1.29 m were weighted at 0.333 while the remainder were weighted at 1.000.

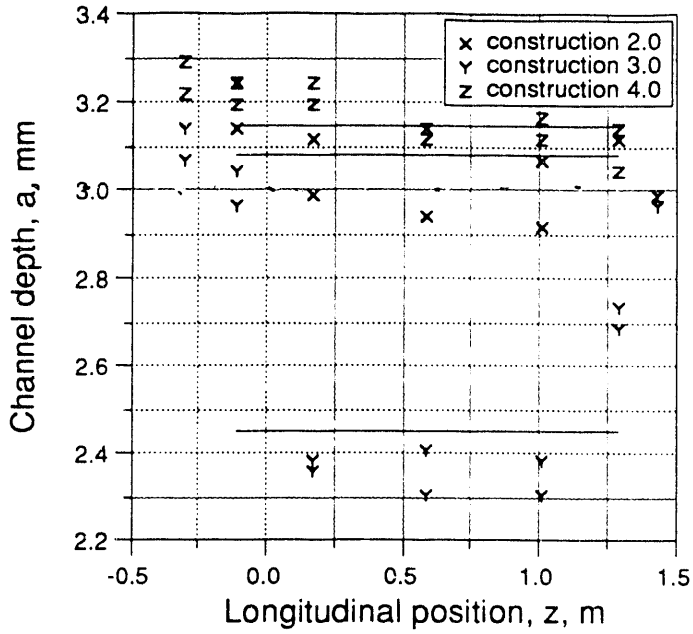

Figure 1-2, Channel depth, b, for construction 2.0 (14 June 1993), 3.0 (17 June 1993), and 4.0 (1 July 1993)

Hydraulic Length, L

The hydraulic length is the distance between the instrument ports which were connected to instruments PD02472, and PD22472. This distance was directly measured using a tape measure. The distance was 1.3970 ± 0.0008 m (55.00 ± 0.03 inches).

Rib Thickness

The rib thickness was directly measured using a micrometer. The rib thickness was 3.25 mm (0.128 inches). Additional information is presented in Table 1-2.

Channel Heated Width, a_h

The width of the heated area was estimated as the width of the wetted aluminum surface. This width is 76.2 mm (3 inches). This is 3.4 mm (0.01 inch) smaller than the overall channel width for construction 4.

Channel Heated Length, L_h

The channel heated length was estimated from the heater inspection results described in Chapter 4. The nominal heater length was 1.219 m (48 inches). The effective heater length as estimated by the distance between the start and end of the most significant discoloration described in Chapter 3 was 1.156 m (45.51 inches). The effective start of the heated length is 48±2 mm (1.88 inches) below the nominal start of the heated length.

APPENDIX 2

INSTRUMENT CALIBRATIONS

Measurements used during this test program included volumetric flow, local pressure, differential pressure, absolute pressure, heater voltage, heater current, heater temperature, and fluid temperature. This appendix presents the methods used to develop the engineering unit transformation equations. The final equations are summarized in Appendix 7, Table 7-2. Table 2-1 provides a coss-index between the instrument loop numbers used during the test program and the Measurement and Teste Equipment (M&TE) numbers used in tracking instrument histories in the HTL.

Flow Calibrations

Flow Calibration Uncertainty

The turbine flow meter (instrument FT01001) and the orifice flow meter (instrument FT01002) were loop calibration checked using a weigh tank method. Water was flowed through the meters for approximately three minutes. During this period all of the flow was caught in a weigh tank. The mass of this water could then be used to estimate the standard flow using Equation 2-1

(2-1) $$Q = \frac{W}{t\rho}$$

The instruments used in this effort are listed in Table 2-1. The elemental uncertainties for the measurements are listed in Table 2-2. The systematic uncertainties for the temperature and time measurements are based on the HTL tolerances. The systematic error for the displacement was assumed based on twice the maximum error observed during the previous calibration for the scale. The density curve fit bias is established by DPSTM-140. The random uncertainties for the displacement and temperature measurements are

Table 2-0.--Measurement and test equipment (M&TE) summary.

Instrument loop number	Channel number	M&TE number	Description
PL11000	...	TR-419	Pressure gauge
PL12000	...	TR-418	Pressure gauge
PL13000	...	...	Pressure gauge
PL33000	...	...	Pressure gauge
TT00001	...	TR-2256	Thermometer
TP01317	1	TR-2833	Thermocouple, EMQSS-020G-12
TP01308	2	TR-2831	Thermocouple, EMQSS-020G-12
TP01413	3	TR-2832	Thermocouple, EMQSS-020G-12
TP01702	4	TR-2829	Thermocouple, EMQSS-020G-12
TP01505	5	TR-2830	Thermocouple, EMQSS-020G-12
TP11917	6	TR-2838	Thermocouple, EMQSS-020G-12
TP12008	7	TR-2836	Thermocouple, EMQSS-020G-12
TP12113	8	TR-2837	Thermocouple, EMQSS-020G-12
TP12105	9	TR-2835	Thermocouple, EMQSS-020G-12
TP12302	10	TR-2834	Thermocouple, EMQSS-020G-12
TP22917	11	TR-2843	Thermocouple, EMQSS-020G-12
TP23008	12	TR-2841	Thermocouple, EMQSS-020G-12
TP23013	13	TR-2842	Thermocouple, EMQSS-020G-12
TP23105	14	TR-2840	Thermocouple, EMQSS-020G-12
TP23302	15	TR-2839	Thermocouple, EMQSS-020G-12
TP33917	16	TR-2848	Thermocouple, EMQSS-020G-12
TP34013	17	TR-2847	Thermocouple, EMQSS-020G-12
TP33908	18	TR-2846	Thermocouple, EMQSS-020G-12
TP34105	19	TR-2845	Thermocouple, EMQSS-020G-12
TP34302	20	TR-2844	Thermocouple, EMQSS-020G-12
TP45008	21	TR-2853	Thermocouple, EMQSS-020G-12
TP45105	22	TR-2852	Thermocouple, EMQSS-020G-12
TP45302	23	TR-2851	Thermocouple, EMQSS-020G-12
TP45613	24	TR-2849	Thermocouple, EMQSS-020G-12
TP45717	25	TR-2850	Thermocouple, EMQSS-020G-12
TP45808	26	TR-2856	Thermocouple, EMQSS-020G-12
TP45905	27	TR-2855	Thermocouple, EMQSS-020G-12
TP46102	28	TR-2854	Thermocouple, EMQSS-020G-12
TP46308	29	TR-2861	Thermocouple, EMQSS-020G-12
TP46217	30	TR-2858	Thermocouple, EMQSS-020G-12
TP46413	31	TR-2857	Thermocouple, EMQSS-020G-12
TP46505	32	TR-2860	Thermocouple, EMQSS-020G-12
TP46602	33	TR-2859	Thermocouple, EMQSS-020G-12
TP46808	34	TR-2864	Thermocouple, EMQSS-020G-12
TP47005	35	TR-2863	Thermocouple, EMQSS-020G-12
TP47202	36	TR-2862	Thermocouple, EMQSS-020G-12

Table 2-0.--Continued

Instrument loop number	Channel number	M&TE number	Description
TC00001	37	TR-2947	Thermocouple, EQSS-116G-12
TC00002	38	TR-2948	Thermocouple, EQSS-116G-12
TC00003	39	TR-2885	Thermocouple, EMQSS-020G-12
TF01202	40	TR-2701	Thermocouple, EMQSS-020G-12
TF01204	41	TR-2702	Thermocouple, EMQSS-020G-12
TF02522	42	TR-2698	Thermocouple, EMQSS-020G-12
TF02524	43	TR-2700	Thermocouple, EMQSS-020G-12
TF04172	44	TR-2884	Thermocouple, EMQSS-020E-12
TF04174	45	TR-2694	Thermocouple, EMQSS-020G-12
TF05822	46	TR-2248	Thermocouple, EMQSS-020G-6
TF05824	47	TR-2249	Thermocouple, EMQSS-020G-6
TF06922	48	TR-2692	Thermocouple, EMQSS-020G-12
TF06924	49	TR-2699	Thermocouple, EMQSS-020G-12
TF08022*	50	TR-2697	Thermocouple, EMQSS-020G-12
		TR-2883	Thermocouple, EMQSS-020E-12
TF08024	51	TR-2696	Thermocouple, EMQSS-020G-12
TL01001	52	TR-2949	Thermocouple, E19012G0004X
TL02001	53	TR-2950	Thermocouple, E19012G0004X
TL03001	54	TR-2953	Thermocouple, E19012G0004X
TL03002	55	TR-2956	Thermocouple, E19012G0004X
...	56	...	not used
...	57	...	not used
...	58	...	not used
...	59	...	not used
...	60	...	not used
PA20072	61	TR-20333	Rosemount pressure transducer, model 1151AP6E
PD22472	62	TR-2916	Rosemount pressure transducer, model 1151DP6E
FT01002	63	TR-20304	Rosemount pressure transducer, model 1151DP6E
PG00024	64	TR-2148	Rosemount pressure transducer, model 1144G02
PL00001	65	TR-532	Rosemount pressure transducer, model 1151DP6E
PD00024	66	TR-20302	Rosemount pressure transducer, model 1151DP6E
PA00072	67	TR-20331	Rosemount pressure transducer, model 1151AP6E
PD02472	68	TR-20312	Rosemount pressure transducer, model 1151DP6E

Table 2-0.--Continued

Instrument loop number	Channel number	M&TE number	Description
PD00072	69	TR-20305	Rosemount pressure transducer, model 1151DP6E
PL00002	70	TR-2146	Rosemount pressure transducer, model 1144G02
PD07284	71	TR-20303	Rosemount pressure transducer, model 1151DP6E
PD00084	72	TR-20313	Rosemount pressure transducer, model 1151DP6E
FT01001	73	TR-076	Flow Technology turbine flow meter, model FT-12NEXW-LAD-1
WV00001	74	TR-30013	Voltage transducer
	74	TR-30032	
WC00001	75	TR-295	Shunt

*After Constuction 2.0 this thermocouple was switched from M&TE number TR-2697 to TR-2883.

estimated as half the minimum discernible increment. The random component for time is based on the recommendation in ASME 19.12.

The partial differentials for Equation 2-1 are:

$$\frac{\partial Q}{\partial W} = \frac{Q}{W} \qquad \frac{\partial Q}{\partial t} = \frac{-Q}{t} \qquad \frac{\partial Q}{\partial \rho} = \frac{-Q}{\rho}$$

$$\frac{\partial \rho}{\partial T} = -0.2685 - 0.003627T - \frac{0.51123T^2}{10^5}$$

Table 2-1.--Instruments used in the loop calibration check of FT01001 and FT01002

Element	Description	M&TE Number	HTL Tolerance
Pretest calibration, 15 and 16 April 1993			
Displacement	0 to 1000# scale	TR-30076	±1 pound*
Temperature	-1 to 101°C thermometer	TR-2897	±0.2°C
Time	stopwatch	TR-2235	±500 μsec/second
Mid-test calibration, 10 June 1993			
Displacement	0 to 1000# scale	TR-30076	±1 pound*
Temperature	0 to 50°C thermometer	TR-320	±1°C
Time	stopwatch	TR-2269	±500 μsec/second
Post-test calibration, 27 July 1993			
Displacement	0 to 1000# scale	TR-30076	±1 pound*
Temperature	0 to 50°C thermometer	TR-320	±1°C
Time	stopwatch	TR-2269	±500 μsec/second

*The maximum error during the pre-test calibration for this scale was 0.1#

Table 2-2.--Operating parameters and elemental uncertainties for the loop calibration check of FT01001 and FT01002

Element	Median	Minimum	Maximum	B	P
Displacement (#)	208.05	54.1	495.50	0.2	0.05
Temperature (°C)	24.3	20.5	28.1	0.2	0.05
Time (seconds)	180.31	179.72	180.70	0.09	0.2
Density (kg/m3)	997.27	995.88	998.61	0.50	...

The total uncertainty for the applied flow can be estimated using the Equation 2-2. Calculated values are presented in Table 2-3.

$$\omega_Q = \sqrt{\left(\frac{\partial Q}{\partial W}\omega_W\right)^2 + \left(\frac{\partial Q}{\partial t}\omega_t\right)^2 + \left(\frac{\partial Q}{\partial \rho}\omega_\rho\right)^2 + \left(\frac{\partial Q}{\partial \rho}\frac{\partial \rho}{\partial T}\omega_T\right)^2} \qquad (2\text{-}2)$$

Table 2-3.--Calibration standard uncertainties estimated from information presented in Table 2-2.

	Flow cm³/s	Displacement #	B cm³/s	P cm³/s
Minimum	136	54.1	0.5	0.2
Median	525	208.1	0.6	0.6
Maximum	1250	495.5	1.1	1.4

Instrument FT01001

The turbine meter, FT01001 is a linear device that can be evaluated using the method presented in WSRC-TR-91-106. A least-square-mean fit of the three calibration data sets was made after pooling the data as suggested by WSRC-TR-91-435. The uncertainty estimates of these fits were made using the methodology presented in Appendix C of WSRC-TR-91-106. The confidence interval to contain the mean was used to evaluate the random curve fit uncertainty and has been treated as a systematic error. This is presented in Figure 2-1. The fixed curve uncertainty is presented in Figure 2-2. The system noise (See Figure 2-3.) was evaluated as a random uncertainty. Figure 2-4 presents the conversion equation. The combined uncertainty estimate is presented in Table 2-4.

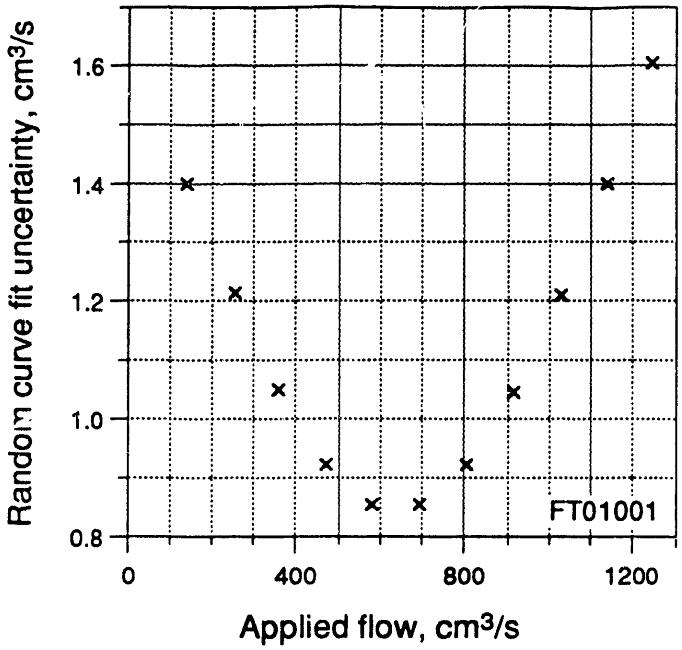

Figure 2-1. Random curve fit uncertainty for FT01001

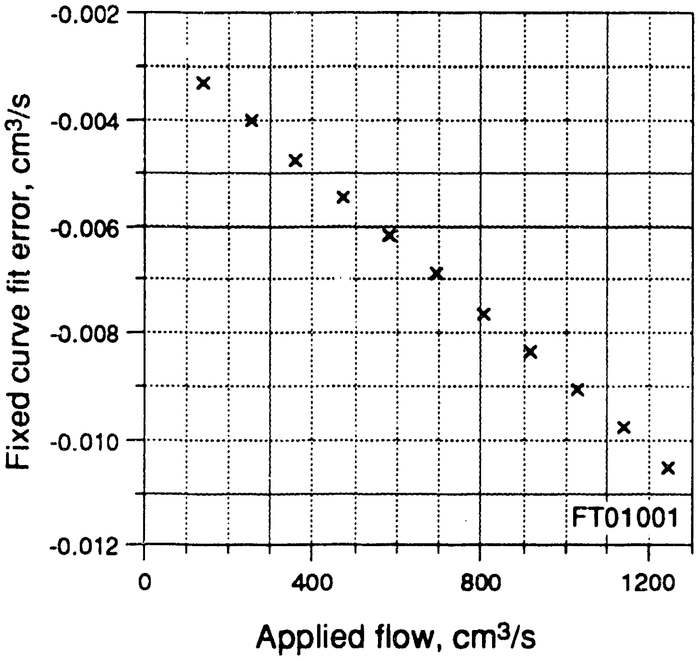

Figure 2-2. Fixed curve fit error for FT01001.

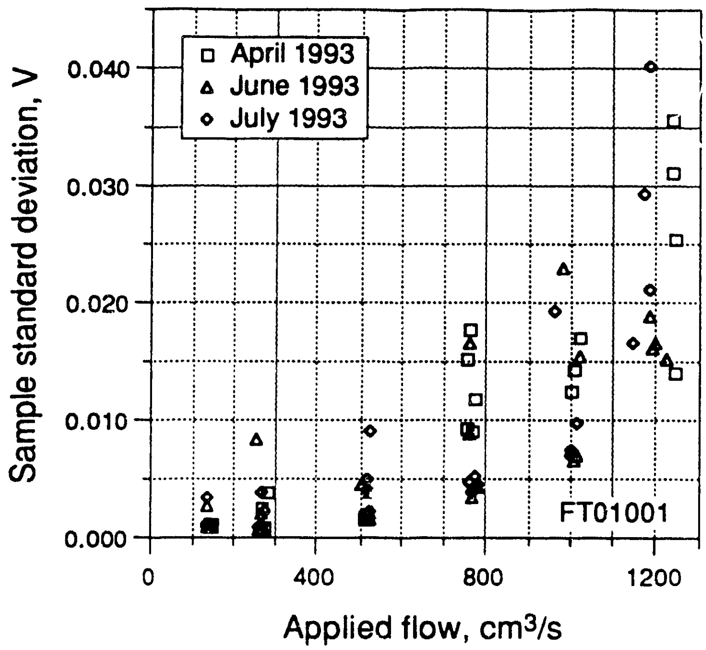

Figure 2-3, FT01001 sample standard deviation during flow calibrations

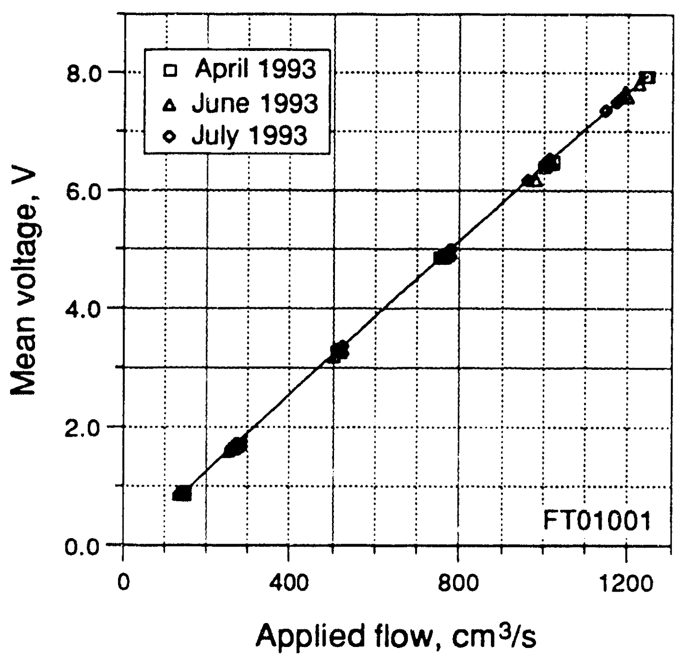

Figure 2-4, FT01001 output during flow calibrations.

Table 2-4.--Uncertainty estimate for FT01001

Flow, cm^3/s Flow, gpm	126 2	631 10	1262 20
Systematic Uncertainty			
Calibration Standard Uncertainty, cm^3/s (Table 2-3)	0.5	0.6	1.1
Random curve fit uncertainty, cm^3/s (Figure 2-1)	1.43	0.85	1.63
Fixed curve uncertainty, cm^3/s (Figure 2-2)	0.0	0.01	0.01
Combined Systematic Uncertainty, cm^3/s	1.5	1.0	2.0
Random Uncertainty			
System noise, volts (Figure 2-3)	0.003	0.007	0.030
Combined Random Uncertainty, cm^3/s	0.3	1.1	4.7

Instrument FT02002

The orifice meter, FT01002 is an intrinsically linear device that can be evaluated using the method presented in TR-91-106 where the confidence interval to contain the mean is used to evaluate the random curve fit uncertainty. The system noise is evaluated as a random component. The non-linear form of the calibration equation is:

(2-3)
$$V = a + bU^m$$

linearized form of the calibration equation is:

(2-4)
$$\log(V - a) = \log(b) + m \cdot \log(Q)$$
$$Y = B + mX$$

The value a is taken as the mean of the outputs at zero flow, 0.7580 volts. The values of B and m are then 6.7449 and 2.00828. The random curve fit uncertainty term must be converted from an uncertainty of the value X to an uncertainty in terms of Q.

(2-4)
$$Q = 10^X$$

$$\frac{\partial Q}{\partial X} = 2.303\ 10^X$$

(2-5)
$$\frac{\partial Q}{\partial X} = 2.303\ Q$$

The uncertainty of Q is then:

(2-6)
$$\omega_Q = \frac{\partial Q}{\partial X}\omega_X$$

The fixed curve uncertainty is computed using:

(2-7)
$$Q = 10^X$$
$$\omega_F = |Q - Q_F| = \left| \left(\frac{b_F}{b} Q_F{}^2 \right)^{1/m} - Q_F \right|$$

The systematic uncertainties are combined using:

(2-8)
$$\omega_Q = \sqrt{\omega_C{}^2 + \left(\frac{\partial Q}{\partial X}\omega_X \right)^2 + \omega_F{}^2}$$

The random error is computed from the standard deviation of the system noise using Equation 2-9.

(2-9)
$$\omega_P = \frac{\partial Q}{\partial V}\omega_V = \frac{1}{bmQ}\omega_V = \frac{t_{\alpha/2}\sigma_V}{bmQ}$$

the confidence interval to contain the mean was used to evaluate the random curve fit uncertainty and has been treated as systematic error It is presented in Figure 2-5. The fixed curve uncertainty is presented in Figure 2-6. The system noise (See Figure 2-7.) was evaluated as a random uncertainty. Figure 2-8 presents the conversion equation. The combined uncertainty estimate is presented in Table 2-5.

Table 2-5.--Uncertainty estimate for FT01002

Flow, cm^3/s Flow, gpm log (Q)	126 2 -3.900	631 10 -3.200	1262 20 -2.899
Systematic Uncertainty			
Calibration Standard Uncertainty, cm^3/s (Table 2-3)	0.5	0.6	1.1
Random curve fit uncertainty, cm^3/s (Figure 2-5)	0.0176	0.0086	0.0128
Fixed curve uncertainty, cm^3/s (Figure 2-6)	4.7	19.5	35.2
Combined Systematic Uncertainty, cm^3/s	7.0	23.2	51.2
Random Uncertainty			
System noise, volts (Figure 2-7)	.005	.028	0.07
Combined Random Uncertainty, cm^3/s	7.1	8.0	10.0

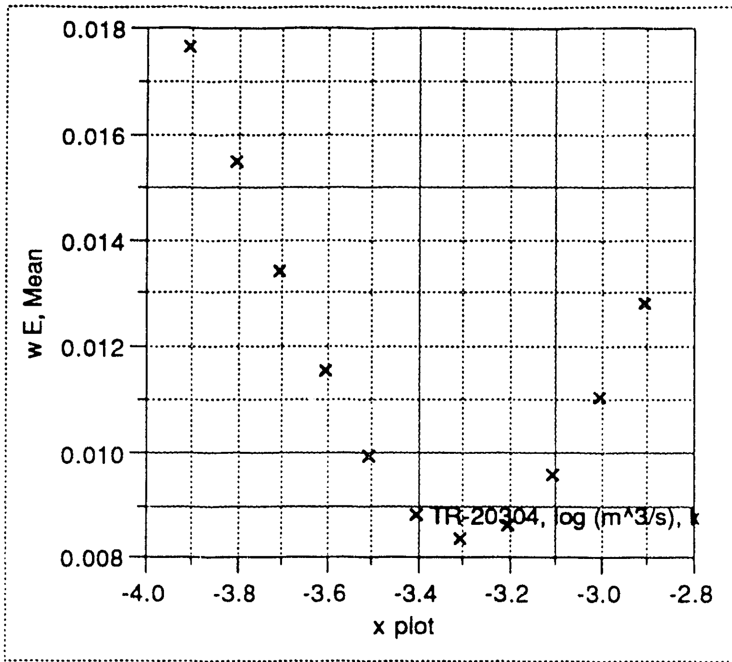

Figure 2-5. Random uncertainty component of curve fit for FT01002 in terms of X

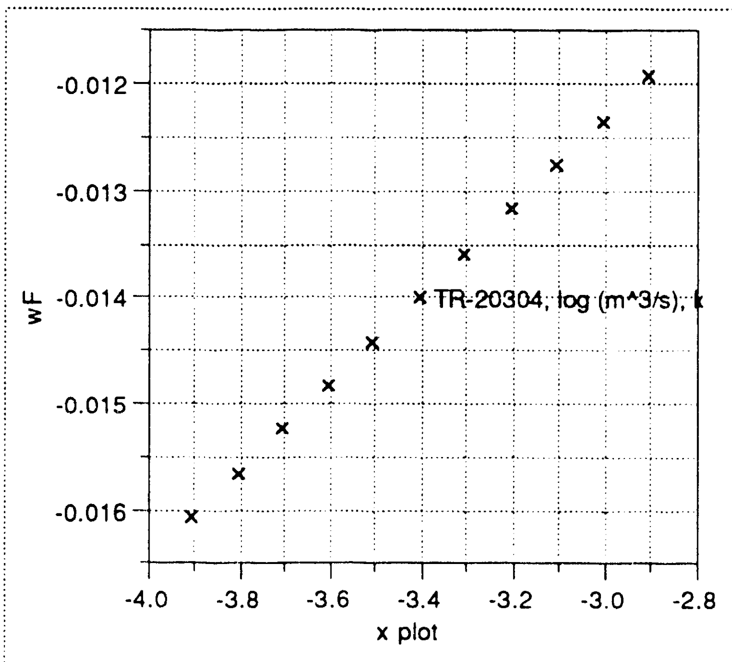

Figure 2-6. Systematic curve fit uncertainty

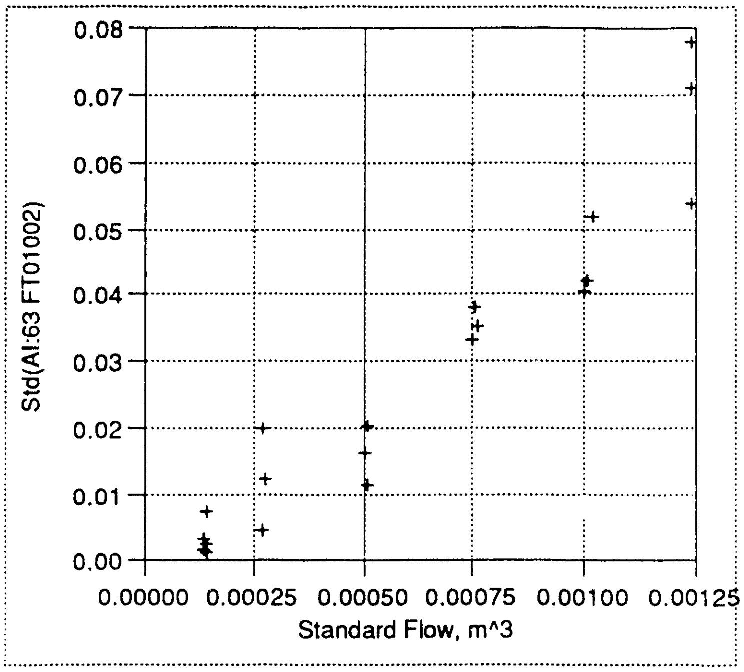

Figure 2-7. Sample standard deviation of output for FT01002 during pretest calibration

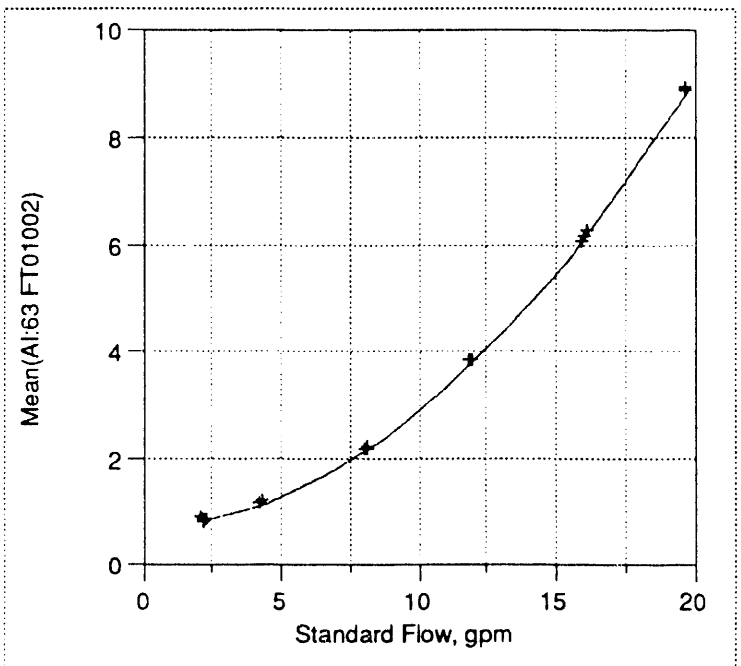

Figure 2.8 Output of FT01002 during pretest flow calibration

Pressure Transducer Calibrations

Pressure Transducer Calibration Uncertainty

Zero and span checks were completed for each pressure transducer at the start and end of each day's testing. This resulted in an extensive set of data for each transducer at two different operating conditions: open to atmosphere and under a static head tank pressure. In addition each pressure transducer was calibrated using a pneumatic dead-weight tester. The slope of the data reduction curve specified in Tables 2-6 and 7-2 were established by the calibration curves as specified in Table 2-6. The zero specified in Table 7-2 was taken from Table 2-8 for the daily zero check data. Since the calculated quantities in Table 2-8 were based on the data reduction curve in Table 7-2, the errors for the zero checks will identically go to zero. The span checks will then exhibit a small systematic error. This systematic error was then assumed constant over the entire range of the transducer.

Table 2-6.--Pressure transducer slope estimates based on calibration data

Instrument loop number	Slope from calibration data, mA/psi		Pressure, Pa	Elevations from SHL for pressure transducer analysis, inches	
	Pretest	Post-test	b, µV/Pa	gauge	channel tap
PA20072	0.2909	0.2908	26.37	-17.25	-50.75
PD22472	0.2908	0.2908	26.36	-17.25	4.25
PG00024	0.3182	...	28.84	-32.50	4.25
PL00001	0.0800	...	7.25	-30.88	34.5
PD00024	1.9991	...	181.22	-30.88	21.6
PA00072	0.2910	0.2910	26.38	-44.25	-50.75
PD02472	0.2910	0.2910	26.38	-44.25	4.25
PD00072	0.1601	...	14.51	-44.25	-50.75
PL00002	0.3190	...	28.92	-57.88	-60.00
PD07284	0.9411	...	85.31	-57.88	-50.75
PD00084	0.2910	...	26.38	-59.5	21.6

Table 2-7.--Daily check files excluded from pressure transducer analysis

File name	Instrument loop number	Comment
SN_930430_1350	PD02472	
SN_930430_1605	PD02472	
SN_930505_1610	PD00024	
SN_930528_1333	PD00072	
SN_930712_1911	PD22472, PD00024, PD02472, PD00072, PD07284, and PD00084	Data is not constant with expected results. This appears to be the result of a valving error.
ZO_930430_1328	PD02472	
ZO_930430_1610	PD02472	
ZO_930506_1613	PL00001	Excluded by information on data sheet

The zero voltages for the absolute pressure transducers (PA00072, and PA20072) must be converted based on the barometric pressure. The mean barometric pressure during the zero checks was 29.691"Hg. The zero voltages would then be calculated using Equation 2-10.

(2-10)
$$V_0 = a + b\left(29.69\text{"Hg} \cdot 3.3864\,\frac{\text{kPa}}{\text{"Hg}}\right)$$

The zero adjustments for PA00072 and PA20072 are listed below:

	N	b, µV/Pa	V_0, V	S, V	a, V
PA00072	55	26.38	0.8305	0.0118	-1.8218
PA20072	55	26.37	0.8161	0.0126	-1.8352

The sample standard deviation for the barometric pressure was 0.126"Hg. The HTL tolerance for the barometric standard is 0.072"Hg. The uncertainty of this measurement is calculated in Equation 2-11.

Table 2-8.--Pressure transducer behavior during daily zero and span checks

Instrument loop number	N	Voltage, V		Pressure*, kPa		
		$\bar{X}$	S	$\bar{X}$	calc.	S
PA20072	55	1.3884	0.0299	122.43	122.25	0.18
	55	0.8161	0.0120	100.55	100.54	0.00
PD22472	54	1.4683	0.0318	21.92	21.70	0.22
	55	0.8963	0.0020	0.00	-0.00	0.00
PG00024	55	0.6426	0.0382	25.73	25.48	0.25
	55	-0.0922	0.0330	0.00	0.00	-0.00
PL00001	55	0.1833	0.0088	25.35	25.06	0.29
	54	0.0016	0.0010	0.00	-0.01	0.01
PD00024	53	5.7294	0.2221	25.33	25.09	0.24
	55	1.1821	0.0060	0.00	0.00	-0.00
PA00072	55	1.5849	0.0298	129.13	129.14	-0.00
	55	0.8305	0.0118	100.55	100.54	0.00
PD02472	52	1.6637	0.0319	28.70	28.54	0.15
	53	0.9108	0.0010	0.00	0.00	-0.00
PD00072	53	0.4004	0.0178	28.60	28.59	0.01
	55	-0.0145	0.0009	0.00	-0.00	0.00
PL00002	55	0.7645	0.0347	31.98	32.03	-0.05
	55	-0.1618	0.0267	0.00	0.00	-0.00
PD07284	54	2.7765	0.0976	31.97	31.76	0.21
	55	0.0671	0.0065	0.00	0.00	-0.00
PD00084	54	1.7559	0.0319	32.43	31.87	0.56
	55	0.9152	0.0015	0.00	-0.00	0.00

*The pressure measured by PL12002 was found to read low by 1.25 kPa. This is documented by tests conducted on 28 May, and 1 June 1993.

(2-11)
$$U_{bar} = \sqrt{(0.072\text{"Hg})^2 + \left(\frac{2 \cdot 0.126\text{"Hg}}{\sqrt{55}}\right)^2}$$
$$= 0.08\text{"Hg}$$
$$= 0.27 \text{ kPa}$$

The total systematic pressure measurement uncertainties are estimated in Table 2-8a. The systematic uncertainty for the calibration standard is estimated as 0.34 kPa (0.05 psi) which is based on the uncertainty of PL12002.

Table 2-8a.--Pressure transducer systematic uncertainties

Instrument loop number	Calibration standard uncertainties kPa		Error from Table 2-8 kPa	B kPa
	Gauge	Barometric		
PA20072	0.34	0.27	0.00	0.43
PD22472	0.34	0.00	0.18	0.38
PG00024	0.34	0.00	0.24	0.42
PL00001	0.34	0.00	0.01	0.34
PD00024	0.34	0.00	0.56	0.66
PA00072	0.34	0.27	0.15	0.46
PD02472	0.34	0.00	0.21	0.40
PD00072	0.34	0.00	0.22	0.40
PL00002	0.34	0.00	0.25	0.42
PD07284	0.34	0.00	0.29	0.44
PD00084	0.34	0.00	0.05	0.34

Voltage Transducer Calibration

The rig voltage was measured using a voltage transducer that was connected to the DAS through an amplifier. Two different transducers were used during the test program. On 3 June 1993 the transducer, M&TE number TR-30013 was replaced with the transducer TR-30032. This increased the range of WV00001 from 50 to 150 volts. To reduce the uncertainty of the voltage measurements the instrument loop was calibration checked by applying a signal across the connections at the DAS-amplifier panel and recording the DAS response in a standard 1 minute log (~120 samples).

Linear least-square-mean fits of the pooled calibration data sets for each transducer were completed as suggested by WSRC-TR-91-435. The uncertainty estimates of these fits were made using the methodology presented in Appendix C of WSRC-TR-91-106. Equation 2-12 should be used to transform the raw data collected prior to 3 June 1993. Equation 2-13 should be used to reduce raw data collected on or after this date.

(2-12) $$V_{DAS} = -0.0001 + 0.20075\ V_{applied}$$ TR-30013

(2-13) $$V_{DAS} = 0.0003 + 0.06668\ V_{applied}$$ TR-30032

Tables 2-9 and 2-10 provide an estimate of the elemental and combined uncertainty estimates for the voltage measurements. The uncertainty of the meter used to measure the applied voltage was 9 ppm + 100 μV. This estimate is based on the HTL theoretical tolerance. The random component of the curve fit has also been treated as a bias and was estimated based on the confidence interval of the mean. (See Figure 2-9.) The fixed curve error was computed as described in Appendix C of WSRC-TR-106. (See Figure 2-10).

The random error was estimated from Figure 2-11. Figure 2-12 presents the conversion equations.

The heater voltage measurements were accomplished by terminals connected to the buss connector blocks. The measured voltage therefore includes the voltage drop between the buss blocks and the heater plate. The buss-to-buss resistance was measured as 36.99 ± 0.09 mΩ, the heater resistance was measured as 36.7 ± 0.1 mΩ. The buss losses can therefore be estimated from Equation 2-14.

(2-14)
$$\frac{36.99 - 36.7}{36.99} \bullet 100\% = 0.8\%$$

The buss loss will be handled separately from the voltage uncertainty estimate as discussed in Appendix 3.

Table 2-9.--Uncertainty estimate for applied voltage, WV00001, prior to 3 July 1993

Applied voltage, V DAS voltage, V	40 V 8.0299	45 V 9.0336	50 V 10.0374
Systematic uncertainty			
Calibration standard uncertainty, V	0.0005	0.0005	0.0006
Random curve fit uncertainty, V (Figure 2-9)	0.0083	0.0091	0.0104
Fixed curve uncertainty, V (Figure 2-10)	0.0000	0.0000	0.0000
Combined systematic uncertainty, V	0.0083	0.0091	0.0104
Random Uncertainty			
System noise, V (Figure 2-11)	0.0012	0.0013	0.0014
Combined random uncertainty, V	0.0012	0.0013	0.0014

Table 2-10.--Uncertainty estimate for applied voltage, WV00001, on and after 3 July 1993

Applied voltage, V DAS voltage, V	40 V 8.0317	45 V 9.0357	60 V 10.0397
Systematic uncertainty			
Calibration standard uncertainty, V	0.0005	0.0005	0.0006
Random curve fit uncertainty, V (Figure 2-9)	0.0074	0.0077	0.0101
Fixed curve uncertainty, V (Figure 2-10)	-0.0007	-0.0008	-0.0011
Combined systematic uncertainty, V	0.0074	0.0078	0.0102
Random Uncertainty			
System noise, V (Figure 2-11)	0.0006	0.0008	0.0008
Combined random uncertainty, V	0.0006	0.0008	0.0008

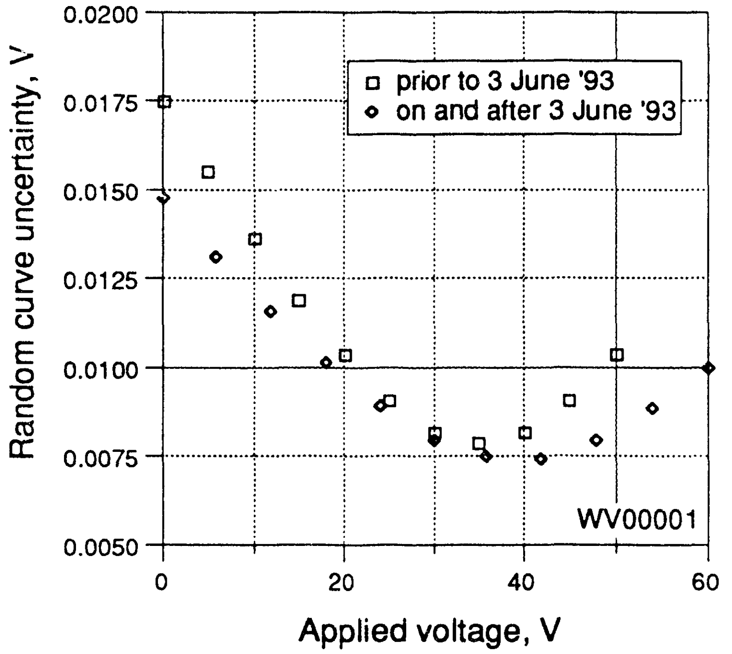

Figure 2-9. Confidence intervals for the mean response for WV00001

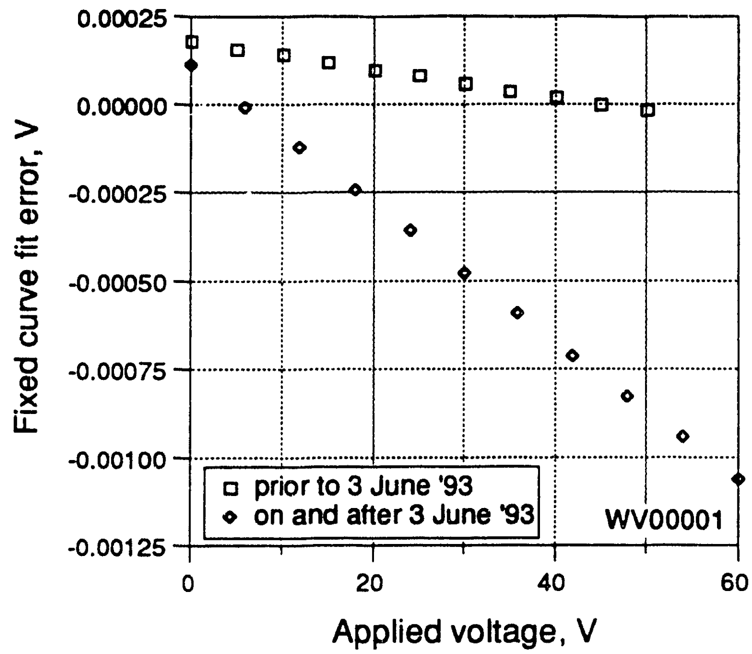

Figure 2-10. Vixed curve fit errors for WV00001

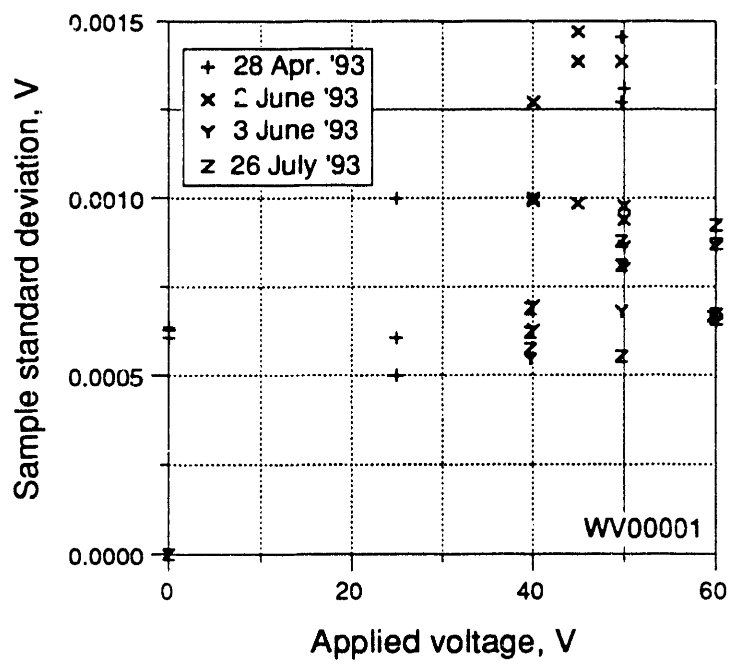

Figure 2-11 WV00001 smple standard deviation of output during calibrations

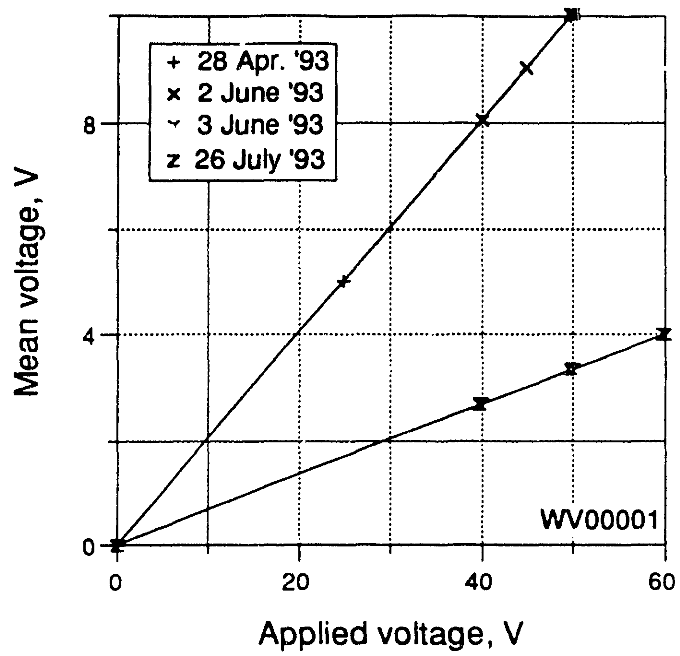

Figure 2-12. WV00001 output during calibrations.

Current Measurement Calibration

The current is measured using a voltmeter (0 to 50 mV range) and a shunt with a resistance of 10.21 ±0.04 μΩ. The voltmeter is connected to the DAS through the rectifier controllers and an amplifier. To reduce the uncertainty of the current measurement the voltage loop was calibration checked by applying a millivolt signal across the shunt leads and the data displayed at the DAS. The uncertainty of the meter used to complete this calibration check was 9 ppm + 0.8 μV. This estimate is based on the HTL theoretical tolerance

The shunt resistance was measured using a Kelvin Bridge (TR-2232) on 4 August 1991. Five resistance measurements were made at that time: 10.18, 10.22, 10.22, 10.22, and 10.21 μΩ. The calibration uncertainty for these measurements was 0.03% reading + 0.03μΩ.

(2-15) $$\bar{X} = 10.21\ \mu\Omega$$

(2-16) $$\omega_E = \frac{t\,\sigma}{\sqrt{N}} = \frac{(2.776)(0.01732\ \mu\Omega)}{\sqrt{5}} = 0.02\ \mu\Omega$$

(2-17) $$\omega_C = (10.21\ \mu\Omega)\left(\frac{0.03\%}{100}\right) + 0.03\ \mu\Omega = 0.033\ \mu\Omega$$

(2-18) $$\begin{aligned} B_{shunt} &= \sqrt{(\omega_E)^2 + (\omega_C)^2} \\ &= \sqrt{(0.02\ \mu\Omega)^2 + (0.033\ \mu\Omega)^2} \\ &= 0.04 \end{aligned}$$

A linear fit of this data where the input is in volts would be:

(2-19) $$V_{out} = -0.004278 + 199.70\ V_{in}$$

Using the resistance data from the shunt the final engineering conversion calculation can be derived.

(2-20)
$$V_{DAS} = V_{out'} = -0.004278 + 0.002039\ i$$

The partial differentials necessary for the calculation of the sensitivity indices are:

(2-21)
$$\frac{\partial i}{\partial V_{DAS}} = \frac{1}{0.002039\ \Omega} = 490.4\ \Omega^{-1}$$

(2-22)
$$\frac{\partial i}{\partial R} = \frac{-i}{R} = -97{,}943\ \frac{A}{\Omega}$$

(2-23)
$$\frac{\partial V_{DAS}}{\partial V_{in}} = 199.70$$

The total uncertainty can be estimated using the equation:

(2-24)
$$\omega_i = \sqrt{\left[\left(\frac{\partial i}{\partial V_{DAS}}\right)\left(\frac{\partial V_{DAS}}{\partial V_{in}}\right)\omega_{in}\right]^2 + \left[\left(\frac{\partial i}{\partial V_{DAS}}\right)\omega_{DAS}\right]^2 + \left[\left(\frac{\partial i}{\partial R}\right)\omega_{in}\right]^2}$$

The random component of the curve fit has been treated as a bias and was estimated based on the confidence interval of the mean. (See Figure 2-13.) The fixed curve error was computed as described in Appendix C of WSRC-TR-106 and is presented in Figure 2-14. The system noise during the calibration for the current range of 650 to 850 A, was about 740 μV as shown in Figure 2-15. This is slightly larger than the 500 μV that must exist because of DAS roundoff when the data is written to a log. The random uncertainty may then be estimated as:

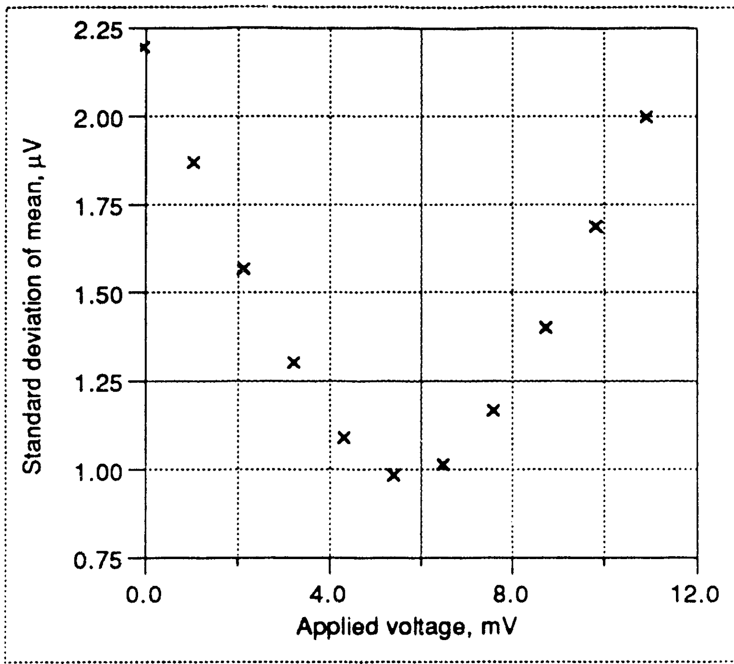

Figure 2-13. Confidence intervals for the mean response for WC00001

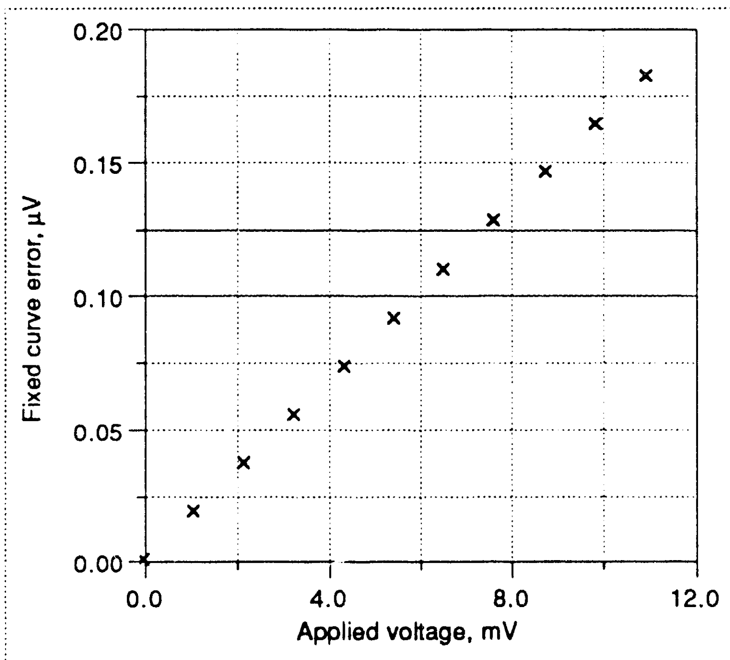

Figure 2-14. Systematic fixed curve errors for WC00001

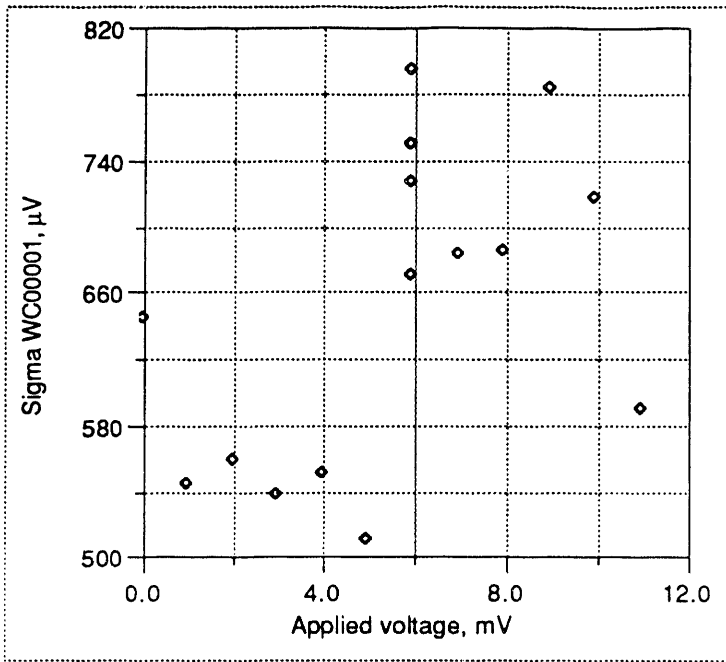

Figure 2-15 Sample standard deviation of output for WC00001 during pretest calibration

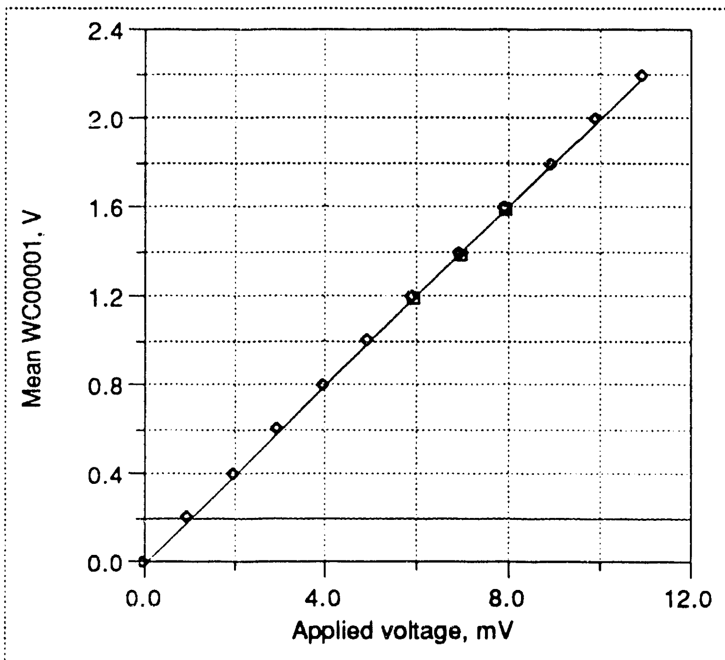

Figure 2-16. Output of WC00001 during calibrations.

Table 2-11.--Systematic uncertainty estimate for WC00001 loop calibration

Current, A	650	700	850
DAS voltage, V	1.321	1.423	1.729
Input voltage, mV	6.636	7.146	8.677
Systematic uncertainty			
Calibration standard uncertainty, µV	0.8	0.9	0.9
Random curve fit uncertainty, µV (Figure 2-11)	1.0	1.1	1.4
Fixed curve uncertainty, µV (Figure 2-12)	0.1	0.1	0.1
Combined systematic uncertainty, µV	1.3	1.4	1.7

Table 12.--Current measurement systematic uncertainties

	Elemental systematic error, B_i	Sensitively index θ_i	Systematic uncertainty $\theta_i B_i$
Systematic uncertainty, 650 A			
Input voltage uncertainties, mV	0.0013	97.93	0.13
Resistance uncertainty, µΩ	0.04	0.0979	0.004
Total systematic uncertainty, A (650 A)	...	...	0.13
Systematic uncertainty, 700 A			
Input voltage uncertainties, mV	0.0014	97.93	0.14
Resistance uncertainty, µΩ	0.04	0.0979	0.004
Total systematic uncertainty, A (700 A)	...	...	0.14
Systematic uncertainty, 850 A			
Input voltage uncertainties, mV	0.0017	97.93	0.17
Resistance uncertainty, µΩ	0.04	0.0979	0.004
Total systematic uncertainty, A (850 A)	...	...	0.17

(2-25) $$P = \frac{t\,\sigma}{\sqrt{N}} = \frac{2 \cdot 740\,\mu V}{\sqrt{120}} = 135\,\mu V$$

Figure 2-16 presents the DAS voltage to shunt voltage conversion equations.

Temperature Measurements

Fluid Thermocouples

Data from the daily flow checks can be used to evaluate the accuracy of the thermocouple temperature measurements. The fluid temperature as measured by TT00001 is compared with the output of each of the fluid thermocouples (except TC00003, impulse line temperature; and TL03002, head tank temperature) in Table 2-13. The nominal equation was used to convert the DAS voltage units to engineering units. Figure 2-17 demonstrates that the differences between the calculated thermocouple temperatures and TT00001 temperature are normally distributed. Table 2-14 presents the quartile information for Figure 2-17.

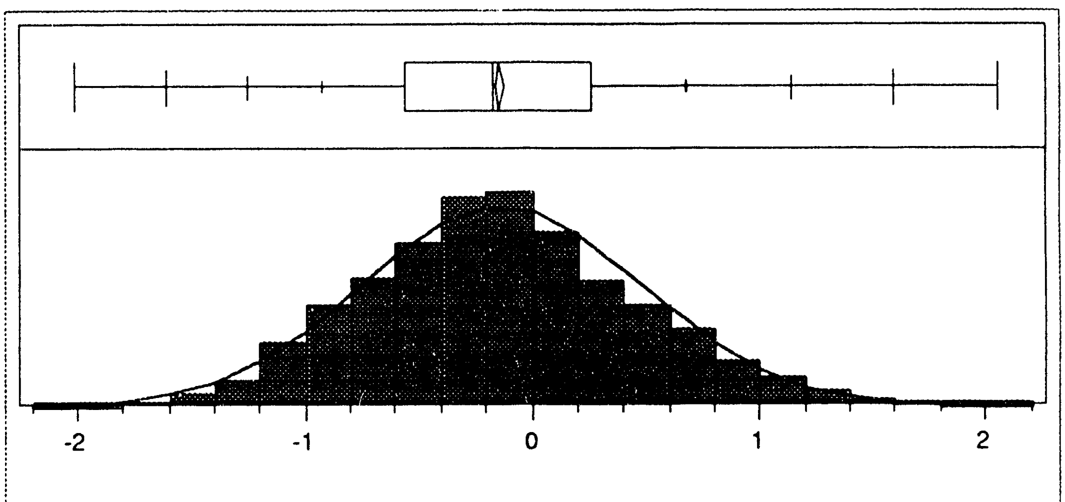

Figure 2.17, Error distribution for thermocouples as compared with TT00001 (Excluding TC00001, TC00002, TC00003, and TL03002)

Table 2-13.--Results from daily flow checks, temperature calculated from DAS mean as compared with TT00001.

Instrument Number	N	Mean °C	S °C	S_m °C	Curve coefficients a, V	Curve coefficients b, V/°C
TC00001	61	0.46	1.11	0.28	0	0.010000
TC00002	61	-0.09	1.77	0.45	0	0.010000
TF01202	61	-0.12	0.47	0.12	0	0.033333
TF01204	61	-0.01	0.47	0.12	0	0.033333
TF02522	61	0.00	0.46	0.12	0	0.033333
TF02524	61	-0.15	0.45	0.12	0	0.033333
TF04172	61	-0.03	0.46	0.12	0	0.033333
TF04174	61	0.10	0.44	0.11	0	0.033333
TF05822	61	-0.10	0.43	0.11	0	0.033333
TF05824	61	-0.22	0.43	0.11	0	0.033333
TF06922	61	0.25	0.42	0.11	0	0.033333
TF06924	61	0.15	0.44	0.11	0	0.033333
TF08022	61	0.16	0.44	0.11	0	0.033333
TF08024	61	-0.02	0.44	0.11	0	0.033333
TL01001	61	-0.09	0.51	0.13	0	0.033333
TL02001	61	0.02	0.41	0.11	0	0.033333
TL03001	61	0.18	0.56	0.14	0	0.033333
TP01308	61	-0.65	0.52	0.13	0	0.033333
TP01317	61	-0.20	0.60	0.15	0	0.010000
TP01413	61	-0.02	0.67	0.17	0	0.010000
TP01505	61	-0.65	0.49	0.13	0	0.033333
TP01702	61	-0.81	0.55	0.14	0	0.033333
TP11917	61	-0.50	0.67	0.17	0	0.010000
TP12008	61	-0.76	0.55	0.14	0	0.033333
TP12105	61	-0.80	0.54	0.14	0	0.033333
TP12113	61	-0.31	0.64	0.16	0	0.010000
TP12302	61	-0.66	0.50	0.13	0	0.033333
TP22917	61	-0.25	0.65	0.17	0	0.010000
TP23008*	21	-0.46	0.46	0.20	0	0.033333
TP23013	61	-0.12	0.62	0.16	0	0.010000
TP23105	61	-0.65	0.48	0.12	0	0.033333
TP23302	61	-0.56	0.49	0.12	0	0.033333
TP33908	61	-0.31	0.45	0.12	0	0.033333
TP33917	61	0.53	0.63	0.16	0	0.010000
TP34013	61	0.54	0.51	0.13	0	0.010000
TP34105	61	-0.27	0.44	0.11	0	0.033333
TP34302†	56	-0.23	0.46	0.12	0	0.033333
TP45008	61	-0.11	0.45	0.11	0	0.033333
TP45105	61	-0.44	0.44	0.11	0	0.033333
TP45302‡	59	-0.35	0.43	0.11	0	0.033333
TP45613	61	0.39	0.50	0.13	0	0.010000

Table 2-13.--Continued

Instrument Number	N	Mean °C	S °C	S_m °C	Curve coefficients	
					a, V	b, V/°C
TP45717	61	0.27	0.52	0.13	0	0.010000
TP45808	61	-0.21	0.44	0.11	0	0.033333
TP45905	61	-0.27	0.46	0.12	0	0.033333
TP46102	61	-0.20	0.44	0.11	0	0.033333
TP46217§	44	0.90	0.52	0.16	0	0.010000
TP46308	61	-0.29	0.45	0.12	0	0.033333
TP46413	61	0.75	0.53	0.13	0	0.010000
TP46505	61	-0.08	0.45	0.12	0	0.033333
TP46602	61	-0.19	0.47	0.12	0	0.033333
TP46808	61	0.04	0.45	0.12	0	0.033333
TP47005	61	-0.02	0.46	0.12	0	0.033333
TP47202	61	-0.05	0.45	0.12	0	0.033333
Mean		-0.12	0.53	...	...	...
Minimum		-0.81	0.42	...	...	...
Maximum		0.90	1.77	...	...	...

*TP23008 was damaged on 14 May 1993 during channel disassembly.

†TP34302 was functioning correctly on 16 July 1993 and did not function correctly on and after 20 July 1993.

‡TP45302 did not function on 30 April 1993 because of loose connections. This was corrected for the remainder of the testing.

§TP46217 was damaged on 24 June 1993 during channel assembly.

The uncertainty of the thermometers used for TT00001 was 0.5°C. The data in Table 2-13 can be used to estimate the temperature measurement uncertainties for most of the thermocouples used for this task. The overall temperature measurement uncertainty can be estimated using Equation 2-26.

Table 2-14.--Statistical information for data presented in Figure 2-17.

	Value, °C
Maximum quartile (100.0%)	2.06
99.5%	1.59
97.5%	1.14
90.0%	0.68
75.0% quartile	0.26
Median	-0.17
25.0% quartile	-0.55
10.0%	-0.92
2.5%	-1.25
0.5%	-1.60
Minimum quartile (0.0%)	-2.01
Mean	-0.14
Sample standard deviation	0.61
Standard deviation of the mean	0.01
N	3047

Several thermocouples failed during use. The date of failure is noted in Table 2-13.

(2-26)
$$B_T{}^2 = B_{TT00001}{}^2 + \bar{\Delta}^2 + \left(\frac{2\,\sigma}{\sqrt{N}}\right)^2$$

$$= (0.5°C)^2 + (-0.12°C)^2 + \left(\frac{2 \cdot 0.53}{\sqrt{61}}\right)^2$$

$$B_T = 0.53°C$$

Thermocouples TC00003 and TL03002

The accuracy of the thermocouples TC00003, impulse line temperature, and TL03002, head tank temperature can be estimated by comparison with the ambient air or loop temperature recorded during the pretest zero checks. This is appropriate because the ambient air and loop temperatures were fairly stable in after sitting idle over night. To eliminate the potential of including data where transient ambient temperatures exist only data within as specified in Equation 2-27 were considered.

(2-27) $$|TT00001 - T_{amb}| < 2°C$$

The HTL tolerance of the thermometer used for ambient temperature checks was ±1°C. The data in Tables 2-15, and 2-16 can be used to estimate the temperature measurement uncertainties as was done previously for the fluid thermocouples. The evaluation could have been based on either the ambient air temperature or the loop temperature as measured by TT00001. Since the errors were smaller when TT00001 was used as the standard the thermocouples were evaluated based on TT00001. The uncertainties are sumarized in Table 2-17.

Table 2-15.--Statistical information for TC00003 where $|TT00001 - T_{amb}| < 2°C$

	Error based on TT00001	Error based on T_{amb}
Mean	0.59	1.00
Sample standard deviation	1.04	0.33
Standard deviation of the mean	0.23	0.074
N	20	20

Table 2-16.--Statistical information for TL03002 where $|TT00001 - T_{amb}| < 2°C$

	Error based on TT00001 °C	Error based on T_{amb} °C
Mean	0.75	1.15
Sample standard deviation, S	1.16	0.62
Standard deviation of the mean, S_m	0.26	0.14
N	20	20

Table 2-17.--Uncertainty estimate for TC00003, and TL03002

Instrument number	B_{T00001} °C	$\bar{\Delta}$ °C	$2 \cdot S_m$ °C	B °C
TC00003	0.5	0.59	0.46	0.90
TL03002	0.5	0.75	0.52	1.04

APPENDIX 3

MEASUREMENT UNCERTAINTY ANALYSIS

Measurement Uncertainty Efforts

This appendix presents the systematic uncertainty estimate calculations for selected parameters (resultants). The application of these estimates is discussed in the body of this report. All uncertainties have been estimated at 95% confidence. Uncertainties have been assumed symmetric and normal. They have been combined using Equation 80.

Geometric Uncertainties

Most of the geometric uncertainties had negligible measurement variation There were two exceptions to this: the channel width, a, and the channel depth, b. Both spatial and time dependent variations were observed. Spatial variations were the result of slight variations in the channel cross-section at different longitudinal locations. Some time dependent variations are also noticeable in the data presented in Appendix 1. Table 3-0 provides a systematic uncertainty estimate for the channel width and depth. The total systematic uncertainty for the respective measurement was calculated using Equation 3-1.

$$B_i = \sqrt{B_{M\&TE}^2 + \frac{t_{\alpha/2}\, S^2}{\sqrt{N}}} \qquad (3\text{-}1)$$

Table 3-0.--Channel width and depth uncertainty estimates

	Const.	S mm	$B_{M\&TE}$ mm	N	$t_{\alpha/2}$	B_i mm
channel width, a	2	0.113	0.076	8	2.365	0.1
	4	0.207	0.076	7	2.447	0.2
channel depth, b	2	0.102	0.076	10	2.262	0.07
	4	0.093	0.076	10	2.262	0.07

Friction Factor

The friction factor is defined by Equation 18. When written in terms of the data reduction input quantities (directly measured, estimated, and channel geometry values) Equation 18 becomes:

$$f = \frac{\Delta p_{2\text{-}3} - L\,g\,(\rho_\infty - \rho_{23})}{\left(\frac{L}{D}\right)\left(\frac{\rho_{23}}{2}\right)\left(\frac{Q}{A_f}\right)^2} \tag{3-2}$$

Most of the partial derivative equations necessary for the use of Equation 80 are not readily calculated. An iterative forward-difference calculation was used to estimate the more complex partial derivatives. These finite difference calculations are summarized in Tables 3-1, 3-2, 3-3, 3-4.

The uncertainty terms, ρ_∞ and ρ_{23} could be considered as a composite of two uncertainties: (1) the curve fit error, and (2) the measured temperature uncertainty. For this analysis the curve fit uncertainties have been handled separately from those which are the result of temperature uncertainties. The fluid property uncertainties resulting from temperature uncertainty have been folded into the temperature measurement uncertainties by the numeric evaluation method used to calculate the sensitivity coefficients.

Several of the uncertainty terms are partially correlated. The three temperature terms are correlated as well as the two density terms. For construction 4.0 operating at a Reynolds number of 10,000 the effect of the correlated uncertainty components is estimated as:

$$B_{cor}^2 = 2\left(\frac{\partial f}{\partial T_2}\right)\left(\frac{\partial f}{\partial T_3}\right) B^{\bullet}_{T_2} B^{\bullet}_{T_3} + 2\left(\frac{\partial f}{\partial T_2}\right)\left(\frac{\partial f}{\partial T_\infty}\right) B^{\bullet}_{T_2} B^{\bullet}_{T_\infty} + 2\left(\frac{\partial f}{\partial T_3}\right)\left(\frac{\partial f}{\partial T_\infty}\right) B^{\bullet}_{T_3} B^{\bullet}_{T_\infty} + 2\left(\frac{\partial f}{\partial \rho_{23}}\right)\left(\frac{\partial f}{\partial \rho_\infty}\right) B^{\bullet}_{\rho_{23}} B^{\bullet}_{\rho_\infty} \tag{3-3}$$

Table 3-1.--Friction factor sensitivity coefficient estimates for open channel, construction 4, inlet temperature 60°C, Re = 10,000

		x_i	$x_i + \Delta x_i$	$\frac{\partial f}{\partial x_i}$
Friction factor	f	0.03160	...	...
Channel width, mm	a	79.8	80.6	811e-6
Channel depth, mm	b	3.16	3.19	30.0e-3
Rib width, mm	x_o	0.0	...	0.000
Channel length	L	1.397	1.411	-0.0245
Measured pressure loss, kPa	Δp_{2-3}	2.414	2.438	14.3e-3
Impulse line density, kg/m³	ρ_∞	997.0	1007.0	-196e-6
Bulk density, kg/m³	ρ_{23}	981.9	991.7	-31.9e-6
Flow, cm³/s	Q	198.4	200.4	-314e-6
Inlet temperature, °C	T_{in}	60.00	60.60	-91.1e-6
Exit temperature, °C	T_{out}	60.00	60.60	8.17e-6
Impulse line temperature, °C	T_∞	25.00	25.30	71.2e-6

Table 3-2.--Friction factor sensitivity coefficient estimates for open channel, construction 4.0, inlet temperature 60°C, Re = 20,000

		x_i	$x_i + \Delta x_i$	$\frac{\partial f}{\partial x_i}$
Friction factor	f	0.02657	...	...
Channel width, mm	a	79.8	80.6	579e-6
Channel depth, mm	b	3.16	3.19	22.4e-3
Rib width, mm	x_o	0	...	0.000
Channel length	L	1.397	1.411	-25.2e-3
Measured pressure loss, kPa	Δp_{2-3}	7.629	7.705	2.50e-3
Impulse line density, kg/m³	ρ_∞	997.0	1007.0	-57.3e-6
Bulk density, kg/m³	ρ_{23}	981.9	991.7	-35.2e-6
Flow, cm³/s	Q	396.8	400.8	-152e-6
Inlet temperature, °C	T_{in}	60.0	60.6	-155e-6
Exit temperature, °C	T_{out}	60.0	60.6	-130e-6
Impulse line temperature, °C	T_∞	25.0	25.3	-257e-6

Table 3-3.--Friction factor sensitivity coefficient estimates for rib channel, construction 2, inlet temperature 60°C, Re = 10,000

		x_i	$x_i + \Delta x_i$	$\frac{\partial f}{\partial x_i}$
Friction factor	f	0.03160	...	...
Channel width, mm	a	79.6	80.4	850e-6
Channel depth, mm	b	3.09	3.12	30.2e-3
Rib width, mm	x_o	2.07	2.09	-845e-6
Channel length	L	1.397	1.411	-24.2e-3
Measured pressure loss, kPa	Δp_{2-3}	2.580	2.606	12.0e-3
Impulse line density, kg/m^3	ρ_∞	997.0	1007.0	-164e-6
Bulk density, kg/m^3	ρ_{23}	981.9	991.7	-31.9e-6
Flow, cm^3/s	Q	200.2	202.2	-311e-6
Inlet temperature, °C	T_{in}	60.00	60.60	-74.7e-6
Exit temperature, °C	T_{out}	60.00	60.60	8.13e-6
Impulse line temperature, °C	T_∞	25.00	25.30	59.4e-6

Table 3-4.--Friction factor sensitivity coefficient estimates for rib channel, construction 2.0, inlet temperature 60°C, Re = 20,000

		x_i	$x_i + \Delta x_i$	$\frac{\partial f}{\partial x_i}$
Friction factor	f	0.02662	...	...
Channel width, mm	a	0.0796	0.0804	716e-6
Channel depth, mm	b	0.00309	0.00312	25.4e-3
Rib width, mm	x_o	0.00207	0.00209	-712e-6
Channel length	L	1.397	1.411	-19.3e-3
Measured pressure loss, kPa	Δp_{2-3}	9.112	9.203	2.99e-3
Impulse line density, kg/m^3	ρ_∞	997.0	1007.0	-41.0e-6
Bulk density, kg/m^3	ρ_{23}	981.9	991.7	-26.8e-6
Flow, cm^3/s	Q	400.3	404.3	-131e-6
Inlet temperature, °C	T_{in}	60.00	60.60	-13.9e-6
Exit temperature, °C	T_{out}	60.00	60.60	6.85e-6
Impulse line temperature, °C	T_∞	25.00	25.30	14.9e-6

Using the partial derivatives presented in Table 3-5 Equation 3-3 becomes:

$$B_{cor}^2 = 10^{-12}\left[2\left(\frac{-91.1}{°C}\right)\left(\frac{8.17}{°C}\right)(0.5°C)(0.5°C) + 2\left(\frac{-91.1}{°C}\right)\left(\frac{71.2}{°C}\right)(0.5°C)(0.5°C) + 2\left(\frac{8.17}{°C}\right)\left(\frac{71.2}{°C}\right)(0.5°C)(0.5°C) + 2\left(\frac{-31.9}{kg/m^3}\right)\left(\frac{-196}{kg/m^3}\right)\left(0.5\frac{kg}{m^3}\right)\left(.5\frac{kg}{m^3}\right)\right]$$

$$B_{cor}^2 = -198e\text{-}12$$

For the above case the correlated systematic uncertainties tend to reduce the overall uncertainty estimate by a negligible quantity. The uncertainty estimates presented in Tables 3-5, 3-6, 3-7, and 3-8 have therefore been treated as independent.

Table 3-5.--Friction factor systematic uncertainty estimate for open channel, construction 4, inlet temperature 60°C, Re = 10,000

		B_i	θ_i	$\theta_i B_i$
Channel width, mm*	a	0.4	811e-6	0.00032
Channel depth, mm†	b	0.2	30.0e-3	0.00600
Rib width, mm	x_o	0.04	0.000	0.00000
Channel length, m	L	0.0008	-0.0245	-0.00002
Measured pressure loss, kPa	Δp_{2-3}	0.400	14.3e-3	0.00572
Impulse line density, kg/m³	ρ_∞	1	-196e-6	-0.00020
Bulk density, kg/m³	ρ_{23}	1	-31.9e-6	-0.00003
Flow, cm³/s	Q	1.4	-314e-6	-0.00044
Inlet temperature, °C	T_{in}	0.53	-91.1e-6	-0.00005
Exit temperature, °C	T_{out}	0.53	8.17e-6	0.00000
Impulse line temperature, °C	T_∞	0.53	71.2e-6	0.00004
Root-sum-square				0.0083

*The elemental uncertainty was taken as the difference between two measurement methods. This is presented in Table 1-4.

†The elemental uncertainty was taken as twice the standard deviation for the 1 July 1993 data as presented in Table 1-7.

Table 3-6.--Friction factor systematic uncertainty estimate for open channel, construction 4.0, inlet temperature 60°C, Re = 20,000

		B_i	θ_i	$\theta_i B_i$
Channel width, mm	a	0.4	579e-6	0.00023
Channel depth, mm	b	0.2	22.4e-3	0.00448
Rib width, mm	x_o	0.04	0.000	0.00000
Channel length, m	L	0.0008	-25.2e-3	-0.00002
Measured pressure loss, kPa	Δp_{2-3}	0.400	2.50e-3	-0.00100
Impulse line density, kg/m³	ρ_∞	1	-57.3e-6	-0.00006
Bulk density, kg/m³	ρ_{23}	1	-35.2e-6	-0.00004
Flow, cm³/s	Q	1.2	-152e-6	-0.00018
Inlet temperature, °C	T_{in}	0.53	-155e-6	-0.00008
Exit temperature, °C	T_{out}	0.53	-130e-6	-0.00007
Impulse line temperature, °C	T_∞	0.53	-257e-6	-0.00014
Root-sum-square				0.0046

Table 3-7.--Friction factor systematic uncertainty estimate for rib channel, construction 2, inlet temperature 60°C, Re = 10,000

		B_i	θ_i	$\theta_i B_i$
Channel width, mm	a	0.4	850e-6	0.00034
Channel depth, mm	b	0.2	30.2e-3	0.00604
Rib width, mm	x_o	0.04	-845e-6	-0.00003
Channel length, m	L	0.0008	-24.2e-3	-0.00002
Measured pressure loss, kPa	Δp_{2-3}	0.400	12.0e-3	0.00480
Impulse line density, kg/m^3	ρ_∞	1	-164e-6	-0.00016
Bulk density, kg/m^3	ρ_{23}	1	-31.9e-6	-0.00003
Flow, cm^3/s	Q	1.4	-311e-6	-0.00044
Inlet temperature, °C	T_{in}	0.53	-74.7e-6	-0.00004
Exit temperature, °C	T_{out}	0.53	8.13e-6	0.00000
Impulse line temperature, °C	T_∞	0.53	59.4e-6	0.00003
Root-sum-square				0.0077

Table 3-8.--Friction factor systematic uncertainty estimate for rib channel, construction 2.0, inlet temperature 60°C, Re = 20,000

		B_i	θ_i	$\theta_i B_i$
Channel width, mm	a	0.4	716e-6	0.00029
Channel depth, mm	b	0.2	25.4e-3	0.00508
Rib width, mm	x_o	0.04	-712e-6	-0.00003
Channel length, m	L	0.0008	-19.3e-3	-0.00002
Measured pressure loss, kPa	Δp_{2-3}	0.400	2.99e-3	0.00120
Impulse line density, kg/m^3	ρ_∞	1	-41.0e-6	-0.00004
Bulk density, kg/m^3	ρ_{23}	1	-26.8e-6	-0.00003
Flow, cm^3/s	Q	1.4	-131e-6	-0.00018
Inlet temperature, °C	T_{in}	0.53	-13.9e-6	-0.00001
Exit temperature, °C	T_{out}	0.53	6.85e-6	0.00000
Impulse line temperature, °C	T_∞	0.53	14.9e-6	0.00001
Root-sum-square				0.00523

Energy Balance Ratio

The energy balance ratio, η_p is defined by Equation 3-4. For this analysis both the power and fluid energy loss terms will be considered zero.

$$\eta_p = \frac{P_{elec}}{P_{fluid}} = \frac{Vi - \text{losses}}{Q\,\rho\,c_p\left(T_{out} - T_{in}\right) + \text{losses}} \qquad (3\text{-}4)$$

The uncertainty terms for the specific heat could be considered as a composite of three uncertainties: (1) the curve fit error, (2) the error introduced by the linear property assumption, and (3) the measured temperature uncertainty. For this analysis the first two uncertainties have been handled separately. The third uncertainty has been folded into the temperature measurement uncertainty by numeric evaluation method used to calculate some of the sensitivity coefficients. The density uncertainty consists of only the first and last of the three error terms since the density is taken at inlet conditions.

The error introduced by the linear property assumption could be evaluated numerically, however this level of rigor would have little impact on the final uncertainty estimate associated with assuming that the fluid properties are linear. It must be remembered that the linear temperature rise as the fluid passes through the channel is an assumption. Figure 3-1 presents specific heat estimates obtained using two methods: (1) The specific heat is estimated using Equation 75 at the bulk temperature (the mean of the inlet and outlet temperature). (2) The specific heat is estimated as the mean of the inlet and exit specific heats as calculated using Equation 75. The error introduced by the linearity assumption will be taken as the difference between these two values as described in Equation 3-5. The uncertainty values are tabulated in Table 3-8a.

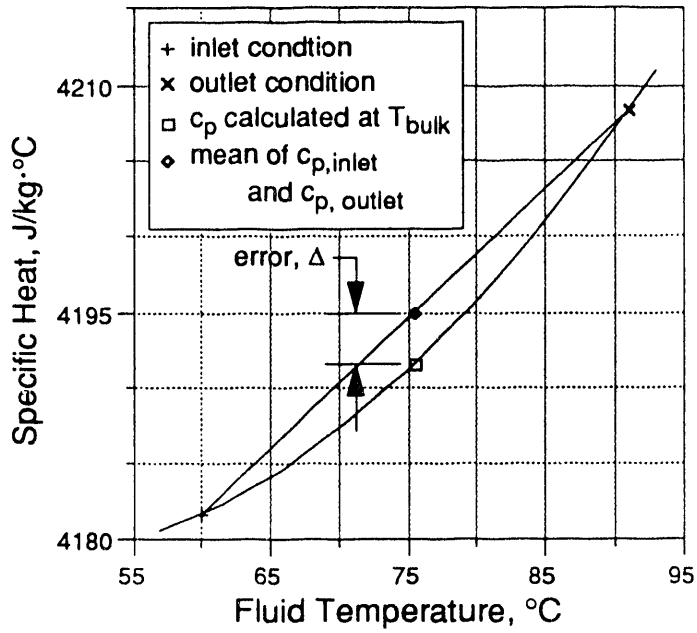

Figure 3-1, Specific heat estimates using alternate linearity assumptions.

Table 3-8a.--Specific heat estimates using alternate linearity assumptions (T_{in} = 60°C)

T_{out} °C	T_b °C	$c_{p,\,b}$ J/kg·°C	$c_{p,\,mean}$ J/kg·°C	Δ J/kg·°C
65.00	62.50	4182.8	4182.9	0.1
70.00	65.00	4184.2	4184.5	0.4
75.00	67.50	4185.6	4186.4	0.8
80.00	70.00	4187.3	4188.7	1.4
85.00	72.50	4189.2	4191.4	2.2
90.00	75.00	4191.2	4194.4	3.2
95.00	77.50	4193.4	4197.7	4.3

(3-5)
$$B = \Delta = \frac{\psi\left(T_{out}\right) - \psi\left(T_{in}\right)}{2} - \psi\left(T_{ave}\right)$$

Some of the partial derivatives necessary for the solution of Equation 80 can be solved directly These solutions are listed below.

$$\frac{\partial \eta_p}{\partial V} = \frac{\eta_p}{V} \qquad \frac{\partial \eta_p}{\partial i} = \frac{\eta_p}{i} \qquad \frac{\partial \eta_p}{\partial Q} = \frac{-\eta_p}{Q}$$

$$\frac{\partial \eta_p}{\partial \rho} = \frac{-\eta_p}{\rho} \qquad \frac{\partial \eta_p}{\partial c} = \frac{-\eta_p}{c}$$

The directly solved and iterative forward-difference solutions of the partial derivatives necessary to solve Equation 80 are presented in Tables 3-9 and 3-10. The systematic uncertainty estimates for the energy balance ratio are presented in Tables 3-11 and 3-12.

Table 3-9.--Energy balance ratio sensitivity coefficient estimates for construction 4 (open channel) at 7.5 gpm

		x_i	$x_i + \Delta x_i$	$\frac{\partial \eta_P}{\partial x_i}$
Energy balance ratio	η_P	0.970	...	...
Applied voltage, V	V	43.83	...	0.0221
Applied current, A	i	699	...	0.00139
Flow, cm^3/s	Q	495	...	-0.00196
Density, inlet (curve fit), kg/m^3	ρ	981.9	...	-0.000988
Specific heat, bulk (curve fit), J/kg·°C	c_p	4186.0	...	-0.000232
Fluid property linearity assumption, J/kg·°C	c_p	4186.0	...	-0.000232
Exit temperature, °C	T_{out}	60.00	60.60	0.0624
Inlet temperature, °C	T_{in}	76.25	77.01	-0.0571

Table 3-10.--Energy balance ratio sensitivity coefficient estimates for construction 4 (open channel) at 1260 cm^3/s (20 gpm)

		x_i	$x_i + \Delta x_i$	$\frac{\partial \eta_P}{\partial x_i}$
Energy balance ratio	η_P	0.970	...	...
Applied voltage, V	V	43.83	...	0.0221
Applied current, A	i	699	...	0.00139
Flow, cm^3/s	Q	1261	...	-0.000769
Density, inlet (curve fit), kg/m^3	ρ	981.9	...	-0.000988
Specific heat, bulk (curve fit), J/kg·°C	c_p	4183.1	...	-0.000232
Fluid property linearity assumption, J/kg·°C	c_p	4183.1	...	-0.000232
Exit temperature, °C	T_{out}	60.00	60.60	0.1768
Inlet temperature, °C	T_{in}	66.1	77.01	-0.0947

Table 3-13.--Energy balance ratio systematic uncertainty estimate for construction 4 (open channel) at 473 cm^3/s (7.5 gpm)

		B_i	θ_i	$\theta_i B_i$
Applied voltage, V	V	0.0089	0.0221	0.0002
Applied current, A	i	1.4	0.00139	0.0019
Flow, cm^3/s	Q	1.2	-0.00196	-0.0024
Density, inlet (curve fit), kg/m^3	ρ	1	-0.000988	-0.0010
Specific heat, bulk (curve fit), J/kg·°C	c_p	4	-0.000232	-0.0009
Fluid property linearity assumption, J/kg·°C	c_p	6	-0.000232	-0.0014
Exit temperature, °C	T_{out}	0.5	0.0624	0.0312
Inlet temperature, °C	T_{in}	0.5	-0.0571	-0.0285
Root-sum-square				0.042

Table 3-14.--Energy balance ratio systematic uncertainty estimate for construction 4 (open channel) at 1261 cm^3/s (20 gpm)

		B_i	θ_i	$\theta_i B_i$
Applied voltage, V	V	0.0089	0.0221	0.0002
Applied current, A	i	1.4	0.00139	0.0019
Flow, cm^3/s	Q	2	-0.000769	-0.0015
Density, inlet (curve fit), kg/m^3	ρ	1	-0.000988	-0.0010
Specific heat, bulk (curve fit), J/kg·°C	c_p	4	-0.000232	-0.0009
Fluid property linearity assumption, J/kg·°C	c_p	6	-0.000232	-0.0014
Exit temperature, °C	T_{out}	0.5	0.1768	0.0884
Inlet temperature, °C	T_{in}	0.5	-0.0947	-0.0473
Root-sum-square				0.10

Heat Flux

The heat flux can be calculated using three different methods. Two methods are based on assuming that the power applied the rig is uniform over the entire heated area so that the heat flux is then the power divided by the heated area. The third method is independent of the heated area estimate. It utilizes the thermocouples which are placed in different positions in the heated plate. These thermocouples measure the temperature gradient in the plate and therefore can be used to estimate the heat flux.

Electrical

The heat flux calculated from the electrical energy balance, ϕ_e, is defined by Equation 3-6. As with the energy balance ratio, the loss term will be assumed zero.

(3-6)
$$\phi_e = \frac{P_e}{A_h} = \frac{Vi - \text{losses}}{L_h\, a_h}$$

All of the necessary partial differential can readily be solved for directly. Their solutions are:

$$\frac{\partial \phi_e}{\partial V} = \frac{\phi_e}{V} \qquad \frac{\partial \phi_e}{\partial i} = \frac{\phi_e}{i}$$

$$\frac{\partial \phi_e}{\partial L_h} = \frac{-\phi_e}{L_h} \qquad \frac{\partial \phi_e}{\partial a_h} = \frac{-\phi_e}{a_h}$$

The heat flux for Construction 2 was calculated based on the heated surface that was exposed to forced convection. This reduced the heated width by the rib width. Equation 3-6 then becomes:

(3-7) $$\phi_e = \frac{P_e}{A_h} = \frac{Vi - \text{losses}}{L_h(a_h - x_o)}$$

The partial differential solutions of Equation 3-7 are the same as for Equation 3-6 except as listed below.

$$\frac{\partial \phi_e}{\partial a_h} = \frac{-\phi_e}{a_h - x_o} \qquad \frac{\partial \phi_e}{\partial x_o} = \frac{-\phi_e}{a_h - x_o}$$

The sensitivity coefficient estimates necessary to evaluate the uncertainties are presented in Tables 3-17 and 3-17b. Tables 3-18 and 3-18a provide the systematic uncertainty estimates.

Table 3-17.--Heat flux (electrical) sensitivity coefficient estimates for construction 4 (open channel) at 473 cm^3/s (7.5 gpm), 30.64 kW

		x_i	$x_i + \Delta x_i$	$\frac{\partial \phi_e}{\partial x_i}$
Heat flux, kW/m^2	ϕ_e	330.0	...	...
Applied voltage, V	V	43.83	...	7.53
Applied current, A	i	699	...	0.472
Heated width, mm	a_h	76.2	...	·4.33
Rib width, mm	x_o	0.00	...	0.00
Heated length, m	L_h	1.219	...	-271

Table 3-17b.--Heat flux (electrical) sensitivity coefficient estimates for construction 2 (rib) at 473 cm^3/s (7.5 gpm), 30.64 kW.

		x_i	$x_i + \Delta x_i$	$\frac{\partial \phi_e}{\partial x_i}$
Heat flux, kW/m^2	ϕ_e	339.0	...	...
Applied voltage, V	V	43.83	...	7.73
Applied current, A	i	699	...	0.485
Heated width, mm	a_h	76.2	...	-4.57
Rib width, mm	x_o	2.07	...	4.57
Heated length, m	L_h	1.219	...	-278

Table 3-18.--Heat flux (electrical) systematic uncertainty estimate for construction 4 (open channel) at 473 cm^3/s (7.5 gpm), 30.64 kW

		B_i	θ_i	$\theta_i B_i$
Applied voltage, V	V	0.0089	7.53	0.07
Applied current, A	i	1.4	0.472	0.66
Heated width, mm	a_h	1.6	-4.33	-6.93
Rib width, mm	x_o	0.00	0.00	0.00
Heated length, m	L_h	0.001	-271	-0.27
Root-sum-square				7.0

Table 3-18.--Heat flux (electrical) systematic uncertainty estimate for construction 2 (rib) at 7.5 gpm

		B_i	θ_i	$\theta_i B_i$
Applied voltage, V	V	0.0089	7.73	0.1
Applied current, A	i	1.4	0.485	0.7
Heated width, mm	a_h	3.4	-4.57	-15.5
Rib width, mm	x_o	0.04	4.57	0.2
Heated length, m	L_h	0.001	-278	-0.3
Root-sum-square				15.6

Fluid

The heat flux calculated from the fluid energy balance, ϕ_f, is defined by Equation 3-8. The loss term will again be assumed zero.

$$\phi_f = \frac{P_f}{A_h} = \frac{Q\,\rho_{in}\,c_p\left(T_{out} - T_{in}\right) - \text{losses}}{L_h\,a_h} \tag{3-8}$$

As with the energy balance ratio, the specific heat and the density uncertainty terms are a composite of several uncertainties. They will be handles in the same manner as used for the energy balance ratio uncertainty estimate.

Some of the partial derivatives listed in Equation 3-8 can be readily solved. These solutions are listed below.

$$\frac{\partial \phi_f}{\partial Q} = \frac{\phi_f}{Q} \qquad \frac{\partial \phi_f}{\partial \rho_{in}} = \frac{\phi_f}{\rho_{in}} \qquad \frac{\partial \phi_f}{\partial c_p} = \frac{\phi_f}{c_p}$$

$$\frac{\partial \phi_f}{\partial L} = \frac{-\phi_f}{L} \qquad \frac{\partial \phi_f}{\partial a} = \frac{-\phi_f}{a}$$

The directly solved and iterative forward-difference solutions the partial derivatives necessary to solve Equation 80 are presented in Table 3-19. The systematic uncertainty estimates for the energy balance ratio are presented in Table 3-20. Since the uncertainty for this method is higher than the uncertainty calculated using the electrical energy balance, only the uncertainty estimate for Construction 4.0 is presented.

Table 3-19.--Heat flux (fluid) sensitivity coefficient estimates for construction 4 (open channel) at 7.5 gpm

		x_i	$x_i + \Delta x_i$	$\frac{\partial \phi_f}{\partial x_i}$
Heat flux, kW/m^2	ϕ_f	330.0	...	...
Flow, cm^3/s	Q	473.0	...	0.698
Density, inlet (curve fit), kg/m^3	ρ	981.9	...	0.336
Specific heat, bulk (curve fit), J/kg·°C	c_p	4186.0	...	78.8e-3
Fluid property linearity assumption, J/kg·°C	c_p	4186.0	...	78.8e-3
Inlet temperature, °C	T_{in}	60.00	60.60	-5.36
Exit temperature, °C	T_{out}	76.25	77.01	34.4
Heated width, mm	a_h	76.2	...	-4.33
Rib width, mm	x_o	0.00	...	0.00
Heated length, m	L_h	1.219	...	-271

Table 3-20.--Heat flux (fluid) systematic uncertainty estimate for construction 4 (open channel) at 7.5 gpm

		B_i	θ_i	$\theta_i B_i$
Flow, cm^3/s	Q	3	0.698	2.1
Density, inlet (curve fit), kg/m^3	ρ	20	0.336	6.7
Specific heat, bulk (curve fit), J/kg·°C	c_p	80	78.8e-3	6.3
Fluid property linearity assumption, J/kg·°C	c_p	10	78.8e-3	0.8
Inlet temperature, °C	T_{in}	0.5	-5.36	-2.7
Exit temperature, °C	T_{out}	0.5	34.4	17.2
Heated width, mm	a_h	3.4	-4.33	-14.7
Rib width, mm	x_o	0.04	0.00	0.0
Heated length, m	L_h	0.001	-271	-0.3
Root-sum-square				24.7

Conduction

The wall temperature thermocouples could be used to estimate the local heat flux. The wall temperature data for File FS_930601_1136 presented in Tables 41 will be used for this analysis. The grand mean of the wetted thermocouple locations was -0.33 ± 0.05 mm. The locations of the dry thermocouples were assumed to be at -2.92 ± 0.08 mm. The thermal conductivity of aluminum at 130°C was taken as 173 W/m·°C. (77)

(3-9)

$$\phi_c = \frac{k\left(T_{dry} - T_{wet}\right)}{\left|y_{dry} - y_{wet}\right|}$$

$$= \frac{\left(173\,\frac{W}{m\cdot{}^\circ C}\right)(133.98^\circ C - 127.43^\circ C)}{\left|-2.92\ mm + 0.33\ mm\right|}$$

$$= 438\,\frac{W}{m^2\cdot{}^\circ C}$$

The partial derivatives necessary for evaluation of the sensitivity coefficients are listed below.

$$\frac{\partial\phi_c}{\partial k} = \frac{\phi_c}{k} \qquad \frac{\partial\phi_c}{\partial T_{dry}} = \frac{\phi_c}{\left|T_{dry} - T_{wet}\right|} \qquad \frac{\partial\phi_c}{\partial T_{wet}} = \frac{-\phi_c}{\left|T_{dry} - T_{wet}\right|}$$

$$\frac{\partial\phi_c}{\partial y_{dry}} = \frac{-\phi_c}{\left|y_{dry} - y_{wet}\right|} \qquad \frac{\partial\phi_c}{\partial y_{wet}} = \frac{\phi_c}{\left|y_{dry} - y_{wet}\right|}$$

The temperature uncertainty terms would be a combination of the basic measurement uncertainty presented in Appendix 2 and the variability observed during the testing.

$$U_{T_{dry}} = \sqrt{(0.5^\circ C)^2 + (2\cdot 0.66^\circ C)^2}$$

$$= 1.41^\circ C$$

and

$$U_{T_{wet}} = \sqrt{(0.5°C)^2 + (2 \cdot 0.76°C)^2}$$
$$= 1.60°C$$

Table 3-22 presents the uncertainty analysis for the heat flux calculated in Equation 3-9. The uncertainty is very large, 144 W/m^2. This large uncertainty bounds the heat flux calculated by alternate methods for File FS_930601_1136 and indicates that either the electrical or fluid energy balance methods are more appropriate for most of the data reduction.

Table 3-22.--Heat flux (conduction) systematic uncertainty estimate for construction 4 (open channel) based on data presented in Table 403 for FS_930601_1136

		B_i	θ_i	$\theta_i B_i$
Thermal conductivity , W/m·°C	k	2	2.53	5
Wet wall temperature	T_{wet}	1.41	-66.9	-94
Dry wall temperature	T_{dry}	1.60	66.9	107
Wet wall location	y_{wet}	0.05	169	8
Dry wall location	y_{dry}	0.08	-169	-14
Root-sum-square				144

Q_{ratio}

The Q_{ratio} is defined by Equation 3-10.

$$Q_{ratio} = \frac{\phi_{applied}}{\phi_{sat\,@\,exit}} \tag{3-10}$$

When it is rewritten for directly measured or estimated values:

$$Q_{ratio} = \frac{V\,i}{Q\,\rho_{in}\,c_p\left(T_{sat} - T_{in}\right)} \tag{3-11}$$

As with other fluid energy terms the fluid property uncertainties are not independent of temperature uncertainties. Their uncertainties will be handled in the same manner as the energy balance ratio. Some of the partial derivatives necessary for the solution of Equation 80 can readily be solved directly. These solutions are listed below.

$$\frac{\partial Q_{ratio}}{\partial V} = \frac{Q_{ratio}}{V} \qquad \frac{\partial Q_{ratio}}{\partial i} = \frac{Q_{ratio}}{i} \qquad \frac{\partial Q_{ratio}}{\partial Q} = \frac{-Q_{ratio}}{Q}$$

$$\frac{\partial Q_{ratio}}{\partial \rho_{in}} = \frac{-Q_{ratio}}{\rho_{in}} \qquad \frac{\partial Q_{ratio}}{\partial c_p} = \frac{-Q_{ratio}}{c_p}$$

The directly solved and iterative forward-difference solutions of the partial derivatives necessary to solve Equation 80 are presented in Table 3-23. The uncertainty estimate for Construction 4 is presented in Table 3-24a. For this estimate the effect of using the bulk specific heat based on the bulk channel temperature, rather than the bulk specific heat based on the inlet temperature and saturation temperature has been neglected.

Table 3-23.--Q_{ratio} sensitivity coefficient estimates for Equation 3-11 (Construction 4, open channel) at OFI

		x_i	$x_i + \Delta x_i$	$\frac{\partial Q_{ratio}}{\partial x_i}$
Q_{ratio}		0.7616	...	...
Applied voltage, V	V	43.83	...	17.4e-3
Applied current, A	i	699	...	1.09e-3
Flow, 10^{-6} m^3/s	Q	210.2	...	-4.76e-3
Density, inlet (curve fit), kg/m^3	ρ_{in}	982.1	...	-775e-6
Specific heat, bulk (curve fit), J/kg·°C	c_p	4214.5	...	-181e-6
Fluid property linearity assumption, J/kg·°C	c_p	4214.5	...	-181e-6
Inlet temperature, °C	T_{in}	59.52	60.12	-5.11e-3
Outlet temperature, °C	T_{out}	95.53	96.49	18.8e-3
Exit pressure, kPa abs	p_{ehl}	128.5	129.8	-5.50e-3
Saturation temperature, °C	T_{sat}	106.80	107.87	-18.1e-3

Table 3-24.--Q_{ratio} systematic uncertainty estimate for construction 4 (open channel) at OFI

		B_i	θ_i	$\theta_i B_i$
Applied voltage, V	V	0.01	17.4e-3	0.0002
Applied current, A	i	1.4	1.09e-3	0.0015
Flow, 10^{-6} m^3/s	Q	1.4	-4.76e-3	-0.0067
Density, inlet (curve fit), kg/m^3	ρ_{in}	1	-775e-6	-0.0008
Specific heat, bulk (curve fit), J/kg·°C	c_p	80	-181e-6	-0.0145
Fluid property linearity assumption, J/kg·°C	c_p	20	-181e-6	-0.0036
Inlet temperature, °C	T_{in}	0.5	-5.11e-3	-0.0026
Outlet temperature, °C	T_{out}	0.5	18.8e-3	0.0094
Exit pressure, kPa abs	p_{ehl}	0.46	-5.50e-3	-0.0025
Saturation temperature, °C	T_{sat}	0.01	-18.1e-3	-0.0002
Root-sum-square				0.019

There is a second method that can be used to calculate the Q_{ratio}. For this method applied heat flux is calculated using the fluid energy balance. If the bulk specific heat calculated for the numerator is assumed equal to the bulk specific heat calculated in the denominator, Equation 3-10 then becomes:

(3-12) $$Q_{ratio} = \frac{T_{out} - T_{in}}{T_{sat} - T_{in}}$$

Table 3-24b illustrates the difference between the bulk specific heats calculated using on the exit saturation temperature, T_{sat}, and the exit temperature, T_{out}. The specific heat assumption can be treated as a constant in the Q_{ratio} equation such that:

(3-13) $$Q_{ratio} = c_p^* \frac{T_{out} - T_{inlet}}{T_{sat} - T_{inlet}}$$

where: $$c_p^* = \frac{c_{p,\ subcooled}}{c_{p,\ sat\ @\ exit}}$$

For construction 4.0:

$$c_{p,\ 4.0}^* = \frac{4193.6}{4199.4}$$
$$= 0.9986$$

Table 24b.--Specific heat estimates used in Q_{ratio} uncertainty analysis

Construction	Exit Condition	P_{exit}	T_{out}	T_b	$c_{p,b}$
2	Subcooled	129.3	88.83	74.42	4190.7
	Saturated	129.3	106.98	83.49	4199.4
4	Subcooled	128.5	95.53	77.76	4193.6
	Saturated	128.5	106.80	83.40	4199.3

The forward-difference solutions of the partial derivatives for Equations 3-12 are presented in Tables 3-24c and 3-24d. The systematic uncertainty estimates for the Q_{ratio} calculated using Equation 3-12 are presented in Tables 3-25 and 3-26.

Table 3-24c.--Q_{ratio} sensitivity coefficient estimates for construction 4 based on Equation 3-12 (open channel) at OFI

		x_i	$x_i + \Delta x_i$	$\frac{\partial Q_{ratio}}{\partial x_i}$
Q_{ratio}		0.7616	...	...
Inlet temperature, °C	T_{in}	59.52	60.12	-5.11e-3
Outlet temperature, °C	T_{out}	95.53	96.49	21.1e-3
Exit pressure, kPa abs	p_{ehl}	128.5	129.8	-3.62e-3
Saturation temperature, °C	T_{sat}	106.80	107.87	-15.8e-3
Specific heat simplification	c_p^*	1.00	...	0.759

Table 3-24d.--Q_{ratio} sensitivity coefficient estimates for construction 2 (rib channel) at OFI

		x_i	$x_i + \Delta x_i$	$\frac{\partial Q_{ratio}}{\partial x_i}$
Q_{ratio}		0.6196	...	...
Inlet temperature, °C	T_{in}	59.26	59.85	-8.07e-3
Outlet temperature, °C	T_{out}	88.83	89.72	21.0e-3
Exit pressure, kPa abs	p_{ehl}	129.3	130.6	-2.92e-3
Saturation temperature, °C	T_{sat}	106.98	108.05	-12.7e-3
Specific heat simplification	$c_p{}^*$	1.00	...	0.620

Table 3-25.--Q_{ratio} systematic uncertainty estimate for construction 4 (open channel) at OFI

		B_i	θ_i	$\theta_i B_i$
Inlet temperature, °C	T_{in}	0.5	-5.11e-3	-0.0026
Outlet temperature, °C	T_{out}	0.5	21.1e-3	0.0105
Exit pressure, Pa abs	p_{ehl}	0.46	-3.62e-3	-0.0017
Saturation temperature, °C	T_{sat}	0.01	-15.8e-3	-0.0002
Specific heat simplification	$c_p{}^*$	0.0014	0.759	0.0011
Root-sum-square				0.0110

Table 3-26.--Q_{ratio} systematic uncertainty estimate for construction 2 (rib channel) at OFI

		B_i	θ_i	$\theta_i B_i$
Inlet temperature, °C	T_{in}	0.5	-8.07e-3	-0.0040
Outlet temperature, °C	T_{out}	0.5	21.0e-3	0.0105
Exit pressure, Pa abs	p_{ehl}	0.46	-2.92e-3	-0.0013
Saturation temperature, °C	T_{sat}	0.01	-12.7e-3	-0.0001
Specific heat simplification	$c_p{}^*$	0.0021	0.620	0.0013
Root-sum-square				0.0114

Q_{ratio} Rib-Effect-Ratio

The Q_{ratio} rib-effect-ratio is a comparative test result where the correlation of systematic uncertainties is important. This topic is discussed more fully in Chapter 3. The Q_{ratio} rib-effect-ratio is defined as:

(3-14) $$\eta_{Q_{ratio}} = \frac{Q_{ratio,\, r}}{Q_{ratio,\, o}}$$

The partial derivatives necessary for the evaluation of Equation 80 can be derived from the information in Tables 3-24c, or 3-24d, and the partial derivatives of Equation 3-14.

(3-15) $$\frac{\partial \eta_{Q_{ratio}}}{\partial Q_{ratio,\, r}} = \frac{\eta_{Q_{ratio}}}{Q_{ratio,\, r}} \qquad \frac{\partial \eta_{Q_{ratio}}}{\partial Q_{ratio,\, o}} = \frac{-\eta_{Q_{ratio}}}{Q_{ratio,\, o}}$$

The partial derivatives necessary for the solution of Equation 80 are listed in Table 3-27. Table 3-28 provides the weighted elemental uncertainties for the first term in Equation 80. Table 28a provides the weighted uncertainties for the second term in Equation 80. These may be combined to determine the total systematic uncertainty of the Q_{ratio} rib-effect-ratio.

(3-16) $$B_{\eta_{Q_{ratio}}} = \sqrt{(0.0191)^2 - 0.00353} \\ = 0.0034$$

Table 3-27.--Q_{ratio} rib-effect-ratio sensitivity coefficient estimates for construction 2 (rib channel) at OFI

		$\frac{\partial Q_{ratio,j}}{\partial x_i}$	$\frac{\partial \eta_{Q_{ratio}}}{\partial Q_{ratio,j}}$	$\frac{\partial \eta_{Q_{ratio}}}{\partial x_i}$
Open channel (construction 4)				
Q_{ratio}		1.00	-1.076	-1.07
Inlet temperature, °C	T_{in}	-5.11e-3	-1.076	5.49e-3
Outlet temperature, °C	T_{out}	21.1e-3	-1.076	-22.7e-3
Exit pressure, kPa abs	p_{ehl}	-3.62e-3	-1.076	3.89e-3
Saturation temperature, °C	T_{sat}	-15.8e-3	-1.076	17.0e-3
Specific heat simplification	$c_p{}^*$	0.759	-1.076	-816.e-3
Open channel (construction 2)				
Q_{ratio}		1.00	1.318	1.31
Inlet temperature, °C	T_{in}	-8.07e-3	1.318	-10.6e-3
Outlet temperature, °C	T_{out}	21.0e-3	1.318	27.6e-3
Exit pressure, kPa abs	p_{ehl}	-2.92e-3	1.318	-3.84e-3
Saturation temperature, °C	T_{sat}	-12.7e-3	1.318	-16.7e-3
Specific heat simplification	$c_p{}^*$	0.620	1.318	817.e-3

Table 3-28.--Q_{ratio} rib-effect-ratio systematic uncertainty estimate for construction 4 (open channel) at OFI

		B_i	θ_i	$\theta_i B_i$
Open channel (construction 4)				
Inlet temperature, °C	T_{in}	0.5	5.49e-3	0.0027
Outlet temperature, °C	T_{out}	0.5	-22.7e-3	-0.0114
Exit pressure, kPa abs	p_{ehl}	0.46	3.89e-3	0.0018
Saturation temperature, °C	T_{sat}	0.01	17.0e-3	0.0002
Specific heat simplification	$c_p{}^*$	0.0014	-816.e-3	-0.0011
Open channel (construction 2)				
Inlet temperature, °C	T_{in}	0.5	-10.6e-3	-0.0053
Outlet temperature, °C	T_{out}	0.5	27.6e-3	0.0138
Exit pressure, kPa abs	p_{ehl}	0.46	-3.84e-3	-0.0018
Saturation temperature, °C	T_{sat}	0.01	-16.7e-3	-0.0002
Specific heat simplification	$c_p{}^*$	0.0021	817.e-3	0.0017
Root-sum-square				0.0191

Table 3-28a.--Stanton number rib-effect-ratio systematic uncertainty for rib channel, construction 2 at OFI, inlet temperature 60°C

	ρ_{ik}	B_i		θ_i		$2\rho_{ik}\theta_{i,o}\theta_{i,r}B_{i,o}B_{i,r}$
		open	rib	open	rib	
T_{in}	1	0.5	0.5	5.49e-3	-10.6e-3	-0.000029
T_{out}	1	0.5	0.5	-22.7e-3	27.6e-3	-0.000313
p_{ehl}	1	0.46	0.46	3.89e-3	-3.84e-3	-0.000006
T_{sat}	1	0.01	0.01	17.0e-3	-16.7e-3	-0.000000
c_p^*	1	0.0014	0.0021	-816.e-3	817.e-3	-0.000004
Sum						-0.000353

Reynolds Number

Equation 3-17 provides the Reynolds number in terms of the data reduction input quantities

$$Re = \frac{Q \rho_b D}{A_F \mu_b} \qquad (3\text{-}17)$$

As with the friction factor, the physical property terms are correlated with the temperature measurements. The analysis will be completed using the same methodology as used for the friction factor. Some of the partial derivatives of Equation 3-17 are listed below.

$$\frac{\partial Re}{\partial Q} = \frac{Re}{Q} \qquad \frac{\partial Re}{\partial \rho_b} = \frac{Re}{\rho_b} \qquad \frac{\partial Re}{\partial \mu_b} = \frac{-Re}{\mu_b}$$

The more complicated partial derivatives have been solved using a forward-difference technique. The partial derivatives are listed in Tables 3-29, 3-30, 3-31, and 3-32. The uncertainty estimates are contained in Table 3-33, 3-34, 3-35, and 3-36.

Table 3-29.--Reynolds number sensitivity coefficient estimates for open channel, construction 4, inlet temperature 60°C, Re = 10,000

		x_i	$x_i + \Delta x_i$	$\frac{\partial Re}{\partial x_i}$
Reynolds number	Re	10,000	...	...
Channel width, mm	a	79.8	80.6	-119
Channel depth, mm	b	3.16	3.19	-121
Rib width, mm	x_o	0.00	...	0.000
Bulk density, kg/m^3	ρ_b	981.9	991.7	10.2
Flow, cm^3/s	Q	198.4	200.4	50.4
Inlet temperature, °C	T_{in}	60.00	60.60	72.73
Exit temperature, °C	T_{out}	60.00	60.60	72.73
Viscosity, bulk, µPa·s	μ_b	469.6	474.3	-21.1

Table 3-30.--Reynolds number sensitivity coefficient estimates for open channel, construction 4.0, inlet temperature 60°C, Re = 20,000

		x_i	$x_i + \Delta x_i$	$\frac{\partial Re}{\partial x_i}$
Reynolds number	Re	20,000	...	...
Channel width, mm	a	79.8	80.6	-239
Channel depth, mm	b	3.16	3.19	-241
Rib width, mm	x_o	0	...	0.000
Bulk density, kg/m^3	ρ_b	981.9	991.7	20.4
Flow, cm^3/s	Q	396.8	400.8	101e-3
Inlet temperature, °C	T_{in}	60.00	60.60	145
Exit temperature, °C	T_{out}	60.00	60.60	145
Viscosity, bulk, µPa·s	μ_b	469.6	474.3	-42.2

Table 3-31.--Reynolds number sensitivity coefficient estimates for rib channel, construction 2, inlet temperature 60°C, Re = 10,000

		x_i	$x_i + \Delta x_i$	$\frac{\partial Re}{\partial x_i}$
Reynolds number	Re	10,000	...	...
Channel width, mm	a	79.6	80.4	-118
Channel depth, mm	b	3.09	3.12	-239
Rib width, mm	x_o	2.07	2.09	120
Bulk density, kg/m^3	ρ_b	981.9	991.7	10.2
Flow, cm^3/s	Q	200.2	202.2	50.0
Inlet temperature, °C	T_{in}	60.00	60.60	72.7
Exit temperature, °C	T_{out}	60.00	60.60	72.7
Viscosity, bulk, μPa·s	μ_b	469.6	474.3	-21.1

Table 3-32.--Reynolds number sensitivity coefficient estimates for rib channel, construction 2.0, inlet temperature 60°C, Re = 20,000

		x_i	$x_i + \Delta x_i$	$\frac{\partial Re}{\partial x_i}$
Reynolds number	Re	20,000	...	...
Channel width, mm	a	79.6	80.4	-237
Channel depth, mm	b	3.09	3.12	-477
Rib width, mm	x_o	2.07	2.09	239
Bulk density, kg/m^3	ρ_b	981.9	991.7	20.4
Flow, cm^3/s	Q	400.3	404.3	50.0
Inlet temperature, °C	T_{in}	60.00	60.60	145.4
Exit temperature, °C	T_{out}	60.00	60.60	145.4
Viscosity, bulk, μPa·s	μ_b	469.6	474.30	-42.2

Table 3-33.--Reynolds number systematic uncertainty estimate for open channel, construction 4, inlet temperature 60°C, Re = 10,000

		B_i	θ_i	$\theta_i B_i$
Channel width, mm	a	0.4	-119	-48
Channel depth, mm	b	0.2	-121	-24
Rib width, mm	x_o	0.04	0.000	0
Bulk density, kg/m^3	ρ_b	1	10.2	10
Flow, 10^{-6} m^3/s	Q	1.4	50.4	71
Inlet temperature, °C	T_{in}	0.53	72.73	39
Exit temperature, °C	T_{out}	0.53	72.73	39
Viscosity, bulk, µPa·s	μ_b	2	-21.1	-42
Root-sum-square				113

Table 3-34.--Reynolds number systematic uncertainty estimate for open channel, construction 4.0, inlet temperature 60°C, Re = 20,000

		B_i	θ_i	$\theta_i B_i$
Channel width, mm	a	0.4	-239	-96
Channel depth, mm	b	0.2	-241	-48
Rib width, mm	x_o	0.04	0.000	0
Bulk density, kg/m^3	ρ_b	1	20.4	20
Flow, 10^{-6} m^3/s	Q	1.4	101e-3	0
Inlet temperature, °C	T_{in}	0.53	145	77
Exit temperature, °C	T_{out}	0.53	145	77
Viscosity, bulk, µPa·s	μ_b	2	-42.2	-84
Root-sum-square				176

Table 3-35.--Reynolds number systematic uncertainty estimate for rib channel, construction 2, inlet temperature 60°C, Re = 10,000

		B_i	θ_i	$\theta_i B_i$
Channel width, mm	a	0.4	-118	-47
Channel depth, mm	b	0.2	-239	-48
Rib width, mm	x_o	0.04	120	5
Bulk density, kg/m^3	ρ_b	1	10.2	10
Flow, 10^{-6} m^3/s	Q	1.4	50.0	70
Inlet temperature, °C	T_{in}	0.53	72.7	39
Exit temperature, °C	T_{out}	0.53	72.7	39
Viscosity, bulk, μPa·s	μ_b	2	-21.1	-42
Root-sum-square				120

Table 3-36.--Reynolds number systematic uncertainty estimate for rib channel, construction 2.0, inlet temperature 60°C, Re = 20,000

		B_i	θ_i	$\theta_i B_i$
Channel width, mm	a	0.4	-237	-95
Channel depth, mm	b	0.2	-477	-95
Rib width, mm	x_o	0.04	239	10
Bulk density, kg/m^3	ρ_b	1	20.4	20
Flow, 10^{-6} m^3/s	Q	1.4	50.0	70
Inlet temperature, °C	T_{in}	0.53	145.4	77
Exit temperature, °C	T_{out}	0.53	145.4	77
Viscosity, bulk, μPa·s	μ_b	2	-42.2	-84
Root-sum-square				206

Stanton Number

The Stanton number is defined in Equation 3. When it is rewritten for directly measured or estimated values:

$$St = \frac{a\,b\,V\,i}{A_h\,Q\,\rho_{in}\,c_{p,out}\left(T_{sat} - T_{out}\right)} \qquad \text{(3-18)}$$

As with other fluid energy terms, the fluid property uncertainties are not independent of temperature uncertainties. Their uncertainties will be handled in the same manner as the energy balance ratio. Some of the partial derivatives necessary for the solution of Equation 80 can readily be solved directly. These solutions are listed below.

$$\frac{\partial St}{\partial a} = \frac{St}{a} \qquad \frac{\partial St}{\partial b} = \frac{St}{b} \qquad \frac{\partial St}{\partial V} = \frac{St}{V}$$

$$\frac{\partial St}{\partial i} = \frac{St}{i} \qquad \frac{\partial St}{\partial Q} = \frac{-St}{Q} \qquad \frac{\partial St}{\partial \rho_{in}} = \frac{-St}{\rho_{in}}$$

$$\frac{\partial St}{\partial c_{p,\,out}} = \frac{-St}{c_{p,\,out}} \qquad \frac{\partial St}{\partial L_h} = \frac{-St}{L_h} \qquad \frac{\partial St}{\partial a} = \frac{St}{\left(a_h - x_o\right)}$$

The directly solved and iterative forward-difference solutions of the partial derivatives necessary to solve Equation 80 are presented in Table 3-37 and 3-38. The uncertainty estimates are presented in Tables 3-39 and 3-40.

Table 3-37.--Stanton number sensitivity coefficient estimates for open channel, construction 4 at OFI, inlet temperature 60°C

		x_i	$x_i + \Delta x_i$	$\frac{\partial St}{\partial x_i}$
Stanton number	St	0.008444	...	...
Channel width, mm	a	79.8	...	106e-6
Channel depth, mm	b	3.16	...	2.67e-3
Rib width, mm	x_o	0.00	...	0.000
Applied voltage, V	V	43.83	...	193e-6
Applied current, A	i	699	...	12.1e-6
Heated width, mm	a_h	76.2	...	-111e-6
Heated length, m	L_h	1.219	...	-6.93e-3
Flow, cm^3/s	Q	210.2	...	-40.2e-6
Density, kg/m^3	ρ_{in}	982.1	...	-8.60e-6
Specific heat, kJ/kg·°C	c_p	4.2145	...	-2.00e-6
Inlet temperature, °C	T_{in}	59.52	60.12	4.35e-6
Exit temperature, °C	T_{out}	95.53	96.49	819e-6
Exit pressure, kPa	p_{ehl}	128.5	129.8	-166e-6
Saturation temperature, °C	T_{sat}	106.80	107.87	-686e-6

Table 3-38.--Stanton number sensitivity coefficient estimates for rib channel, construction 2 at OFI, inlet temperature 60°C

		x_i	$x_i + \Delta x_i$	$\frac{\partial St}{\partial x_i}$
Stanton number	St	0.004141	...	...
Channel width, mm	a	79.6	...	53.4e-6
Channel depth, mm	b	3.09	...	1.34e-3
Rib width, mm	x_o	2.07	2.09	-67.0e-6
Applied voltage, V	V	43.83	...	94.5e-6
Applied current, A	i	699	...	5.92e-6
Heated width, mm	a_h	67.2	...	-63.6e-6
Heated length, m	L_h	1.219	...	-45.6e-6
Flow, cm^3/s	Q	261.0	...	-15.9e-6
Density, kg/m^3	ρ_{in}	981.9	...	-4.22e-6
Specific heat, kJ/kg·°C	c_p	4.2056	...	-985e-6
Inlet temperature, °C	T_{in}	59.26	59.85	-2.90e-6
Exit temperature, °C	T_{out}	88.83	89.72	238e-6
Exit pressure, kPa	p_{ehl}	129.3	130.6	-51.7e-6
Saturation temperature, °C	T_{sat}	106.98	108.05	-217e-6

Table 3-39.--Stanton number rib-effect-ratio systematic uncertainty for open channel, construction 4 at OFI, inlet temperature 60°C

		B_i	θ_i	$\theta_i B_i$
Channel width, mm	a	0.4	106e-6	0.000042
Channel depth, mm	b	0.2	2.67e-3	0.000534
Rib width, mm	x_o	0.04	0.000	0.000000
Applied voltage, V	V	0.0089	193e-6	0.000002
Applied current, A	i	1.4	12.1e-6	0.000017
Heated width, mm	a_h	3.4	-111e-6	-0.000377
Heated length, m	L_h	0.001	-6.93e-3	-0.000007
Flow, cm³/s	Q	1.4	-40.2e-6	-0.000056
Density, kg/m³	ρ_{in}	1	-8.60e-6	-0.000009
Specific heat, kJ/kg·°C	c_p	0.08	-2.00e-3	0.000000
Inlet temperature, ·C	T_{in}	0.5	4.35e-6	0.000160
Exit temperature, °C	T_{out}	0.5	819e-6	0.000409
Exit pressure, kPa	p_{ehl}	0.4	-166e-6	-0.000066
Saturation temperature, °C	T_{sat}	0.01	-686e-6	-0.000007
Root-sum-square				0.00079

Table 3-40.--Stanton number rib-effect-ratio systematic uncertainty for rib channel, construction 2 at OFI, inlet temperature 60°C

		B_i	θ_i	$\theta_i B_i$
Channel width, mm	a	0.4	53.4e-6	0.000021
Channel depth, mm	b	0.2	1.34e-3	0.000268
Rib width, mm	x_o	0.04	-67.0e-6	-0.000003
Applied voltage, V	V	0.0089	94.5e-6	0.000001
Applied current, A	i	1.4	5.92e-6	0.000008
Heated width, mm	a_h	3.4	-63.6e-6	-0.000216
Heated length, m	L_h	0.001	-45.6e-6	-0.000000
Flow, cm³/s	Q	1.4	-15.9e-6	-0.000022
Density, kg/m³	ρ_{in}	1	-4.22e-6	-0.000004
Specific heat, J/kg·°C	c_p	0.08	-985e-6	-0.000079
Inlet temperature, ·C	T_{in}	0.5	-2.90e-6	-0.000001
Exit temperature, °C	T_{out}	0.5	238e-6	0.000119
Exit pressure, kPa	p_{ehl}	0.4	-51.7e-6	-0.000021
Saturation temperature, °C	T_{sat}	0.01	-217e-6	-0.000002
Root-sum-square				0.00037

Stanton Number Rib-Effect-Ratio

The Stanton number rib-effect-ratio is defined by Equation 3-19

(3-19)
$$\eta_{St} = \frac{St_r}{St_o}$$

This quantity is a comparative test result and as with the Q_{ratio} rib-effect-ratio the correlation of systematic uncertainties is important. The partial derivatives necessary for the evaluation of Equation 80 can be derived from the information in Tables 3-37, or 3-38, and the partial derivatives of Equation 3-19.

(3-20)
$$\frac{\partial \eta_{St}}{\partial St_r} = \frac{\eta_{St}}{St_r} \qquad \frac{\partial \eta_{St}}{\partial St_o} = \frac{-\eta_{St}}{St_o}$$

The partial derivatives necessary for the evaluation of Equation 80 are listed in Table 3-41. Table 3-42 provides the weighted elemental uncertainties for the first term in Equation 80. Table 3-43 provides the weighted uncertainties for the second term in Equation 80. These may be combined to determine the total systematic uncertainty of the Stanton number rib-effect-ratio.

(3-21)
$$\begin{aligned} B_{\eta_{St}} &= \sqrt{(0.063891)^2 - 0.003383} \\ &= 0.026 \end{aligned}$$

Table 3-41.--Stanton number ratio sensitivity coefficient estimates at OFI, inlet temperature 60°C

		$\frac{\partial St_j}{\partial x_i}$	$\frac{\partial \eta_{St}}{\partial St_j}$	$\frac{\partial \eta_{St}}{\partial x_i}$
Open channel				
Stanton number	St	1.0	-58.08	-58.0e0
Channel width, mm	a	106e-6	-58.08	-6.15e-3
Channel depth, mm	b	2.67e-3	-58.08	-155.e-3
Rib width, mm	x_o	0.000	-58.08	0.00
Applied voltage, V	V	193e-6	-58.08	-11.2e-3
Applied current, A	i	12.1e-6	-58.08	-702.e-6
Heated width, mm	a_h	-111e-6	-58.08	6.44e-3
Heated length, m	L_h	-6.93e-3	-58.08	402.e-3
Flow, cm^3/s	Q	-40.2e-6	-58.08	2.33e-3
Density, kg/m^3	ρ	-8.60e-6	-58.08	499.e-6
Specific heat, J/kg·°C	c_p	-2.00e-3	-58.08	116.e-3
Inlet temperature, ·C	T_{in}	4.35e-6	-58.08	-252.e-6
Exit temperature, °C	T_{out}	819e-6	-58.08	-47.5e-3
Exit pressure, kPa	p_{ehl}	-166e-6	-58.08	9.64e-3
Saturation temperature, °C	T_{sat}	-686e-6	-58.08	39.8e-3
Ribbed channel				
Stanton number	St	1.0	118.4	118.e0
Channel width, mm	a	53.4e-6	118.4	6.32e-3
Channel depth, mm	b	1.34e-3	118.4	158.e-3
Rib width, mm	x_o	-67.0e-6	118.4	-7.93e-3
Applied voltage, V	V	94.5e-6	118.4	11.1e-3
Applied current, A	i	5.92e-6	118.4	700.e-6
Heated width, mm	a_h	-63.6e-6	118.4	-7.53e-3
Heated length, m	L_h	-45.6e-6	118.4	-5.39e-3
Flow, cm^3/s	Q	-15.9e-6	118.4	-1.88e-3
Density, kg/m^3	ρ	-4.22e-6	118.4	-499.e-6
Specific heat, J/kg·°C	c_p	-985e-6	118.4	-116.e-3
Inlet temperature, ·C	T_{in}	-2.90e-6	118.4	-343.e-6
Exit temperature, °C	T_{out}	238e-6	118.4	28.1e-3
Exit pressure, kPa	p_{ehl}	-51.7e-6	118.4	-6.12e-3
Saturation temperature, °C	T_{sat}	-217e-6	118.4	-25.6e-3

Table 3-42.--Stanton number rib-effect-ratio systematic uncertainty for rib channel, construction 2 at OFI, inlet temperature 60°C

		B_i	θ_i	$\theta_i B_i$
Open channel	St			
Channel width, mm	a	0.4	-6.15e-3	-0.002460
Channel depth, mm	b	0.2	-155.e-3	-0.031000
Rib width, mm	x_o	0.04	0.00	0.000000
Applied voltage, V	V	0.0089	-11.2e-3	-0.000100
Applied current, A	i	1.4	-702.e-6	-0.000983
Heated width, mm	a_h	3.4	6.44e-3	0.021896
Heated length, m	L_h	0.001	402.e-3	0.000402
Flow, cm³/s	Q	1.4	2.33e-3	0.003262
Density, kg/m³	ρ	1	499.e-6	0.000499
Specific heat, J/kg·°C	c_p	0.08	116.e-3	0.009280
Inlet temperature, ·C	T_{in}	0.5	-252.e-6	-0.000126
Exit temperature, °C	T_{out}	0.5	-47.5e-3	-0.023750
Exit pressure, kPa	p_{ehl}	0.4	9.64e-3	0.003856
Saturation temperature, °C	T_{sat}	0.01	39.8e-3	0.000398
Ribbed channel				
Channel width, mm	a	0.4	6.32e-3	0.002528
Channel depth, mm	b	0.2	158.e-3	0.031600
Rib width, mm	x_o	0.04	-7.93e-3	-0.000317
Applied voltage, V	V	0.0089	11.1e-3	0.000099
Applied current, A	i	1.4	700.e-6	0.000980
Heated width, mm	a_h	3.4	-7.53e-3	-0.025602
Heated length, m	L_h	0.001	-5.39e-3	-0.000005
Flow, cm³/s	Q	1.4	-1.88e-3	-0.002632
Density, kg/m³	ρ	1	-499.e-6	-0.000499
Specific heat, J/kg·°C	c_p	0.08	-116.e-3	-0.009280
Inlet temperature, ·C	T_{in}	0.5	-343.e-6	-0.000171
Exit temperature, °C	T_{out}	0.5	28.1e-3	0.014050
Exit pressure, kPa	p_{ehl}	0.4	-6.12e-3	-0.002448
Saturation temperature, °C	T_{sat}	0.01	-25.6e-3	-0.000256
Root-sum-square				0.063891

Table 3-43.--Stanton number rib-effect-ratio systematic uncertainty for rib channel, construction 2 at OFI, inlet temperature 60°C

	ρ_{ik}	B_i		θ_i		$2\rho_{ik}\theta_{i,o}\theta_{i,r}B_{i,o}B_{i,r}$
		open	rib	open	rib	
a	1	0.4	0.4	-6.15e-3	6.32e-3	-0.000012
b	0.7	0.2	0.2	-155.e-3	158.e-3	-0.001371
x_o	0	0.04	0.04	0.00	-7.93e-3	-0.000000
V	0.5	0.0089	0.0089	-11.2e-3	11.1e-3	-0.000000
i	1	1.4	1.4	-702.e-6	700.e-6	-0.000002
a_h	1	3.4	3.4	6.44e-3	-7.53e-3	-0.001121
L_h	1	0.001	0.001	402.e-3	-5.39e-3	-0.000000
Q	1	1.4	1.4	2.33e-3	-1.88e-3	-0.000017
ρ	1	1	1	499.e-6	-499.e-6	-0.000000
c_p	1	0.08	0.08	116.e-3	-116.e-3	-0.000172
T_{in}	1	0.5	0.5	-252.e-6	-343.e-6	0.000000
T_{out}	1	0.5	0.5	-47.5e-3	28.1e-3	-0.000667
p_{ehl}	1	0.4	0.4	9.64e-3	-6.12e-3	-0.000019
T_{sat}	1	0.01	0.01	39.8e-3	-25.6e-3	-0.000000
Sum						-0.003383

APPENDIX 4

TASK REFERENCE DOCUMENTS

Table 4-1.--Procedures and Test Plans

Description	Document Number	Date	Revision
Heat Transfer Laboratory Rectifier Operation/Startup/Shutdown	HTL-92-017		0
Local Fl Rig - Operation	TP-93-005		0
Task Plan	91-063-1		0
Task Plan	91-063-1		1
Test Plan and Pretest Predictions	...	1 Apr 93	0
Test Plan and Pretest Predictions	...	21 Apr 93	1
Test Plan and Pretest Predictions	...	30 Apr 93	2
Test Plan and Pretest Predictions	...	8 May 93	3
Test Plan and Pretest Predictions	...	11 May 93	4
Test Plan and Pretest Predictions	...	20 May 93	5
Test Plan and Pretest Predictions	...	3 June 93	6
Test Plan and Pretest Predictions	...	21 June 93	7
Test Plan and Pretest Predictions	...	6 July 93	8
Test Plan and Pretest Predictions	...	7 July 93	9

Table 4-2.--Design drawings

Drawing Number	Revision	Title
ST-MDX4-10178	0	P&I Diagram for Fl Test Rig
ST-MDX5-10171	0	Transient Boiling Behavior Tests, Heater Plate Machining Detail
ST-MDX5-10172	0	Transient Boiling Behavior Tests, T/C Installation & Plasma Spray Details
ST-MDX5-10175	0	Transient Boiling Behavior Tests, Flat Plate Assembly
ST-MDX5-10176	5	Transient Boiling Behavior Tests, Detail Sheet #1
ST-MDX5-10177	1	Transient Boiling Behavior Tests, Detail Sheet #2
ST-MDX5-10188	0	Transient Boiling Behavior Tests, Piping Arrangement & Bill of Material
ST-MDX5-10189	0	Transient Boiling Behavior Tests, Piping Details and Pump-Motor Stand
ST-MDX5-10198	0	Transient Boiling Behavior Tests, Flat Plate Heater Shipping Box Details

Table 4-3.--Photographs

Document Number	Description
92-1769-01	Heater plate #1, end of heater thermocouple countersinks
92-1769-02	Heater plate #1, damaged sealing surface near end of heated length
92-1769-03	Heater plate #1, damaged sealing surface near end of heated length
92-1769-04	Heater plate #1, end of heated length thermocouple countersinks
92-1769-05	Heater plate #1, thermocouple countersinks 34 inches from start of heated length
92-1769-06	Heater plate #1, downstream buss connection counterbore
92-1769-07	Heater plate #1, dimples at end of heated length thermocouples
92-1769-08	Heater plate #1, dimples at end of heated length thermocouples
92-1769-09	Heater plate #1, downstream buss connection counterbore
92-1769-10	Heater plate #1, dimples at heater thermocouples 1-1/2 inches from start of heated length
92-1769-11	Heater plate #1, overview of machining
92-1769-12	Heater plate #1, heated section overview
92-1769-13	Heater plate #1, heated section overview
93-1200-01	Heater plate #1, buss connection at end of heated length
93-1200-02	Heater plate #1, detailed view of plasma sprayed surface at end of heated length
93-1200-03	Heater plate #1, view of back at end of heated length
93-1200-04	Heater plate #1, view of back
93-1200-05	Heater plate #1, view of back
93-1414-01	Construction #1, open channel, supply system
93-1414-02	Construction #1, open channel, supply system
93-1414-03	Construction #1, open channel, back of pressure transducer rack
93-1414-04	Construction #1, open channel, test loop overview
93-1414-05	Construction #1, open channel, test loop overview
93-1414-06	Construction #1, open channel, test section inlet
93-1414-07	Construction #1, open channel, test section
93-1414-08	Construction #1, open channel, test section
93-1414-09	Construction #1, open channel, thermocouple connector details
93-1414-10	Construction #1, open channel, end of heated length
93-1414-11	Construction #1, open channel, channel pressure taps below end of heated length
93-1414-12	Construction #1, open channel, test section exit
93-1414-13	Construction #1, open channel, pressure transducer rack and secondary cooling system

Table 4-3.--Continued

Document Number	Description
93-1414-14	Construction #1, open channel, pressure transducer rack
93-1414-15	Construction #1, open channel, amplifier rack interior
93-1414-16	Construction #1, open channel, amplifier rack cable connections
93-1414-17	Construction #1, open channel, amplifier rack, front view
93-1414-18	Construction #1, open channel, test loop overview, right side
93-1414-19	Construction #1, open channel, test loop overview, left side
93-1566-01	Construction #2, ribbed channel, test loop overview
93-1566-02	Construction #2, ribbed channel, test loop overview
93-1566-03	Construction #2, ribbed channel, buss connections and back of pressure transducer rack
93-1566-04	Construction #2, ribbed channel, top buss connection
93-1566-05	Construction #2, ribbed channel, DAS and power controller
93-1566-06	Construction #2, ribbed channel, DAS and power controller
93-1566-07	Construction #2, ribbed channel, amplifier rack
93-1566-08	Construction #2, ribbed channel, pressure transducer rack
93-1566-09	Construction #2, ribbed channel, pressure transducer rack and secondary cooling system
93-1566-10	Construction #2, ribbed channel, secondary cooling system
93-1566-11	Construction #2, ribbed channel, top buss connection
93-1566-12	Construction #2, ribbed channel, end of heated length detail
93-1566-13	Construction #2, ribbed channel, end of heated length detail
93-1566-14	Construction #2, ribbed channel, channel thermocouple details
93-1697-01	Construction #4, open channel, test loop overview
93-1697-02	Construction #4, open channel, heater frame back view
93-1697-03	Construction #4, open channel, pressure transducer rack and secondary cooling system
93-1697-04	Construction #4, open channel, shims near top of channel
93-1697-05	Construction #4, open channel, shims just above end of heated length

Table 4-4.--Video Tapes

Document Number	Description
LFIE-93-01-M	Local FI Effects
LFIE-93-02-M	Local FI Effects
LFIE-93-03-M	Local FI Effects
LFIE-93-04-M	Local FI Effects
LFIE-93-05-M	Local FI Effects
LFIE-93-06-M	Local FI Effects
LFIE-93-07-M	Local FI Effects
LFIE-93-08-M	Local FI Effects
LFIE-93-09-M	Local FI Effects
LFIE-93-10-M	Local FI Effects
LFIE-93-11-M	Local FI Effects

Table 4-5.--Data Files Listing

File name	Date	Size*	Comments
SF_930414_0141a	4/14/93	109	
SF_930415_1436	4/15/93	123	
SF_930415_1450	4/15/93	122	
SF_930415_1455	4/15/93	154	
SF_930415_1506	4/15/93	123	
SF_930415_1515	4/15/93	129	
SF_930415_1445	4/15/93	122	
SF_930415_1524	4/15/93	122	
SF_930415_1536	4/15/93	121	
SF_930415_1540	4/15/93	138	
SF_930415_1546	4/15/93	121	
SF_930415_1554	4/15/93	121	
SF_930415_1601	4/15/93	167	
SF_930415_1609	4/15/93	122	
SF_930416_0906	4/16/93	122	
SF_930416_0917	4/16/93	122	
SF_930416_0927	4/16/93	121	
SF_930416_0933	4/16/93	195	
SF_930416_0939	4/16/93	121	
SF_930416_0951	4/16/93	121	
SF_930416_0958	4/16/93	133	
SF_930416_1004	4/16/93	74	
SF_930416_1013	4/16/93	123	
SF_930416_1018	4/16/93	135	
SF_930416_1022	4/16/93	127	
SF_930416_1028	4/16/93	181	
SF_930416_1034	4/16/93	121	
SF_930416_1040	4/16/93	160	
SF_930416_1045	4/16/93	122	
SF_930416_1050	4/16/93	125	
SF_930416_1054	4/16/93	119	
LP_930428_1330	4/28/93	131	
LP_930428_1350	4/28/93	123	
LP_930428_1352	4/28/93	126	
LP_930428_1354	4/28/93	122	
LP_930428_1357	4/28/93	122	
LP_930428_1400	4/28/93	130	
LP_930428_1403	4/28/93	133	
LP_930428_1407	4/28/93	122	
LP_930428_1408	4/28/93	123	
LP_930428_1413	4/28/93	127	
LP_930428_1416	4/28/93	126	
LP_930428_1419	4/28/93	141	
LP_930428_1424	4/28/93	156	

LP_930428_1425	4/28/93	122
LP_930428_1442	4/28/93	132
SF_930428_1248	4/28/93	122
SF_930428_1250	4/28/93	125
SF_930428_1253	4/28/93	122
SF_930428_1255	4/28/93	124
SF_930428_1258	4/28/93	124
SF_930428_1300	4/28/93	148
SF_930428_1309	4/28/93	124
SF_930428_1311	4/28/93	122
SF_930428_1313	4/28/93	122
SF_930428_1450	4/28/93	123
SF_930428_1509	4/28/93	123
SF_930428_1510	4/28/93	123
SF_930428_1514	4/28/93	126
SF_930428_1516	4/28/93	138
SF_930428_1518	4/28/93	123
SF_930428_1520	4/28/93	123
SN_930428_1315	4/28/93	135
SN_930428_1531	4/28/93	124
ZO_930428_1219	4/28/93	132
ZO_930428_1538	4/28/93	121
LP_930428_1427	4/28/93	127
SF_930428_1040	4/28/93	123
FS_930430_1502	4/30/93	121
FS_930430_1508	4/30/93	123
FS_930430_1515	4/30/93	122
FS_930430_1520	4/30/93	120
FS_930430_1526	4/30/93	121
FS_930430_1530	4/30/93	124
FS_930430_1540	4/30/93	121
FS_930430_1544	4/30/93	120
FS_930430_1548	4/30/93	123
FS_930430_1552	4/30/93	120
FS_930430_1556	4/30/93	122
SN_930430_1350	4/30/93	118
SN_930430_1605	4/30/93	120
ZO_930430_1328	4/30/93	120
ZO_930430_1610	4/30/93	121

*number of rows

APPENDIX 5

REFERENCE DATA

Table 5-1.--Experimental OSV data calculated from the tables prepared by Dorra, Lee, and Bankoff (69)

Pe number	St number	Pe number	St number	Pe number	St number
Sekoguchi, et al. (tube)					
29,011	0.00366	29,000	0.00368	164,000	0.00305
29,113	0.00323	43,600	0.00372	40,000	0.00472
43,861	0.00237	47,300	0.00284	39,700	0.00374
66,216	0.00204	40700	0.00404	26,200	0.00446
43,887	0.00276	53,500	0.00264	50,500	0.00527
66,132	0.00289	165,000	0.00286	104,000	0.00369
Edelman & Elias (tube)					
1,928	0.18465	3,891	0.11258	9,470	0.03967
2,138	0.20717	4,311	0.11211	10,734	0.03455
2,313	0.17439	5,188	0.07160	11,858	0.03214
2,629	0.15798	5,609	0.07243	12,981	0.03157
3,014	0.18107	6,801	0.06653	...	...
3,435	0.13972	7,994	0.06041	...	...
Staub, et al. (rectangle)					
60,900	0.02235	260,000	0.00984	258,000	0.00764
60,900	0.02297	265,000	0.00843	516,000	0.00793
166,000	0.00972	524,000	0.00702	516,000	0.00732
249,000	0.00967	64,400	0.01876	...	...
Evangelisti & Lupoli (annulus)					
150,000	0.00580	152,000	0.00693	64,900	0.00986
Rogers, et al. (annulus)					
9,850	0.14525	62,200	0.02726	48,000	0.03329
10,100	0.12505	27,200	0.06641	48,800	0.04189
10,300	0.11072	38,600	0.04399	55,700	0.03210
12,300	0.08422	54,000	0.02965	65,100	0.02482
29,300	0.05124	32,700	0.05965	...	...
47,900	0.03783	37,800	0.04773	...	...
Ferrell (tube)					
39,700	0.01340	78,400	0.01017	...	...

Table 5-2.--Selected data from Columbia University tube tests (20)

Pe number	St number	Pe number	St number	Pe number	St number
280,000	0.00723	564,000	0.00653	190,000	0.00607
240,000	0.00608	465,000	0.00552	395,000	0.00538
360,000	0.00612	571,000	0.00605	470,000	0.00608
673,000	0.00233	699,000	0.00653	161,000	0.00767
391,000	0.00606	271,000	0.00734	213,000	0.00519
479,000	0.00610	225,000	0.00514	247,000	0.00468
616,000	0.00573	226,000	0.00574	202,000	0.00106
493,000	0.00557	358,000	0.00684	339,000	0.00173
296,000	0.00739	527,000	0.00742	402,000	0.00218
478,000	0.00520	732,000	0.00592	404,000	0.00687
625,000	0.00576	269,000	0.00727	326,000	0.00206
471,000	0.00619	414,000	0.00656	397,000	0.00326
590,000	0.00595	543,000	0.00683	556,000	0.00083
807,000	0.00525	690,000	0.00621	200,000	0.00165
328,000	0.00770	911,000	0.00625	261,000	-0.00371
414,000	0.00724	233,000	0.00722	220,000	0.00105

Table 5-3.--OFI data derived from the work of Whittle and Forgan

Pe number	St number	Pe number	St number	Pe number	St number
Test section 1, rectangle, 25.4 mm x 3.23 mm, L_h/D_h = 94.5, uniform heat flux					
83,300	0.01131	133,000	0.00938	144,000	0.01058
119,000	0.00995	164,000	0.00995	165,000	0.00995
146,000	0.01203	108,000	0.01058	174,000	0.01297
205,000	0.00995	121,000	0.01058	78,500	0.01058
66,500	0.01058	136,000	0.01131	...	...
110,000	0.01058	99,300	0.01058	...	...
Test section 1A, rectangle, 25.4 mm x 3.23 mm, L_h/D_h = 94.5, non-uniform heat flux					
...	0.01430	...	0.01495	...	0.01131
...	0.01058	...	0.01297	...	0.00995
...	0.01131	...	0.01203	...	...
Test section 1, rectangle, 25.4 mm x 3.23 mm, L_h/D_h = 94.5, uniform heat flux					
53,300	0.00995	94,500	0.00995	29,100	0.00938
79,200	0.00995	61,600	0.00995	...	...
99,800	0.01058	118,000	0.01060	...	...
Test section 2, rectangle, 25.4 mm x 2.43 mm, L_h/D_h = 83, uniform heat flux					
83,513	0.01064	85,000	0.01064	132,000	0.01064
96,580	0.01064	125,000	0.01128	70,600	0.01282
102,000	0.01064	143,000	0.01128	90,200	0.01130
121,000	0.01128	153,000	0.01149	82,300	0.01064
92,606	0.01064	87,700	0.01064	...	...
118,000	0.01064	95,600	0.01200	...	...
Test section 3, rectangle, 25.4 mm x 2.03 mm, L_h/D_h = 100, uniform heat flux					
101,000	0.00940	212,000	0.01000	89,100	0.00940
125,000	0.00940	77,900	0.01000	74,500	0.00940
158,000	0.00940	105,000	0.00940	55,300	0.01000
99,807	0.01000	134,000	0.01070	212,000	0.01000
154,000	0.01000	117,000	0.00890	38,200	0.00889
Test section 4, rectangle, 25.4 mm x 140 mm, L_h/D_h = 191, uniform heat flux					
120,000	0.00803	103,000	0.00803	104,000	0.00879
65,530	0.00803	39,242	0.00803	84,684	0.00963
91,602	0.00803	133,957	0.00740	73,408	0.00803
76,192	0.00689	61,887	0.007340	93,728	0.00803
Test section 5, tube, 6.45 mm dia., L_h/D_h = 94.5, uniform heat flux					
185,000	0.00754	119,000	0.00840	104,000	0.00840
261,000	0.00754	223,000	0.00754	222,000	0.00754
136,000	0.00840	296,000	0.00680	449,000	0.00618

Table 5-4.--Conditions at the demand curve minimums for the Creare OFI program (9)

Test Number	Geometry	Q_{ratio}	Pe number	St number
1	annulus	0.898	77,250	0.00747
1A	annulus	0.797	87,380	0.00335
2	annulus	0.940	65,734	0.01329
3	annulus	0.905	75,983	0.00800
4	annulus	0.904	155,573	0.00799
1	ribbed	0.867	69,704	0.00564
2	ribbed	0.849	64,907	0.00482
3	ribbed	0.835	73,711	0.00437
1A	ribbed	0.842	73,117	0.00459
4	ribbed	0.822	151,586	0.00399
10	ribbed	0.818	90,927	0.00351
15	ribbed	0.762	80,141	0.00278
16	ribbed	0.842	154,261	0.00438
5	ribbed	0.810	76,021	0.00367
6	ribbed	0.837	223,928	0.00438
7	ribbed	0.828	197,891	0.00414
9	ribbed	0.849	281,362	0.00483
13	ribbed	0.805	76,689	0.00354
3A	ribbed	0.799	76,962	0.00341

Table 5-5.--Demand curve minimum data from work of Johnston and Neff (40)

Test number	Pe at OFI	St at OFI	Test number	Pe at OFI	St at OFI
"open" annulus					
snbnr4	68,000	0.00841	snbnr10	121,500	0.00675
snbnr4x	65,500	0.00984	snbnr11	159,500	0.00630
snbnr5	95,000	0.00747	snbnr12	148,000	0.00844
snbnr5x	10,500	0.00701	snbnr13	132,500	0.00670
snbnr6	107,000	0.00755	snbnr14	157,500	0.00610
snbnr7	113,000	0.00717	snbnr15x	170,000	0.00736
snbnr8	93,000	0.00689	snbnr15x1	150,500	0.00931
snbnr8x	118,000	0.00740	snbnr15	161,000	0.00825
snbnr8x	136,000	0.00660	snbnr4h	45,000	0.00533
snbnr9	131,000	0.00751	snbnr5h	50,000	0.00824
snbnr9x	121,500	0.00927	snbnr6h	63,000	0.00754
ribbed annulus					
snbx4	104,500	0.00447	snbx13	120,000	0.00588
snbx5	131,000	0.00477	snbx14	158,000	0.00585
snbx6	123,000	0.00571	snbx15	193,000	0.00598
snbx7	115,000	0.00527	snbx15x	165,000	0.00633
snbx8	141,000	0.00578	snbx15x1	180,000	0.00690
snbx9	143,000	0.00626	half	51,000	0.00383
snbx10	100,500	0.00621	half1	50,500	0.00356
snbx11	142,500	0.00569	half2	53,000	0.00420
snbx11x	110,000	0.00711	mid	58,000	0.00599

APPENDIX 6

OPERATIONAL DETAILS

The tests described in this document were conducted to the requirements of the technical procedure TP-93-005, *Local FI Rig - Operation*. This procedure provided the directions necessary to: (1) verify M&TE operation, and (2) produce steady state demand curves. The operating procedure was supplemented with routinely issued test plans that specified the operating parameters for each specific set of demand curves. (These test plans are part of the task records.) This appendix summarizes the contents of the Test Procedure TP-93-005 and test plans.

Test Phases

The testing of each channel was separated into 3 phases. Each phase had a separate purpose. These are described in Table 6-1. The isothermal tests were completed both before and after diabatic testing. The isothermal tests, Phases 1 and 2, were directed towards verifying if the test channel was operating as expected by current theory, establishing flow constants for the rig, and establishing that the channel behavior did not vary with use. Phase 3 generated the data necessary to compare OFI behavior in a ribbed and unobstructed channel.

Table 6-1.--Test phase descriptions

Phase	Description	Comment
1	Cold isothermal tests	Establish the channel demand curves at ambient temperatures.
2	Hot isothermal tests	Establish the channel demand curves at elevated temperatures.
3	Diabatic tests	Establish the diabatic (heated) demand curves.

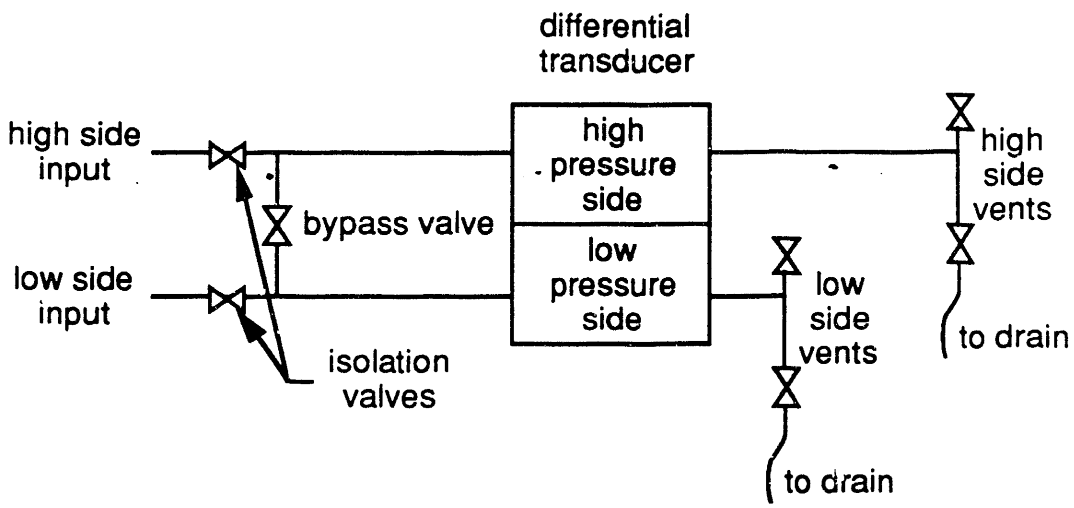

Figure 6-1, Differential pressure transducer schematic

Daily Function Checks

Three types of daily checks were conducted both before and after each day of demand curve testing. The data presented in Figure 6-1 was recorded for each function check. Sixty seconds of data was recorded on the DAS for each function check.

Zero Check

The purpose of the zero check was to verify the operation (at zero pressure) of the pressure gauges and transducers. This was accomplished by venting the instruments to atmosphere while recording a set of data. Prior to recording the zero data the toggle valving for the pressure transducers and gauges were set as stated in Table 6-2. The valving nomenclature is provided in Figure 6-1.

Table 6-2.--Valving arrangements for zero, span and flow function checks

	Zero	Span	Flow
Differential pressure transducers			
HP isolation valves	closed	open	open
LP isolation valves	closed	closed	open
Bypass valves	open	closed	closed
HP vent valves (2)	open	closed	closed
LP vent valves (2)	open	open	closed
Local pressure transducers			
isolation valves	closed	open	open
vent valves (2)	open	closed	closed
Local pressure gauges			
isolation valves	closed	open	open
vent valves	open	closed	closed

Span Check

The purpose of the span check was to verify the operation (at a specified pressure) of the pressure gauges and transducers. This was accomplished by measuring their output for an applied static head of water. The head tank was filled to 3.5 ± 0.1 m (11.5 ± 0.3 feet) at the start of testing. The valving for the pressure transducers and gauges was set as stated in Table 6-2 for the span checks. Prior to collecting data the valves were cycled to purge air from the impulse lines. Purging continued until no air was visible in the vent discharge lines.

Flow Check

The purpose of the flow check was to verify the operation of the thermocouples, and flow instruments. It also served as a check of the channel integrity. The flow check was conducted by measuring the output of each instrument while flowing 473 cm^3/s (7.5 gpm) of water through the test channel as measured by the digital output from the turbine meter FT00001. The valving for the pressure transducers and gauges was set as stated in Table 6-2 for the flow checks. Prior to collecting data the valves were cycled to purge air from the impulse lines. Purging continued until no air was visible in the vent discharge lines.

Test Procedures

Three types of steady-state demand curves were completed during this testing. The types and the principle purpose of each type are listed in Table 6-1. The loop piping valving during demand curve testing was set as specified in Table 6-3; the valving for the pressure transducers was as specified for the flow function check in Table 6-2. The manual data recorded for these tests is listed in Figure 6-2.

For diabatic testing, rectifier operation was controlled using the HTL Building Procedure HTL-92-017, revision 0. The flow was initially set at the maximum available. The rectifiers were then used to increase the test section inlet water temperature to that specified in the test plan. The power to accomplish this was normally kept below 10 kW. After the specified inlet conditions were achieve the power was then increased to that specified by the test plan. The backpressure was then set by decreasing the head tank level.

When the inlet temperature, power, and exit pressure conditions specified in the test plan were achieved a 60 second data set was recorded. The flow would then be decreased to a new rate specified by the test plan. The conditions would then be allowed to stabilize prior to data collection. This iterative process was repeated in decreasing flow increments until the flow was reduced below OFI flow. This was recognized as an increased in pressure drop across the heated section for a step decrease in flow. If time permitted the flow

Table 6-3.--Standard valving arrangements

Valve number	Description	Normal position
LW001	Flow regulator	throttled to provide required test flow
LW006	Channel inlet	open
LW007	Impulse line for PL11000	closed
LW008	Impulse line for PL11000	open
LW011	Vent	closed
LW014	Impulse line for PL33000	open
LW015	Impulse line for PL12002	open
LW016	Quench line	closed
LW017	Bypass line	open
LW018	Bypass line	open
LW019	Bypass line	open
LW020	Channel exit	open
LW022	Tank drain	closed
LW023	Loop drain	closed
CW003	60°C cooling water valve	closed
CW004	80°C cooling water valve	closed
CW005	Roughing cooling water valve	closed
CW006	Tuning cooling water valve	throttled to provide required test loop temperature

was increase to eliminate boiling in the channel and the demand curve minimum was traced two additional times for each demand curve.

The flow to the test section for isothermal testing was set as specified in Table 6-4. These flows were selected to provide equidistant spacing of the Reynolds number on a log-log plot. The specified exit pressure was controlled by regulating the standpipe volume. Once established during a test run the standpipe level was not reset. If leakage occurred during the test the standpipe level would decrease. For elevated temperature (40 and 60°C) the rectifiers were used to heat the loop to operating condition and the pump heat was able to maintain the specified temperature.

Table 6-4.--Phase 1 and 2 test conditions

Test number*	Phase or replicate	Temperature °C	Back pressure psig	Flow rate gpm
1.001	replicate	20.00	6.0781	7.50
1.002	1	20.00	6.0781	2.00
1.003	1	20.00	6.0781	3.56
1.004	1	20.00	6.0781	6.32
1.005	1	20.00	6.0781	11.25
1.006	1	20.00	6.0781	20.00
1.007	2	60.00	6.0781	1.70
1.008	2	60.00	6.0781	3.03
1.009	2	60.00	6.0781	5.39
1.010	2	60.00	6.0781	9.58
1.011	2	60.00	6.0781	17.04
1.012	2	60.00	6.0781	20.00
1.019	2	40.00	6.0781	1.70
1.020	2	40.00	6.0781	2.35
1.021	2	40.00	6.0781	4.18
1.022	2	40.00	6.0781	7.44
1.023	2	40.00	6.0781	13.22
1.024	2	40.00	6.0781	20.00

*Test numbers 1.013 through 1.018 were for conditions not used during the testing.

Date: ________ Sheet No: ____ of ____

DAILY CHECK DATA SHEET, TASK 91-063-1

Procedure Number: TP-93-005 | Procedure Revision:

	Printed	Signature
Test Engineer		
Technician		

DATA

	Instrument Loop Number	M&TE Number	Zero Check	Span Check	Flow Check
Time Started	-				
DAS A time (as found)	_			NA	NA
DAS A time (if reset)	_			NA	NA
DAS B time (as found)	_			NA	NA
DAS B time (if reset)	_			NA	NA
Ambient air temperature, °C	-				
Barometric pressure, "Hg	-				
Upstream pressure, psig	PL11000				
Downstream pressure, psig	PL12002				
Loop flow, gpm	FT01001				
Loop temperature, °C	TT00001				
Log name (less suffix)	-				
Time completed	-				

Comments: ______________________________

____

____

____

Figure 6-1, Typical daily check log sheet

Date: ________					Sheet No: ____ of ____
STEADY STATE AND TRANSIENT DATA SHEET, TASK 91-063-1					
Procedure Number: TP-93-005			Procedure Revision:		
P&ID Drawing Revision:			HTL-92-017 Revision:		
Rig Construction Number:			Test Matrix Revision:		

	Printed	Signature
Test Engineer		
Technician		

DATA

Test Matrix Number	File Name (less suffix)	Initial Indicated Flow	Initial Exit Pressure	Exit Temp.	Comment (s)
	Units	gpm	psig	°C	
	Loop Number	FT01001	PL12002	TT00001	
	M&TE Number				

Figure 6-2, Typical steady-state log sheet

APPENDIX 7

CALCULATIONS AND DATA REDUCTION

Development of a Generalized Q_{ratio} Equation

Dougherty, et al. (29) present a relationship that combines the Q_{ratio} and Stanton number correlations. The form of this equation is:

(7-1) $$Q_{ratio} = \frac{1}{1 + \frac{0.25}{St\,(L/D)}}$$

This equation is applicable only to round tubes. For other geometries this equation will not necessarily hold. Starting with the definition for the Q_{ratio}:

$$Q_{ratio} = \frac{\phi}{\phi_{sat}} = \frac{T_{out} - T_{in}}{T_{sat} - T_{in}}$$

$$= \frac{T_{out} - T_{in}}{\frac{\phi}{Gc_p St} + T_{out} - T_{in}}$$

$$= \frac{1}{\frac{\phi}{Gc_p St(T_{out} - T_{in})} + 1}$$

(7-2) $$Q_{ratio} = \frac{1}{1 + \frac{A_f}{A_h St}}$$ QED

Table 7-1.--Raw data and reduced data file columns and formats

Raw data file		Reduced raw data file		Data type
Column name	Column number	Column name	Column number	
Date	1	Date	3	Date
Time	2	...	...	Character
AI:1 TP01317	3	Mean(AI:1 TP01317)	4	Numeric
		Std(AI:1 TP01317)	79	Numeric
AI:2 TP01308	4	Mean(AI:2 TP01308)	5	Numeric
		Std(AI:2 TP01308)	80	Numeric
AI:3 TP01413	5	Mean(AI:3 TP01413)	6	Numeric
		Std(AI:3 TP01413)	81	Numeric
AI:4 TP01702	6	Mean(AI:4 TP01702)	7	Numeric
		Std(AI:4 TP01702)	82	Numeric
AI:5 TP01505	7	Mean(AI:5 TP01505)	8	Numeric
		Std(AI:5 TP01505)	83	Numeric
AI:6 TP11917	8	Mean(AI:6 TP11917)	9	Numeric
		Std(AI:6 TP11917)	84	Numeric
AI:7 TP12008	9	Mean(AI:7 TP12008)	10	Numeric
		Std(AI:7 TP12008)	85	Numeric
AI:8 TP12113	10	Mean(AI:8 TP12113)	11	Numeric
		Std(AI:8 TP12113)	86	Numeric
AI:9 TP12105	11	Mean(AI:9 TP12105)	12	Numeric
		Std(AI:9 TP12105)	87	Numeric
AI:10 TP12302	12	Mean(AI:10 TP12302)	13	Numeric
		Std(AI:10 TP12302)	88	Numeric
AI:11 TP22917	13	Mean(AI:11 TP22917)	14	Numeric
		Std(AI:11 TP22917)	89	Numeric
AI:12 TP23008	14	Mean(AI:12 TP23008)	15	Numeric
		Std(AI:12 TP23008)	90	Numeric
AI:13 TP23013	15	Mean(AI:13 TP23013)	16	Numeric
		Std(AI:13 TP23013)	91	Numeric
AI:14 TP23105	16	Mean(AI:14 TP23105)	17	Numeric
		Std(AI:14 TP23105)	92	Numeric
AI:15 TP23302	17	Mean(AI:15 TP23302)	18	Numeric
		Std(AI:15 TP23302)	93	Numeric
AI:16 TP33917	18	Mean(AI:16 TP33917)	19	Numeric
		Std(AI:16 TP33917)	94	Numeric
AI:17 TP34013	19	Mean(AI:17 TP34013)	20	Numeric
		Std(AI:17 TP34013)	95	Numeric
AI:18 TP33908	20	Mean(AI:18 TP33908)	21	Numeric
		Std(AI:18 TP33908)	96	Numeric
AI:19 TP34105	21	Mean(AI:19 TP34105)	22	Numeric
		Std(AI:19 TP34105)	97	Numeric
AI:20 TP34302	22	Mean(AI:20 TP34302)	23	Numeric
		Std(AI:20 TP34302)	98	Numeric

Table 7-1.--Continued

Raw data file		Reduced raw data file		Data type
Column name	Column number	Column name	Column number	
AI:21 TP45008	23	Mean(AI:21 TP45008)	24	Numeric
		Std(AI:21 TP45008)	99	Numeric
AI:22 TP45105	24	Mean(AI:22 TP45105)	25	Numeric
		Std(AI:22 TP45105)	100	Numeric
AI:23 TP45302	25	Mean(AI:23 TP45302)	26	Numeric
		Std(AI:23 TP45302)	101	Numeric
AI:24 TP45613	26	Mean(AI:24 TP45613)	27	Numeric
		Std(AI:24 TP45613)	102	Numeric
AI:25 TP45717	27	Mean(AI:25 TP45717)	28	Numeric
		Std(AI:25 TP45717)	103	Numeric
AI:26 TP45808	28	Mean(AI:26 TP45808)	29	Numeric
		Std(AI:26 TP45808)	104	Numeric
AI:27 TP45905	29	Mean(AI:27 TP45905)	30	Numeric
		Std(AI:27 TP45905)	105	Numeric
AI:28 TP46102	30	Mean(AI:28 TP46102)	31	Numeric
		Std(AI:28 TP46102)	106	Numeric
AI:29 TP46308	31	Mean(AI:29 TP46308)	32	Numeric
		Std(AI:29 TP46308)	107	Numeric
AI:30 TP46217	32	Mean(AI:30 TP46217)	33	Numeric
		Std(AI:30 TP46217)	108	Numeric
AI:31 TP46413	33	Mean(AI:31 TP46413)	34	Numeric
		Std(AI:31 TP46413)	109	Numeric
AI:32 TP46505	34	Mean(AI:32 TP46505)	35	Numeric
		Std(AI:32 TP46505)	110	Numeric
AI:33 TP46602	35	Mean(AI:33 TP46602)	36	Numeric
		Std(AI:33 TP46602)	111	Numeric
AI:34 TP46808	36	Mean(AI:34 TP46808)	37	Numeric
		Std(AI:34 TP46808)	112	Numeric
AI:35 TP47005	37	Mean(AI:35 TP47005)	38	Numeric
		Std(AI:35 TP47005)	113	Numeric
AI:36 TP47202	38	Mean(AI:36 TP47202)	39	Numeric
		Std(AI:36 TP47202)	114	Numeric
AI:37 TC00001	39	Mean(AI:37 TC00001)	40	Numeric
		Std(AI:37 TC00001)	115	Numeric
AI:38 TC00002	40	Mean(AI:38 TC00002)	41	Numeric
		Std(AI:38 TC00002)	116	Numeric
AI:39 TC00003	41	Mean(AI:39 TC00003)	42	Numeric
		Std(AI:39 TC00003)	117	Numeric
AI:40 TF01202	42	Mean(AI:40 TF01202)	43	Numeric
		Std(AI:40 TF01202)	118	Numeric
AI:41 TF01204	43	Mean(AI:41 TF01204)	44	Numeric
		Std(AI:41 TF01204)	119	Numeric

Table 7-1.--Continued

Raw data file		Reduced raw data file		Data type
Column name	Column number	Column name	Column number	
AI:42 TF02522	44	Mean(AI:42 TF02522)	45	Numeric
		Std(AI:42 TF02522)	120	Numeric
AI:43 TF02524	45	Mean(AI:43 TF02524)	46	Numeric
		Std(AI:43 TF02524)	121	Numeric
AI:44 TF04172	46	Mean(AI:44 TF04172)	47	Numeric
		Std(AI:44 TF04172)	122	Numeric
AI:45 TF04174	47	Mean(AI:45 TF04174)	48	Numeric
		Std(AI:45 TF04174)	123	Numeric
AI:46 TF05822	48	Mean(AI:46 TF05822)	49	Numeric
		Std(AI:46 TF05822)	124	Numeric
AI:47 TF05824	49	Mean(AI:47 TF05824)	50	Numeric
		Std(AI:47 TF05824)	125	Numeric
AI:48 TF06922	50	Mean(AI:48 TF06922)	51	Numeric
		Std(AI:48 TF06922)	126	Numeric
AI:49 TF06924	51	Mean(AI:49 TF06924)	52	Numeric
		Std(AI:49 TF06924)	127	Numeric
AI:50 TF08022	52	Mean(AI:50 TF08022)	53	Numeric
		Std(AI:50 TF08022)	128	Numeric
AI:51 TF08024	53	Mean(AI:51 TF08024)	54	Numeric
		Std(AI:51 TF08024)	129	Numeric
AI:52 TL01001	54	Mean(AI:52 TL01001)	55	Numeric
		Std(AI:52 TL01001)	130	Numeric
AI:53 TL02001	55	Mean(AI:53 TL02001)	56	Numeric
		Std(AI:53 TL02001)	131	Numeric
AI:54 TL03001	56	Mean(AI:54 TL03001)	57	Numeric
		Std(AI:54 TL03001)	132	Numeric
AI:55 TL03002	57	Mean(AI:55 TL03002)	58	Numeric
		Std(AI:55 TL03002)	133	Numeric
AI:56 Analog Input	58	Mean(AI:56 Analog Input)	59	Numeric
		Std(AI:56 Analog Input)	134	Numeric
AI:57 Analog Input	59	Mean(AI:57 Analog Input)	60	Numeric
		Std(AI:57 Analog Input)	135	Numeric
AI:58 Analog Input	60	Mean(AI:58 Analog Input)	61	Numeric
		Std(AI:58 Analog Input)	136	Numeric
AI:59 Analog Input	61	Mean(AI:59 Analog Input)	62	Numeric
		Std(AI:59 Analog Input)	137	Numeric
AI:60 Analog Input	62	Mean(AI:60 Analog Input)	63	Numeric
		Std(AI:60 Analog Input)	138	Numeric
AI:61 PA20072	63	Mean(AI:61 PA20072)	64	Numeric
		Std(AI:61 PA20072)	139	Numeric
AI:62 PD22472	64	Mean(AI:62 PD22472)	65	Numeric
		Std(AI:62 PD22472)	140	Numeric

Table 7-1.--Continued

Raw data file		Reduced raw data file		Data type
Column name	Column number	Column name	Column number	
AI:63 FT01002	65	Mean(AI:63 FT01002)	66	Numeric
		Std(AI:63 FT01002)	141	Numeric
AI:64 PG00024	66	Mean(AI:64 PG00024)	67	Numeric
		Std(AI:64 PG00024)	142	Numeric
AI:65 PL00001	67	Mean(AI:65 PL00001)	68	Numeric
		Std(AI:65 PL00001)	143	Numeric
AI:66 PD00024	68	Mean(AI:66 PD00024)	69	Numeric
		Std(AI:66 PD00024)	144	Numeric
AI:67 PA00072	69	Mean(AI:67 PA00072)	70	Numeric
		Std(AI:67 PA00072)	145	Numeric
AI:68 PD02472	70	Mean(AI:68 PD02472)	71	Numeric
		Std(AI:68 PD02472)	146	Numeric
AI:69 PD00072	71	Mean(AI:69 PD00072)	72	Numeric
		Std(AI:69 PD00072)	147	Numeric
AI:70 PL00002	72	Mean(AI:70 PL00002)	73	Numeric
		Std(AI:70 PL00002)	148	Numeric
AI:71 PD07284	73	Mean(AI:71 PD07284)	74	Numeric
		Std(AI:71 PD07284)	149	Numeric
AI:72 PD00084	74	Mean(AI:72 PD00084)	75	Numeric
		Std(AI:72 PD00084)	150	Numeric
AI:73 FT01001	75	Mean(AI:73 FT01001)	76	Numeric
		Std(AI:73 FT01001)	151	Numeric
AI:74 WV00001	76	Mean(AI:74 WV00001)	77	Numeric
		Std(AI:74 WV00001)	152	Numeric
AI:75 WC00001	77	Mean(AI:75 WC00001)	78	Numeric
		Std(AI:75 WC00001)	153	Numeric
DI:81 Digital Input	78	...	...	Numeric
MT11 Stopwatch	79	...	...	Numeric
File name	80	File name	1	Character
Number of rows	...	N	2	Numeric

Engineering Unit Conversions

Table 7-2 presents the conversion equations used in the JMP® Worksheet "Engineering Units.06". This worksheet converts the voltage units from the Reduced Data Worksheet "Raw Data Table.25" and converts it to SI engineering units. The majority of the conversions take the form:

(7-3)
$$\psi = \frac{V - a}{b}$$

where:
$$S_\psi = \frac{V}{b}$$

The orifice flow meter, FT01002, is of the form:

(7-4)
$$\psi = \sqrt{\frac{V - a}{b}}$$

where:

(7-5)
$$S_\psi = \frac{1}{2\sqrt{b(V - a)}}$$

Table 7-2..--Engineering units conversions

Instrument	Channel	Coefficients a	b	c	Form
TP01317	1	0.0000 V	10.000 mV/°C	...	V=a+bT
TP01308	2	0.0000 V	33.333 mV/°C	...	V=a+bT
TP01413	3	0.0000 V	10.000 mV/°C	...	V=a+bT
TP01702	4	0.0000 V	33.333 mV/°C	...	V=a+bT
TP01505	5	0.0000 V	33.333 mV/°C	...	V=a+bT
TP11917	6	0.0000 V	10.000 mV/°C	...	V=a+bT
TP12008	7	0.0000 V	33.333 mV/°C	...	V=a+bT
TP12113	8	0.0000 V	10.000 mV/°C	...	V=a+bT
TP12105	9	0.0000 V	33.333 mV/°C	...	V=a+bT
TP12302	10	0.0000 V	33.333 mV/°C	...	V=a+bT
TP22917	11	0.0000 V	10.000 mV/°C	...	V=a+bT
TP23008	12	0.0000 V	33.333 mV/°C	...	V=a+bT
TP23013	13	0.0000 V	10.000 mV/°C	...	V=a+bT
TP23105	14	0.0000 V	33.333 mV/°C	...	V=a+bT
TP23302	15	0.0000 V	33.333 mV/°C	...	V=a+bT
TP33917	16	0.0000 V	10.000 mV/°C	...	V=a+bT
TP34013	17	0.0000 V	10.000 mV/°C	...	V=a+bT
TP33908	18	0.0000 V	33.333 mV/°C	...	V=a+bT
TP34105	19	0.0000 V	33.333 mV/°C	...	V=a+bT
TP34302	20	0.0000 V	33.333 mV/°C	...	V=a+bT
TP45008	21	0.0000 V	33.333 mV/°C	...	V=a+bT
TP45105	22	0.0000 V	33.333 mV/°C	...	V=a+bT
TP45302	23	0.0000 V	33.333 mV/°C	...	V=a+bT
TP45613	24	0.0000 V	10.000 mV/°C	...	V=a+bT
TP45717	25	0.0000 V	10.000 mV/°C	...	V=a+bT
TP45808	26	0.0000 V	33.333 mV/°C	...	V=a+bT
TP45905	27	0.0000 V	33.333 mV/°C	...	V=a+bT
TP46102	28	0.0000 V	33.333 mV/°C	...	V=a+bT
TP46308	29	0.0000 V	33.333 mV/°C	...	V=a+bT
TP46217	30	0.0000 V	10.000 mV/°C	...	V=a+bT
TP46413	31	0.0000 V	10.000 mV/°C	...	V=a+bT
TP46505	32	0.0000 V	33.333 mV/°C	...	V=a+bT
TP46602	33	0.0000 V	33.333 mV/°C	...	V=a+bT
TP46808	34	0.0000 V	33.333 mV/°C	...	V=a+bT
TP47005	35	0.0000 V	33.333 mV/°C	...	V=a+bT
TP47202	36	0.0000 V	33.333 mV/°C	...	V=a+bT
TC00001	37	0.0000 V	10.000 mV/°C	...	V=a+bT
TC00002	38	0.0000 V	10.000 mV/°C	...	V=a+bT
TC00003	39	0.0000 V	33.333 mV/°C	...	V=a+bT
TF01202	40	0.0000 V	33.333 mV/°C	...	V=a+bT
TF01204	41	0.0000 V	33.333 mV/°C	...	V=a+bT
TF02522	42	0.0000 V	33.333 mV/°C	...	V=a+bT
TF02524	43	0.0000 V	33.333 mV/°C	...	V=a+bT

Table 7-2..--Continued

Instrument	Channel	Coefficients			Form
		a	b	c	
TF04172	44	0.0000 V	33.333 mV/°C	...	V=a+bT
TF04174	45	0.0000 V	33.333 mV/°C	...	V=a+bT
TF05822	46	0.0000 V	33.333 mV/°C	...	V=a+bT
TF05824	47	0.0000 V	33.333 mV/°C	...	V=a+bT
TF06922	48	0.0000 V	33.333 mV/°C	...	V=a+bT
TF06924	49	0.0000 V	33.333 mV/°C	...	V=a+bT
TF08022	50	0.0000 V	33.333 mV/°C	...	V=a+bT
TF08024	51	0.0000 V	33.333 mV/°C	...	V=a+bT
TL01001	52	0.0000 V	33.333 mV/°C	...	V=a+bT
TL02001	53	0.0000 V	33.333 mV/°C	...	V=a+bT
TL03001	54	0.0000 V	33.333 mV/°C	...	V=a+bT
TL03002	55	0.0000 V	33.333 mV/°C	...	V=a+bT
unused	56	...	...	...	...
unused	57	...	...	...	...
unused	58	...	...	...	...
unused	59	...	...	...	...
unused	60	...	...	...	...
PA20072	61	-1.8352 V	26.37 μV/P	...	V=a+bP
PD22472	62	0.8963 V	26.36 μV/P	...	V=a+bP
FT01002	63	0.7580 V	5.5578 MV·s^2/m^6	2	V=a+bQ^2
PG00024	64	-0.0922 V	28.84 μV/P	...	V=a+bP
PL00001	65	0.0016 V	7.25 μV/Pa	...	V=a+bP
PD00024	66	1.1820 V	181.22 μV/	...	V=a+bP
PA00072	67	-1.8218 V	26.38 μV/P	...	V=a+bP
PD02472	68	0.9108 V	26.38 μV/P	...	V=a+bP
PD00072	69	-0.0145 V	14.51 μV/P	...	V=a+bP
PL00002	70	-0.1618 V	28.92 μV/P	...	V=a+bP
PD07284	71	0.0671 V	85.31 μV/P	...	V=a+bP
PD00084	72	0.9152 V	26.38 μV/P	...	V=a+bP
FT01001	73	-0.0169 V	6.414 kV·s/m^3	...	V=a+bQ
WV00001*	74	-0.1 mV	0.20075	...	V=a+bV
		0.3 mV	0.06668		
WC00001	75	-4.278 mV	2.039 mΩ	...	V=a+bC

* The top coefficients should be used for data collected prior to 3 June 1993. The lower coefficients should be used to reduce raw data collected on or after this date.

Table 7-3.--Demand curve inputs JMP worksheet description

Column name	Column type	Source	Comment
File name	character	input value	
N	numeric	input value	
Date	date	input value	
TP33917	numeric	input value	instrument TP33917, °C
TP34013	numeric	input value	instrument TP34013, °C
TP33908	numeric	input value	instrument TP33908, °C
TP34105	numeric	input value	instrument TP34105, °C
TP34302	numeric	input value	instrument TP34302, °C
TC00003	numeric	input value	instrument TC00003, °C
TL01001	numeric	input value	instrument TL01001, °C
TL02001	numeric	input value	instrument TL02001, °C
PA20072	numeric	input value	instrument PA20072, Pa abs
PD22472	numeric	input value	instrument PD22472, Pa
PA00072	numeric	input value	instrument PA00072, Pa abs
PD02472	numeric	input value	instrument PD02472, Pa
FT01001	numeric	input value	instrument FT01001, m3/s
WV00001	numeric	input value	instrument WV00001, V
WC00001	numeric	input value	instrument WC00001, A
T inlet	numeric	calculation	TL01001
T exit, C	numeric	calculation	TL02001
T impulse, C	numeric	calculation	TC00003
P exit	numeric	calculation	$\frac{PA00072 + PA02472}{2}$
DP24-72	numeric	calculation	$\frac{PD02472 + PD22472}{2}$
Flow	numeric	calculation	$\frac{PA00072 + PA20072}{2}$
Voltage	numeric	calculation	WV00001
Current	numeric	calculation	WC00001
T dry, C	numeric	calculation	$\frac{TP33917 + TP34013}{2}$
T wet, C	numeric	calculation	$\frac{TP33908 + TP34105 + TP34302}{3}$ after 7/20/93: $\frac{TP33908 + TP34105}{2}$

Table 7-4.--Demand curves JMP worksheet description

	Column name	Column type	Equation	Comment
Date	date	character	...	input value
File name	File name	character	...	input value
Flow milestone	Milestone	character	...	input value
Row states, basic	Row, active	row state	...	input value
Row states, isothermal	Row, iso	row state	...	input value
Row states, OFI	Row, OFI	row state	...	input value
Current, i, A	amps	numeric	...	input value
Flow rate, m^3/s	Flow	numeric	...	input value
Number of samples at specified condition, N	N	numeric	...	input value
P exit, p_3, Pa abs	P exit	numeric	...	input value
Pressure drop, measured, $\Delta p_{24\text{-}72}$, Pa	Dp, 2472	numeric	...	input value
Temperature, dry wall, °C	T, dry	numeric	...	input value
Temperature, impulse, T_∞, °C	T, imp	numeric	...	input value
Temperature, inlet, T_2, °C	T, in	numeric	...	input value
Temperature, outlet, T_3, °C	T, out	numeric	...	input value
Temperature, wet wall, T_w, °C	T, wet	numeric	...	input value
Test Number	Test #	numeric	...	input value
Voltage, volts	volts	numeric	...	input value
Construction	Const.	character	...	from Table 23
Geometry	Geometry	character	...	from Table 23
Channel depth, b, mm	b	numeric	...	from Table 23
Channel width, a, mm	a	numeric	...	from Table 23
Heated area, A_h, m^2	Ah	numeric	...	from Table 23

Table 7-4.--Continued

	Column name	Column type	Equation	Comment
Length, hydraulic, L, m	L flow	numeric	...	from Table 23
Rib width, x_o, mm	x_o	numeric	...	from Table 23
Y dry, m	Y, dry	numeric	...	from Table 24
Y wet, m	Y, wet	numeric	...	from Table 24
Conductivity, exit, k_3, W/m·C	k, exit	numeric	76	based on T_5
Density, bulk, ρ_b, kg/m^3	d, bulk	numeric	74	based on T_b
Density, in, ρ_2, kg/m^3	d, in	numeric	74	based on T_0
Density, out, ρ_3, kg/m^3	d, out	numeric	74	based on T_5
Density, pipe, ρ_∞, kg/m^3	d, pipe	numeric	74	based on T_∞
Reduced temperature, bulk	Tr bulk	numeric	77	based on T_{bulk}
Reduced temperature, exit	Tr exit	numeric	77	based on T_{exit}
Reduced temperature, inlet	Tr inlet	numeric	77	based on T_{inlet}
Reduced temperature, wall	Tr wall	numeric	77	based on $T_{wet\ wall}$
Specific heat, $c_{p,3}$, J/kg·C	Cp, exit	numeric	75	based on T_5
Specific heat, $c_{p,bulk}$, J/kg·C	Cp, bulk	numeric	75	based on T_b
Temperature, saturation, T_{sat}, °C	T, sat	numeric	78	based on p3
Viscosity, bulk, μ_b, Pa-s	μ, bulk	numeric	77	based on T_b
Viscosity, inlet, μ_2, Pa-s	μ, in	numeric	77	based on T_0
Viscosity, wall, , μ_w, Pa-s	μ, wall	numeric	77	based on T_w
Conductivity Constant, W/m²·C	Kc	character	$\frac{236.8}{y_{dry} - y_{wet}}$	
Equivalent diameter, D_e, mm	De	numeric	D	
Flow area, A_f, mm²	Af	numeric	$A_f = b(a - x_o)$	x_o is zero for open channel

Table 7-4.--Continued

	Column name	Column type	Equation	Comment
Flow, gpm	Flow, gpm	numeric	$Q_{gpm} = Q\left(264.2\ \frac{gal}{m^3}\right)\left(60\ \frac{s}{min}\right)$	
Friction factor	f	numeric	$f = \frac{\Delta p_f}{\left(\frac{L_{23}}{D}\right)\left(\frac{\rho_{bulk}\, u^2}{2}\right)}$	
Friction factor, isothermal	f iso	numeric	$f_{iso} = C_1\, Re^{C_2}$	C1 and C2 are defined in Table 33
Friction ratio for wall effect	f ratio	numeric	$\eta_f = \frac{f}{f_{iso}}$	
Gravity constant, g, m/s2	g	numeric	9.80665	
Heat Balance Ratio	power ratio	numeric	$\eta_P = \frac{P_{elec}}{P_{fluid}}$	
Heat flux, conduction, W/m^2	heat, con	numeric	$\phi_c = K_c(T_{dry} - T_{wet})$	
Heat flux, nominal W/m^2	heat, flux	numeric	$\phi_P = \frac{P_e}{A_h}$	

Table 7-4.--Continued

	Column name	Column type	Equation	Comment
Hydraulic diameter, D, m	D	numeric	$D_{open} = \frac{2\,A_f}{a + b}$ $D_{rib} = \frac{2\,A_f}{a - x_o + 2\,b}$	
k = *f*Re, Equation XX	k	numeric	$k_{open} = \frac{64}{\frac{2}{3} + \frac{11}{24}\frac{b}{a}\left(2 - \frac{b}{a}\right)}$ $k_{rib} = \frac{64}{\frac{2}{3} + \frac{11}{24}\frac{2\,b}{a - x_o}\left(2 - \frac{2\,b}{a - x_o}\right)}$	
Mass Flux, G, kg/s-m^2	G flow	numeric	$G = \frac{Q\,\rho_2}{A_f}$	
Nusselt number, exit, Nu	Nu #	numeric	$Nu = \frac{\phi\,D}{k_3\left(T_{sat} - T_3\right)}$	
Peclet number, exit	Pe #	numeric	$Pe = \frac{G\,D\,c_{p,3}}{k_3}$	
Power, electric losses, W	P e, loss	numeric	0	

Table 7-4.--Continued

	Column name	Column type	Equation	Comment
Power, electric, P_e, W	Power, e	numeric	$P_e = V\,i - \text{losses}$	
Power, fluid losses, W	P f, loss	numeric	0	
Power, fluid, P_f, W	Power, f	numeric	$P_f = Q\,\rho_2\,c_{p,b}(T_3 - T_2) + \text{losses}$	
Pressure drop, acceleration, Δp_a, Pa	Dp, acc	numeric	0	
Pressure drop, elevation, Δp_e, Pa	Dp, den	numeric	$\Delta p_e = -\,g\,L_f\,\rho_2$	
Pressure drop, friction, Δp_f, Pa	Dp, fric	numeric	$\Delta p_f = \Delta p_t - \Delta p_e - \Delta p_a$	
Pressure drop, isothermal, Δp_{iso}, Pa	Dp, iso	numeric	$\Delta p_{iso} = \frac{f_{so}\,L_f\,\rho_2 u^2}{2\,D}$	
Pressure drop, measured, $\Delta p_{24\text{-}72}$, psid	Dp, psid	numeric	$\Delta p_{24-72,\,psid} = \frac{\Delta p_{24-72}}{6894.76}$	
Pressure drop, total, Δp_t, Pa	Dp, tot	numeric	$\Delta p_t = \Delta p_{24-72} - g\,L_f\,\rho_\infty$	
Pressure ratio	P ratio	numeric	$\phi_{LO} = \frac{\Delta p_f}{\Delta p_{iso}}$	
Q_{Ratio}	Q ratio	numeric	$Q_{ratio} = \frac{T_{out} - T_{in}}{T_{sat} - T_{in}}$	

Table 7-4.--Continued

	Column name	Column type	Equation	Comment
Reynolds number, isothermal, Re_{iso}	Re, iso	numeric	$Re_2 = \frac{u \rho_2 D_e}{\mu_2}$	
Reynolds number, Re	Re #	numeric	$Re = \frac{u \rho_b D_e}{\mu_b}$	
Stanton number, exit, St	St #	numeric	$St = \frac{\phi}{G c_{p,3} (T_{sat} - T_3)}$	
Temperature, bulk, T_{bulk}, °C	T, bulk	numeric	$T_b = \frac{T_2 + T_3}{2}$	
Temperature, wall at ONB, T_{ONB}, °C	T, onb	numeric	XX	
Velocity, u, m/s	u	numeric	$u = \frac{Q}{A_f}$	
Viscosity ratio for wall effect	μ ratio	numeric	$\eta_\mu = \frac{\mu_w}{\mu_b}$	
Log f iso	Log f iso	numeric	$\log_{10} f_{iso}$	
Log of f	Log of f	numeric	$\log_{10} f$	
Log of Re	Log of Re	numeric	$\log_{10} Re$	

Table 7-5.--Temperature profiles JMP worksheet description

Column Name	Column Type	Source	Comment
XX_93XXXX_XXXX	character	input value	Mean voltage units from reduced raw data file for one file.
Axial Temp, C	row state	...	Selects rows to be plotted.
Paste File	row state	...	Selects rows to be pasted with new data
a Volts	numeric	Table 7-2	
b Volts/°C	numeric	Table 7-2	
Channel #	numeric	Table 24	
z location, meters	numeric	Table 24	
y location, mm	numeric	Table 24	
x, mm	numeric	Table 24	
in and out	character	Table 24	
Instrument Number	character	Table 24	
Surface	character	Table 24	
Prefix	character	Table 24	Prefix from instrument number
M&TE Number	character	Table 2-0	
Temperature, °C	numeric	...	$T = \frac{V_{XX\_93XXXX\_XXXX} - a}{b}$
Range	character		
Description	character		

Table 7-6.--Pressure profiles JMP worksheet description

Column name	Column type	Source and comment
XX_93XXXX_XXXX	character	input value -- mean voltage units from reduced raw data file for one file.
Axial Pressure	row state	selects rows to be plotted.
Paste File	row state	selects rows to be pasted with new data
Channel #	numeric	from Table 7-0
Instrument #	character	from Table 7-0
Manual data	numeric	from raw data sheets
z location, m	numeric	$\dfrac{-L_{inlet}}{39.37\,\frac{inches}{meters}}$
Elev, ref, inch	numeric	Figure 51 or 52, Chapt. 3
Elev, inlet, inch	numeric	Figure 52, Chapt. 3
Correction, inch	numeric	$L_{ref} - L_{inlet}$
a, curve	numeric	Table 7-2
b, curve	numeric	Table 7-2
Row type	character	instrument or plot, locked column to allow plotting
Ref. type	character	type of instrument: absolute, differential, gauge, or plot
P raw, Pa	numeric	if Channel # = 0 $p_{raw} = [\text{Manual data}] \cdot b_{curve} + a_{curve}$ if row type = "plot" $P_{raw} = 0$ otherwise $p_{raw} = \dfrac{XX\_93XXXX\_XXXX - a_{curve}}{b_{curve}}$
P ref, Pa	numeric	if Ref. type = "absolute" P_{ref} = -BP, Pa, from Manual data if Ref. type = "delta" $P_{ref} = \dfrac{\Delta p_{grad}(L_{ref} + 50.75)}{39.37\,\frac{inch}{meter}} + p_3$ if Ref. type = "local" $P_{ref} = 0$ if Ref. type = "plot" $P_{ref} = \dfrac{\Delta p_{grad}(L_{ref} + 50.75)}{39.37\,\frac{inch}{meter}} + p_3$

Table 7-6.--Continued

Column name	Column type	Source and comment
P corrected, Pa	numeric	$\frac{L_{ref}\,\rho_{pipe}\,9.80665\ m/s^2}{39.37\,\frac{inch}{meter}}$
P local, kPa	numeric	$\frac{p_{raw} + p_{cor} + p_{ref}}{1000}$
P error, kPa	numeric	$p_{error} = p_{local} - \frac{\Delta p_{grad}\left(L_{inlet} - 50.75\right)}{\left(39.37\,\frac{inch}{meter}\right)(1000)} + \frac{P_3}{1000}$
T, pipe	numeric	$T_{pipe} = \frac{T_{TC00003} - a_{TC00003}}{b_{TC00003}}$
T, bulk	numeric	$T_{bulk} = \frac{\frac{T_{TL01001} - a_{TL01001}}{b_{TL01001}} + \frac{T_{TL02001} - a_{TL02001}}{b_{TL02001}}}{2}$
density, pipe	numeric	Equation 74, based on T_{pipe}
density, bulk	numeric	Equation 74, based on T_{bulk}
BP, Pa	numeric	$p_{BP} = [\text{BP in manual data}] \cdot \frac{3386.4\ Pa}{"Hg}$
Flow rate, cm^3/s	numeric	$1{,}000{,}000 \cdot Q_{m^3/s}$
Tr bulk	numeric	Equation 77, based on T_{bulk}
μ, bulk	numeric	Equation 77, based on $T_{r,\ bulk}$
u	numeric	$\frac{Q_{m^3/s}}{A_f}$
Re	numeric	$Re = \frac{u\,\rho_{bulk}\,D}{\mu_{bulk}}$
f, iso	numeric	$0.316\ Re^{-0.25}$
a	numeric	from Table 23
D	numeric	$D_{open} = \frac{2\,A_f}{a + b}$ $D_{rib} = \frac{2\,A_f}{a - x_o + 2\,b}$
xo	numeric	from Table 23
Geometry	character	from Table 23
Af	numeric	$A_f = b\left(a - x_o\right)$

Table 7-6.--Continued

Column name	Column type	Source and comment
b	numeric	from Tabie 23
Dp grad, Pa/m	numeric	$\frac{dp}{dL} = \frac{f_{iso}\,\rho_{bulk}\,u^2}{2\,D} - \rho_{bulk}\,g$
Zero flow	numeric	if $Q \leq 10$ cm3/s then $Q_{zero} = 0$ otherwise $Q_{zero} = 1$
Construction	character	from Table 23
Flow rate, m^3/s	numeric	$Q = Q_{zero}\frac{XX\_93XXXX\_XXXX_{FT01001} - a_{FT01001}}{b_{FT01001}}$
P expand, Pa	numeric	$\Delta p_{4-5} = \frac{\rho_{bulk}\,u^2}{2}$
P3, Pa	numeric	$p_3 = \frac{(p_{raw} + p_{cor})_{PA00072} + (p_{raw} + p_{cor})_{PA20072}}{2} - p_{BP}$

APPENDIX 8

TEST DATA

Diabatic Test Results

This appendix section contains a summary of all diabatic demand curves produced during this test program. Information is presented in four formats. The first table provides the boundary condtions for each data file collectec during the production of a demand curve. The files are presented in the order they were produced. The second table presents the flow and channnel pressure drop condtions for each file. The pressure drop is the mean measured by PD02472 and PD202472 after adjustments for impulse line corrections. The files in this table are sorted by flow rate. The boiling conditon at the EHL has been included in this table. The file at the lowest observe pressure drop has been highlighted. Two figures comprise the last two formats. These figures present the same data. The second figure provides a detail of the region in the vicinity of the demand curve minimum.

Table 8-1.--Boundary conditions for demand curve 2.001, construction 1.0, open channel

File name	Row number	Inlet Temperature °C	EHL pressure kPa abs	Power kW	Energy balance
FS_930510_1500	64	59.86	134.1	30.50	0.954
FS_930510_1515	65	58.56	133.9	30.23	0.952
FS_930510_1525	66	57.60	133.9	30.36	0.953
FS_930510_1535	67	58.99	133.3	30.54	0.954
FS_930510_1542	68	58.85	132.2	30.39	0.946
FS_930510_1745	72	62.44	130.9	30.29	0.947
FS_930510_1752	73	60.86	130.0	30.57	0.957
FS_930510_1800	74	61.33	129.8	30.51	0.963
FS_930510_1801	75	58.36	129.7	30.49	0.951
FS_930510_1802	76	58.37	129.7	30.12	0.952
FS_930510_1804*	77	57.86	129.6	30.25	0.960
FS_930510_1831	78	57.27	129.7	30.22	0.953
FS_930510_1842†	79	57.22	129.6	30.21	0.952
FS_930510_1848	80	59.52	129.6	30.17	0.965
FS_930510_1858	81	60.38	129.5	30.19	0.957
FS_930510_1900	82	60.50	129.5	30.21	0.952
FS_930510_1901	83	60.78	129.9	30.22	0.960
FS_930510_1904	84	62.00	130.9	30.28	0.926
Mean	...	59.49	130.9	30.32	0.9528
S	...	1.61	1.7	0.14	0.0084

*The test engineer identified this as a transient point where the temperature chaneged with time.

†This point was taken while the temperature was dropping.

Table 8-2.--Test data for demand curve 2.001, construction 1.0, open channel

File name	Row number	Flow cm^3/s	Δp kPa	EHL condition*
FS_930510_1500	64	1221	57.3	LO
FS_930510_1515	65	1096	45.3	
FS_930510_1525	66	940	31.7	
FS_930510_1535	67	786	19.7	
FS_930510_1542	68	643	9.9	
FS_930510_1745	72	493	1.3	
FS_930510_1904	84	490	1.2	
FS_930510_1752	73	326	-6.4	
FS_930510_1800	74	267	-8.5	
FS_930510_1831	78	266	-8.5	
FS_930510_1801	75	258	-8.8	NB
FS_930510_1802	76	247	-9.1	
FS_930510_1842	79	227	-9.6	
FS_930510_1804	77	215	-9.8	NB/V
FS_930510_1848	80	215	-9.8	NB
FS_930510_1858	81	211	-9.4	V
FS_930510_1900	82	210	-9.0	
FS_930510_1901	83	195	-7.7	

*LO, liquid only; NB, nucleate boiling; RB, nucleate boiling at the rib; V, signficant void; NB/V, a transitions beteen nucleate boiling and significant void during the log (These transitions were long-term and not related to the cyclic behavior discussed in Chapter 4. They appearred to be a transition between two different boiling conditons.)

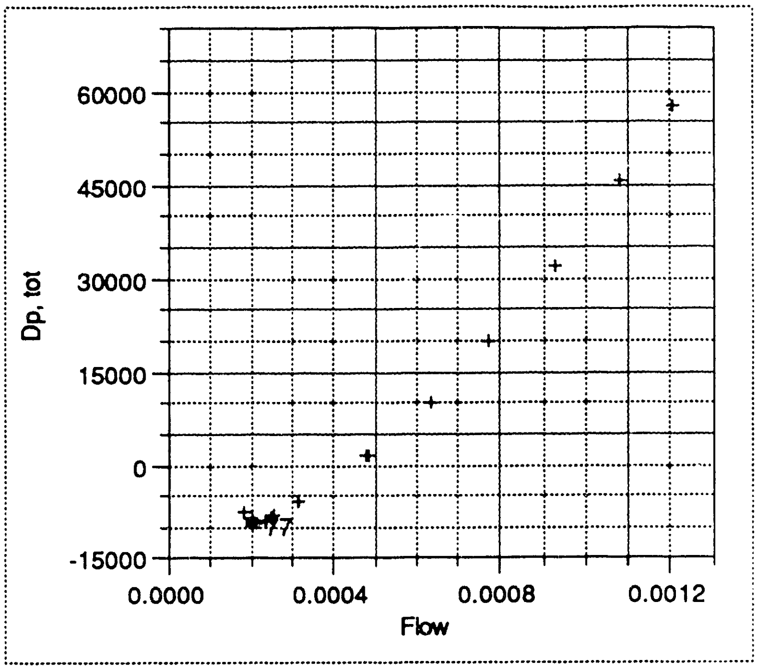

Figure 8-1, Demand curve 2.001, construction 1.0, open channel

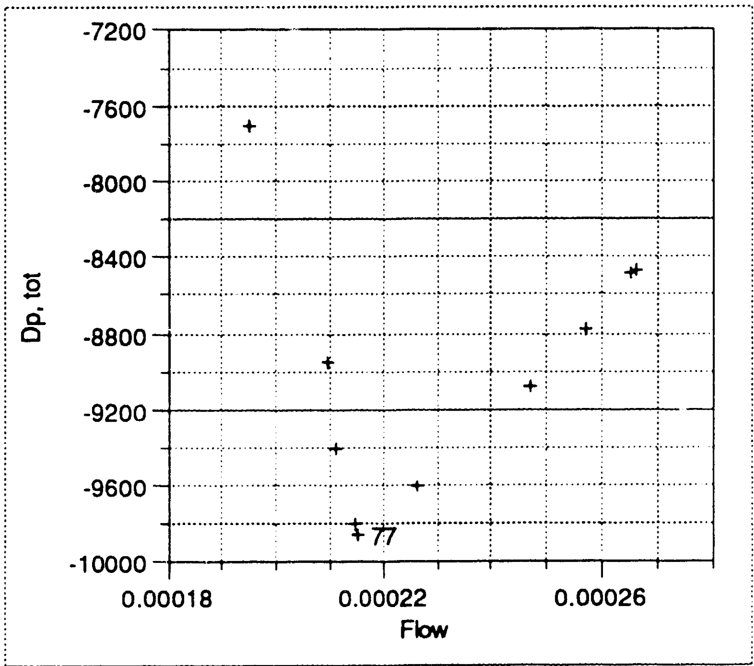

Figure 8-2, Detail of minima region for demand curve 2.001, construction 1.0, open channel

Table 8-3.--Boundary conditions for demand curve 2.002, construction 1.0, open channel

File name	Row number	Inlet Temperature °C	EHL pressure kPa abs	Power kW	Energy balance
FS_930511_1118	88	62.58	132.5	30.38	0.939
FS_930511_1125	89	61.29	129.3	30.69	0.935
FS_930511_1130	90	61.27	133.2	30.62	0.936
FS_930511_1140	91	59.07	132.0	30.54	0.933
FS_930511_1150	92	60.60	130.9	30.67	0.933
FS_930511_1200	93	60.21	130.1	30.57	0.945
FS_930511_1207	94	59.49	130.0	30.68	0.946
FS_930511_1214	95	59.69	129.9	30.62	0.947
FS_930511_1224	96	59.67	129.8	30.59	0.947
FS_930511_1241	97	59.53	129.7	30.59	0.943
FS_930511_1246	98	59.52	129.7	30.58	0.941
FS_930511_1252	99	59.34	129.7	30.57	0.940
FS_930511_1256	100	60.73	129.7	30.53	0.949
FS_930511_1304	101	61.00	129.7	30.53	0.938
FS_930511_1314	102	59.02	130.0	30.51	0.949
FS_930511_1328	103	60.86	130.1	30.52	0.937
FS_930511_1412	104	59.99	130.0	30.55	0.943
FS_930511_1420	105	59.06	129.8	30.60	0.944
FS_930511_1430					
FS_930511_1445	107	59.36	129.7	30.60	0.947
FS_930511_1455	108	59.28	129.6	30.64	0.944
FS_930511_1456	109	59.91	129.6	30.54	0.947
FS_930511_1458	110	60.05	129.6	30.52	0.943
Mean	...	60.07	130.2	30.57	0.9421
S	...	0.91	1.0	0.07	0.0050

Table 8-4.--Test data for demand curve 2.002, construction 1.0, open channel

File name	Row number	Flow cm^3/s	Δp kPa	EHL condition
FS_930511_1118	88	1202	55.7	
FS_930511_1125	89	941	32.3	
FS_930511_1130	90	941	31.9	
FS_930511_1140	91	634	9.4	
FS_930511_1150	92	480	0.5	
FS_930511_1328	103	323	-6.5	
FS_930511_1200	93	321	-6.6	
FS_930511_1412	104	296	-7.4	
FS_930511_1207	94	290	-7.7	
FS_930511_1214	95	266	-8.5	NB
FS_930511_1420	105	265	-8.5	
FS_930511_1224	96	239	-9.2	
FS_930511_1430	106			
FS_930511_1241	97	231	-9.4	
FS_930511_1445	107	228	-9.4	
FS_930511_1246	98	223	-9.6	
FS_930511_1455	108	219	-9.6	
FS_930511_1252	99	218	-9.7	
FS_930511_1456	109	213	-9.7	
FS_930511_1256	100	212	-9.0	NB/V
FS_930511_1304	101	212	-8.6	V
FS_930511_1458	110	208	-8.9	
FS_930511_1314	102	196	-8.5	

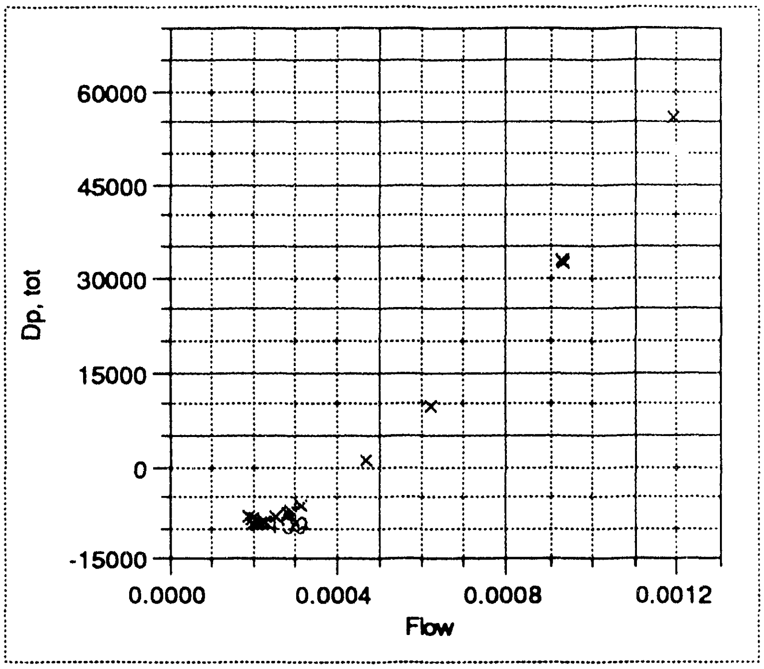

Figure 8-3, Demand curve 2.002, construction 1.0, open channel

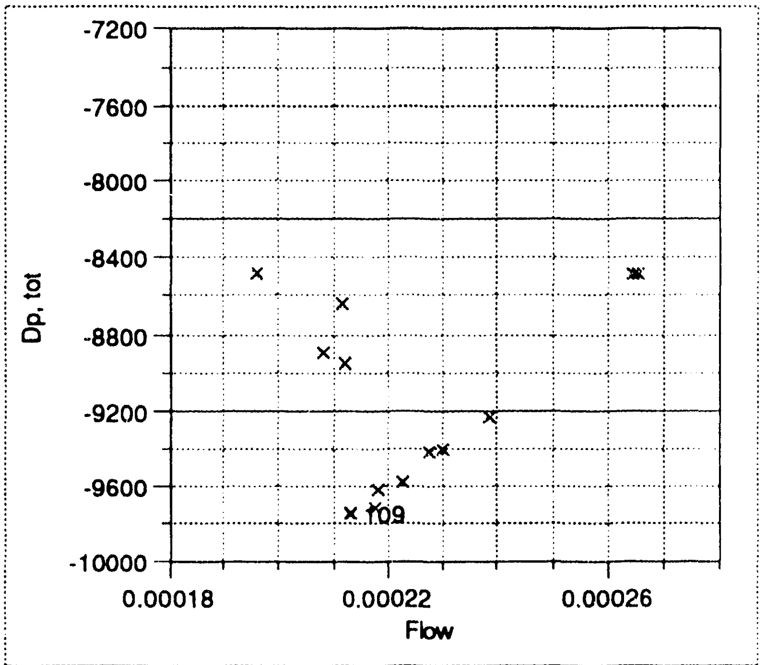

Figure 8-4, Detail of minima region for demand curve 2.002, construction 1.0, open channel

Table 8-5.--Boundary conditions for demand curve 2.003, construction 1.0, open channel

File name	Row number	Inlet Temperature °C	EHL pressure kPa abs	Power kW	Energy balance
FS_930511_1605	111	59.12	133.2	30.59	0.927
FS_930511_1630	112	60.94	130.0	30.43	0.937
FS_930511_1648	114	59.08	132.0	30.62	0.939
FS_930511_1705	115	59.37	130.8	30.82	0.943
FS_930511_1715	116	59.32	129.9	30.77	0.952
FS_930511_1725	117	59.96	129.7	30.50	0.952
FS_930511_1735	118	60.65	129.6	30.66	0.950
FS_930511_1750	119	59.92	129.4	30.59	0.945
FS_930511_1755	120	60.36	129.4	30.74	0.943
FS_930511_1810	121	60.30	129.4	30.64	0.943
FS_930511_1811	122	59.69	129.4	30.60	0.941
FS_930511_1812	123	59.38	129.4	30.55	0.942
FS_930511_1816	124	59.09	129.3	30.47	0.941
FS_930511_1830	125	60.05	130.7	30.68	0.949
FS_930511_1835	126	60.43	129.6	30.56	0.943
FS_930511_1840	127	59.49	129.4	30.65	0.944
FS_930511_1850	128	60.77	129.4	30.66	0.956
FS_930511_1900*	129	61.60	129.4	30.71	0.938
FS_930511_1910	130	59.55	129.5	30.52	0.941
FS_930511_1915	131	59.29	129.4	30.67	0.948
FS_930511_1920	132	59.47	129.4	30.54	0.950
FS_930511_1925	133	61.10	129.4	30.54	0.954
Mean	...	59.95	129.9	30.61	0.9444
S	...	0.73	0.9	0.10	0.0067

*This file is not plotted since the inlet temperature is much greater than the mean inlet temperature.

Table 8-6.--Test data for demand curve 2.003, construction 1.0, open channel

File name	Row number	Flow cm³/s	Δp kPa	EHL condition*
FS_930511_1605	111	1218.1	58.55	LO
FS_930511_1630	112	945.9	33.30	
FS_930511_1648	114	637.6	10.20	
FS_930511_1705	115	482.0	0.96	
FS_930511_1715	116	326.2	-6.28	
FS_930511_1725	117	292.1	-7.56	ONB
FS_930511_1835	126	272.5	-8.19	
FS_930511_1735	118	266.3	-8.41	
FS_930511_1910	130	246.8	-8.97	
FS_930511_1915	131	234.7	-9.26	
FS_930511_1840	127	233.9	-9.27	
FS_930511_1750	119	231.1	-9.37	
FS_930511_1755	120	227.1	-9.41	
FS_930511_1810	121	223.8	-9.50	
FS_930511_1920	132	220.9	-9.56	
FS_930511_1850	128	219.9	-9.44	
FS_930511_1900	129	219.4	-8.16	
FS_930511_1925	133	218.6	-9.26	
FS_930511_1811	122	218.6	-9.66	
FS_930511_1812	123	216.7	-9.71	
FS_930511_1816	124	206.6	-8.94	
FS_930511_1830	125	197.8	-7.39	

*The log were voiding was first observed was not recorded.

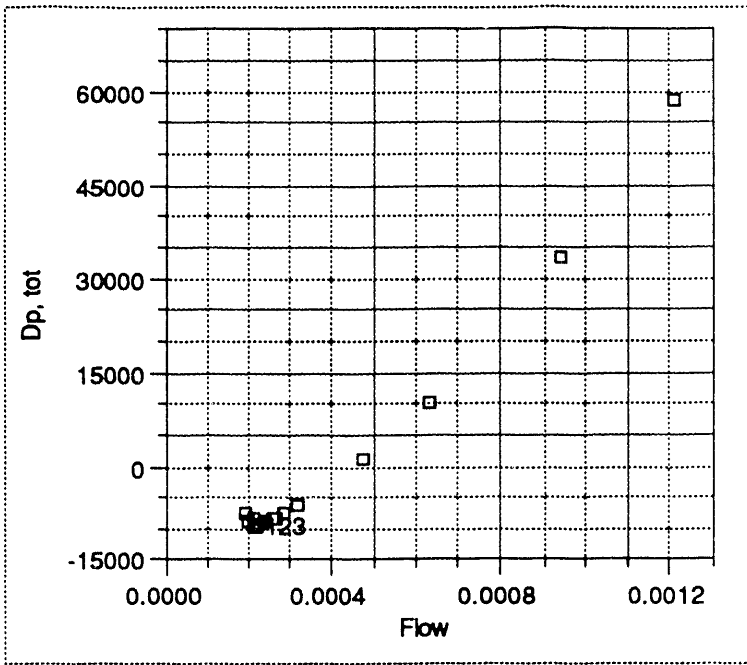

Figure 8-5, Demand curve 2.003, construction 1.0, open channel

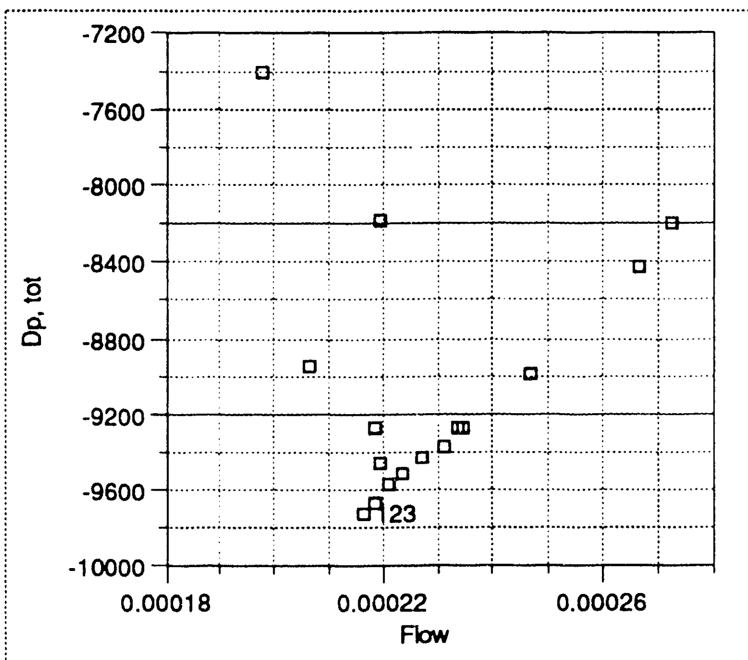

Figure 8-6, Detail of the demand curve minimum 2.003, construction 1.0, open channel

Table 8-7.--Boundary conditions for demand curve 2.004, construction 1.0, open channel

File name	Row number	Inlet Temperature °C	EHL pressure kPa abs	Power kW	Energy balance
FS_930512_1015	136	60.47	135.8	30.69	0.960
FS_930512_1016	137	60.79	131.3	30.64	0.953
FS_930512_1025	138	59.93	131.4	30.65	0.943
FS_930512_1035	139	59.11	130.2	30.67	0.943
FS_930512_1045	140	59.62	129.4	30.70	0.955
FS_930512_1055	141	60.19	129.2	30.60	0.953
FS_930512_1105	142	60.10	129.2	30.60	0.957
FS_930512_1107	143	59.60	129.1	30.69	0.947
FS_930512_1115	144	60.47	129.1	30.57	0.953
FS_930512_1125	145	59.81	129.1	30.66	0.946
FS_930512_1130	146	60.19	129.1	30.51	0.943
FS_930512_1131	147	59.94	129.5	30.63	0.949
FS_930512_1155	148	60.92	129.2	30.70	0.948
FS_930512_1200	149	59.55	129.1	30.51	0.953
FS_930512_1205	150	60.79	129.1	30.62	0.948
FS_930512_1210	151	60.99	129.1	30.47	0.950
FS_930512_1211*	152	61.68	129.4	30.60	0.953
Mean	...	60.24	129.9	30.62	0.9503
S	...	0.65	1.7	0.70	0.0051

*This file is not plotted since the inlet temperature is much greater than the mean inlet temperature.

Table 8-8.--Test data for demand curve 2.004, construction 1.0, open channel

File name	Row number	Flow cm³/s	Δp kPa	EHL condition*
FS_930512_1015	136	1283.9	66.29	LO
FS_930512_1016	137	946.5	33.79	
FS_930512_1025	138	638.7	10.54	
FS_930512_1035	139	474.0	0.76	
FS_930512_1045	140	324.9	-6.24	
FS_930512_1055	141	291.8	-7.50	NB
FS_930512_1105	142	264.7	-8.40	
FS_930512_1155	148	260.8	-8.44	
FS_930512_1107	143	248.2	-8.89	
FS_930512_1115	144	231.5	-9.27	
FS_930512_1200	149	229.1	-9.33	
FS_930512_1205	150	222.5	-9.41	
FS_930512_1125	145	221.6	-9.50	
FS_930512_1210	151	218.3	-9.42	
FS_930512_1211	152	213.7	-7.76	
FS_930512_1130	146	212.9	-9.48	
FS_930512_1131	147	206.3	-7.88	

*The log where voiding was first observed was not noted.

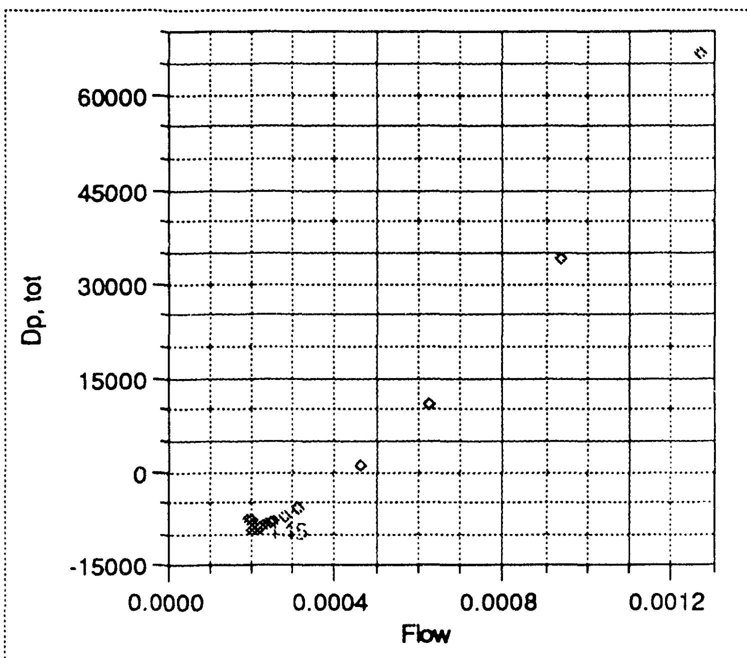

Figure 8-7, Demand curve 2.004, construction 1.0, open channel

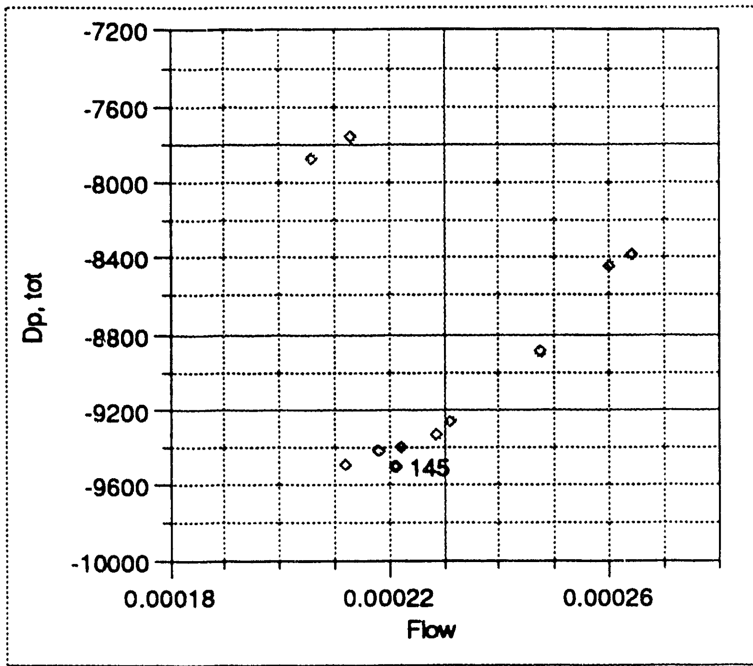

Figure 8-8, Detail of minima region for demand curve 2.004, construction 1.0, open channel

Table 8-9.--Boundary conditions for demand curve 3.001, construction 2.0, rib channel

File name	Row number	Inlet Temperature °C	EHL pressure kPa abs	Power kW	Energy balance
FS_930526_1527	234	60.67	135.5	30.52	0.944
FS_930526_1539*	235	59.42	131.2	30.47	0.939
FS_930526_1545	236	59.45	134.8	30.56	0.938
FS_930526_1554	237	59.19	131.0	30.60	0.942
FS_930526_1630	238	59.98	131.2	30.61	0.935
FS_930526_1645	239	60.38	130.2	30.63	0.956
FS_930526_1650	240	60.72	130.1	30.60	0.946
FS_930526_1705	241	59.13	130.0	30.62	0.946
FS_930526_1715	242	59.39	129.9	30.57	0.951
FS_930526_1720	243	59.24	129.9	30.63	0.950
FS_930526_1725	244	59.13	129.9	30.55	0.954
FS_930526_1740	245	59.20	129.9	30.44	0.956
FS_930526_1750	246	59.43	129.4	30.53	0.959
FS_930526_1810	247	59.37	129.9	30.62	0.947
FS_930526_1811	248	59.64	129.8	30.57	0.951
FS_930526_1820	249	59.21	129.8	30.43	0.952
FS_930526_1825	250	59.32	129.7	30.58	0.952
FS_930526_1830	251	59.46	129.3	30.55	0.955
FS_930526_1840	252	59.84	129.9	30.28	0.947
FS_930526_1850	253	59.33	129.9	30.62	0.948
FS_930526_1900	254	59.12	129.9	30.65	0.945
FS_930526_1910	255	59.27	129.9	30.56	0.942
FS_930526_1925	256	59.31	130.0	30.49	0.942
FS_930526_1945	257	59.95	130.2	30.62	0.936
FS_930526_1950	258	59.23	130.1	30.71	0.936
FS_930526_2005	259	59.55	129.8	30.57	0.945
FS_930526_2010	260	59.31	129.7	30.63	0.948
FS_930526_2015	261	59.39	129.7	30.66	0.947
FS_930526_2020	262	59.39	129.7	30.51	0.948
FS_930526_2021	263	59.25	129.3	30.53	0.953
Mean	...	59.51	130.3	30.56	0.9420
S	...	0.43	1.4	0.08	0.0064

*Low EHL pressure.

Table 8-10.--Test data for demand curve 3.001, construction 2.0, rib channel

File name	Row number	Flow cm³/s	Δp kPa	EHL condition
FS_930526_1527	234	1207.7	49.77	LO
FS_930526_1545	236	938.4	26.81	
FS_930526_1539	235	938.0	26.82	
FS_930526_1554	237	630.7	6.18	
FS_930526_1630	238	482.4	-1.39	RB
FS_930526_1945	257	364.2	-6.18	LO
FS_930526_1950	258	353.7	-6.54	RB
FS_930526_1645	239	329.1	-7.33	
FS_930526_1650	240	316.5	-7.77	
FS_930526_1925	256	313.6	-7.88	
FS_930526_1910	255	308.6	-8.04	
FS_930526_1705	241	303.8	-8.16	
FS_930526_1900	254	303.2	-8.20	
FS_930526_1715	242	291.8	-8.53	
FS_930526_1810	247	291.6	-8.55	NB
FS_930526_1850	253	289.7	-8.61	
FS_930526_2005	259	285.3	-8.72	
FS_930526_1720	243	280.4	-8.85	RB
FS_930526_1840	252	280.3	-8.87	NB
FS_930526_1811	248	279.1	-8.90	
FS_930526_2010	260	271.4	-9.09	
FS_930526_1725	244	267.6	-9.18	
FS_930526_1820	249	266.5	-9.22	
FS_930526_2015	261	263.2	-9.25	
FS_930526_1740	245	261.5	-9.31	V
FS_930526_1825	250	260.5	-9.14	
FS_930526_2020	262	260.5	-9.30	
FS_930526_2021	263	254.8	-8.54	
FS_930526_1830	251	253.9	-8.41	
FS_930526_1750	246	252.0	-8.34	

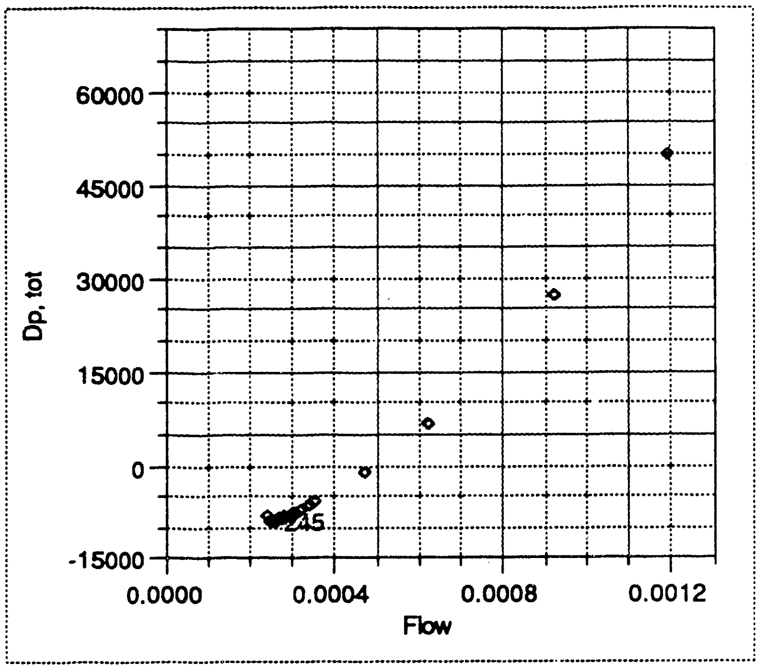

Figure 8-9, Demand curve 3.001, construction 2.0, rib channel

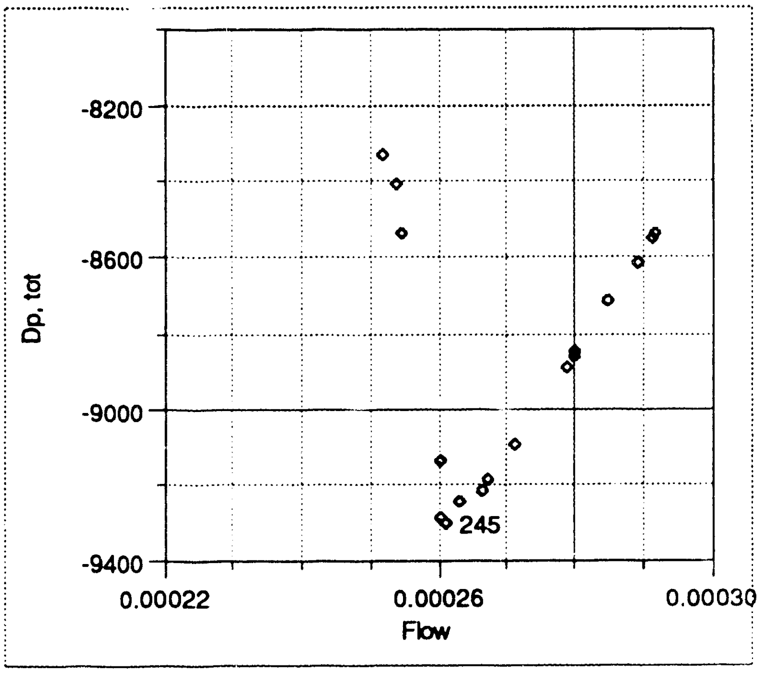

Figure 8-10, Detail of minima region for demand curve 3.001, construction 2.0, rib channel

Table 8-11.--Boundary conditions for demand curve 3.002, construction 2.0, rib channel

File name	Row number	Inlet Temperature °C	EHL pressure kPa abs	Power kW	Energy balance
FS_930601_1007	267	60.33	133.8	30.61	0.961
FS_930601_1018	268	59.58	135.1	30.60	0.958
FS_930601_1025	269	59.47	132.4	30.51	0.957
FS_930601_1036	270	59.58	130.2	30.64	0.953
FS_930601_1050	271	60.26	129.2	30.59	0.956
FS_930601_1100	272	59.76	129.1	30.59	0.960
FS_930601_1110	273	59.40	129.0	30.50	0.958
FS_930601_1120	274	59.24	129.0	30.59	0.959
FS_930601_1125	275	59.17	128.9	30.62	0.965
FS_930601_1130	276	59.21	129.1	30.58	0.963
FS_930601_1135	277	59.25	129.0	30.61	0.970
FS_930601_1136	278	59.19	129.0	30.65	0.972
FS_930601_1140	279	59.30	128.7	30.73	0.978
FS_930601_1150	280	59.09	128.8	30.57	0.977
FS_930601_1220	281	59.18	129.3	30.60	0.955
FS_930601_1230	282	59.29	129.1	30.77	0.962
FS_930601_1240	283	59.32	129.1	30.55	0.960
FS_930601_1241	284	59.59	129.0	30.48	0.960
FS_930601_1248	285	59.54	129.0	30.65	0.958
FS_930601_1252	286	59.65	128.9	30.80	0.965
FS_930601_1257	287	59.84	128.9	30.50	0.964
FS_930601_1259	288	59.97	128.5	30.67	0.963
FS_930601_1335	289	59.56	129.2	30.62	0.969
FS_930601_1340	290	59.59	129.1	30.11	0.956
FS_930601_1355	291	59.27	129.0	30.59	0.966
FS_930601_1400	292	59.62	129.0	30.80	0.971
FS_930601_1410	293	59.53	128.9	30.42	0.957
FS_930601_1415	294	59.21	128.9	30.49	0.959
FS_930601_1420	295	59.69	128.9	30.51	0.962
FS_930601_1425	296	59.69	128.4	30.35	0.964
FS_930601_1430	297	59.27	128.4	30.66	0.967
FS_930601_1431	298	59.83	128.4	30.52	0.980
FS_930601_1455	299	59.41	129.2	30.69	0.967
FS_930601_1500	300	59.76	130.2	30.82	0.961
FS_930601_1530	301	60.14	131.7	30.53	0.946
FS_930601_1545	302	60.37	135.3	30.56	0.953
Mean	...	59.55	129.7	30.59	0.962
S	...	0.34	1.8	0.13	0.007

Table 8-12.--Test data for demand curve 3.002, construction 2.0, rib channel

File name	Row number	Flow cm^3/s	Δp kPa	EHL condition
FS_930601_1007	267	1163.8	46.87	
FS_930601_1545	302	941.0	27.60	
FS_930601_1018	268	923.6	26.25	
FS_930601_1025	269	701.3	10.74	
FS_930601_1530	301	644.1	7.39	
FS_930601_1500	300	489.8	-0.73	
FS_930601_1036	270	474.7	-1.48	
FS_930601_1455	299	330.9	-7.15	
FS_930601_1220	281	329.1	-7.24	RB*
FS_930601_1335	289	328.8	-7.24	
FS_930601_1050	271	323.9	-7.42	
FS_930601_1100	272	323.7	-7.42	
FS_930601_1230	282	298.7	-8.22	
FS_930601_1110	273	297.9	-8.24	
FS_930601_1340	290	296.0	-8.27	
FS_930601_1355	291	287.0	-8.53	
FS_930601_1240	283	285.3	-8.59	
FS_930601_1120	274	283.6	-8.66	
FS_930601_1400	292	273.2	-8.90	
FS_930601_1241	284	270.5	-8.99	
FS_930601_1125	275	269.4	-9.05	NB*
FS_930601_1410	293	267.2	-9.06	
FS_930601_1130	276	265.6	-9.13	
FS_930601_1248	285	264.5	-9.13	
FS_930601_1252	286	262.5	-9.05	
FS_930601_1257	287	262.3	-9.08	
FS_930601_1420	295	261.5	-9.15	
FS_930601_1415	294	261.4	-9.18	
FS_930601_1135	277	259.5	-9.23	
FS_930601_1136	278	259.5	-9.19	
FS_930601_1259	288	255.4	-8.23	
FS_930601_1140	279	254.1	-8.43	
FS_930601_1150	280	253.4	-8.67	V
FS_930601_1425	296	253.1	-8.39	
FS_930601_1430	297	248.8	-8.24	
FS_930601_1431	298	238.7	-8.20	

*The EHL conditions were only noted for logs between FS_930601_1120 through FS_930601_1150.

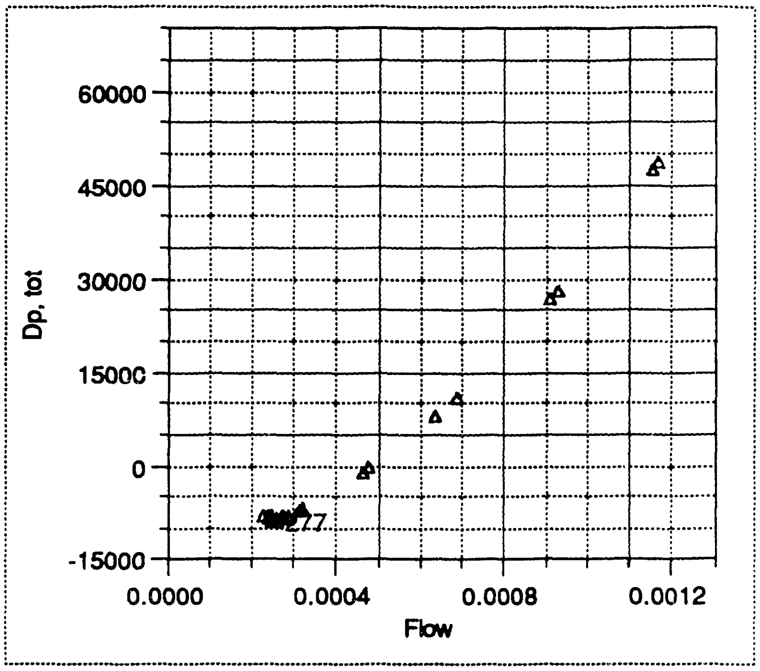

Figure 8-11, Demand curve 3.002, construction 2.0, rib channel

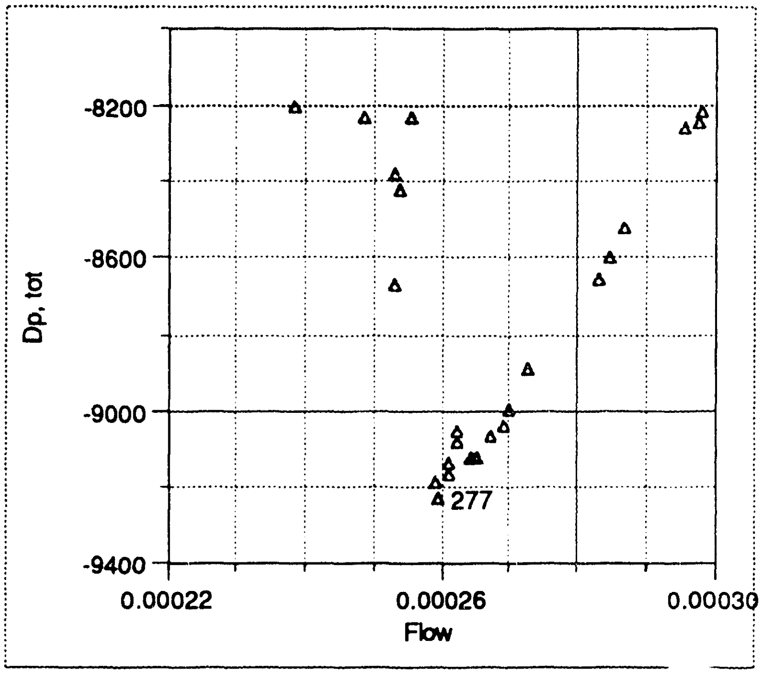

Figure 8-12, Detail of minima region for demand curve 3.002, construction 2.0, rib channel

Table 8-13.--Boundary conditions for demand curve 3.003, construction 2.0, rib channel

File name	Row number	Inlet Temperature °C	EHL pressure kPa abs	Power kW	Energy balance
FS_930601_1600	303	59.26	132.4	30.58	0.953
FS_930601_1610	304	59.71	134.0	30.59	0.952
FS_930601_1630	305	59.52	133.9	30.59	0.948
FS_930601_1645	306	60.23	131.9	30.68	0.947
FS_930601_1646	307	59.37	130.3	30.59	0.942
FS_930601_1650	308	59.17	129.3	30.55	0.966
FS_930601_1710	310	59.54	129.1	30.69	0.962
FS_930601_1715	311	59.90	129.0	30.49	0.965
FS_930601_1720	312	60.00	129.0	30.40	0.965
FS_930601_1730	313	59.40	128.9	30.86	0.958
FS_930601_1735	314	59.30	128.9	30.55	0.957
FS_930601_1736	315	59.12	128.5	30.54	0.964
FS_930601_1745	316	59.51	128.5	30.60	0.964
FS_930601_1750	317	59.20	128.5	30.59	0.963
FS_930601_1810	318	59.19	129.2	30.53	0.955
FS_930601_1830	319	59.48	129.1	30.50	0.951
FS_930601_1831	320	59.39	129.1	30.67	0.954
FS_930601_1835	321	59.78	129.0	30.65	0.957
FS_930601_1845	322	59.54	128.9	30.55	0.955
FS_930601_1900	323	59.28	128.9	30.69	0.959
FS_930601_1910	324	59.32	128.9	30.58	0.959
FS_930601_1915	325	59.40	128.5	30.69	0.961
FS_930601_1916	326	59.37	128.4	30.57	0.964
FS_930601_1917	327	59.13	128.5	30.63	0.963
FS_930601_1930	328	59.36	129.2	30.63	0.960
FS_930601_1935	329	59.91	129.3	30.76	0.956
FS_930601_1940	330	59.88	129.3	30.56	0.950
FS_930601_1945	331	59.89	129.4	30.62	0.951
Mean	···	59.51	129.5	30.61	0.9573
S	···	0.30	1.5	0.09	0.0064

Table 8-14.--Test data for demand curve 3.003, construction 2.0, rib channel

File name	Row number	Flow cm^3/s	Δp kPa	EHL condition*
FS_930601_1600	304	1180.0	48.30	LO
FS_930601_1610	303	1180.0	48.22	
FS_930601_1630	305	953.3	28.41	
FS_930601_1645	306	642.4	7.13	
FS_930601_1646	307	482.0	-1.14	
FS_930601_1945	331	348.3	-6.55	
FS_930601_1940	330	342.4	-6.76	RB
FS_930601_1935	329	336.4	-6.97	
FS_930601_1650	308	328.8	-7.24	
FS_930601_1810	318	328.6	-7.26	
FS_930601_1930	328	327.4	-7.27	
FS_930601_1831	320	297.1	-8.26	
FS_930601_1830	319	297.1	-8.26	
FS_930601_1710	310	294.3	-8.35	
FS_930601_1715	311	285.9	-8.59	
FS_930601_1835	321	285.1	-8.59	
FS_930601_1720	312	272.4	-8.95	
FS_930601_1845	322	272.3	-8.94	
FS_930601_1730	313	266.9	-9.08	
FS_930601_1900	323	266.8	-9.08	
FS_930601_1910	324	262.1	-9.19	
FS_930601_1735	314	260.3	-9.19	
FS_930601_1915	325	255.2	-8.34	V
FS_930601_1736	315	254.0	-8.55	
FS_930601_1916	326	250.1	-8.23	
FS_930601_1745	316	246.3	-8.18	
FS_930601_1917	327	243.4	-8.22	
FS_930601_1750	317	239.1	-8.19	

*The point of nucleate boiling (NB) was not noted during this test.

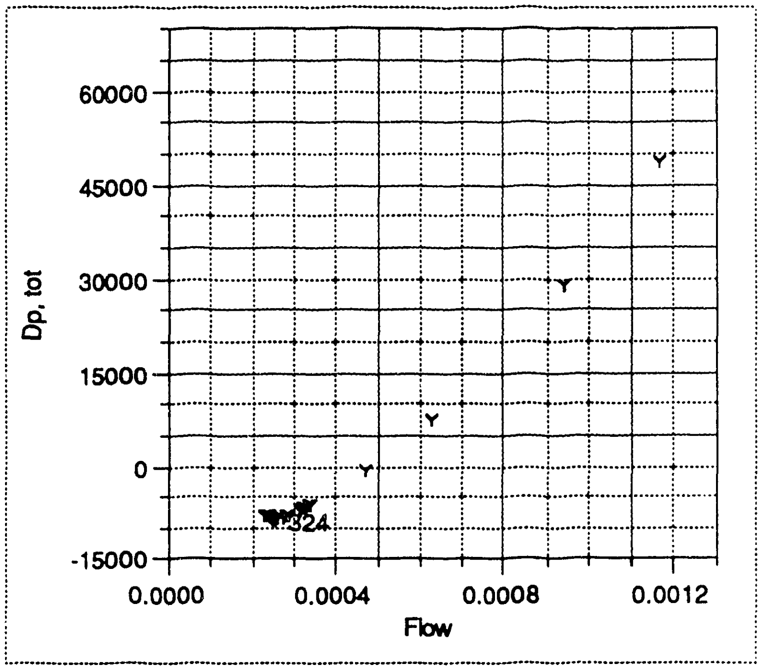

Figure 8-13, Demand curve 3.003, construction 2.0, rib channel

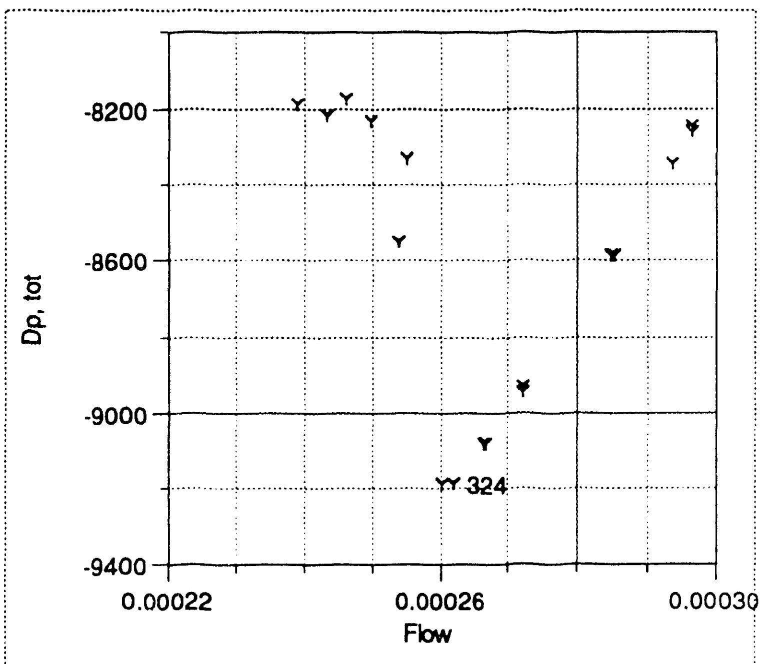

Figure 8-14, Detail of minima region for demand curve 3.003, construction 2.0, rib channel

Table 8-15.--Boundary conditions for demand curve 4.001, construction 2.0, rib channel

File name	Row number	Inlet Temperature °C	EHL pressure kPa abs	Power kW	Energy balance
FS_930603_1433	337	59.47	139.5	52.43	0.985
FS_930603_1442	338	58.66	134.5	52.26	0.982
FS_930603_1455	339	59.71	133.8	52.32	0.978
FS_930603_1507	340	59.75	133.3	51.97	0.976
FS_930603_1520	341	59.77	131.6	51.99	0.979
FS_930603_1529	342	59.55	131.3	52.23	0.983
FS_930603_1538	343	59.78	130.9	52.22	0.985
FS_930603_1542	344	59.55	130.7	52.33	0.988
FS_930603_1547	345	59.61	130.4	52.15	0.991
FS_930603_1554	346	59.76	130.2	52.18	0.990
FS_930603_1558	347	59.72	130.2	52.12	0.989
FS_930603_1602	348	59.61	130.1	52.24	0.989
FS_930603_1606	349	59.58	130.1	52.07	0.987
FS_930603_1611	350	59.30	130.0	51.97	0.987
FS_930603_1715	352	59.72	130.9	52.28	0.982
FS_930603_1722	353	59.94	130.5	52.18	0.985
FS_930603_1726	354	59.67	130.3	52.23	0.985
FS_930603_1730	355	59.68	129.9	52.13	0.987
FS_930603_1735	356	59.89	129.9	52.23	0.985
FS_930603_1740	357	59.76	129.8	51.90	0.983
FS_930603_1745	358	59.74	129.7	52.02	0.983
FS_930603_1750	359	59.66	129.7	52.13	0.985
FS_930603_1752	360	59.93	129.6	51.96	0.988
FS_930603_1755	361	59.89	129.6	52.02	0.987
FS_930603_1756	362	59.80	129.6	51.89	0.986
FS_930603_1800	363	59.73	129.6	52.03	0.985
FS_930603_1802	364	59.60	129.5	52.06	0.988
FS_930603_1815	365	59.44	130.2	52.12	0.981
FS_930603_1825	366	59.78	129.9	52.05	0.979
FS_930603_1835	367	59.32	129.8	51.77	0.979
FS_930603_1840	368	59.76	129.7	51.87	0.988
FS_930603_1845	369	59.63	129.6	52.60	0.989
FS_930603_1850	370	59.91	129.5	52.16	0.984
FS_930603_1855	371	59.65	129.4	51.78	0.982
FS_930603_1857	372	59.69	129.2	52.17	0.986
FS_930603_1900	373	59.79	129.2	52.07	0.986
FS_930603_1905	374	59.50	129.2	51.89	0.985
FS_930603_1906	375	59.39	129.1	51.99	0.984
FS_930603_1908	376	59.30	129.1	52.02	0.989
FS_930603_1915	377	59.44	129.1	52.05	0.987
FS_930603_1916	378	59.30	128.9	52.16	0.987

FS_930603_1918	379	59.29	128.9	52.15	0.990
FS_930603_1920	380	59.21	128.7	52.11	0.987
FS_930603_1925	381	59.22	128.6	52.01	0.988
FS_930603_1928	382	59.18	128.6	52.10	0.989
FS_930603_1930	383	59.37	128.3	52.12	0.990
Mean	...	59.59	130.2	52.10	0.9854
S	...	0.25	1.9	0.16	0.0034

Preliminary Data -- 9 September 1993

Table 8-16.--Test data for demand curve 4.001, construction 2.0, rib channel

File name	Row number	Flow cm^3/s	Δp kPa	EHL condition*
FS_930603_1433	337	1183.8	47.04	LO
FS_930603_1442	338	1183.5	47.22	
FS_930603_1455	339	947.0	26.84	
FS_930603_1507	340	795.0	15.84	
FS_930603_1520	341	633.3	5.96	
FS_930603_1529	342	603.4	4.34	
FS_930603_1715	352	581.2	3.11	NB
FS_930603_1538	343	563.7	2.28	RB
FS_930603_1722	353	543.5	1.20	NB
FS_930603_1542	344	541.6	1.20	RB
FS_930603_1726	354	519.3	0.05	NB
FS_930603_1815	365	515.2	-0.15	...
FS_930603_1547	345	509.1	-0.31	RB
FS_930603_1554	346	484.2	-1.41	NB
FS_930603_1825	366	483.9	-1.53	
FS_930603_1730	355	476.9	-1.81	
FS_930603_1558	347	475.5	-1.79	
FS_930603_1835	367	471.4	-2.06	
FS_930603_1602	348	471.3	-1.95	
FS_930603_1735	356	466.8	-2.22	
FS_930603_1606	349	465.4	-2.19	
FS_930603_1611	350	458.8	-2.46	
FS_930603_1840	368	458.2	-2.57	
FS_930603_1740	357	453.0	-2.75	V
FS_930603_1745	358	447.4	-2.92	
FS_930603_1845	369	446.1	-2.91	
FS_930603_1850	370	442.1	-2.97	
FS_930603_1750	359	439.2	-3.03	
FS_930603_1752	360	434.0	-2.92	
FS_930603_1855	371	432.2	-3.16	
FS_930603_1755	361	427.9	-2.76	
FS_930603_1756	362	427.5	-2.88	
FS_930603_1857	372	425.9	-2.77	
FS_930603_1900	373	425.3	-2.73	
FS_930603_1800	363	423.5	-2.77	
FS_930603_1905	374	418.2	-2.85	
FS_930603_1802	364	414.9	-2.72	
FS_930603_1906	375	409.0	-2.77	
FS_930603_1908	376	401.5	-2.77	
FS_930603_1915	377	398.0	-2.56	
FS_930603_1916	378	390.6	-2.19	
FS_930603_1918	379	385.4	-1.94	
FS_930603_1920	380	377.4	-1.40	

FS_930603_1925	381	371.7	-1.08
FS_930603_1928	382	365.7	-0.65
FS_930603_1930	383	359.3	0.10

*The EHL flow condtions were not recorded for files FS_930603_1850 through FS_930603_1815.

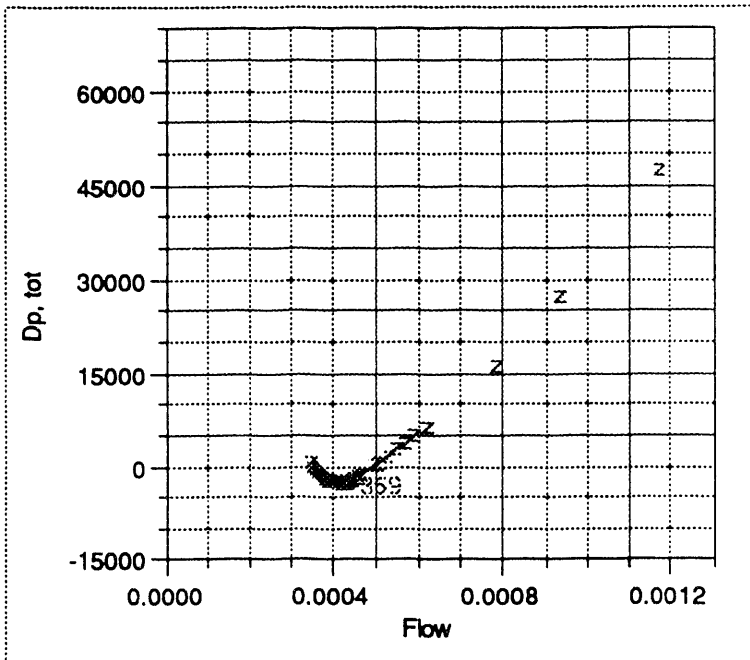

Figure 8-15, Demand curve 3.004, construction 2.0, rib channel

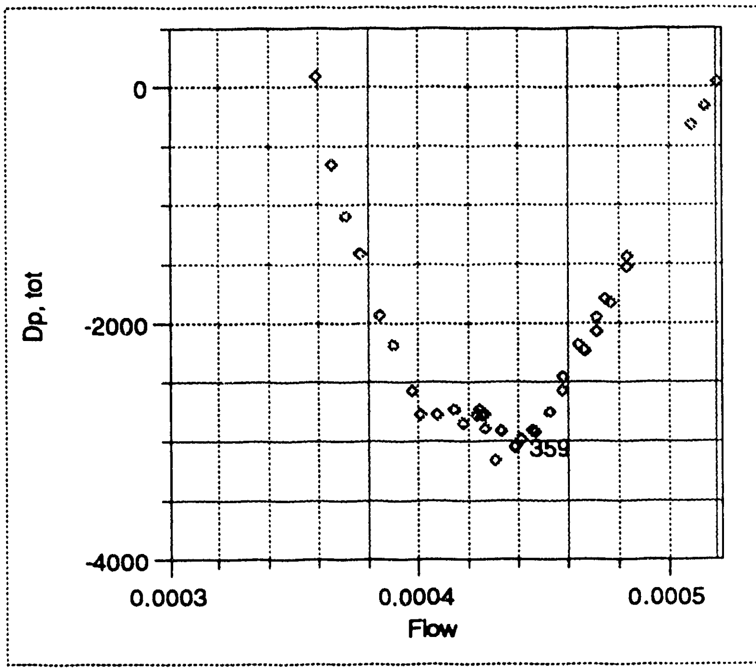

Figure 8-16, Detail of minima region for demand curve 3.004, construction 2.0, rib channel

Table 8-17.--Boundary conditions for demand curve 2.005, construction 4.0, open channel

File name	Row number	Inlet Temperature °C	EHL pressure kPa abs	Power kW	Energy balance
FS_930707_1123	468	60.86	138.6	30.54	0.845
FS_930707_1128	469	60.94	133.4	30.49	0.843
FS_930707_1139	470	60.17	129.0	30.43	0.843
FS_930707_1156	471	61.03	127.4	30.46	0.841
FS_930707_1209	472	60.65	126.1	30.52	0.864
FS_930707_1223	473	60.27	126.1	30.48	0.859
FS_930707_1229	474	60.53	126.2	30.50	0.867
FS_930707_1234	475	60.71	126.4	30.50	0.867
FS_930707_1239	476	61.07	126.4	30.62	0.864
FS_930707_1325	477	61.01	126.4	30.45	0.852
FS_930707_1329	478	60.15	126.2	30.52	0.861
FS_930707_1336	479	60.20	126.2	30.44	0.856
FS_930707_1353	480	60.86	126.3	30.47	0.857
FS_930707_1414	481	60.25	126.3	30.55	0.863
FS_930707_1418	482	60.42	126.3	30.53	0.863
FS_930707_1422	483	60.86	126.3	30.52	0.866
FS_930707_1426	484	60.89	126.3	30.53	0.861
FS_930707_1428	485	60.29	126.3	30.50	0.855
FS_930707_1432	486	60.23	126.6	30.54	0.861
FS_930707_1441	487	60.98	126.8	30.53	0.848
FS_930707_1520	488	60.13	126.2	30.56	0.861
FS_930707_1541	489	60.05	126.1	30.51	0.864
FS_930707_1550	490	60.78	126.1	30.53	0.879
Mean	...	60.58	127.3	30.51	0.8583
S	...	0.35	2.9	0.04	0.0093

Table 8-18.--Test data for demand curve 2.005, construction 4.0, open channel

File name	Row number	Flow cm³/s	Δp kPa	EHL condition
FS_930707_1123	468	1184.0	34.27	LO
FS_930707_1128	469	919.4	17.77	
FS_930707_1139	470	627.8	2.81	
FS_930707_1156	471	470.9	-3.58	
FS_930707_1441	487	411.1	-5.44	
FS_930707_1239	476	358.7	-7.12	NB
FS_930707_1325	477	358.2	-7.16	
FS_930707_1520	488	328.4	-7.91	
FS_930707_1209	472	323.0	-8.05	
FS_930707_1329	478	315.8	-8.27	
FS_930707_1541	489	295.3	-8.73	
FS_930707_1223	473	280.7	-8.97	
FS_930707_1336	479	277.6	-9.14	
FS_930707_1353	480	273.0	-9.18	
FS_930707_1550	490	266.6	-9.31	
FS_930707_1414	481	263.6	-9.38	
FS_930707_1418	482	254.3	-9.53	
FS_930707_1422	483	247.8	-9.32	
FS_930707_1426	484	247.8	-9.12	V
FS_930707_1229	474	246.3	-8.29	
FS_930707_1234	475	244.9	-8.19	
FS_930707_1428	485	242.4	-8.99	
FS_930707_1432	486	225.5	-7.77	

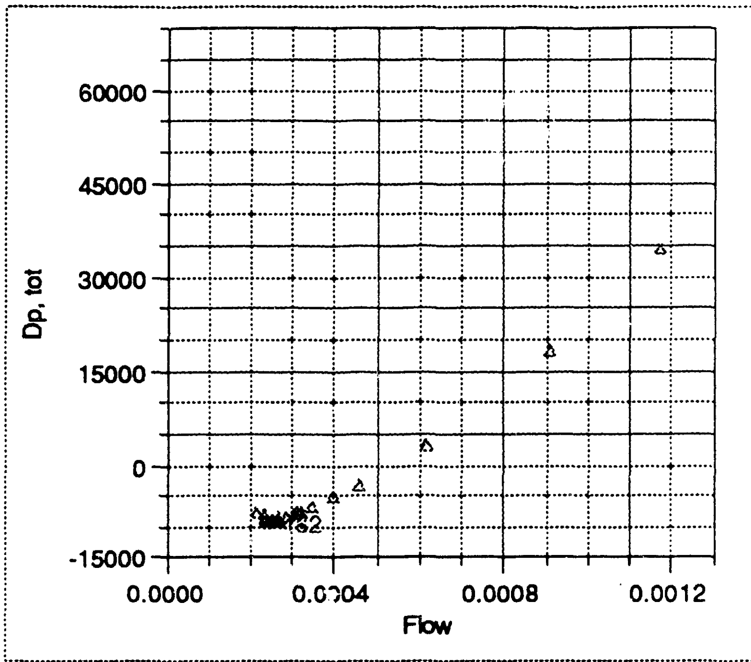

Figure 8-17, Demand curve 2.005, construction 4.0, open channel

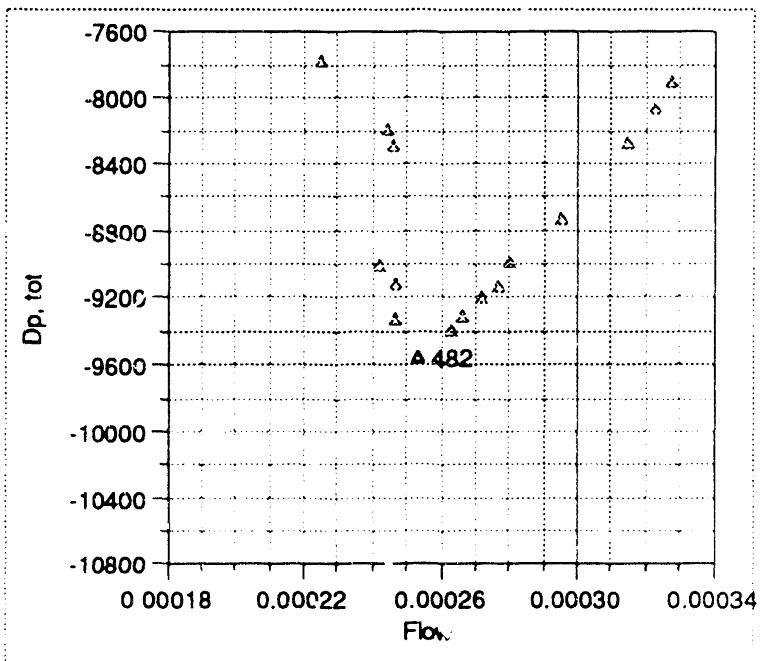

Figure 8-18, Detail of minima region for demand curve 2.005, construction 4.0, open channel

Table 8-19.--Boundary conditions for demand curve 2.006, construction 4.0, open channel

File name	Row number	Inlet Temperature °C	EHL pressure kPa abs	Power kW	Energy balance
FS_930712_1359	493	60.96	139.5	30.51	0.953
FS_930712_1431	494	60.75	134.1	30.47	0.953
FS_930712_1440	495	60.06	129.4	30.53	0.947
FS_930712_1454	496	60.06	127.7	30.47	0.946
FS_930712_1509*	497	61.10	126.5	30.87	0.965
FS_930712_1529	498	60.08	126.5	30.50	0.953
FS_930712_1534	499	60.08	126.2	30.52	0.964
FS_930712_1542	500	60.39	126.1	30.60	0.971
FS_930712_1553	501	60.86	126.1	30.46	0.980
FS_930712_1602	502	60.63	126.1	30.54	0.972
FS_930712_1608	503	60.20	126.1	30.59	0.981
FS_930712_1617	504	60.00	126.3	30.41	0.961
FS_930712_1621	505	60.18	126.5	30.46	0.966
FS_930712_1645	506	60.80	126.2	30.65	0.968
FS_930712_1653	507	59.99	126.1	30.48	0.977
FS_930712_1703	508	60.05	126.1	30.70	0.976
FS_930712_1714	509	59.97	126.1	30.50	0.977
FS_930712_1718	510	60.66	126.1	30.65	0.987
FS_930712_1724	511	60.98	126.1	30.42	0.973
FS_930712_1732	512	61.02	126.2	30.53	0.971
FS_930712_1735	513	60.50	126.3	30.66	0.962
FS_930712_1739	514	60.73	126.7	30.51	0.959
FS_930712_1757	515	60.39	126.1	30.36	0.979
FS_930712_1806	516	60.14	126.1	30.55	0.990
FS_930712_1820	517	60.30	126.1	30.51	0.979
FS_930712_1825	518	59.84	126.1	30.46	0.975
FS_930712_1827	519	59.60	126.1	30.48	0.981
FS_930712_1837	520	59.74	126.1	30.63	0.978
FS_930712_1841	521	59.95	126.2	30.64	0.974
FS_930712_1847	522	59.79	126.3	29.61	0.951
Mean	...	60.33	127.1	30.51	0.9690
S	...	0.43	2.8	0.20	0.0119

*The power and inlet temperature are higher than acceptable. This point has not been plotted.

Table 8-20.--Test data for demand curve 2.006, construction 4.0, open channel

File name	Row number	Flow cm^3/s	Δp kPa	EHL condition
FS_930712_1359	493	1189.4	36.48	LO
FS_930712_1431	494	926.2	19.37	
FS_930712_1440	495	616.5	2.93	
FS_930712_1454	496	473.7	-3.11	
FS_930712_1739	514	357.5	-7.09	
FS_930712_1621	505	331.5	-7.86	NB
FS_930712_1509	497	323.8	-8.10	NB
FS_930712_1529	498	323.5	-8.10	LO
FS_930712_1534	499	286.1	-9.07	LO
FS_930712_1645	506	286.1	-9.06	NB
FS_930712_1757	515	266.7	-9.50	
FS_930712_1542	500	265.7	-9.54	
FS_930712_1653	507	261.8	-9.62	
FS_930712_1[illegible]03	508	244.6	-9.95	
FS_930712_1[illegible]14	509	236.4	-10.10	
FS_930712_1553	501	232.3	-10.15	
FS_930712_1806	516	231.3	-10.17	
FS_930712_1718	510	230.8	-10.15	
FS_930712_1724	511	225.9	-10.25	
FS_930712_1602	502	225.3	-10.28	
FS_930712_1820	517	224.4	-10.27	
FS_930712_1732	512	223.4	-10.30	
FS_930712_1608	503	218.6	-10.41	
FS_930712_1825	518	215.6	-10.45	V
FS_930712_1735	513	212.5	-9.29	V
FS_930712_1841	521	211.4	-9.86	V
FS_930712_1827	519	211.3	-10.48	NB
FS_930712_1837	520	211.3	-10.07	V
FS_930712_1617	504	208.1	-9.38	V
FS_930712_1847	522	203.0	-9.90	V

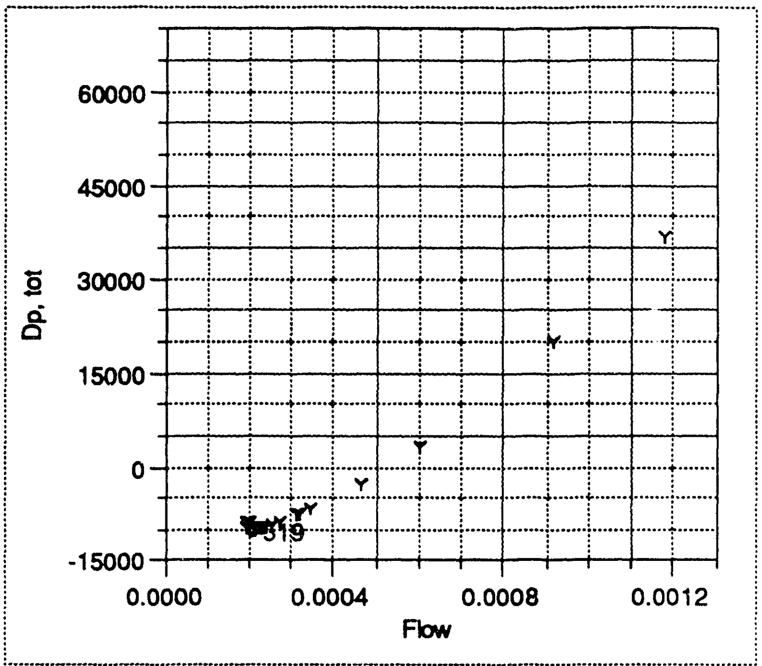

Figure 8-19, Demand curve 2.006, construction 4.0, open channel

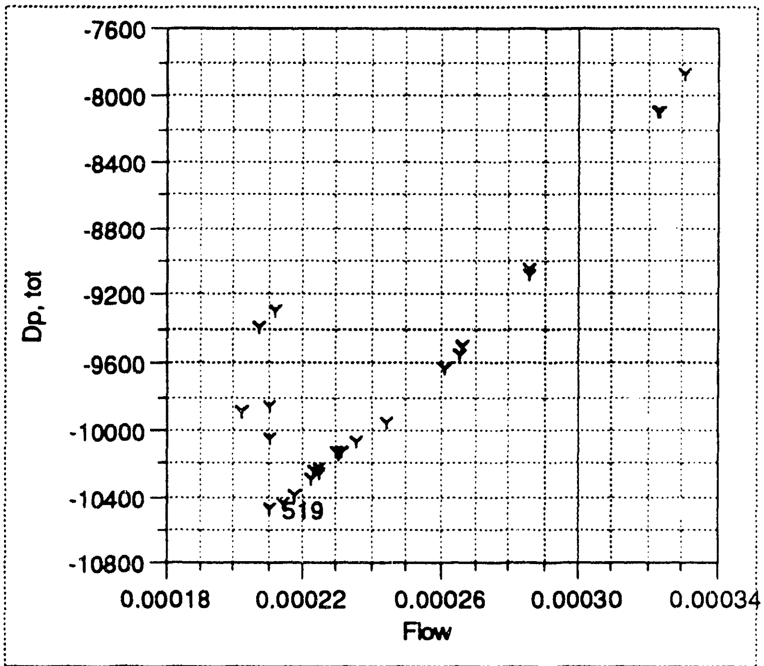

Figure 8-20, Detail of minima region for demand curve 2.006, construction 4.0, open channel

Table 8-21.--Boundary conditions for demand curve 2.007, construction 4.0, open channel

File name	Row number	Inlet Temperature °C	EHL pressure kPa abs	Power kW	Energy balance
FS_930715_1148	527	59.79	140.2	30.60	0.958
FS_930715_1153	528	59.78	138.7	30.61	0.956
FS_930715_1207	529	59.22	133.9	30.47	0.955
FS_930715_1216	530	61.12	130.5	30.55	0.944
FS_930715_1252	531	59.55	128.5	30.68	0.942
FS_930715_1324	532	59.62	129.7	30.51	0.956
FS_930715_1337	533	59.21	129.5	30.60	0.965
FS_930715_1400	534	59.79	129.4	30.30	0.972
FS_930715_1420	535	59.43	129.3	30.35	0.979
FS_930715_1430	536	59.87	129.3	30.47	0.984
FS_930715_1440	537	59.56	129.4	30.24	0.977
FS_930715_1442	538	59.39	129.3	30.90	0.996
FS_930715_1455	539	59.42	129.4	30.38	0.978
FS_930715_1459	540	59.40	129.4	30.32	0.975
FS_930715_1505	541	59.68	129.4	30.44	0.979
FS_930715_1525	542	59.69	129.8	30.45	0.964
FS_930715_1550	543	60.63	129.4	30.71	0.973
FS_930715_1600	544	59.20	129.3	30.57	0.975
FS_930715_1605	545	60.32	129.7	30.60	0.983
Mean	...	59.72	130.7	30.51	0.9689
S	...	0.50	3.3	0.16	0.0142

Table 8-22.--Test data for demand curve 2.007, construction 4.0, open channel

File name	Row number	Flow cm³/s	Δp kPa	EHL condition
FS_930715_1148	527	1178.7	36.78	LO
FS_930715_1153	528	1178.2	36.88	
FS_930715_1207	529	952.3	21.86	
FS_930715_1216	530	644.4	4.49	
FS_930715_1252	531	478.5	-2.78	
FS_930715_1324	532	331.0	-7.82	
FS_930715_1337	533	299.4	-8.71	NB
FS_930715_1400	534	268.8	-9.49	
FS_930715_1420	535	238.0	-10.14	
FS_930715_1430	536	229.7	-10.26	
FS_930715_1440	537	221.1	-10.43	
FS_930715_1455	539	217.6	-10.48	
FS_930715_1442	538	217.6	-10.45	
FS_930715_1550	543	212.1	-10.00	
FS_930715_1459	540	211.6	-10.58	V
FS_930715_1600	544	206.5	-10.45	
FS_930715_1505	541	206.4	-10.33	
FS_930715_1605	545	197.1	-8.64	
FS_930715_1525	542	196.1	-8.85	

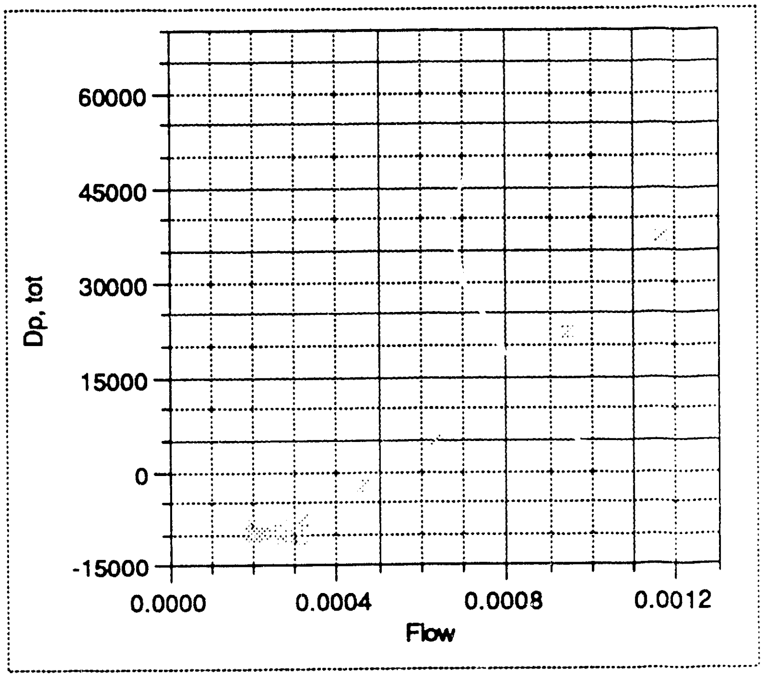

Figure 8-21, Demand curve 2.007, construction 4.0, open channel

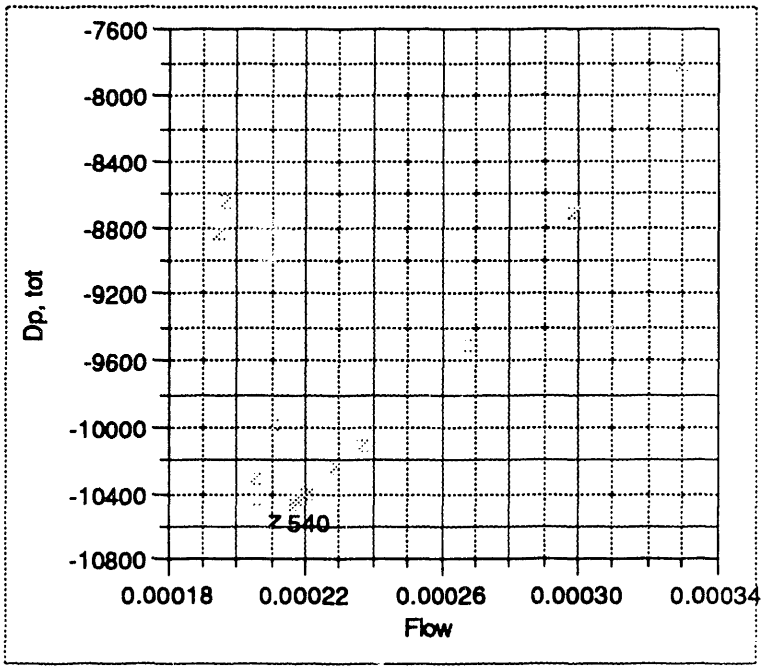

Figure 8-22, Detail of minima region for demand curve 2.007, construction 4.0, open channel

Table 8-23.--Boundary conditions for demand curve 2.008, construction 4.0, open channel

File name	Row number	Inlet Temperature °C	EHL pressure kPa abs	Power kW	Energy balance
FS_930716_0957	548	59.53	138.4	30.45	0.955
FS_930716_1010	549	59.59	137.8	30.47	0.948
FS_930716_1027	550	59.41	132.5	30.41	0.948
FS_930716_1101	551	59.69	130.7	30.37	0.945
FS_930716_1120	552	60.09	129.4	30.54	0.958
FS_930716_1134	553	60.15	129.2	30.45	0.968
FS_930716_1142	554	60.00	129.1	30.48	0.965
FS_930716_1204	555	59.22	129.1	30.67	0.975
FS_930716_1210	556	59.26	129.1	30.34	0.981
FS_930716_1218	557	59.30	129.1	30.50	0.993
FS_930716_1242	558	59.30	129.2	30.56	0.986
FS_930716_1250	559	59.32	129.3	30.58	0.983
FS_930716_1310	560	60.04	129.3	30.54	0.988
FS_930716_1355	562	59.79	129.3	30.48	0.991
FS_930716_1500	563	59.76	129.2	30.38	0.975
FS_930716_1505	564	59.56	129.0	30.40	0.954
FS_930716_1525	565	59.31	128.9	30.55	0.975
FS_930716_1530	566	59.33	129.0	30.02	0.973
FS_930716_1535	567	59.52	129.0	30.10	0.986
FS_930716_1545	568	60.09	129.2	30.50	0.962
FS_930716_1555	569	59.52	129.1	30.60	0.991
FS_930716_1600					
Mean	...	59.54	130.2	30.44	0.9706
S	...	0.42	2.7	0.15	0.0155

Table 8-24.--Test data for demand curve 2.008, construction 4.0, open channel

File name	Row number	Flow cm^3/s	Δp kPa	EHL condition
FS_930716_0957	548	1168.8	36.50	LO
FS_930716_1010	549	950.8	21.55	
FS_930716_1027	550	640.1	4.50	
FS_930716_1101	551	482.4	-2.48	
FS_930716_1120	552	332.3	-7.65	
FS_930716_1500	563	330.1	-7.68	
FS_930716_1134	553	295.2	-8.68	NB
FS_930716_1142	554	267.8	-9.36	
FS_930716_1505	564	265.1	-9.38	
FS_930716_1204	555	235.7	-10.05	
FS_930716_1525	565	234.3	-10.03	
FS_930716_1210	556	228.4	-10.18	
FS_930716_1530	566	222.5	-10.26	
FS_930716_1218	557	222.0	-10.27	
FS_930716_1535	567	217.3	-10.34	
FS_930716_1242	558	216.4	-10.36	V
FS_930716_1250	559	209.7	-10.45	
FS_930716_1545	568	209.2	-10.01	
FS_930716_1310	560	204.6	-9.85	
FS_930716_1555	569	202.9	-9.77	
FS_930716_1355	562	200.4	-9.50	
FS_930716_1600	570	196.1	-8.92	

*The EHL flow condtions were not recorded for files FS_930716_1500 through FS_930716_1600.

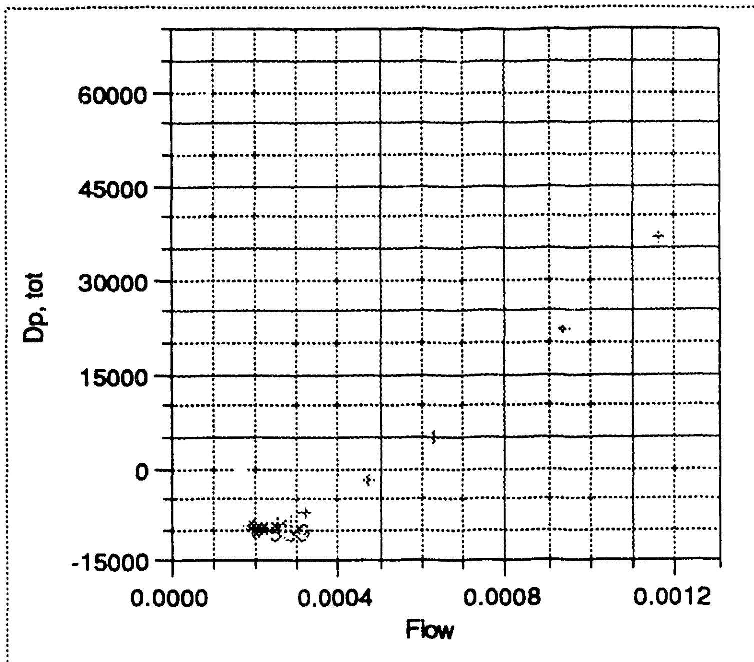

Figure 8-23, Demand curve 2.008, construction 4.0, open channel

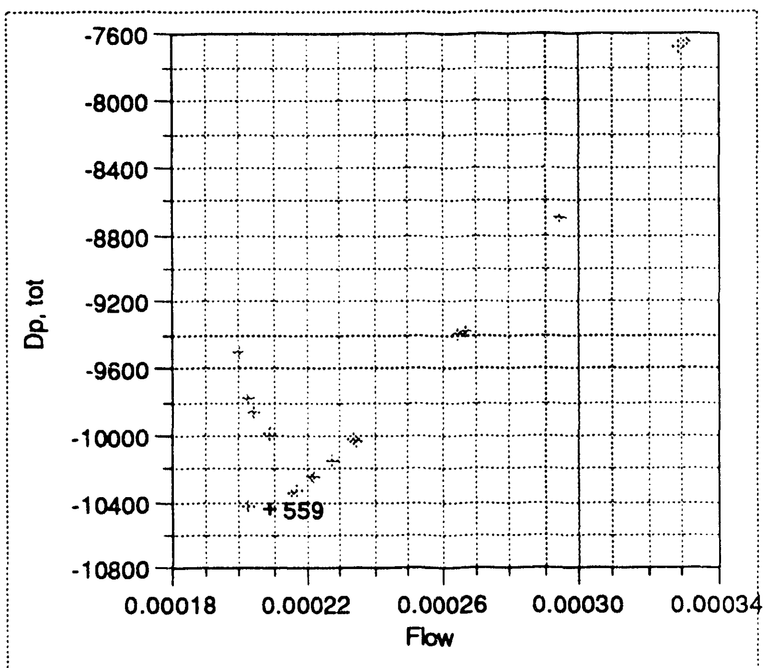

Figure 8-24, Detail of minima region for demand curve 2.008, construction 4.0, open channel

Table 8-25.--Boundary conditions for demand curve 2.009, construction 4.0, open channel

File name	Row number	Inlet Temperature °C	EHL pressure kPa abs	Power kW	Energy balance
FS_930720_0958	573	60.28	140.7	30.51	0.949
FS_930720_1007	574	59.79	135.6	30.51	0.948
FS_930720_1033	575	59.63	132.9	30.53	0.946
FS_930720_1044	576	59.80	130.8	30.52	0.946
FS_930720_1056	577	59.91	129.3	30.53	0.964
FS_930720_1106	578	59.78	129.1	30.51	0.958
FS_930720_1116	579	59.85	129.0	30.65	0.975
FS_930720_1125	580	59.55	129.0	30.58	0.970
FS_930720_1130	581	59.59	129.0	30.46	0.971
FS_930720_1135	582	60.15	129.1	30.27	0.976
FS_930720_1140	583	60.01	129.1	30.53	0.977
FS_930720_1145	584	59.95	129.2	30.52	0.976
FS_930720_1150	585	59.87	129.2	30.44	0.976
FS_930720_1200	586	59.75	129.3	30.44	0.968
FS_930720_1201	587	59.60	129.3	30.51	0.968
FS_930720_1205	588	59.65	129.3	30.50	0.976
FS_930720_1210	589	60.61	129.6	30.44	0.979
FS_930720_1232	590	60.47	129.5	30.61	0.953
FS_930720_1302	591	59.59	129.3	30.53	0.961
FS_930720_1346	592	60.46	129.1	30.26	0.963
FS_930720_1350	593	59.77	129.0	30.66	0.968
FS_930720_1400	594	59.70	129.0	30.63	0.961
FS_930720_1405	595	59.50	129.0	30.68	0.972
FS_930720_1415	596	59.60	129.1	30.43	0.973
FS_930720_1420	597	59.59	129.1	30.70	0.983
FS_930720_1435	598	59.66	129.1	30.46	0.980
FS_930720_1445	599	59.80	129.2	30.66	0.972
FS_930720_1446	600	59.29	129.2	30.42	0.975
FS_930720_1450	601	60.28	129.5	30.69	0.986
FS_930720_1530	602	59.51	129.4	30.63	0.985
FS_930720_1545	603	59.80	129.0	30.44	0.980
FS_930720_1550	604	60.63	129.1	30.39	0.979
FS_930720_1615	605	60.75	129.2	30.66	0.975
FS_930720_1630	606	60.10	129.1	30.55	0.974
FS_930720_1635	607	60.13	129.2	30.70	0.980
FS_930720_1636	608	60.64	129.2	30.41	0.980
FS_930720_1640	609	60.74	129.5	30.19	0.971
FS_930720_1643	610	60.17	129.8	30.69	0.970
Mean	...	59.95	129.8	30.52	0.9701
S	...	0.39	2.2	0.12	0.0107

Table 8-26.--Test data for demand curve 2.009, construction 4.0, open channel

File name	Row number	Flow cm^3/s	Δp kPa	EHL condition
FS_930720_0958	573	1166.2	36.30	LO
FS_930720_1007	574	944.9	21.49	
FS_930720_1033	575	639.9	4.45	
FS_930720_1044	576	486.0	-2.38	
FS_930720_1232	590	347.5	-7.29	
FS_930720_1056	577	327.4	-7.87	NB
FS_930720_1302	591	315.0	-8.21	
FS_930720_1106	578	294.9	-8.77	
FS_930720_1346	592	281.3	-9.11	
FS_930720_1350	593	266.1	-9.48	
FS_930720_1116	579	265.8	-9.49	
FS_930720_1400	594	248.3	-9.87	
FS_930720_1125	580	243.5	-9.96	
FS_930720_1405	595	235.8	-10.10	
FS_930720_1545	603	232.9	-10.15	
FS_930720_1130	581	232.4	-10.18	
FS_930720_1415	596	230.0	-10.21	
FS_930720_1550	604	230.0	-10.16	
FS_930720_1135	582	229.3	-10.22	
FS_930720_1420	597	222.0	-10.31	
FS_930720_1140	583	221.7	-10.34	
FS_930720_1615	605	219.8	-10.29	
FS_930720_1145	584	217.1	-10.42	
FS_930720_1435	598	216.1	-10.42	
FS_930720_1630	606	215.3	-10.39	
FS_930720_1150	585	212.9	-10.49	
FS_930720_1445	599	212.2	-10.48	
FS_930720_1200	586	208.4	-10.57	
FS_930720_1201	587	208.3	-10.57	
FS_930720_1636	608	208.1	-10.19	V
FS_930720_1635	607	207.8	-10.17	
FS_930720_1446	600	205.9	-10.58	
FS_930720_1450	601	204.3	-9.36	
FS_930720_1640	609	203.7	-9.11	
FS_930720_1643	610	203.3	-8.67	
FS_930720_1205	588	203.2	-10.19	
FS_930720_1530	602	198.4	-9.30	
FS_930720_1210	589	196.5	-8.81	

*The EHL flow condtions were not recorded for files FS_930720_1232 through FS_930720_1615.

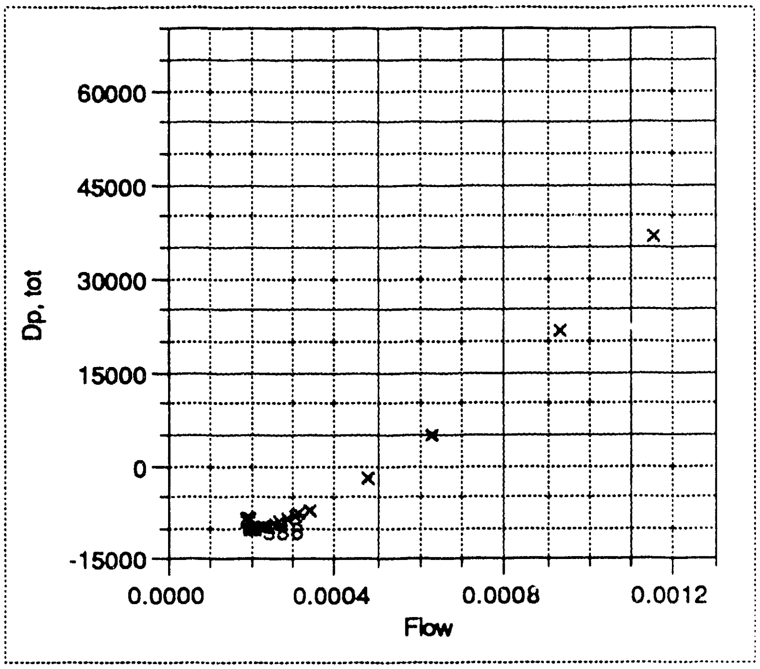

Figure 8-25, Demand curve 2.009, construction 4.0, open channel

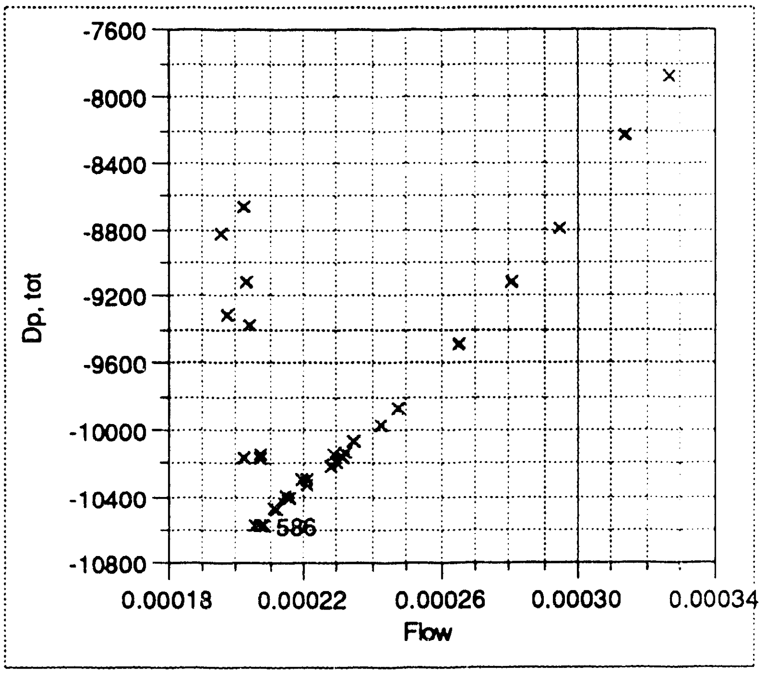

Figure 8-26, Detail of minima region for demand curve 2.009, construction 4.0, open channel

Isothermal Test Results

This appendix section contains a summary of the isothermal demand curve data for the four test sections. Information is presented in a graphical format in terms of the friction factor and the Reynolds number. Two different curves are provided on the graphs. The bold line is calculated from Equation 22, it is the expected curve for a smooth channel. The second curve is a linear fit of the plotted data. This second curve is provided with two confidence intervals. The larger intermal contains the data at 95% and the tighter interval contains the curve fit at 95%. Both these intervals do not include systematic errors.

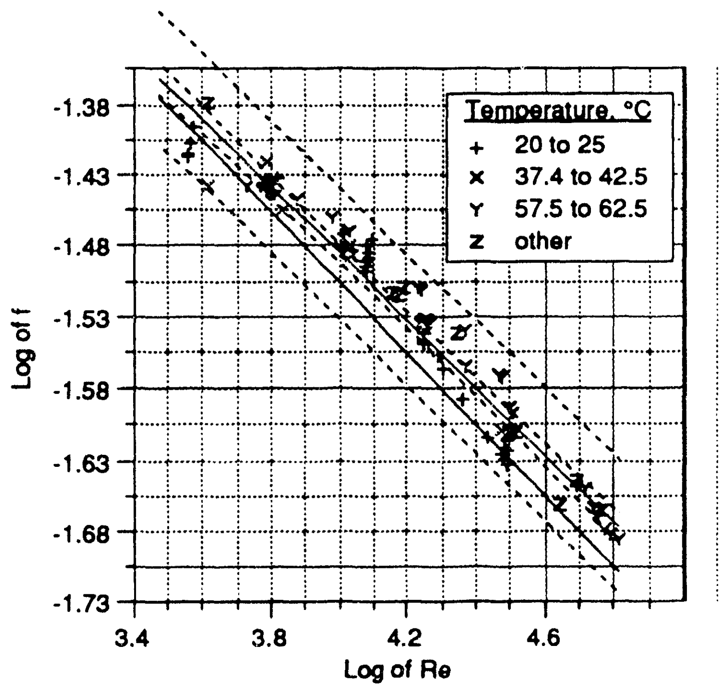

Figure 8-27, Isothermal demand curve for construction 1.0, open channel,

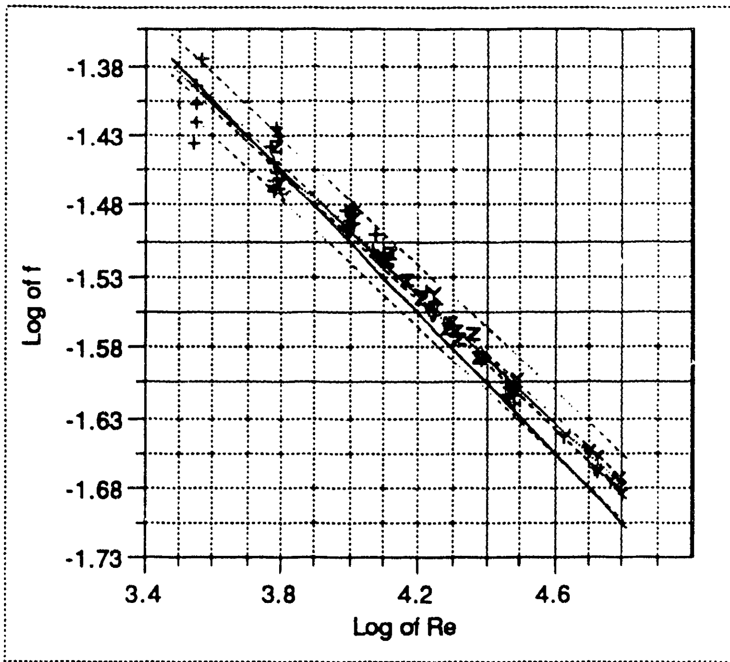

Figure 8-28, Isothermal demand curve for construction 2.0, rib channel

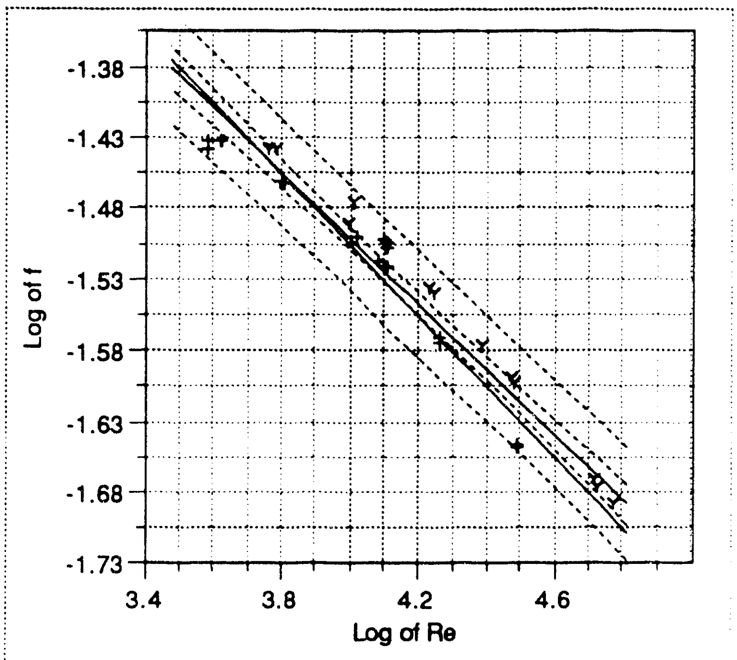

Figure 8-29, Isothermal demand curve for construction 3.0, open channel

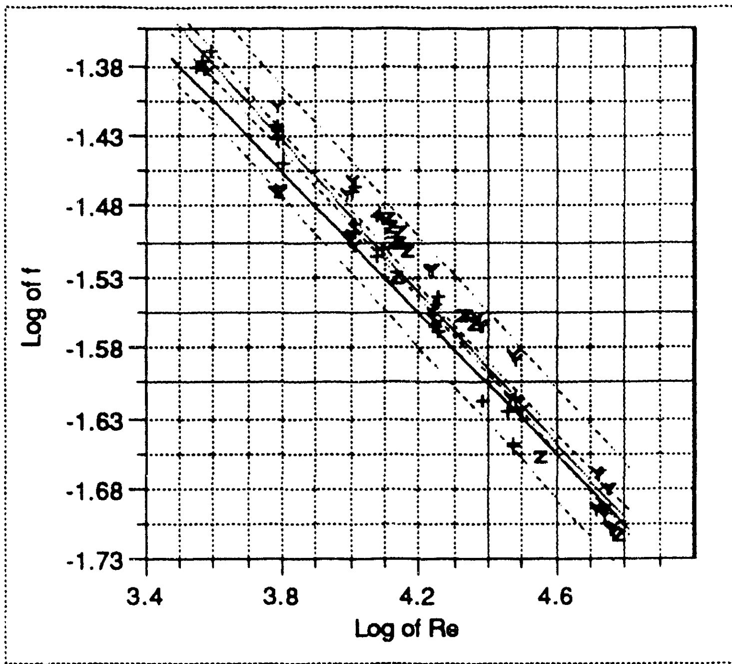

Figure 8--30, Isothermal demand curve for construction 4.0, open channel

WORKS CITED

1. American Society of Mechanical Engineers. 1987. *Pressure Measurement.*. New York: American Society of Mechanical Engineers, ASME/ASTM PTC 19.2-1987.

2. American Society of Mechanical Engineers. 1958. *Measurement of Time Measurement.*. New York: American Society of Mechanical Engineers, ASME/ASTM PTC 19.12-1958.

3. Automatic Flow Rate Controllers, Ferndale, Michigan: Kates Co. Bulletin 186.

4. Bankoff, S. G., S. C. Lee and A. Knaani. 1991. *Literature Review on Forced-Convection Subcooled Boiling (U),* Westinghouse Savannah River Company. WSRC-TR-91-98. February.

5. Bartolini, R., Bartolini, B. Guglielmini and E. Nannei, "Experimental Study on Nucleate Boiling of Water in Vertical Upflow and Downflow", *International Journal Multiphase Flow*, Volume 9, no. 2, pp 161-165, 1983.

6. Bergles, A. E., R. F. Lopina, and M. P. Fiori, 1967. Critical-Heat-Flux and Flow-Pattern Observations for Low-Pressure Water Flowing in Tubes. In *ASME Journal of Heat Transfer* 89: 69-74.

7. Bergles, A. E., and T. Dormer, Jr. 1969. Subcooled Boiling Pressure Drop with Water at Low Pressure. In *International Journal of Heat and Mass Transfer* 12: 459-70.

8. Blevins, Robert D., 1984. *Applied Fluids Dynamics Handbook.* New York: Von Nostrand Reihold Co.

9. Block, James A., Christopher J. Crowley, Francis X. Dolan, Richard G. Sam, and Brant H. Stoedefalke. 1990. *Nucleate Boiling Pressure Drop in an Annulus.* Hanover, N.H., Creare TN-499, October.

10. Bouré, J. A., A. E. Bergles, and L. S. Tong. 1973. Review of Two-Phase Flow Instability. *Nuclear Engineering and Design* 25: 165-92.

11. Bowring, R. W. 1962. *Physical Model, Based on Bubble Detachment, and Calculation of Steam Voidage in the Subcooled Region of a Heated Channel.* Oak Ridge, TN: Department of Energy, Office of Scientific and Technical Information. December. HPR-10.

12. Carrano, V., C. F. Fighetti, S. Kokolis, C. Maciuca, E. V. McAssey, Jr., D. G. Reddy, and B. W. Yang, September 1992, *Westinghouse Savannah River Company Flow Excursion Experimental Program, Single Annulus Tests, Transeint Test Program*, Columbia Unviersity HTRF, NY, CU-HTRF-T3B.

13. Chakroun, Walid, Robert P. Taylor, W. G. Steele, and H. W. Coleman. 1993. *Bias Error Reduction in Experimental Results by Presentation as a Ratio to a Baseline Experiment--A Heat Transfer Case Study*. Washington: American Institute of Aeronautics and Astronautics. AIAA 93-0922.

14. Cheh, H. Y., and C. F. Fighetti. 1990, *Westinghouse Savannah River Company Flow Excursion Experimental Program, Non-uniformly Heated Tube Tests*. New York: Heat Transfer Research Facility, Columbia University, (October) CU-HTRF-T5, CU-90-05.

15. Cheh, H. Y., and C. F. Fighetti. 1990. *Westinghouse Savannah River Company Flow Excursion Experimental Program, Parallel Flow Tests*. New York: Heat Transfer Research Facility, Columbia University, (June) CU-HTRF-T6, CU-90-04.

16. Cheh, H. Y., and C. F. Fighetti. 1990. *Westinghouse Savannah River Company Flow Excursion Experimental Program, Single Tube Uniformly Heated Tests*. New York: Heat Transfer Research Facility, Columbia University, (January) CU-HTRF-T4, CU-90-01.

17. Cheh, H. Y., and C. F. Fighetti. 1991. *Westinghouse Savannah River Company Flow Excursion Experimental Program, Single Annulus Tests, Steady State Test Program*. New York: Heat Transfer Research Facility, Columbia University, (July) CU-HTRF-T3A.

18. Cheh, H. Y., E. V. McAssey, Jr., and C. F. Fighetti. 1992, *Westinghouse Savannah River Company Flow Excursion Experimental Program, Single Tube Tests, Critical Heat Flux Test Program*. New York: Heat Transfer Research Facility, Columbia University, (September) CU-HTRF-T8.

19. Cheh, H. Y., E. V. McAssey, Jr., and C. F. Fighetti. 1993, *Westinghouse Savannah River Company Flow Excursion Experimental Program, Single Annulus Tests, Final Report*. New York: Heat Transfer Research Facility, Columbia University, (October) CU-HTRF-05-92.

20. Chen, K., P. K. Paul, and K. L. Barbour. 1990. *FLOWTRAN Benchmarking with Onset of Flow Instability Data from 1988 Columbia University Single-Tube OFI Experiment.*. Aiken SC: Westinghouse Savannah River Company, WSRC-RP-89-870 (June).

21. Chen, K.. 1991. *Benchmarking of FLOWTRAN with Mark-22 Mockup Flow Excursion Test Data from Babcock & Wilcox*. Aiken SC: Westinghouse Savannah River Company, WSRC-TR-91-629 (November).

22. Cheng, S. C., W. W. L. Ng, K. T. Heng, D. C. Groeneveld. 1978. Measurements of Transition Boiling Data for Water Under Forced Convective Conditions. *ASME Journal of Heat Transfer* 100: 382-4.

23. Cheng, S. C., W. W. L. Ng, and K. T. Heng. 1978. Measurements of Boiling Curves of Subcooled Water Under Forced Convective Conditions. *International Journal of Heat and Mass Transfer* 21: 1385-92.

24. Collier, John G. 1972. *Convective Boiling and Condensation.* 2d ed., New York, McGraw-Hill Book Co.

25. Coleman, Hugh W., and W. Glenn Steele, Jr., 1989. *Experimentalation and Uncertainty Analysis for Engineers.* New York: John Wiley & Sons.

26. Coutts, D. A. 1991. *Uncertainty and Calibration Analysis (U).* Aiken, SC.: Savannah River Laboratory. DOE. (March) WSRC-TR-91-106.

27. Coutts, D. A. 1993. *SRS OFI Program (U).* Aiken, SC: Savanah River Technology Center. DOE. draft.

28. Dormer Jr., Thomas, and Arthur E. Bergles. 1964. *Pressure Drop with Surface Boiling in Small-Diameter Tubes,* Cambridge: MIT Department of Mechanical Engineering 8767-31. September 1.

29. Dougherty, T., C. Fighetti, G. Reddy, B. Yang, E. McAssey, Jr., and Z. Qureshi. 1991. Flow Instability in Vertical Channels. In *Phase Change Heat Transfer,* HTD-Vol. 159. American Society of Mechanical Engineers. 177-86.

30. Feng, Qijing, and Klaus Johannsen. 1990. The High-Temperature Limit of the Transition Boiling Regime for Water in Vertical Upflow at Medium Pressure. In *9th International Heat Transfer Conference, Jerusalem, Israel, August 19-24, 1990,* 29-34.

31. Figliola, Richard S., and Donald E. Beasley. 1991. *Theory and Design for Mechanical Measurements.* New York: John Wiley & Sons.

32. Hewitt, G. F. 1982. Flow Regimes. In *Handbook of Multiphase Systems,* ed. Gad Hetsroni, chapt. 2. Hemisphere Publishing Corporation, Washington.

33. Hino, Ryutaro, and Tatsuhiro Ueda. 1985. Studies on Heat Transfer and Flow Characteristics in Subcooled Flow Boiling - Part 1. Boiling Characteristics. *International Journal of Multiphase Flow* 11: 269-281.

34. Hodges, M. W. 1971. Technical Memorandum from Aiken, to J. M. Boswell, Aiken, 8 April. *Effect of Rib on Burnout Heat Flux.* Aiken, SC.: Savannah River Laboratory. AEC. DPST-71-317.

35. Hodges, M. W. 1973. Technical Memorandum from Aiken, to J. M. Boswell, Aiken, 6 March. *Burnout Heat Flux with Rib Contact..* Aiken, SC.: Savannah River Laboratory. AEC. DPST-73-206.

36. *Insulating Button Assembly (Single Annulus with Fins)*, [1991]. fabrication drawing. New York: Columbia University Chemical Engineering Research Lab. 10 October. SR-2-T3-500-85.

37. Ishibashi, E., and K. Nishikawa. 1969. Saturated Boiling Heat Transfer in Narrow Spaces. *International Journal of Heat and Mass Transfer* 12: 863-94.

38. Jones, G. F., E. V. McAssey, Jr., B.W. Yang. 1993. Heat Conduction in an Energy-Generating Slab Subject to a Nonuniform Heat Transfer Coefficient. New York: Heat Transfer Research Facility, Chemical Engineering Research Laboratories, Columbia University. proposed for publication in *ASME Journal of Heat Transfer.*

39. JMP®. version 2.0.4. SAS Institute Inc. Cary NC.

40. Johnston, B. S., and J. M. Neff. 1990. Effect of Longitudinal Spacer Ribs on the Minimum Pressure Drop in a Heated Annulus, *Advances in Nuclear Reactors* 150: 159-64.

41. Johnston, B. S., A Sharon, and S. G. Bankoff. 1983. Boiling Heat Transfer in a Narrow Eccentric Annulus, Part II: Heat Transfer. *Transactions of the American Nuclear Society, Journal of Engineering for Power* 105: 748-54.

42. Johnston, B. S., A Sharon, Y. Kozawa, and S. G. Bankoff. 1983. Boiling Heat Transfer in a Narrow Eccentric Annulus, Part I: Dryout. *Transactions of the American Nuclear Society, Journal of Engineering for Power* 105: 742-47.

43. Johnston, B. S. 1990. Technical Memorandum from Aiken, SC, to J. E. Laurinat, Aiken, SC, 4 January. Savannah River Site, Aiken, SC. NES-ECS-890222.

44. Johnston, B. S. 1989. Subcooled Boiling of Downward Flow in a Vertical Annulus. In the proceedings of the 1989 National Heat Transfer Conference, HTD-Vol 109, Multiphase Flow, Heat and Mass Transfer 149-156.

45. Kawamura, Hiroshi, Fujio Tachibana, and Mamoru Akiyama, "Heat Transfer and DNB Heat Flux in Transient Boiling", *Forth International Heat Transfer Conference*, Paper B3.3, Paris-Versailles, France, August 31, 1970, pp 1 -11.

46. Klausner, J. F, B. T. Chao, and S. L. Soo. 1990. An Improved Method for Simultaneous Determination of Frictional Pressure drop and Vapor volume fraction in Vertical Flow Boiling. *Experimental Thermal and Fluid Science* 3: 404-415.

47. Kowalski, J. E., P. J. Mills, and S. Y. Shim. 1990. Onset of Nucleate Boiling and Significant Void on Finned Surfaces. In *Advances in Gas-Liquid Flows: Presented at The Winter Annual Meeting of the American Society of Mechanical Engineers, Dallas, Texas, November 25-30, 1990.* edited by J. H. Kim, U. S. Rohatgi, and A Hashemi. 405-11. New York: American Society of Mechanical Engineers.

48. Lahey, Jr., R. T. 1981. The Analysis of System Pressure Drop Characteristics During Flow Boiling. *Transactions of the American Nuclear Society* 38: 770-71.

49. Laurinat, J. E., 1991. Inter-office Memorandum from Aiken, SC, to J. D. Menna, Aiken, SC, 5 September. Savannah River Site, Aiken, SC. NES-ART-910338.

50. Ledinegg, M. 1938. Instability of Flow During Natural And Forced Circulation. *Die Wärme* 61: 891-898. trans. R. B. Lees. Chicago: Argonne National Laboratory.

51. Leung, J. C. M., *Critical Heat Flux under Transient Conditions: A Literature Survey*, NUREG/CR-0056, ANL-78-39, Argonne National Laboratory, June 1978.

52. Maulbetsch, John S., and Peter Griffith. 1965. *A Study of System-Induced Instabilities in Forced Convection Flows with Subcooled Boiling.* Cambridge: MIT, Department of Mechanical Engineering 5382-35. April 15.

53. Mirshak, S. 1955. *Two-Phase Flow in Tubes with Outlet Orifices.* Aiken, SC.: Savannah River Laboratory. AEC. (April) DP-109.

54. Mirshak, S. 1958. *Transient Flow of Boiling Water in Heated Tubes.* Aiken, SC.: Savannah River Laboratory. AEC. (July) DP-301.

55. Mirshak, S., W. S. Durant, and R. H. Towell, *Heat flux at Burnout*, DP-355, Savannah River Laboratory, Aiken, SC, February 1959.

56. Ozawa, M., K. Akagawa, and T Sakaguchi, "Flow Instabilities in Parallel-Channel Flow Systems of Gas-Liquid Two-Phase Mixtures", *International Journal of Multiphase Flow*, Vol 15, No 4, 1989, 639-657.

57. Ramilison, J. M., and J. H. Lienhard. 1987. *Transition Boiling Heat Transfer and the Film Transition Regime.* ASME Journal of Heat Transfer 109: 746-752.

58. Ramilison, Jean Masy. 1985. Transition boiling heat transfer and the film-transition regime. Ph. D. diss, University of Houston.

59. Rogers, J. T., M. Salcudean, Z. Abdullah, D. McLeod, and D. Poirier, "The Onset of Significant Void in Up-Flow Boiling of Water at Low Pressure and

Velocities", *International Journal Multiphase Flow*, Volume 30, No. 11, pp 2247-2260, 1987.

60. Rohsenow, Warren M., and Harry Choi. 1961. *Heat, Mass and Momentum Transfer.* Englewood Cliffs, NJ: Prentice-Hall Inc.

61. Rush, G. C., J. E. Blake, R. M. Privette, and C. A. Nash. 1990. *Flow Excursion Experiments With a Savannah River Mark 22 Fuel Assembly Mockup, Executive Summary.* Alliance, OH: Babcock & Wilcox Research & Development Division, RDD:90:4427-13-01-01:01 (February).

62. Saha, P. and N. Zuber. 1974. Point of Net Vapor Generation and Vapor Void Fraction in Subcooled Boiling. In *Proceedings of the 5th International Heat Transfer Conference, Tokyo, Japan, September 3-7, 1974*, 175-79.

63. Sharon, A., L. Chen, and S. G. Bankoff. Convective Boiling Heat Transfer in a Concentric Annular Gap. In International Journal of Multiphase Flow 9: 545-60.

64. Streeter, Victor L., and E. Benjamin Wylie. 1979. *Fluid Mechanics.* 7th ed., New York: McGraw-Hill Book Co.

65. Teel Industrial Series Operating Instructions & Parts Manual Booster Pumps, Chicago, IL, Dayton Electric Mfg. Co. Form 5S1843-04223

66. Witte, L. C., and J. H. Lienhard. 1987. On the Existence of Two 'Transition' Boiling Curves. *International Journal of Heat and Mass Transfer* 25: 771-79.

67. Whittle, R. H. and R. Forgan. 1967. A Correlation for the Minima in the Pressure Drop Versus Flow-Rate Curves for Sub-Cooled Water Flowing in Narrow Channels. *Nuclear Engineering and Design* 6: 89-99.

68. Zigrang, D. J., and N. D. Sylvester. 1982. Explicit Approximations to the Solution of Colebrook's Friction Factor Equation. *American Institute of Chemical Engineers Journal* 28 (May, no. 3) 514-15.

69. Dorra, H., S. C. Lee, and S. G. Bankoff. 1993. *A Critical Reviewve Models for the Onset of Significant Boid in Forceed-Convection Subcooled Boiling (U).* Aiken SC, Savannah River Technology Center. DOE. (June) WSRC-TR-93-404.

70. not used

71. Chen, K., and J. F. King. 1988. *FLOWTRAN Benchmarking with Onset of Flow Instability Data from 1963 Columbia University Experiment.* Aiken SC: Savannah River Laboratory, DOE, DPST-88-666 (October).

72. Thom, J. R. S., W. M. Walker, T. A. Fallon, and G. F. S. Reising. 1965. "Boiling in Sub-cooled Water During Flow Up Heated Tubes or Annuli. In *Symposium on Boiling Heat Transfer in Steam Generating Units and Heat Exchangers, Manchester, England, September 15-16, 1965.* paper 6, 226-46.

73. Workbench™. version 3.0.4 Mac II. Strawberry Tree Inc. Sunnyvale Ca.

74. Brown, W., Harold Midlin, and C. Y.Hu. 1991. Nonferrous Alloys. Vol. 3. *Aerospace Strutural Metals Handbook.* West Lafayette, IN: CINDAS, Purdue University

75. Yang, Bao-Wen 1992. letter from New York, to Allan Coutts, Aiken, SC, 7 April. Columbia University, New York. AX-721092. Task 92-92-033-1.

76. Aleman, S. E., M. V. Gregory, L. L. Hamm, L. D. Koffman, R. E. Pevey, W. H. Reed, and F. G. Smith. 1989. *FLOWTRAN: An Algorithm for Describing the Thermal-Hydraulic Behavior of SRP Assemblies (U).* Aiken, SC.: Savannah River Laboratory. DOE. (15 September) DPSTM-140, Revision 0, Version 16.2.

77. Beaton, C. F., and G. F. Hewitt. 1989. *Physical Property Data for the Design Engineer.* New York: Hemisphere Publishing Corp.

78. Gehrke, Volker, and S. G. Bankoff. 1993. *Stability of Forced-Convection Subcooled Boiling in Steady-State and Transient Annular Flow (U).* Aiken SC: Savannah River Technology Center. DOE. (June) WSRC-TR-93-406.

END

DATE
FILMED
12/02/93